Development of Novel Cupric-Tirapazamine Liposomes for Hypoxia Selective Therapy

Vera L.D. Silva

University of East Anglia

School of Pharmacy

Norwich Research Park

Norwich, NR4 7TJ

September 2018

A thesis submitted in fulfilment of the requirements for the degree of Doctor of Philosophy of the University of East Anglia.

Declaration

I declare that the research contained in this thesis, submitted for the degree of Doctor of Philosophy, is original, except where due reference is made to other authors, and has not previously been submitted by me for a degree at this or any other universities.

Vera L.D. Silva

Acknowledgements

It's funny how people take pictures of the mountain climbers, only when they reach the top. They are smiling, ecstatic, triumphant. They don't take pictures along the way, because who wants to remember the rest of it? We push ourselves because we have to, not because we like it. The relentless climb of taking it to the next level – nobody takes pictures of that, nobody wants to remember, we just want to remember the view from the top, that moment at the edge of the world. Ironically, that's what keeps us climbing and in the end it's worth the smile, the joy…it's worth anything. Pursuing a PhD is not for the faint-hearted, but for the brave climbers. A rollercoaster of emotions and rationale, that circumvents into a finale of hard-work, perseverance and most importantly, self-achievement and personal growth - "*Success is stumbling from failure to failure with no loss of enthusiasm*" (Winston S. Churchill). I am proud of all that I have accomplished, but success is not a one-person job. I am wholeheartedly grateful to have so many unique and astonishing people in my life that made this climb more encouraging and worthwhile.

I would first like to thank my supervisor, **Dr. Wafa Al-Jamal** for giving me the opportunity to pursue my PhD and for her supervision. I am sincerely thankful to **Prof. Yaroslav Khimyak** for his mentoring and support, especially during the 'writing up' period. Your sincerity and jokes kept me going when things were hard.

I am thankful to **Dr. Chris Morris** for his support and remarkable sense of humour. It was a pleasure learning with you. I am also very grateful to **Dr. Leanne Stokes** for her kindness, unique enthusiasm, and constructive feed-back. To **Dr. Jesús Angulo**, **Dr. László Fabian** and **Dr. Aram Saeed** for always having a kind word. You undoubtedly made me feel welcome at UEA.

I extend my gratitude to **Dr. Julie Sanderson** for the fundamental help with the hypoxia experiments and kind feedback. To **Dr. Andrew Mayes** for the use of his laboratory facilities, during the liposome work; and to **Dr. Paul Thomas** for his patience, advice and training on fluorescence microscopy. I also give a special thanks to the UEA staff. **Jane and Paul**, for their compelling help with all the ordering; **Roy Carter** for always fixing our extremely urgent IT problems with a smile and to **Pete Mayes**…Pete, thank you for always lending a friendly hand, for your hard-work and genuine joy.

Part of this experience compels the responsibility of supervising and teaching fellow students. I was lucky enough to be surrounded by fantastic people that gave me the opportunity to teach, while also learning. To **Raphael, Fuad and Richard**, for the long hours in the DLS, talking about life and mostly food. You made me feel welcome at the beginning of my PhD. **Mene**, long hours, hard work, and so many spheroids…Thank you for teaching me and for the patience throughout the most stressful moments. **Mous**, my star student, your curiosity, eagerness to learn and genuine kind heart were an inspiration. I am so proud of you! My sweet **Gemma**, you made me laugh. It was a pleasure guiding you through your project. **Duong**, I hope you enjoyed your time at UEA, it was a pleasure to work with you. **Chris and Sakib**, it was tough, but we made it! I sincerely wish you all the best.

One of the interesting things about research is the amount of people that come and go, leaving their unique mark. With this, I thank my fellow lab mates and all the UEA pharmacy colleagues, **Remy, Mahmoud, Hui, Valeria, Susana, Champ, Muqdad, Mehrnaz and Carl**, that one way or another, always had a smile or a friendly conversation to keep the days going. Many thanks to the '**Medchem Folks'.** I am particularly grateful to **Dr. Andrew Beekman** and **Dr. Marco Comminetti** for their tremendous patience throughout the HPLC drama, their kindness and willingness to help. You saved me many times and for that I am sincerely grateful.

My warmest gratitude goes to my Portuguese buddies **Raquel, Cris, Ritinha and Sarita**. Despite the distance, you always knew me, how to make me smile when things got tough, and remember 'the good old days'. **Raquel**, thank you for listening to me on the grey days and reminding me of my true value. You all gave a true meaning to the untranslatable feeling *Saudade*. *Desejo-vos uma felicidade tremenda, um bem-haja!* To **Ana**, for bringing a bit of Portugal to Norwich. I am sincerely grateful for your support towards the end of my PhD. I wish you all the best.

My deepest appreciation goes to **Elise**, 'bring on the edge'. I miss our hilarious conversations. I hope to see you one day in sunny Australia and share those amazing mangoes with you. Have fun!

I had the pleasure to meet unique people throughout my PhD, but nobody comes close to my Awesome Norwich Family. To **Gerard**, you were always like a big brother to me. Thank you for all the amazing advice, for seeing eye-to-eye, for the patience and the long TV-show discussions, over pineapple pizza. To **Mar**, you are a true inspiration. Your love for life and for science, your genuine gigantic heart and generosity are what make you truly special. I am so lucky to have met you and shared so much with you. To **Ash**, it was a pleasure working with you and I am grateful to call you a friend. Thanks for all the laughs and fun, singing in the lab. I wish you all the best in the future. To **Liao**, the pillar for anti-stress. I am so happy we got to share this journey together, since day 1. Thank you for always having a helping hand and a kind word, when needed. *Kudos* to you for putting up with all the girly emotion in the office. To **Lučka**, the beacon of joy. Thank you for sharing that unique and contagious light you have. For your kind smile, your warmth, for just sharing the silence. To **Noelia**, my Noe, my princess. I am so grateful for your kind heart, your dedication and your genuine friendship. Your enthusiasm for science is contagious. Never lose that smile, that passion, that fundamental caring, let them drive you. They drove me!

To **Franklin**…I am so fortunate to have you in my life. To have shared this journey with you. I am thankful for all the joy, the affection, the encouragement, the laughter and for growing up together. Thank you for always challenging me, for telling me what I needed to hear and not what I wanted to hear, even in the darkest of times. You are a true mentor, your determination moves mountains and for that I am inspired and most grateful.

Last, my sincerest appreciation goes to my dearest parents, **Rosário and Tó,** and to my brother, **Carlos**. There are no words to describe how grateful I am to you. This journey would not have been possible without your unconditional love, patience, support and friendship. All of my accomplishments were inspired by your values of honest hard-work, perseverance and generosity, which made me the strong person I am today. I am forever grateful and this thesis is a dedication to you!

Abstract

Hypoxia prodrugs have become an emerging topic in cancer therapeutics. Tirapazamine (TPZ) is the most advanced and potent hypoxia prodrug to date, but its clinical outcome has been controversial, due to poor cellular uptake, rapid metabolic reduction and limited tumour diffusion. The reassessment of this drug may offer alternative strategies to overcome its current biological limitations, maintaining its strong selective cytotoxicity. Previous studies have shown that the development of metal-complexes can efficiently modulate the physicochemical properties of its ligand, possibly enhancing their cellular activity.

Herein, TPZ cupric-complexes [$Cu(TPZ)_2$] were synthetised and characterised with the aim of redefining TPZ. $Cu(TPZ)_2$ showed good stability over a wide range of conditions and its fluorescent properties provided an invaluable tool to monitor cellular uptake and localization. In addition, $Cu(TPZ)_2$ exhibited higher lipophilicity and more electronegative redox-potential, compared to TPZ, which conferred potent hypoxia selectivity against a range of prostate cancer cells. More promisingly, the complex showed higher potency in three-dimensional tumour spheroids, and induced S-phase cell cycle arrest, followed by marked cell apoptosis.

This work also focused on the development of $Cu(TPZ)_2$-loaded liposomes, aiming to improve on TPZ retention. The effect of pH, temperature, PEGylation, lipid composition, and lipid:complex ratio on drug loading was systemically studied. Likewise, increased complex loading formed small precipitate aggregates, within the liposomal core, which provided better TPZ retention. The liposomes exhibited good stability over time and sustained release. Furthermore, they displayed potent *in vitro* activity that was formulation-dependant, in both 2D and 3D environments. $Cu(TPZ)_2$-loaded liposomes maintained hypoxia selectivity in 2D models and provided improved cytotoxicity against tumour spheroids, probably due to slower reduction and penetrative capacity, compared to $Cu(TPZ)_2$ alone. In conclusion, these novel $Cu(TPZ)_2$-loaded liposomes could offer a promising approach to overcome TPZ's biological shortcomings, offering a versatile delivery system for hypoxia targeted therapy.

List of publications

1. Vera L. Silva, Wafa' T. Al-Jamal. *Exploiting the cancer niche: Tumour-associated macrophages and hypoxia as promising synergistic targets for nano-based therapy*, J Control Release (2017) https://doi.org/10.1016/j.jconrel.2017.03.013.

2. Vera L. Silva, Ashkan Dehsorkhi, Moustafa Abdelhamid Cédrik-Roland Koffi, Duuamene Nyimanu Christopher J. Morris and Wafa' T. Al-Jamal. *Enhanced selectivity, cellular uptake, and in vitro toxicity of an intrinsically fluorescent copper-tirapazamine nanocomplex for hypoxia targeted therapy.* Under revision, ACS Bioconjugate Chemistry.

3. Vera L. Silva, Franklin L. Nóbrega and Wafa' T. Al-Jamal. *Development, characterization and therapeutic potential of novel Cu(TPZ)$_2$-loaded liposomes for selective hypoxia cancer therapy.* In preparation.

List of presentations/posters/awards

1. European Nanomedicine Meeting – London, April 2017
Best Oral communication*: Targeting Hypoxia in 3D Tumour Spheroids Using Novel Copper-Tirapazamine Liposomes***. Prize Award by SF Nano**

2. 7th APS International PharmSci 2016 – Glasgow, September 2016
Poster: V. L.Silva, A. Dehsorkhi and W.T. Al-Jamal. *Tirapazamine Loaded Nanocontainers for Hypoxia Targeted Therapy in Prostate Cancer.*

3. Pharmacy Research day – UEA, Norwich, United Kingdom, July 2016
Three-minute thesis competition – runner up winner

4. 24th Biennial Congress of The EACR, Manchester, July 2016
Poster: V.L.Silva and W.T. Al-Jamal. *Development of Novel Tirapazamine-Loaded Liposomes for Hypoxia-Targeted Therapy.*

Table of contents

List of figures

Chapter 1:

Chapter 2:

Chapter 3:

Chapter 4:

Chapter 5:

Chapter 6:

List of tables

List of abbreviations

^{18}F Fludeoxyglucose

5-FC 5-fluorocytosine

a.u. Arbitrary units

ADT Androgen Deprivation Therapy

AR Androgen Receptor

ATR Attenuated Total Reflectance

Au Gold

AVT Angiogenesis Vessel-Targeting

BTZ Benzotriazinyl

Calcd Calculated

Ce6 Chlorin e6

CHCA α-cyano-4-hydrocinnamic acid

CHN Carbon-Nitrogen-Hydrogen

Chol Cholesterol

COX cyclooxygenase

CRPC Castrate-Resistant Prostate Cancer

Cryo-EM – Cryogenic Electron Microscopy

CT-DNA Calf-Thymus DNA

Cu Copper

Cu(ATSM) Copper(II)-diacetyl-bis(N_4-methylthiosemicarbazone

Cu(II) Copper – oxidation state II

Cu(TPZ)$_2$ Cupric-tirapazamine

ddH_20 Deionized water

DDS Drug Delivery System

DFO Desferrioxamine

DHB 2,5-Dihydroxybenzoic Acid

DHT Dihydrotestosterone

DLS Dynamic Light Scattering

DMF Dimethylformamide

DMSO Dimethylsulfoxide

DNA Deoxyribonucleic acid

DOPC 1,2-dioleoyl-s*n*-glycero-3-phosphocholine

Dox Doxorubicin

DPPC 1,2-dipalmitoyl-s*n*-glycero-3-phosphocholine

DSC Differential Scanning Calorimetry

DSPC 1,2-distearoyl-s*n*-glycero-3-phosphocholine

DSPE 1,2-distearoyl-s*n*-glycero-3-phosphoethanolamine

DSPE- PEG$_{2000}$ 1,2-distearoyl-sn-glycero-3-phosphoethanolamine polyethylene glycol 2000

E_0' Standard Reductive Potential

EDTA Ethylenediaminetetraacetic Acid

EE Encapsulation Efficiency

EGCG Epigallocatechin 3-gallate

EGFR Epithelial Growth Factor Receptor

EPC Dierucoylphosphatidylcholine;

EPC Egg Phosphatidylcholine

EPG Egg Phosphatidylglycerol

EPR Enhanced Permeability and Retention

EtOH Ethanol

FACS Fluorescence-Activated Cell Sorting

FAT Freeze-thaw Cycling

FBS Fetal Bovine Serum

FDA Food and Drug Administration

FI Fluorescent Intensity

FS forward scatter

FTIR Fourier Transform Infrared

GCV Ganciclovir

GLUT-1 Glucose Transporter

GUV Giant Unilamellar Vesicle

H_2O_2 Hydrogen Peroxide

HA Hyaluronic acid

HA, Hemaglutinin

HAP Hypoxia Activated Prodrug

HBS HEPES-Buffered Saline

HCl Hydrochloric acid

HCR Hypoxia Cytotoxicity Ratio

HDL High Density Lipoproteins

HEPES 4-(2-hydroxyethyl)-1-piperazineethanesulfonic acid

HER-2 Human Epidermal Growth Factor Receptor 2

HIF-1 Hypoxia-inducible factor 1

HK-1 Hexokinase

HNSCC Head and Neck or Skin Squamous Cell Carcinoma

HPLC High Performance Liquid Chromatography

HRE Hypoxia Responsive Elements

HSPC Hydrogenated Soy Phosphatidylcholine

HSPG Hydrogenated Soy Phosphatidylcholine

I.P. Intraperitoneal

I.V. Intravenous

IFN- γ Interferon Gamma

IHC Immunohistochemistry

IL Interleukin

kB Nuclear Factor Kappa-B

LHRH Luteinizing Hormone-Releasing Hormone

LPS Lipopolysaccharide

LUV Large Unilamellar Vesicles

MAC macrophage

MALDI-TOF Matrix Assisted Laser Desorption Ionization Time-Of-Flight

MAPK Mitogen-Activated Protein Kinase

MCTS Multicellular Tumour Spheroids

MDR Multidrug Resistance

MeOH Methanol

MHC Major Histocompatibility Complex

MLV Multilamellar Vesicle

mmHg Millimeter of Mercury

MMP Matrix Metalloproteinases

MMP' Mitochondrial Membrane Potential

MnO_2 Manganese Peroxide

MoA Mechanism of Action

MOF Metal-Organic Frameworks

mRNA Messenger Ribonucleic acid

MS Mass Spectrometry

MSC Methylselenocysteine

MTD Maximum Tolerated Dose

mTOR Mechanistic Target of Rapamycin

MTP Muramyl Tripeptide

mV Milivolt

MVV Multivesicle

MWCO Molecular Weight Cut-Off

N.A. Not Applicable

N.D. Not determined

NaCl Sodium Chloride

NADH Nicotinamide Adenine Dinucleotide

NADPH Nicotinamide Adenine Dinucleotide Phosphate

NaOH Sodium Hydroxide

NMR Nuclear Magnetic Resonance

NO Nitric Oxide

NP Nanoparticle

NQO1 Quinone Oxidoreductase

NSCLC Non-Small Cell Lung Cancer

OH Hydroxyl group

P/S Penicillin/Streptomycin

PA Phospatidic Acid

PARP Poly [ADP-ribose] Polymerase

PBS Phosphate-Buffered Saline

PC Phosphatidylcholine

PCa Prostate Cancer

PCL Polycaprolactone

PCS Photon Correlation Spectroscopy

PD Pharmacodynamics

PDI Polydispersity Index

PDT Photodynamic Therapy

PE Phosphatidylethanolamine

PEG Polyethylene Glycol

PET Positron emission tomography

PFA Paraformaldehyde

PG Phosphatidylglycerol

PHD Prolyl Hydroxylase

PI Phosphatidylinositol

PI3K Phosphatidylinositol 3-Kinase

PK Pharmacokinetics

PL Phospholipids

PLGA Poly (lactic-co-glycolic acid)

pO_2 Oxygen Pressure

PS Phosphatidylserine

PSA Prostate Specific Antigen

PSMA Prostate Specific Membrane Antigen

PSMA Prostate Specific Membrane Antigen

PTT Photothermal Therapy

Rb Retinoblastoma

RES Reticuloendothelial System

RGD Arginine-Glycine-Aspartic Acid Peptide

RNA Ribonucleic acid

ROS Reactive Oxygen Species

RP-HPLC Reverse Phase High Performance Liquid chromatography

RPMI Roswell Park Memorial Institute Medium

RT Radiation Therapy

SAR Structure-activity Relationship

SAX Small Angle X-ray Scattering

SCC Squamous Cell Carcinoma

SCLC Small Cell Lung Cancer

SD Standard Deviation

SEC Size Exclusion Chromatography

siRNA Small Interfering RNA

SM sphingomyelin

SPION Superparamagnetic Iron Oxide Nanoparticles

SS Side Scattering

SUV Small Unilamellar Vesicles

SVI Small Volume Incubation

TAM Tumour Associated Macrophages

TEM Transmission Electron Microscopy

Tf Transferrin

TFH Thin-lipid film hydration

TKI Tyrosine Kinase Inhibitor

TLC Thin-layer chromatography

TLR Toll-like receptors

T_M Transition temperature

TNFα Tumour Necrosis Factor Alpha

ToF Time of Flight

TPZ Tirapazamine

UV/Vis Ultraviolet Visible

VEGF Vascular Endothelial Growth Factor

$W_{18}O_{49}$ Tungsten Oxide

WHO World Health Organization

αvβ3 Vascular Integrin Alpha v Beta

Z-ave Intensity Based Harmonic Mean Size

Chapter 1

Introduction

Part of this chapter has appeared in the following publication:

Silva, V.L and Al-Jamal, Wafa' T. Exploiting the cancer niche: Tumour-associated macrophages and hypoxia as promising synergistic targets for nano-based therapy. *J Control Release,* **2017**. 253: p. 82-96.
DOI: 10.1016/j.jconrel.2017.03.013.

1.1. General background on cancer development

Cancer is the second leading cause of death worldwide, following cardiovascular diseases [1]. The World Health Organization (WHO) estimated a total of 14.2 million new cases in 2012 with a mortality of 8.8 million deaths in 2015 [2]. Globally, nearly 1 in 6 deaths is due to cancer. Lung, breast, colorectal and prostate cancer (PCa) are the most incident and aggressive tumours (**Figure 1.1**), which account for almost half (*ca.*46%) of all cancer related deaths. These values are expected to rise by 68% (with a total of 23.6 million new cases), by 2030, primarily due to increasing lifespan [3].

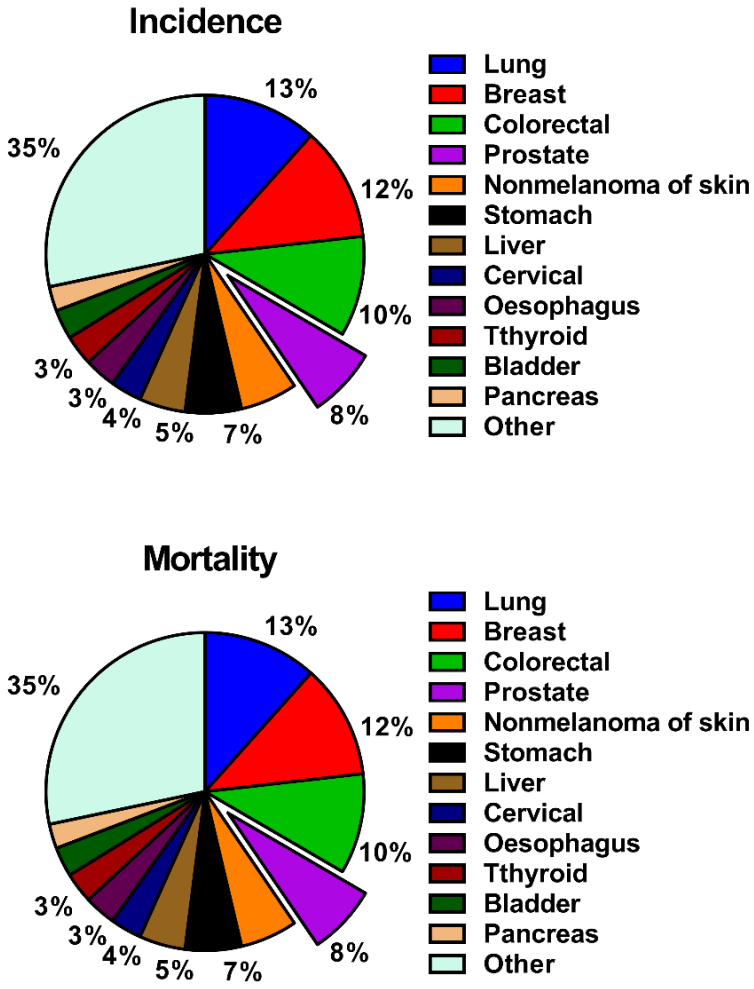

Figure 1.1. Latest cancer statistics worldwide. Incidence and mortality of cancer types worldwide, based on thorough updated statistics by WHO accessed in [2].

The concept of neoplasia has been recognized for centuries, but little was known about the biology and progression of these lesions, until about 50 years ago [4]. After the declaration of 'war on cancer', there was tremendous investment in cancer research; and despite the recent advances in the fields of biology, genetics, chemistry and nanotechnology, cancer therapeutics still remains a challenging and controversial aspect in medicine [5,6].

Targeting a singular molecular abnormality has proven difficult and only shown modest clinical effect, given the ever-evolving genetic diversity, dynamics and inter- or intratumour heterogeneity. Moreover, the development of drug resistance and tumour recurrence has also affected the long-term efficacy of most chemotherapeutics [7]. Nowadays, there is substantial effort to develop novel targeted therapies that selectively kill cancer cells and spare healthy tissues. The use of combinatorial therapies, rather than single agents is predicted to have a better effect, ultimately decreasing clinical dosage, maximizing toxicity; and reducing side-effects of classical chemotherapeutics.

Cancer was initially defined as a unique mass of uncontrolled cell proliferation, which was often associated with vascular abnormalities and cell invasiveness [8,9]. Hanahan and Weinberg's [10,11] influential reviews revolutionized the definition of cancer beyond simplified isolated cell masses, arguing that a complex network of active participants in the tumour niche, are an integral part of cancer initiation, growth and progression. They proposed that the multi-step development of cancer is defined by specific hallmarks (**Figure 1.2)**, such as, sustained proliferation and signaling, evading growth suppressors, induced angiogenesis, reprogrammed metabolism, resistance to cell death, inflammation and hypoxia that lead to invasion/metastasis. Underlying these hallmarks, are ever-evolving genomic instabilities (*e.g.* tumour suppressor protein Rb, tumour oncogene p53 and cyclins of the cell cycle) that lead to hyper activation of survival crosstalk pathways and downregulation of death pathways; which drives cancer development and progression. [12].

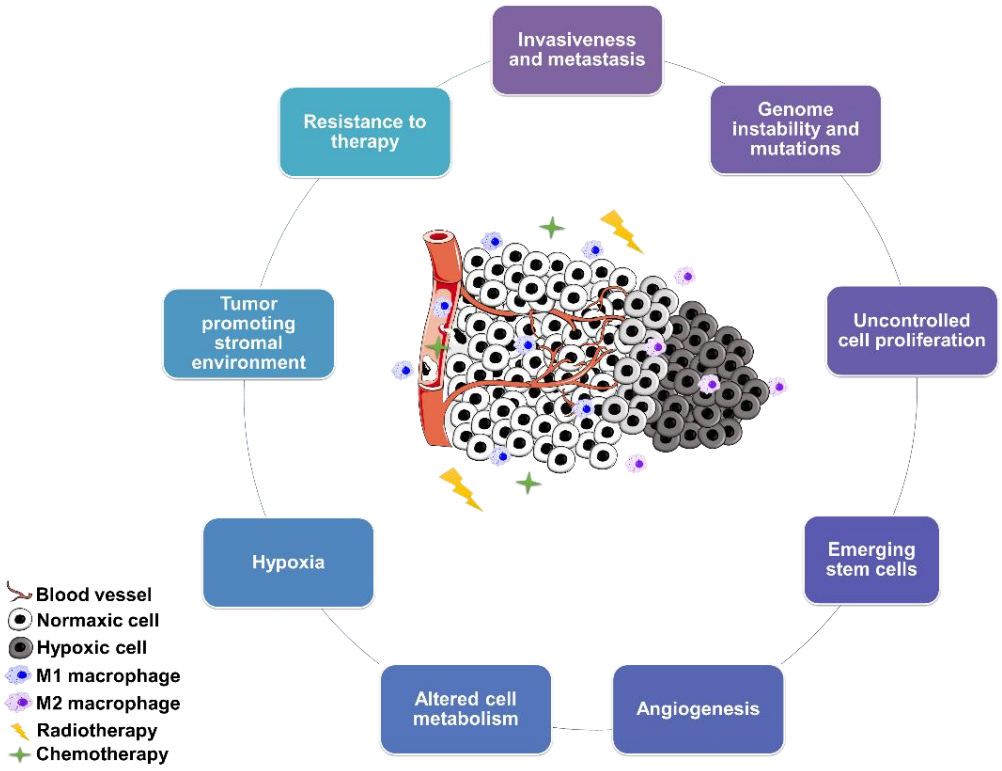

Figure 1.2. Main hallmarks of cancer. The cancer niche is a complex network of endothelial, stromal and malignant cells, comprised of evolutionary genomic features that enhance survival and thrive tumour cells to uncontrolled proliferation and metastasis. This enriched tumour microenvironment supports a shifted metabolism in cells, which allows a quick preadaptation and survival under nutrient and oxygen deprivation (hypoxia) which lead to therapeutic resistance. Adapted from [10].

1.1.1. Summary of current treatment options

The thorough understanding of tumour progression has resulted in significant prospects into the development of new anticancer therapeutics, but only recently have molecular-targeted and immune therapies revolutionized cancer patient care [13]. However, questions remain regarding the long-term survival benefit of these new therapies and the need for a more comprehensive understanding of drug dosing and rational combinatorial therapeutics. Thus, it comes to no surprise that conventional treatment has somewhat remained stationary for the past 30 years [14]. These classical treatment options come in the form of surgery, radiotherapy and classical chemotherapy – all of which are still the first-line therapy for many types of tumours [14]. Among them, surgery remains a prevalent approach for most solid tumours. Unfortunately, a total removal of the tumour mass is sometimes difficult, as cancer cells may be surrounding important vessels or organs, limiting total debulking. Cancer cells that get left behind may then lead to recurrence of disease, which is often accompanied by metastasis [14]. Moreover, the efficacy of chemotherapy has relied on the ability of these compounds to block cell division or disrupt major cellular pathways, eventually leading to cell death. The era of chemotherapeutics was marked by the use of nitrogen mustards, in the 1940's, which were recognized for their potent effect on inhibiting cell proliferation [5]. The use of chemical compounds for cancer treatment then became a practical approach, with the first routinely used Food and Drug Administration (FDA) approved chemotherapeutic in 1960. The most commonly used anticancer drugs are: docetaxel, paclitaxel, doxorubicin (Dox), fluorouracil, cisplatin and tamoxifen [15]. However, the adverse side effects, poor pharmacokinetics (PK) and the emergence of multidrug resistance (MDR), have limited their clinical use [16,17]. Radiation therapy has also shown to provide therapeutic benefit by generating pronounced DNA damage (inhibiting cell replication and division), but the development of hypoxia in tumours has shown to blunt its efficacy [18]. Additionally, a study by Shapiro and Fungman [19] showed that monotherapy can sometimes be inefficient, due to large cell heterogeneity, and combinatorial approaches may provide greater therapeutic outcome and prolonged survival of patients [20]. In line with this, there is an unmet need to develop new anti-cancer strategies that increase the specificity, whilst improving PK and clinical outcome.

1.1.2. The tumour microenvironment

Cancer cells co-evolve with their surrounding environment, through a complex process of cell signaling and metabolic adaptation [21,22]. This microenvironment has been well-established as a network of active components (endothelial cells, pericytes, fibroblasts, various classes of leukocytes, and extracellular matrix) that ultimately creates a vicious cycle of tumour resilience (**Figure 1.3**) [21-23]. The hypoxia inducible factor (HIF-1) is a key transcription factor that modulates the expression of cancer-related genes, responsible for modulating tumour immune suppression, metabolic shifting, angiogenesis, lymphogenesis, matrix remodelling and hypoxia [24,25]. However, from an optimistic point-of-view, this diverse niche offers potentially new 'druggable' targets to develop alternative anticancer therapies [26].

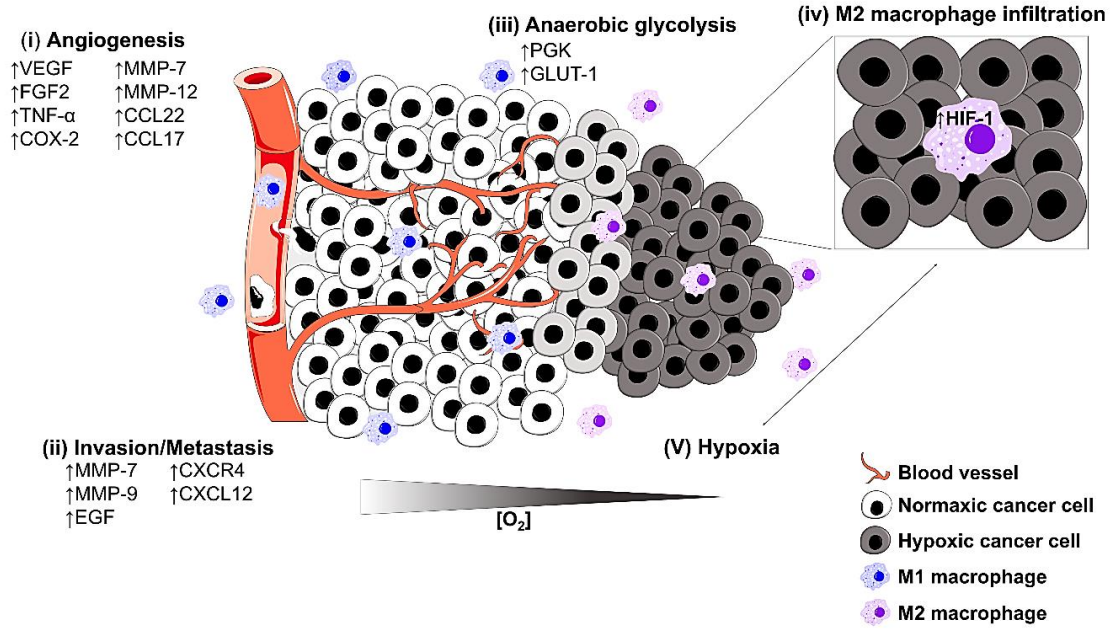

Figure 1.3. The hypoxic tumour microenvironment and its role in oncogenesis. Deprivation of oxygen in the tumour core has been linked to tumour development and poor prognosis. Upregulation of HIF-1 has shown to enhance the expression of many cancer markers related to: (i) tumour angiogenesis, (ii) invasion and metastasis, (iii) metabolism shift and (iv) infiltration of M2 macrophages in the (v) hypoxic regions of tumours. HIF-1 is thus upregulated not only in cancer cells, but also M2 type macrophages; and the futile cycle created by a positive feedback of negative prognosis biomarkers in cancer are responsible for tumour survival and resistance to therapy. This complex environment offers a wide range of targets for nanomedicine application [26].

1.1.2.1. pH and metabolism

Although tumour cells have an intracellular pH like normal cells, their increased anaerobic glycolytic metabolism [acclimation in low oxygen (O_2) environments, also observed under normoxia] leads to a lowered interstitial pH (about 6-7) from physiological conditions. This metabolic shift and adaptation was first proposed by Otto Warburg. He developed novel insights in cancer metabolism in the 1920's and much has been discussed and updated ever since [27,28]. This metabolic shift is not only a survival factor, but contributes to maximum activity of key enzymes for cell metastasis, promotes angiogenesis and inhibits inflammatory pathways.

1.1.2.2. Angiogenesis

As tumour cells grow in an uncontrolled matter, their adaptation to the environment is considered essential in maintaining survival and growth. Once the tumour cells become less exposed to oxygen and nutrients, they develop new blood vessels, a process called '*de novo'* angiogenesis [22]. These newly developed blood vessels contain discontinuous endothelium (10 to 1000 nm gap size, compared to normal endothelium), which renders them leaky in nature [29]. This hyperpermeability, in combination with impaired lymphatic drainage, are known as enhanced permeation and retention (EPR) effect [8]. Such phenomenon has been exploited as a promising approach to deliver drugs to tumours, using drug-conjugates and drug delivery systems (DDS) [19,29], which will be discussed in more detail, further on in this chapter.

1.1.2.3. Stromal cells

The presence of dendritic cells, fibroblasts, endothelial cells, monocytes and macrophages (MACs) in the tumour microenvironment has been repeatedly linked to tumour progression [30]. MACs have an important immunesurveillance role, mainly responsible for tissue repair, wound healing and defense against pathogens, including tumour cells [31]. However, a differential MAC programming in cancer progression has been elucidated, and much needs to be taken into account when describing the primary role of these cells in the tumour microenvironment [32]. Their role has reached a concept of 'friend or foe', recognizing that a well- functioned immune system should destroy tumour cells [33]. Two different polarization statuses have been reported amongst the MACs population and are dependent on the stimuli received, as well as the type of tumour itself [34]. The M1 phenotype (classically activated form) is responsible for host defense and is activated by interferon gamma (IFN- γ) and/or lipopolysaccharides (LPS) [35]. M1 MACs produce large amounts of pro-inflammatory cytokines [nitric oxide, high levels of major histocompatibility complex (MHC) molecules, interleukin 12 (IL-12] and low levels of IL-10), which makes them potent killers of pathogens and tumour cells. On the other hand, the M2 subtype (alternatively activated form) responds to stimulus from IL-4/IL-13, IL-10, toll-like receptors (TLR) and glucocorticoids; and produce high amounts of IL-10, tumour necrosis factor (TNFα) and arginase-1 [36]. They overexpress scavenger receptors, mannose receptors, exhibit anti-inflammatory activity and promote tissue remodeling, angiogenesis, immune-regulation (M2b or M2c) and tumour development (M2a) [37,38]. Tumour associated macrophages (TAMs) have been defined to closely resemble the M2 phenotype, and to constitute up to 80% of the tumour mass [35]. They infiltrate poorly vascularized, hypoxic and necrotic areas, contributing to poor prognosis and exerting a pro-tumour effect in many types of cancer [39].

1.1.2.4. Invasion and metastasis

Metastasis is a multi-step process resulting in spread and infiltration of primary tumour cells to adjacent or distant tissues. It is responsible for over 90% of cancer-related cell deaths [40] and constitutes another hallmark of cancer. Tumour cells secrete proteases that are enzymes capable of hydrolyzing the extracellular matrix, allowing cell extravasation and rapid spread of tumour cells to secondary tissues [41]. This process is quite selective and dependent on cell genome, adaptation and biochemical patterns. Although thousands of cancerous cells may make their way through the extracellular matrix, only few are actually able to colonize new sites [42]. The molecular characteristics of tumour cells define their aggressiveness and rate of metastasis, ultimately determining their therapeutic response.

1.2. Cancer Hypoxia

The rapid proliferation of tumour cells leads to an exhaustion of nutrients and oxygen, and cancer cells acclimate in a so-called hypoxic or low oxygenated environment. Hypoxia has an active role in oncogenesis and contributes to the overall survival of tumours [43]. Structural abnormalities in the tumour vessels lead to reduced oxygen diffusion and eventually generate areas of hypoxia and necrosis, within the tumour. It has been fifty years since Thomlinson and Gray first postulated the role of hypoxia in human tumours [44]. Two types of hypoxia have been proposed: 1) chronic or diffusion limited and 2) acute or perfusion limited; being the first type associated to tumour cells. Chronically hypoxic cells have been described as prone to higher proliferation and survival, so a more aggressive clinical phenotype has been associated to patients with highly hypoxic tumours (**Table. 1.1**) [45].

Table 1.1. Oxygen levels in solid tumours and their corresponding normal tissue. Adapted from [43].

Tumour Type	Median tumour pO_2* (number of patients)	Median normal pO_2 (number of patients)
Glioblastoma	4.9 (10)	ND
	5.6 (14)	ND
Head and neck carcinoma	12.2 (30)	40.0 (14)
	14.7 (23)	43.8 (30)
	14.6 (65)	51.2 (65)
Lung cancer	7.5 (17)	38.5 (17)
Breast cancer	10.0 (15)	ND
Pancreatic cancer	2.7 (7)	51.6 (7)
Cervical cancer	5.0 (8)	51 (8)
	5.0 (74)	ND
	3 (86)	ND
Prostate cancer	2.4 (59)	30.0 (59)

***expressed in mmHg.**

In normal tissues, oxygen levels are heterogeneous and physiological pO_2 can range between 20 mmHg in the liver and brain to 70 mmHg in the kidney (3.1-8.7 % O_2). In contrast, a decrease to about 10-30 mmHg of pO_2 is observed in tumours and most importantly is the fact that 82% of all oxygen readings taken from solid tumours present a 0.33 % O_2 reading (as low as 2.5 mmHg) [46,47]. Hypoxia has been found to potentiate tumour cells resistance to radio and chemotherapy [48].

When oxygen levels decrease, HIF-1α accumulates and translocates to the nucleus, where it forms the active transcription factor HIF-1 by binding to HIF-1β. It regulates a plethora of genes [vascular endothelial growth factor (VEGF), glucose transporter (GLUT-1), hexokinase (HK-1), phosphatidylinositol 3-kinase (PI3K), mitogen-activated protein kinase (MAPK) pathway and matrix metalloproteinases (MMP)] and recruits skewed macrophages, promoting angiogenesis, local invasiveness, and enhanced metastasis (**Figure 1.4**) [43,50]. Hypoxia has arisen as a therapeutic target in cancer. The existing targeted therapies have been classified as HIF-1 inhibitors or hypoxia-activated prodrugs (HAPs), and are discussed in the next sections.

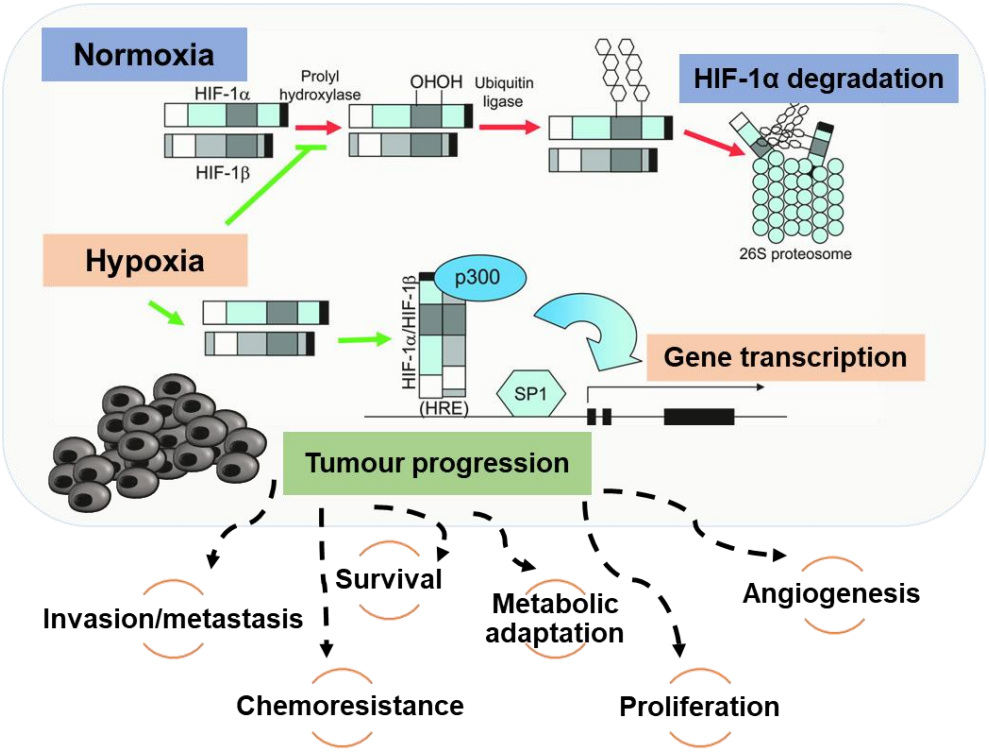

Figure 1.4. Regulation and effect of HIF-1 on tumour progression. In normoxia, prolyl hydroxylase (PHD) hydroxylates proline residues on HIF-1α, allowing ubiquitination and degradation of HIF-1α. When hypoxia sets in, PHD is inactivated and HIF-1α expression exceeds the capacity of ubiquitin–proteasome degradation. HIF-1α then forms a heterodimer with HIF-1β, interacts with transcriptional co-factors such as p300; and translocates to the nucleus binding to hypoxia-responsive elements (HRE) in the promoter. This then induces the expression of various HIF1-responsive genes, responsible for modulating tumour metabolism, apoptosis, angiogenesis metastasis and chemoresistence. Adapted from [51].

1.2.1. HIF-1 inhibitors

The active role of hypoxia and HIFs have positioned them as novel therapeutic targets for cancer therapy [50]. Classical approaches to overcome low oxygenation levels at the tumour site were carried out using hyperbaric chambers. However, such intervention was proven to be unsuccessful in combination with radio- and chemotherapy [47]. Moreover, HIF-1 has been linked to increased mortality in several types of tumours (breast, stomach, cervical, endometrial and ovarian cancers); and has now been referred to as a new target to treat cancer, given its key transcriptional activity. Several small inhibitors have been developed to target HIF-1's activity by promoting HIF-1 protein degradation [52,53], or by blocking at least one of the following pathways: 1) HIF-1 mRNA expression [53,54]; 2) HIF-1 protein translation [55,56]; 3) HIF-1 DNA binding [57] and 4) HIF-1 transcriptional activity [58].

Furthermore, indirect inhibitors of HIF have also been evaluated [59], given its central role in cell signaling. These include molecules that target upstream or cross-talked pathways with the HIF target (*e.g.* inhibitors of VEGF, mechanistic target of rapamycin (mTOR), epithelial growth factor receptor (EGFR), topoisomerase I and II, PI3/AKT/MAPK pathways). Despite the discovery and development of several therapies targeting HIF-1 or the HIF-1 pathway, only a few have progressed into pre-clinical and early clinical development [26]. Unfortunately, there have been no approved drugs that directly inhibit HIF-1 and many small molecule inhibitors have shown a high rate of late stage clinical failure. This is attributed to the high redundancy and complexity of the tumour microenvironment [26]. Also, the desired effects of indirect inhibitors may be difficult to separate, as many different signalling pathways are linked to HIF-1 induced tumourigenesis, leading to the existence of off-target effects that are likely to be less predictable [60]. One good example is the use of VEGF inhibitors as a strategy to overcome hypoxia, due to reoxygenation and formation of neo-blood vessels. However, the results obtained previously have been controversial in terms of hypoxia inhibition [47]. VEGF inhibitors not only failed to produce the desired effect, but have shown therapy-induced hypoxia, becoming ineffective. This complex signalling may be targeted effectively using multifaceted combinatorial treatments, but with careful assessment of drug regimen.

Selective gene therapy has also been considered, by developing strategies that directly down-regulate HIF-1 [61-63] or are mediated by engineered hypoxia-responsive constructs [64,65]. Although these systems have shown an interesting hypoxia-selective outcome, off-target effects are still an issue, if injected intravenously (i.v.). The use of drug carriers could further improve the efficacy and safety of gene delivery to the hypoxic tumour microenvironment.

With a growing understanding of the HIF-1 pathway and its pivotal role in carcinogenesis and tumour metabolism, it's clear that many challenges arise from targeting such a central molecule; and controversy among researchers has arisen, as to whether it should be considered a reliable therapeutic target [66].

Nevertheless, the apparent failure of such strategies, may provide a silver lining, rendering new information and opportunities on how to properly address the targeting of HIF-1. The innovation may rely on re-profiling existing drugs and focusing on combinatorial treatments that allow a more aggressive approach [26].

1.2.1.1. Hypoxia activated prodrugs (HAPs)

The presence of hypoxia in tumours has provided significant biological and therapeutic implications. The development of HAPs has proven to be an interesting strategy to selectively target hypoxic cells, sparing normoxic healthy tissues. They have been defined as cytotoxins that are metabolized by different endogenous reductases (*e.g.* NAD(P)H, cytochrome P450, DT-diaphorase and quinone oxidoreductase - NQO1), in a one-electron or two-electron catalysis, and their activation is dependent on the overexpression of these enzymes in the tumour tissue [67]. The different classes of HAPs are: nitro (hetero) cyclic compounds; aromatic *N*-oxides; aliphatic *N*-oxides; quinones and metal complexes. The most advanced and clinically relevant HAPs have been summarised in **table 1.2**. These compounds fall into two broad categories [68]. Class I HAPs (tirapazamine - TPZ and SN30000 – CEN 209), are generally activated under mild hypoxia and their selectivity towards low oxygenated cells is governed by a one-electron reduction pathway. The lead prodrug generates a free radical that can easily back-oxidize to its original compound if oxygen is present, conferring specificity to highly hypoxic regions [69].

Table 1.2. Bioreductive prodrugs for hypoxia.

Drug	Method of action	Stage	Chemical class	Cancer type	Limitations	Main observations	Ref.
PR-104	DNA inter-strand crosslinking	Phase II	Nitrobenz amine mustard	Leukaemia. NSCLC and SCLC	Activation by aerobic reductases reduces hypoxia selectivity	10- to 100-fold increased activity under hypoxia, *in vitro*, for a broad range of cell lines, as well as xenograft models; Additive effect in combination therapy, both *in vitro* and human panels; Potentiation of drug may be due to a bystander effect; Tolerated dose established in phase I, but phase II trials vs. docetaxel were terminated, due to low levels of drug reduction.	[86-88]
Apaziquone (E09)	DNA inter-strand crosslinking	Phase III	Quinone	Bladder	Poor PK Loss of selectivity (two-electron reductases)	Only 34.7% recurrence over 12 months and 48% after 18 months; Phase II; no activity was seen against a wide range of tumours in subsequent phase II trials, probably due to the drug limitations; Promising outcome, after administration into the urinary bladder. E09 and its active metabolite were not detected in plasma, and there were no systemic side effects. Phase III results are anticipated.	[78-80]

Tirapazamine	DNA damage	Phase III	Aromatic N-oxide	Head, neck and cervix	low drug penetration and accumulation	Phase I/II: overall promising effects of TPZ in combination with radiation and cisplatin; Phase III: no overall significant effect on response rate and survival; Review of populations used may be in order for correct assessment of the activity of the drug.	[70-72]
SN30000 (CEN-209)	DNA damage	Preclinical	Aromatic *N*-oxide (TPZ analogue)	Cervix, ovary and colon	-	Significant *in vitro* and *in vivo* metabolic, PK, photo degradation and toxicity assays have been analysed; Most promising TPZ analogue. Presented higher diffusion and more efficient extravascular transport, with potent selective activity; Scheduled to enter Phase I clinical trials.	[73-77]
Evofosfamide (TH-302)	DNA inter-strand crosslinking	Phase III	Nitroimidazoles	Soft tissue carcinoma, pancreatic, myeloma, etc.	Need for optimized combinatorial therapies	Preclinical studies: potent broad activity in various mouse models, for both mono and combined therapy; Phase I: good tolerance of the drug and partial responses in patients with metastatic lung cancer and melanoma; Phase II: effective combinatorial therapy with gemcitabine and Dox; Phase III: combinatorial chemotherapy, was ineffective in increasing overall survival.	[81-84]
Banoxantrone (AQ4N)	DNA intercalator and topoisomerase II inhibition	Recent phase I/II	Aliphatic N-oxide	Oesophagus, glioblastoma, bladder, head and neck, breast, and cervix	Lack of experimental data in patients, results may not be fully translated into therapeutics	Measurable decreases in hypoxic cells was observed and preclinical activity indicated accumulation of the drug in 24/30 tumor tissue samples; Radiation conditions, cisplatin and other combinatorial chemotherapy regimens have shown to have effect with this drug; AQ4 the active metabolite, after reduction, co-localizes with Glut-1 and hypoxic regions.	[37, 74, 75]
SN-2477	Reduction of metal centres [Co(III)/Co(II)]	Preclinical	Metal complexes	Breast	No clinical use	This compound showed moderate activity *in vitro*, but failed to reproduce activity in *in vivo* hypoxia; It forms an unstable compound that releases its mustard ligand, destabilizing DNA; Other selective metal complexes have been reported, but improvement regarding this class of bioreductive drug is needed.	[85]

In contrast, class II HAPs (PR-104A or TH-302) present maximum activity under extreme hypoxia, where their active metabolites diffuse to cells in the outskirts (with intermediate O_2), causing cytotoxicity through a bystander effect [68]. In general HAPs can be reduced by a one-electron reduction, providing high selectivity conferred by the oxygen-sensitive limiting reduction step (**Figure 1.5**). On the other hand, some HAPs may be reduced by two-electron reduction, bypassing this O_2-dependent reaction. Selectivity is therefore determined by the HAP chemical nature and biological overexpression of reductases in the tumour tissue [48]. Despite their progression into clinical trials, HAP activity has been hindered due to poor extravascular diffusion (caused by rapid reduction/ consumption of the drugs), short blood half-life, instability and poor balance between the reduction/oxidation equilibrium [89,90].

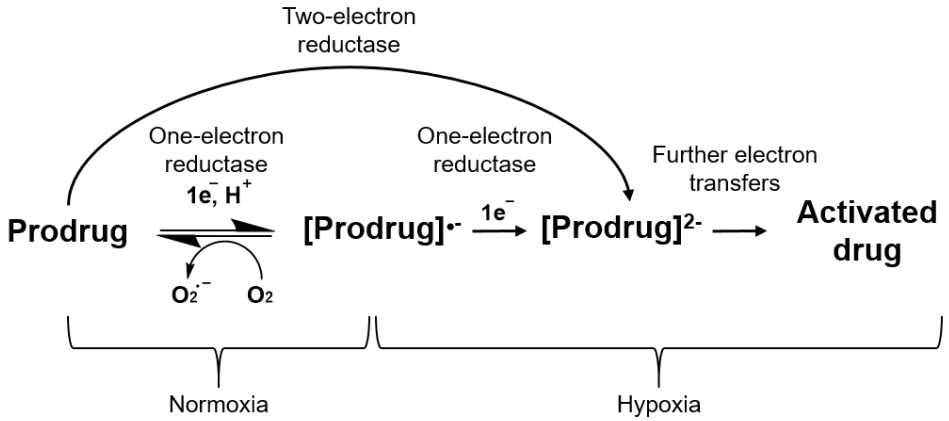

Figure 1.5. Schematic representation of the general mechanism of activation of hypoxia-activated prodrugs. HAPs can be reduced by one-electron reductases, generating a radical anion that is oxygen sensitive. This reaction confers selective activation of the lead prodrug. Two-electron reduction can generate oxygen-independent activation of the prodrug [91].

Five of these compounds (apaziquone, banoxantrone, porfiromycin, PR-104 and RH1) have now been discontinued from clinical evaluation, while two still remain active (evofosfamide/TH-302 and tarloxotinib bromide/TH-4000). However, recent reports of phase III studies for evofosfamide, in combination with chemotherapy, did not achieve primary overall survival endpoints and have also been discontinued [90]. TH-4000 (Hypoxin™), discovered at the University of Auckland is a novel targeted HAP, designed to release an irreversible EGFR tyrosine kinase inhibitor (TKI), under hypoxia, that showed significant promise in preclinical studies [92,93]. Unfortunately, recent phase II trials in advanced non-small-cell lung carcinoma (NSCLC) and metastatic squamous cell carcinoma of the head and neck or skin (HNSCC) failed to achieve the primary interim response rate [89].

Hypoxia-targeted therapies have shown controversial results in mouse models and humans, as results obtained *in vivo* are not easily translatable to humans. The high attrition rates obtained in clinic have been attributed to the high complexity and redundancy of the tumour microenvironment, and also to the lack of veracity and fidelity in existing preclinical models and patient subsets [91].

The reviewed clinical trials have not incorporated biomarkers to identify patients that can truly benefit from such therapies [60].

Moreover, retrospective studies have now shown us the importance of re-evaluating the potential effect of these HAPs [94,95], by developing more reliable *in vitro* methods for successful clinical translation [60]. Establishing cell culture models that resemble hypoxic tumours more reliably should include comprehensive immunohistochemistry (IHC) staining, western blot analysis, mRNA expression of hypoxia markers. Animal models should envision the use of fludeoxyglucose (^{18}F) labelled nitroimidazole hypoxia probes (*e.g.* [^{18}F]-FAZA, [^{18}F]-MISO, [^{18}F]-HX_4) for positron emission tomography (PET) imaging, which could help reduce hypoxia variation and redundancy between experiments [89,96]. Also, substantial efforts have been made to chemically modify current HAPs or develop drug delivery strategies to improve on their current PK limitations and redefine their use as promising cancer therapies.

1.2.1.2. Tirapazamine (TPZ)

TPZ is an aromatic heterocycle di-*N*-oxide (SR4233, 3-amino-1, 2, 4-benzotriazine-1, 4-dioxide) and a well–established and extensively characterised HAP (**Figure 1.6**) [97]. It was first discovered during an herbicide screening program in 1972 by Zeman and colleagues [98] and the authors originally postulated its potential as a clinical compound for hypoxia in 1986. TPZ has shown activity in moderate (1-5% O_2) to severe hypoxic conditions (<0.1% O_2) [99,100]; exhibiting 30 (*e.g.* non-small cell lung cancer cells and colorectal) to 300-fold (*e.g.* Chinese hamster cells, prostate cancer cells) higher toxicity, in hypoxia, compared to normoxia, which was cell line-dependent [101-103]. Studies with multicellular spheroids (Chinese hamster V79, colon carcinoma cells and human cervical carcinoma cells and preclinical models have been essential for PK evaluation and prediction of clinical response [104-107].

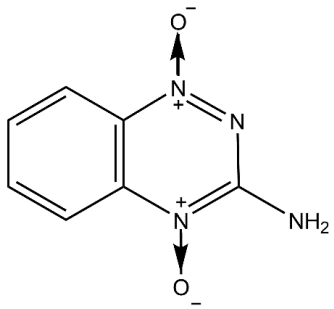

Chemical Formula: $C_7H_6N_4O_2$
Molecular Weight: 178.1510

Figure 1.6. Chemical structure of 3-amino-1, 2, 4-benzotriazine-1, 4-dioxide (TPZ). Structure was obtained using Chemdraw professional 15.0, depicting chemical formula and molecular weight (g/mol).

TPZ undergoes an enzymatic reduction, under moderate to severe hypoxia, by intracellular reductases, mainly NADPH P450 (**Figure 1.7**). The reductive state and the overexpression of certain reductases, in both the nucleus and cytoplasm, have an important role on the toxicity of TPZ even under normoxia [108-111]. This one electron-reduction generates a superoxide radical that causes single and double DNA-strand breaks, leading to chromosomal aberration and apoptosis [112]. Earlier reports define its mechanism of action as a one or two electron reduction. In the first mechanism, the neutral drug undergoes hemolytic cleavage to generate 3-aminobenzo-1, 2, 4-triazine-*N*-oxide (TPZ•) and a hydroxyl radical (OH•), causing extensive single- and double-strand breaks, by hydrogen abstraction of the sugar moieties. In the two-electron reduction, a 1-N-oxide metabolite - SR 4317 - is formed directly from TPZ or by disproportionation of two TPZ radicals, causing cell death by double DNA-strand cleavage. More recently, TPZ• has been proposed to undergo dehydration, generating a more potent benzotriazinyl radical (BTZ•), which is the ultimate DNA damaging intermediate. TPZ has also been shown to interfere with the activity of the topoisomerase II enzyme [100,113] and cell cycle progression [114,115].

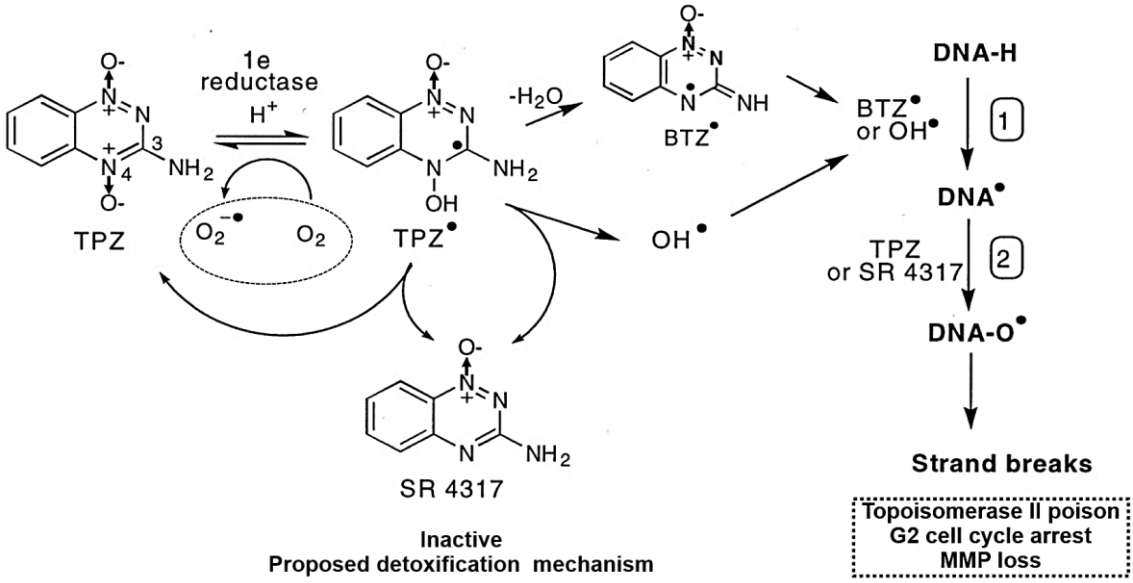

Figure 1.7. Dual mechanism of action of TPZ. One or two electron-reduction may be observed. The first leads to the production of a TPZ radical (TPZ●) that will either lead to the turn-out of hydroxyl radical (OH●) or suffer dehydration into a potent benzotriazinyl intermediate (BTZ●), causing extensive single and double DNA strand damage, thus inhibiting cell growth. The two-electron reduction pathway leads to the production of the SR 4317 intermediate which also possesses DNA damaging properties. TPZ has also been shown to function as a topoisomerase-II poison, interfere with cell cycle progression and induce loss of mitochondrial membrane potential (MMP'). Adapted from [116].

The back-oxidation of the TPZ radical, under oxygenated conditions, or the mitochondrial decoupling/loss of membrane permeability at high doses, have been associated with unselective cytoplasmic reduction [110,117]. This was consistent with acute changes in tumour energy metabolism and pH after administration of TPZ [118], differentiating the aerobic cellular responses at low and high doses of TPZ.

Preclinical studies have been important to elucidate TPZ activity in tumours, suggesting that the translation of its potent efficacy *in vitro* is highly dependent on tumour development of hypoxia and reoxygenation, which can occur as early as a few hours up to days [119]. This calls for careful consideration when designing drug regimens with TPZ and most studies have suggested increased benefit when using combinatorial therapies alternatively to TPZ alone [120,121]. The preclinical and clinical studies of TPZ have been thoroughly summarised in **table 1.3**.

Table 1.3. Preclinical and clinical studies of TPZ. Updated from [99].

Study type	Tumour Type	Dose/Adjuvant	Outcome/conclusions	Ref.
In vivo (Mice)	Murine hepatic carcinoma	Intraperitoneal (i.p.) injection irinotecan 2.5 mg/Kg + TPZ 25 mg/Kg every 2 days, until sacrifice	TPZ alone did not result in any significant activity Combination with irinotecan showed marked tumour inhibition	[122]
In vivo nude mice)	Human SCCVII	i.p. injection of TPZ 36 mg/kg +/- radiation	Single dose of TPZ enhanced radiation-induced tumour inhibition, when drug is administered before, irradiation. Drug regimen with injection after irradiation, resulted in reoxygenation and loss of TPZ efficacy	[123]
In vivo (nude mice)	Human HNSCC xenografts	I. i.p. injection of TPZ 70 mg/kg, 3 or 72 hours before irinotecan 100 mg/kg II. i.p. injection of TPZ 70 mg/kg + methylselenocysteine (MSC) 0.2 mg/mouse	TPZ alone showed significant tumour inhibition when used with MSC ($p=0.0065$) Irinotecan alone had a significant ($p<0.0001$) tumour-inhibitory effect, compared to TPZ, but combination did not. TPZ effects may be counterproductive	[124]
In vivo (nude mice or Sprague-Dawley rats)	Multiple tumour xenografts	Variable i.v. and i.p. injections with different drug regimens	MTD of TPZ was 31.7 mg/kg, significantly lower than other tested analogues Improved PK, bioavailability and tumour inhibition (combined with radiation) of analogues, compared to TPZ, in both mice and rats	[73]
In vivo (nude mice)	Human colon carcinoma (HCT-116)	i.p. injection of TPZ 60 mg/kg	TPZ caused extensive vascular dysfunction (after 24h administration), followed by increased tumour necrosis (48h)	[125]
In vivo (nude mice)	Human cervical carcinoma (Si-Ha) and SCCVII	i.p. injection of TPZ at 20 or 40 mg/kg in SCCVII and SiHa, respectively	*ca.* 3-fold increased selective hypoxia activity of TPZ against *in vivo* TPZ altered blood-flow in murine models, which can explain differential activity *in vitro vs. in vivo*	[126]
In vivo (nude mice)	lung xenografts	i.p. injection of TPZ 70 mg/Kg, prior to paclitaxel 20 mg/Kg or Paraplatin at doses of 100 mg/kg or 50 mg/kg two- and three-way combination regimens	TPZ alone did not cause any tumour inhibition Paclitaxel and Paraplatin, alone, caused *ca.* 40% tumour reduction Tumour inhibition was substantially increased with the triple-agent regimen compared double-agent regimens that did not include TPZ	[127]
Phase I	Multiple	I. TPZ 9-21mg/m^2 1/2-1h prior to radiation II. TPZ single doses of 18-293 mg/m^2 after radiation III. TPZ 36-250 mg/m^2	Muscle cramping was main side-effect	[128]

Table. 1.3. Preclinical and clinical studies of TPZ. Updated from [99] (continued).

Study type	Tumour Type	Dose/Adjuvant	Outcome/conclusions	Ref.
Phase I	Multiple	TPZ 50 courses/ 28 patients (36-450 mg/m^2)	No tumour response observed Maximum tolerate dose TPZ 330 mg/m^2- reversible deafness and tinnitus	[129]
Phase I	Multiple	TPZ 130 to 260 mg/m^2 + cisplatin 75 to 100 mg/m^2, 1 h later	15% partial response Cisplatin clearance was not affected by TPZ MTD of TPZ was 260 mg/m^2- nausea, vomiting, fatigue and muscle cramping	[130]
Phase I	Multiple	TPZ dose escalation from 9 mg/m^2 /dose to 260 mg/m^2 with radiation	MTD of TPZ was 260 mg/m^2- muscle cramps This dose was enough to ensure radiation sensitization	**[131]**
Phase I	Head and neck	I. TPZ 290 mg/m^2 + cisplatin 75 mg/m^2 II. TPZ alone 160 mg/m^2 (radiation over 7 weeks)	75% patients disease-free after 21 months MTD of TPZ was 290 mg/m^2 - febrile neutropenia	[132]
Phase II		I. Cisplatin (75 mg/m^2) + TPZ 290 mg/m^2 + radiation II. TPZ alone (160 mg/m^2) III. Radiation + cisplatin + 5-FU	3-year cancer-free survival with TPZ/cisplatin + 5-Fu TPZ/cisplatin had superior activity and less severe toxicity	[133,134]
Phase II		TPZ 159 mg/m^2 + radiation	64% patients – 1-year control 59% patients – 2-year control TPZ + radiation acceptable toxicity - Muscle cramps, nausea and vomiting	[135]
Phase III		I. Cisplatin 100 mg/m^2 + radiation II. TPZ 290 mg/m^2 before cisplatin 75 mg/m^2 + radiation III. TPZ 160 mg/m^2 + radiation	2-year survival rates were 65.7% for cisplatin and 66.2% for TPZ/cisplatin TPZ did not improve cisplatin-chemotherapy and failed to provide evidence of survival and improved quality of life	[72]
Phase I	Cervix	I. TPZ 190 mg/m^2 + Cisplatin 75 mg/m^2 + radiation II. TPZ alone 160 mg/m^2 III. TPZ 290 mg/m^2 + Cis 75 mg/m^2 + radiation IV. TPZ alone 220 mg/m^2 + radiation	87% of patients with controlled disease after 6 months Acceptable toxicity of drug regimen	[136]
Phase III		TPZ 290 mg/m^2 + cisplatin 75 mg/m^2 or TPZ 220mg/m^2 + cisplatin 60 mg/m2 Patients also received radiation	3-year progression free-survival for the TPZ/cisplatin/radiation and cisplatin/radiation were 63.0% and 64.4%, respectively TPZ did not potentiate cisplatin chemotherapy	[72]
Phase I/II	SCLC	TPZ 260 mg/m^2 1 h before cisplatin (2 cycles cisplatin/etoposide)	80% overall response rate, but warrants further studies MTD of TPZ was 260 mg/m^2- neutropenia and vomiting	[137,138]

Table. 1.3. Preclinical and clinical studies of TPZ. Updated from [99] (continued).

Study Type	Tumour Type	Dose/adjuvant	Outcome/conclusions	Ref.
Phase II		TPZ 330 mg/m^2 + cisplatin 75 mg/m^2 + gemcitabine 1250mg/m^2	35% of patients – 1-year survival 40% of patients – 6.7 months' free survival Combination therapy with moderate toxicity - nausea, vomiting, and neutropenia	[139]
Phase II		TPZ 260 mg/m^2 1 h before cisplatin 75 mg/m^2	23% patients with partial response TPZ + cisplatin more active than TPZ alone Muscle cramps, fatigue, nausea and vomiting	[140]
Phase II		TPZ 390 mg/m^2 1 h before cisplatin 75 mg/m^2	40% of patients – 1-year survival TPZ + cisplatin more active and other combinations are warranted Muscle cramps, fatigue, nausea and vomiting	[141]
Phase III	NSCLC	(CATAPULT I) I. TPZ 390 mg/m^2 1 h before cisplatin 75 mg/m^2 II. cisplatin 75 mg/m^2 alone	TPZ enhances activity of cisplatin No significance between treatment regimens, but more side-effects with TPZ Median survival 34.6 *vs.* 27.7 weeks (p=0.0078)	[142]
Phase III		(CATAPULT II) TPZ 390 mg/m^2 1 h before cisplatin or etoposide + cisplatin	Etoposide provided superior activity to TPZ Median survival 26.7 *vs.* 31.4 weeks (p=0.038)	[143]
Phase II	Metastatic melanoma	TPZ 260 mg/m^2 1 h before cisplatin 75 mg/m^2	19% of patients with good response Combination therapies warrants further studies Muscle cramps, fatigue, nausea and vomiting	[71]
Phase I/II	Hepatic and gastric	Dose-escalating study of i.v. TPZ + embolization in liver	Open trial	[144]
Phase II	Hepatic	Randomized study with TPZ, Dox and embolisation in liver	Open trial	[145]
		TPZ + embolization + PD-1 inhibitor as anti-tumour immune therapy	Open trial	[146]

Phase I studies were essential in determining the maximum tolerated dose (MTD) of the drug (390 mg/m^2), where the most common side-effects were muscle cramping, nausea, vomiting, fatigue and temporary but reversible hear loss. Also, TPZ showed improved sensitizing properties when used in combination with radio- and chemotherapy (compared to TPZ alone), as with the preclinical models. In addition, some Phase II trials further confirmed this beneficial outcome of combinatorial therapies, but more recent phase II/III studies failed to support these findings. A recent randomized clinical trial, for cervical cancer (Phase III), using radiation and cisplatin, resulted in no overall survival rate or benefit of chemo-radiotherapy with TPZ [72] and clinical evaluation has been discontinued.

The translational failure of TPZ was initially attributed to its poor cellular uptake, PK and limited tissue penetration [72]. It is essential to reevaluate TPZs apparent clinical failure and redefine its status as a promising HAP. The use of analogues (SN3000) [73,147], metal ion coordinates [148] or the development of novel drug carriers for TPZ [26], could improve on its current biological drawbacks and therapeutic efficacy. Moreover, recent retrospective studies have also suggested lack of proper hypoxia assessment and standardized biomarkers, in patient subgroups. This poor patient selection, may have blunted positive clinical outcome, due to inadequate hypoxic tumour models [94,95].

Currently, three open trials with TPZ [144-146] have incorporated the use of embolisation in liver cancer (reducing blood flow and oxygen levels), in an effort to amplify the effects of sub lethal hypoxia. These studies may provide evidence of TPZ potentiation in humans, if sufficient control of hypoxia is achieved. Nevertheless, there is an unmet need for clinical reassessment of TPZ therapies.

1.2.1.3. Transition metals: copper and cancer hypoxia

The use of metal-complexes for therapeutic purposes can be dated back to ancient Egypt and China (*ca*. 4000 years ago). However, it was the discovery of platinum compounds (cisplatin) in the 1960's that revolutionized the concept of metals applied to cancer therapy [149]. Over the last decades much research has been dedicated to the rational design of anticancer metal complexes using gallium, zinc, cobalt, silver, vanadium, strontium, manganese and copper (Cu) [150]. These metals have important cellular functions, but when in excess can have deleterious effects, due to their ability to generate cytotoxic reactive oxygen species (ROS) [151]. They have unique properties conferred by the variety of coordination geometries, metal-ligand interactions and redox activity that allow functionalization of ligands and effective cellular targeting (DNA, proteins, enzymes and redox pathways) [152]. Although platinum complexes are still a mainstay treatment for some cancer types (*e.g.* ovarian and lung cancer), their clinical evaluation has been limited due dose-related adverse effects and the development of drug resistance [149]. More recently, ruthenium-based complexes have emerged due to their superior activity and fewer side-effects [152]. Also, many of these complexes have allowed the development of stable fluorescent/luminescent probes [153], which allowed the simultaneous use for therapeutic and bioimaging purposes. In addition, gold complexes have also showed promising anticancer applications (particularly radiotherapy) [154] and in the development of multifunctional NPs [149].

Overall, many transition metals have provided an interesting strategy to develop anticancer therapies, including hypoxia prodrugs [155,156]. The remarkable selectivity of cobalt complexes as hypoxia prodrugs has been subject of interest. An example is SN-2477, a stable nitrogen-based cobalt (III) complex, and one of the first discussed transition metal prodrug for hypoxia. Wilson and co-workers [85] hypothesized that metal-based bioreductive drugs with diffusible cytotoxic ligands, may provide an interesting selective strategy to eradicate hypoxia. These low-reducing compounds

could be activated in hypoxic environments and back-diffuse through the tumour mass to eliminate cancer cells. For the purpose of this work, copper(II) as a metal-ion centre for development of HAPs will be main focus.

Cu is an essential micronutrient, mainly transported in the serum by ceruloplasmin, acting as a catalytic cofactor or structural component in many relevant biological functions [157]. It plays a critical role on active sites of enzymes and proteins (Cu-Zn superoxide dismutase, tyrosinase, ceruloplasmin and cytochrome oxidase), oxygen transport, cellular growth, signalling and even angiogenesis [158,159]. On the other hand, the redox activity of this agent also renders its possible cell toxicity, as it can interfere with protein clusters and catalyse the production of free radicals. This metal ion is normally under tight cellular regulation (mediated by specific cell transporters and efflux pumps), however its cellular imbalance has been associated to many clinical manifestations, including cancer [160,161]. There have been reports on deregulation and elevated copper levels in cancer cells of preclinical and clinical models [162,163]. In addition, Cu levels in different biological samples (blood, hair, nails) were evaluated for prostate tissue in comparison to normal tissue, suggesting that elevated Cu might be a risk factor for PCa and present an interesting target to specifically develop selective anticancer agents [164-166].

The chemistry of copper involves the existence of two oxidation states, where both cations prefer different donor atoms according to the soft and hard Pearson classification [161]. Cu(II) is particularly relevant to this work as it coordinates well with donor atoms, such as nitrogen and oxygen groups in *N*-oxide derivatives, similar to that of TPZ [167-169]. Aiding its promising usage as a selective anticancer agent is the fact that many Cu(II) complexes have a reduction potential (E_0', Cu^{2+}/Cu^{+}) compatible with the cellular potential range [170]. These complexes are then reduced to Cu(I) complexes of lower stability, that liberate the free bioreductive prodrugs from their coordination sphere, hence promoting the desired cytotoxic effect [167,171]. These complexes have been exploited therapeutically with different organic ligands [170,172], applied for radiodiagnosis or radiotherapy [173,174], bearing a dual mechanism of action under low oxygen conditions.

Over the last years, many studies focused on the use of ^{64}Cu (II) bis(thiosemicarbazonates) such as copper(II)-diacetyl-bis(N4-methylthiosemicarbazone [Cu(ATSM)] for the selective imaging of hypoxia by PET [175-177]. This complex presented low molecular weight, high membrane permeability and low redox potential for selective retention within hypoxic tissue. More importantly, PET imaging employing copper isotopes [*e.g.* ^{64}Cu(ATSM)] has been applied to selectively analyse hypoxic head and neck tumours in clinical trials [178]. Following this, copper-based complexes have now been widely exploited for anti-cancer therapy [171,179]. Most of these complexes presented improved chemical characteristics compared to the free ligand, contributing to their increased hypoxic uptake, thus more selective and/or potent biological activity [180-183]. Particular attention has been drawn to Cu(II) complexes including *N*,*N*-diimine ligands, thiosemicarbazones,

bis(thiosemicarbazones), schiff base assemblies and pyridine-*N*-oxides and their ability to induce DNA damage, *via* binding or intercalation [171]. Although this is the primary mechanism of action, new cellular targets such as DNA topoisomerases [184-186], the proteasome complex [187-189], endoplasmic reticulum [190], and lysosome [191,192], have also become interesting pathways of cell death for copper-complex mediated therapeutics, highlighting the versatility and potency of these metal prodrugs.

1.2.1.4. Copper-TPZ

The coordination of Cu to hypoxic cytotoxins is an interesting strategy to overcome drug resistance and develop new selective agents. To date, only one study showed the possible coordination of copper to TPZ and its potential use to treat hepatic tumours. Lin *et al.* [148] were the first to discuss the potential use of cupric-TPZ complexes as a new strategy for hypoxia therapy. They showed the increased cytotoxicity of the complex compared to Cu or TPZ alone, under hypoxia, leading to a fundamental understanding of how to promote TPZs biological activity. They further described the enhanced DNA damage potential of these complexes and further promoted their use as targeted radioisotopes (^{64}Cu-TPZ) for cancer therapy [193]. However, this study lacked substantial information in terms of characterisation of this novel complex, which in turn may be important to understand its biological relevance. Data regarding its potential use as a cytotoxic agent is also still scarce. Other studies involving the use of Cu(II) as a metal coordinate of TPZ derivatives or analogues (quinoxaline complexes), have further promoted these cupric-complexes as promising hypoxia selective agents [168,169,194].

1.3. Prostate cancer (PCa): disease progression

PCa is currently the second most common cancer in men and the fifth leading cause of death by cancer [195]. The primary risk factors for PCa include advanced age, black ancestry, family history, inflammation and genetic polymorphisms [196,197]. PCa screening is still one of the most controversial themes in urology [197]. A recent Cochrane review (register of controlled trials) has suggested that despite the increased diagnosis and detection of primary localized disease, there is currently no overall survival or cancer-specific benefit; and screening for prostate specific antigen (PSA), may lead to over diagnosis and treatment [197]. PSA is a serine protease that is secreted as a proenzyme into the seminal fluid, where it digests the gel forming after ejaculation. In normal prostate, the levels of PSA are controlled by containment of the proenzyme within the glandular ducts. However, due to the damaged architecture and polarisation of PCa epithelial cells, PSA is strongly expressed and leaks into the prostate ducts, eventually reaching the extracellular space and circulation. Despite the aforementioned controversy, PSA remains a well-established and useful biomarker and accounts for a 30-fold increased level in serum, when PCa is present, compared to

normal prostatic epithelium [198]. Nevertheless, complementary tools may aid with a more reliable diagnostics and differentiation of disease stage [199].

Androgens [testosterone and its active metabolite, dihydrotestosterone (DHT)] are primary regulators of the normal prostate, and the role of the androgen receptor (AR) in PCa development and progression has been well established [200]. AR is expressed in normal prostate, but both human and animal studies have suggested that AR cell expression and signalling is somewhat maintained in primary PCa, and also present in metastatic lesions, having a pivotal role in cell survival/proliferation and disease progression [201]. 90% of free testosterone that enters the prostate cells is converted to the active hormone DHT, which presents 5-10 fold higher affinity to the AR. Binding of DHT induces a conformational change and dimerization of the AR receptor, facilitating the nuclear targeting of AR and recognition of androgen response elements (AREs), which consequently regulate genes that are essential for cell growth, survival and PSA expression [202]. Aberrant AR signalling is common in PCa, consequently shifting primary hormonal naïve lesions to a hormonal independent castrate-resistant prostate cancer (CRPC) phenotype, which is the main hallmark of disease progression and poor clinical outcome [203]. After initial diagnosis of localized disease, most patients invariably relapse from surgery, after a median of 18-24 months. Elevated serum PSA, indicates that AR activity is inappropriately restored (activation in the absence of DHT), leading to increased tumour size, symptomatic disease and eventually metastasis. AR deregulated mechanisms of PCa are reflected by AR amplification, mutations, desensitization, ligand independent AR activation (cytokines or growth factors) and mRNA splice variants [204]. This lethal CPRC phenotype is thus responsible for the high mortality rate (mean survival time is around 1 – 2 years) of PCa and poor clinical outcome or resistance to treatment [202].

1.3.1. Current treatments

A large meta-analysis has found that at the time of diagnosis, about 90% of PCa tumours are clinically localized [205]. Many patients may then have indolent lesions that are surgically removed and patients are then carefully monitored, However, 15-50% of these subjects, still show biochemical recurrence, with rising PSA levels, developing aggressive and metastatic tumours, with poor survival rate [206]. PCa disease progression and concurrent treatments have been distinctively summarised in **Figure 1.8.**

Clinically localized PCa is mainly treated through surgery and radiation therapy or left untreated. Radical prostatectomy and pelvic lymph node dissection, along with external-beam radiation and brachytherapy are first-line choices for primary PCa. High-intensity focussed ultrasound has also been compared in a systemic review, but revealed worse disease-free survival at 1 year, compared with the previous treatment options [207,208]. In the 1940's, Huggins and Hodges [209] demonstrated the therapeutic efficacy of androgen deprivation therapy (ADT), which remains a gold-standard treatment in PCa, despite the transient effect and high rate of post-biochemical recurrence.

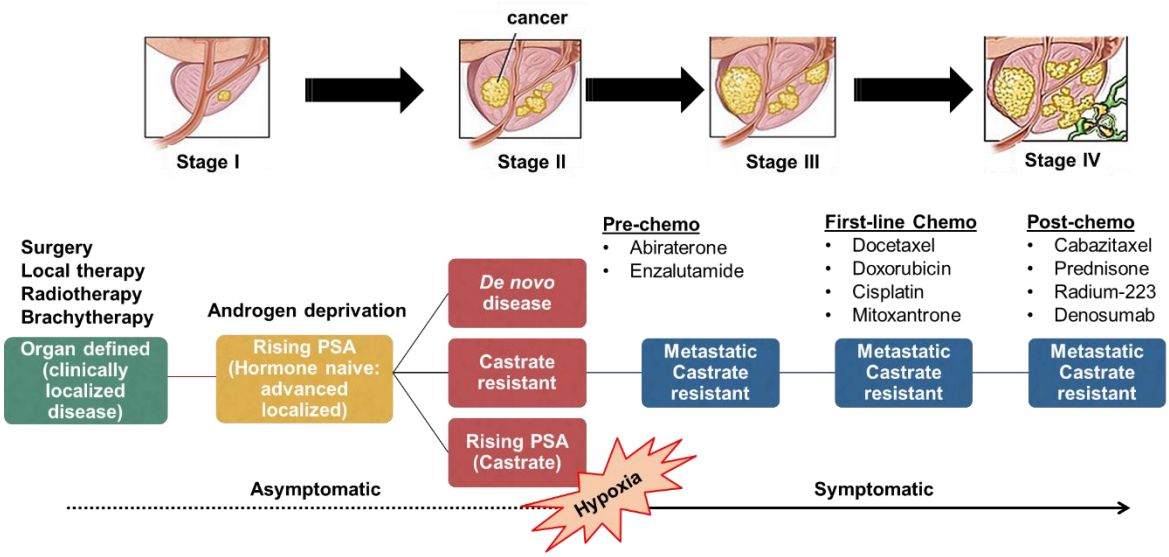

Figure 1.8. Prostate cancer (PCa) disease progression and current treatment options. The scheme differentiates disease stage, highlighting main biomolecular events and respective therapies. The passage of hormonal naïve to castrate-resistant PCa was distinguished, highlighting the occurrence of hypoxia during tumour recurrence and selection of aggressive/metastatic phenotype**.**

Following radical prostatectomy, the standard hormone treatments for PCa include a variety of approaches: 1) orchiectomy and luteinizing hormone-releasing (LHRH) agonists and antagonists (leuprolide, goserelin and triptorelin) that supress androgen circulation by almost 95%; 2) second-line hormonal therapies are used to either block AR receptor (antiandrogens) or by reducing androgen synthesis. Approved antiandrogens include bicalutamide, hydroxyflutamide and nilutamide, and adrenal androgen can be inhibited with corticosteroids, ketoconazole or amino glutethimide [207]. AR gene hypersensitivity and amplification has been reported in about 30% of PCa patients, thereby limiting hormonal therapies and establishing a more aggressive tumour phenotype. More-effective hormonal therapies are now warranted and novel targeted compounds for AR have been extensively reviewed elsewhere [207]. Asymptomatic high risk PCa is treated by utilizing combination of intense ADT treatments (Abiraterone) with radiation therapy. In locally advanced disease, combination with docetaxel only improves relapse-free survival, but with no benefit at 9 years. The first line treatment for symptomatic-metastatic disease (CPRC) includes a combination of hormonal therapy with taxanes and epothilones. Combination of ADT with docetaxel and mitoxantrone plus prednisone therapy, are part of the PCa treatment guidelines [208,210]. Furthermore, second-line treatments include the use of cabazitaxel, a taxane used for acquired docetaxel resistant tumours. Given that most patients at stage IV of the disease suffer from painful bone metastasis, drugs such as zoledronic acid (to reduce skeletal-related events) and denosumab [a human monoclonal antibody for nuclear factor kappa-B (kB) ligand] have been used, but with no translatable survival difference. PCa cells metastasize mostly by the lymphatic route to bones: especially vertebrae, femur, pelvis and ribs [211]. The only bone-targeted drug with significant survival benefit is Ra223. This alpha-emitter is safe to use in PCa with or without docetaxel pre-treatment [210]. To date, the FDA has approved 19 agents for PCa therapy and the majority of these include hormonal targeting moieties of the AR

pathway. However, CRPC is a highly aggressive and recurring PCa subtype, with limited treatment options and more effective/selective therapies are warranted [196]. Hypoxia has become a singular factor in PCa development and can be exploited to develop novel anticancer agents. The role of hypoxia in PCa will be discussed in the next section.

1.3.2. Relevance of hypoxia

Hypoxia is a unique feature of solid tumours that results from a mismatch between oxygen supplies, along with a high metabolic demand. As previously mentioned in **section 1.2**, this then leads to a substantial genetic and metabolic shift that allows tumour cells to readapt, leading to therapeutic resistance [39]. Despite the intense neovascularization in tumours, low vascular density and arteriole network is often linked to poor oxygenation, impairing oxygen transport [212,213]. Previous preclinical data showed that rat vasculature in the prostate suffers rapid capillary degeneration and constriction, during the onset period of castration, leading to loss of blood flow and oxygenation [214,215]. In addition, clinical evidence has connected microvessel density in PCa patients to tumour aggressiveness [216,217]. Analysis of the literature shows over 250 published manuscripts, discussing the role of hypoxia in PCa [218]. This large cohort of data provided preclinical and clinical evidence that hypoxia might be an adequate prognostic predictor or biomarker of PCa, and also an alternative therapeutic target [219].

Hypoxia has been linked to an early onset of PCa [220], but has also been defined as an independent risk factor for CRPC development, particularly in patients who have received radical prostectomy and ADT-treatment [213]. Four key methods have been used to analyse hypoxia in PCa: IHC evaluation of HIF-1 [221,222], intracellular and extracellular hypoxia markers [205,220], microelectrodes [223,224] and imaging of hypoxic fractions [216,217]; leading to a consensus that HIF-1α and hypoxia markers are upregulated in PCa and that prostate tumours thrive under hypoxic conditions [225]. All and all, it has been suggested that hypoxia and androgen signalling are key drivers in PCa development [226].

The current paradigm is that hypoxia increases HIF-1α expression in PCa, androgen ablation increases hypoxia and, in turn, HIF-1α leads to AR amplification (increased level of mRNA expression) and trans-activation; leading to the following cascade of events: 1) hormonal deprivation selects for PCa cells with higher intracellular DHT, which stabilizes HIF-1α dimerization and activity; 2) HIF-1α leads to increased expression, stability and translocation of the AR (hyperactivity/sensitivity); 3) activation of alternate growth-promoting pathways (including those stimulated by EGF and HER2), independent of androgens; 4) HIF-1α cross-talk with AR leads to up-regulation of VEGF, early loss of cellular protection to oxidative damage, increased DNA damage and genetic instability; 5) cooperative activity of HIF-1α and the AR, increases the expression of PSA, driving CPRC development; 6) loss of p53 in tumour development stabilizes HIF-1α, further strengthening previous survival pathways [213]. This complex network of signalling leads to

selection of malignant and resistant PCa clones that prompts re-evaluation of current treatments that overcome treatment resistance, by procuring alternative drugs that specifically target hypoxic tissues (**Figure 1.9**) [227]. An interesting study using TPZ and castration therapy in the Dunning H rat prostate cancer model, proved the enhanced efficacy of this combinatorial therapy, further strengthening the previous hypothesis [228].

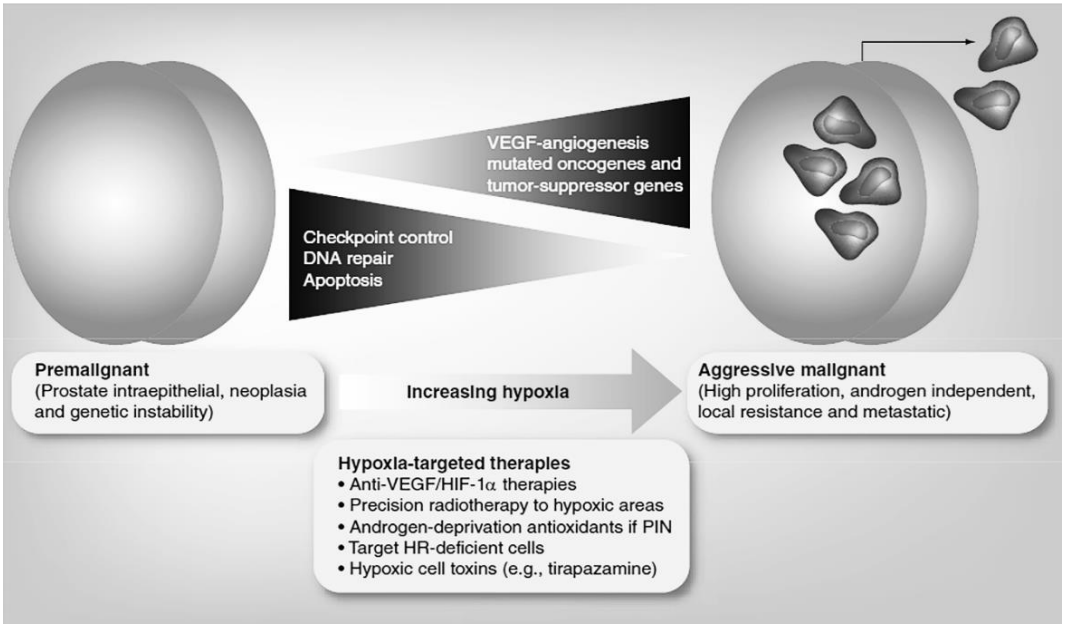

Figure 1.9. Hypoxia and PCa progression. The scheme summarises the role of hypoxia in PCa development and progression, highlighting its effect on androgen deprivation and tumour aggressiveness. This cross-talk between AR and hypoxia suggests the need to develop novel targeted therapies that includes hypoxic selective drugs such as tirapazamine [227].

1.4. Nanomedicine in cancer: a brief overview

Classic chemotherapeutics fail to meet the required bioavailability and potency at the tumour site. These drugs often require high and frequent doses that freely diffuse throughout the whole body, resulting in adverse side effects and high rates of morbidity to patients [229]. Over the last years, much has been devoted to the development and discovery of novel formulations that can achieve a more targeted and beneficial effect [230]. The development of new drug entities is possibly more expensive than optimizing existing drugs, thus the concepts of nanomedicine or DDS have emerged as attractive modalities to improve drug PK, pharmacodynamics (PD), and bioavailability [231]. It is a multidisciplinary field, which aims to bring both commercial and therapeutic value to existing therapies, by improving solubility, circulation time and achieving higher drug content at the desired tumour site [232].

Michael Faraday was the first to acknowledge the promising properties of nanoparticles (NPs) [233] and in the 20th century, Paul Ehrlich proposed the so called 'Magic Bullet', which was described as a special carrier that can actively target a receptor with a specific surface ligand. Ehrlich's extensive work with antibodies was a proof-of-concept that specific molecules can act as

targeting moieties to cells or tissues and that drug carriers can effectively improve drug selectivity and bioavailability.

NPs used in cancer drug delivery are typically smaller than 200 nm, engineered from either soft (organic), hard (inorganic) or hybrid materials and even viral-derived particles (**Figure 1.10**).

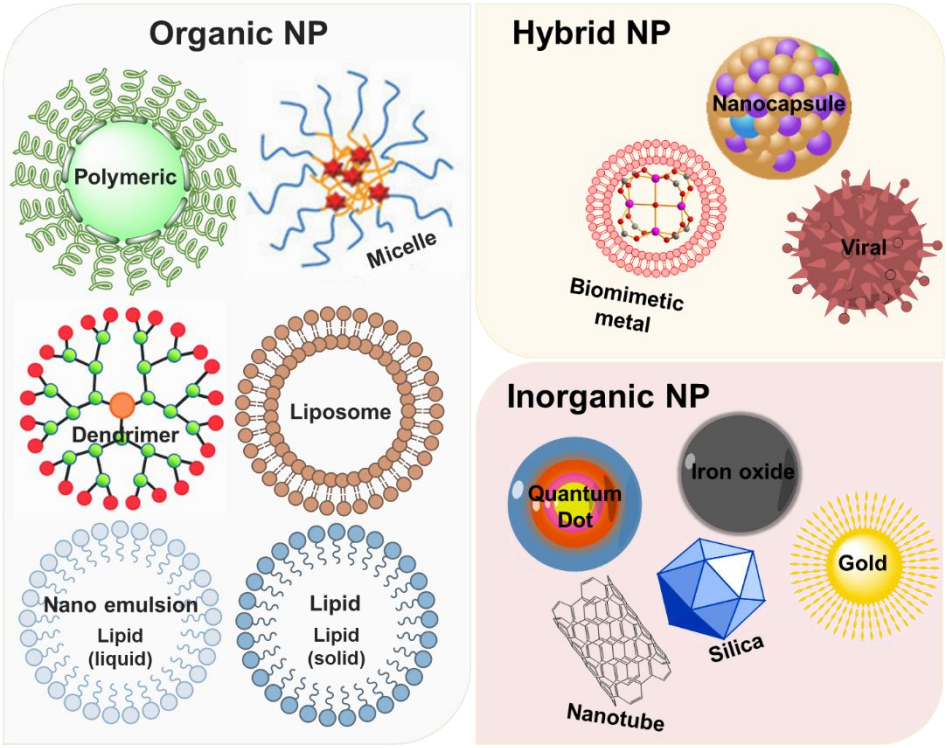

Figure 1.10. Schematic representation of different types of nanoparticle (NP) platforms used in cancer nanomedicine. These NPs have been extensively used in both cancer therapy and for imaging purposes. The carriers have been classified as organic, hybrid or inorganic, depending on the building materials.

These nanocarriers have shown many advantages compared to counterpart micrometer-sized particles, presenting larger surface area, circulation time and deeper penetration in targeted tissues [234,235]. NPs can be fine-tuned by tailoring of their physicochemical properties and modulating factors such as size, shape, structure, morphology and surface properties, which can have a detrimental impact on improving drug PK and overall therapeutic outcome [235,236]. In addition, these properties can also be exploited to develop 'smart' NPs that offer a sustained release profile through various internal and external stimuli, including pH, light/, photosensitivity, temperature, erosion-controlled, hypoxia-responsive, enzyme sensitive [237]. Many NPs have also been used to deliver therapeutic or diagnostic agents, combining cancer imaging and therapy - 'theranostics' [238]. Furthermore, most cancer treatments with higher rates of success involve combinatorial drug regimens. Combined-modality anticancer therapy with newly improved NPs can also revolutionize current treatments involving radiotherapy, hyperthermia and/or immunotherapy, enabling selective and personalized treatment options [230].

The development of a wide spectrum of nanoscale technologies is beginning to change the foundations of disease diagnosis and treatment [239]. A total of 363 products with potential as nanomedicines exist up to date and *ca.* 11% have been approved for clinical application.

Many of these systems incorporated drugs that have already been approved. A large number of clinically approved DDS are liposomes, but polymeric- or lipid-based systems have also shown promise and many more have progressed to clinical trials [231]. Nanoencapsulation offers a means to better solubilize and protect compounds from early degradation. Therefore, many drugs may be delivered in a more efficient way, increasing the therapeutic index and the *in vivo* fate of drugs [240]. Despite the significant therapeutic potential of these systems, their clinical application has not progressed as quickly as expected. Combining the development of more stable formulations with thorough characterization and testing in a multitude of biological environments such as blood, tissue and intracellular components, are essential to better correlate pre-clinical and clinical activity [240].

1.4.1. Liposomes as drug delivery platforms

Liposomes are the most widely reviewed and clinically established nanocarriers [241]. They were first described in the 1960's by Bangham [242] and were later recognized as potential drug carriers in the 1970's [243]. They are small artificial self-enclosed vesicles of spherical shape, which consist mainly natural non-toxic or synthetic phospholipids and cholesterol. Liposomes self-assemble spontaneously in aqueous environment, forming a lipid bilayer, enclosing an aqueous core. This unique structure and composition provide encapsulation of both hydrophobic and hydrophilic drugs in nature. These carriers are highly biocompatible and versatile systems, used in conventional and targeted drug delivery (**Figure 1.11**) [244,245].

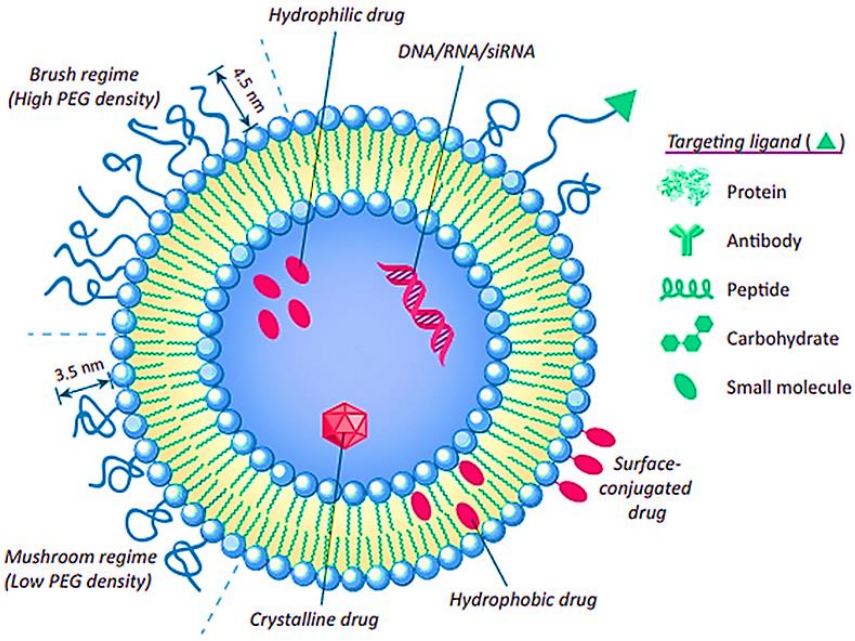

Figure 1.11. Structure and design of liposomes for drug delivery. Liposomes can be used for conventional therapy through delivery of both hydrophobic and hydrophilic drugs in the lipid bilayer and aqueous core, respectively, and even genetic material. These carriers can also be functionalized with different PEG densities ('stealth' liposomes) for prolonged circulation. Furthermore, surface modification with different ligands such as antibodies, peptides, proteins, carbohydrates, and various other small molecules can promote active targeting [247].

Liposomes are mainly classified according to their size and lamellarity (bilayer number) in multivesicles (MVV's), mutilamellar vesicles (MLV's), giant unilamellar vesicles (GUV's), all with size above 1 µm, and large unilamellar vesicles (LUV's, 100-1000 nm) or small unilamellar vesicles (SUV's, <100 nm) [150]. Liposome properties differ considerably with lipid composition, surface charge, size, morphology and the method of preparation, having a detrimental effect on their overall antitumour activity [246].

1.4.1.1. Phospholipids as 'building blocks'

Liposomes are widely known for their versatile and biocompatible nature [248]. These DDS are mainly prepared using phospholipids as the main component. Phospholipids are composed of a polar head group (containing phosphate) and hydrophobic acyl chain that are linked through a glycerol moiety (**Figure 1.12A**). There is a large selection of these molecules used in liposome production, but natural (egg or soybean) and/or synthetic phosphatidylcholines (PCs) are the most commonly used [249]. According to their alcohol group, phospholipids may be classified into glycerophospholipids (**Figure 1.12B**) and sphingomyelins (SMs) (**Figure 1.12C**) [250,251]. Tailoring of the lipid compositions can thus modulate the fluidity of the liposomal bilayer, which in turn affects stability, drug encapsulation and/or leakage [253,254].

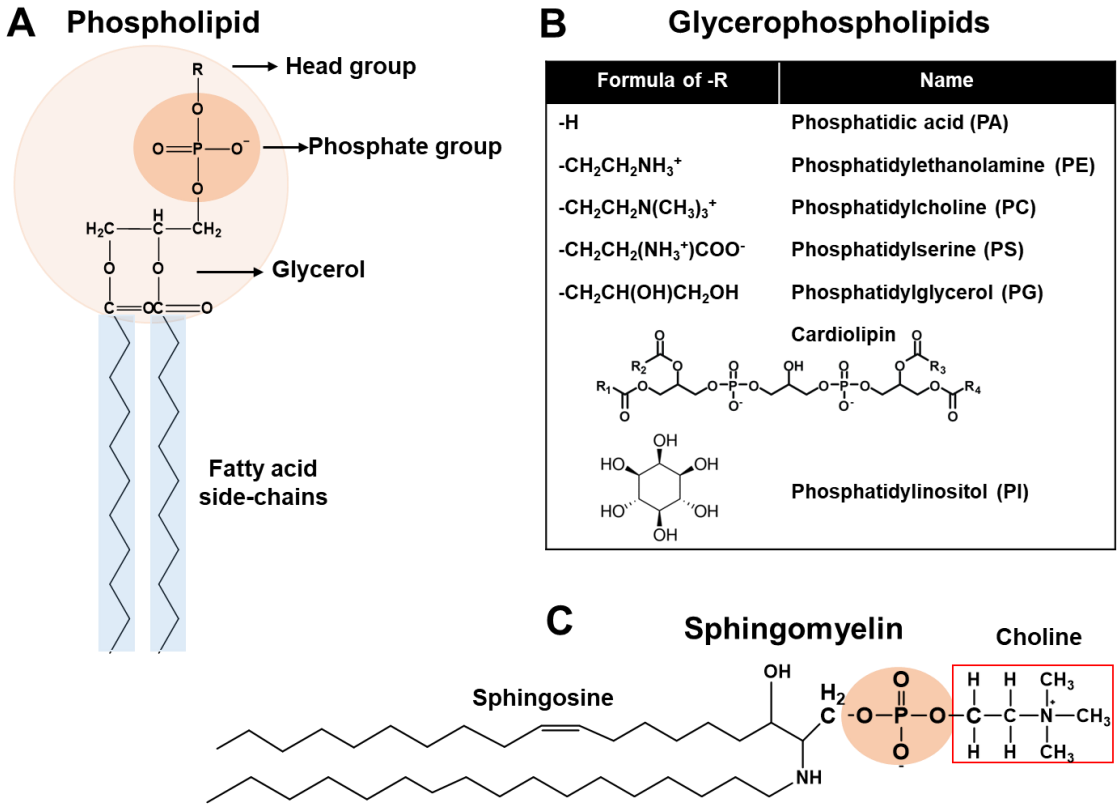

Figure 1.12. Phospholipids and their classification. A) Schematic illustration of phospholipids, mainly composed of a polar head, containing a phosphate group and glycerol moiety that links to two hydrocarbon chains. B) Types of glycerophospholipids, which derive from the substitution of the head group in phospholipids. C) Structure of sphingomyelin, which deviates from the common phospholipid, by adding a sphingosine back-bone and a choline head group. Adapted from [251].

A unique feature of these phospholipid bilayers is their capacity to undergo cooperative temperature-induced phase transition (T_m), which relies on the melting of the acyl-chains composing the bilayer. Therefore, vesicles composed of different lipids will exhibit altered fluidity at the same temperature. T_m varies with: 1) the nature of the head group (glycerophospholipids); 2) the length/degree of saturation of the acyl-chains; 3) the type of bonding and 4) the number of aliphatic chains [249,252].

The lipid bilayer can exist in either a gel state ($T < T_m$) or a fluid state ($T > T_m$) (**Figure 1.13**) [250]. In the former, the hydrocarbon chains are fully extended and packed together in an all-*trans* configuration, generating a well-ordered physical state with low fluidity and permeability. In the fluid state, the hydrocarbon chains are randomly oriented, providing fluidity within the lipid bilayer, with some degree of permeation, due to inter- and intramolecular motion [249,252]. At a temperature equal to T_m, the co-existing gel- and liquid-states generate highly permeable interfacial regions. In general, unsaturated or short length acyl-chain PCs are more permeable and less stable, while saturated and long aliphatic chains, form more rigid and impermeable bilayers [255].

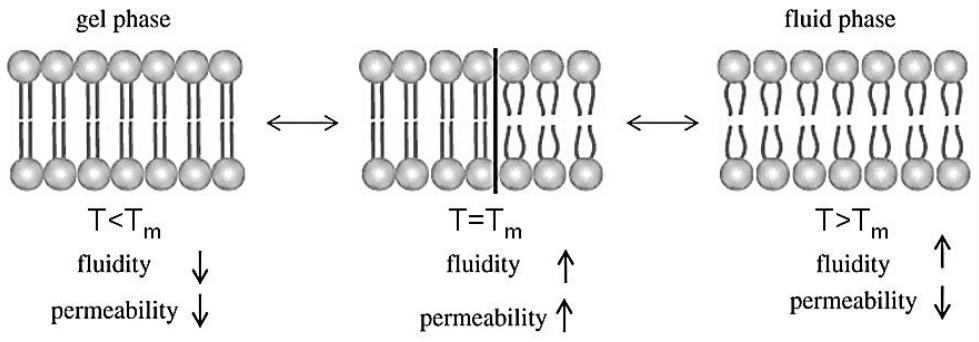

Figure 1.13. Phase transition temperature and bilayer fluidity. Below the phase transition temperature (Tm) the lipids exist in a fully extended and ordered state, with decreased fluidity and permeability (gel phase). As the temperature increases and matches that of Tm, permeability is significantly enhanced by the co-existence of both gel and liquid phases that enhance bilayer motion. In the fluid phase, at temperatures above the Tm, a disordered state of the bilayer is achieved with increased motion of the hydrocarbon chains and pronounced fluidity of the bilayer [249].

1.4.1.2. Cholesterol and stabilization

In order to achieve maximum accumulation and activity at the tumour site, liposomes need to be carefully tuned and characterised to meet a set of structural criteria for enhanced stability and circulation. Aside from the role of phospholipid compositions, it is now widely accepted that formulations stabilized with *ca*. 33% molar ratio (total lipid) of cholesterol (Chol) have increased circulation *in vivo* and overall stability, with more sustained drug release [256,257]. Chol is a major contributor in membrane organization, dynamics and function. It reduces the rotational freedom of the hydrocarbon chains and plays a fundamental role in stabilizing the lipid bilayer, by affecting the T_m [256,257]. Also, formulations containing Chol, have shown to minimize opsonin affinity, phagocytosis, liposome degradation [removal of phospholipids *via* high density lipoproteins (HDL)] and liposome clearance [258].

Liposomes composed of mixtures of phospholipid (especially saturated and with long acyl chains) and cholesterol generally demonstrate decreased permeability and higher stability [255]. The inclusion of Chol is a determinant factor on membrane permeability and can effectively modulate drug encapsulation and release.

1.4.1.3. 'Stealth' liposomes: the role of polyethylene glycol (PEG)

Like most nanocarriers, liposomes are recognized as foreign objects to the body and can be cleared quickly by the RES system. In order to overcome this, coating with amphipathic PEG or chitin derivatives has been employed; as well as, the use of processes like freeze drying, polymerization or microencapsulation of gangliosides [244]. One important surface modification of liposomes is the steric hindrance with PEG molecules to prolong circulation, the so-called 'stealth' liposomes (**Figure 1.14**). This surface coating can vary in length and branching of the PEG molecules, but addition of high molecular weight PEG (2000 Da and higher) is known to increase the surface hydrophilicity of the lipid vesicles, by dehydration of the lipid shell, subsequently compacting the liposomal vesicles [259,260]. This enhanced lateral packing of the acyl chains, also promoted by the addition of Chol, contributes to an increased stability of the liposomes, whilst reducing the interaction with serum proteins, complement activation; thereby minimizing macrophage uptake and significantly prolonging circulation time *in vivo* [261].

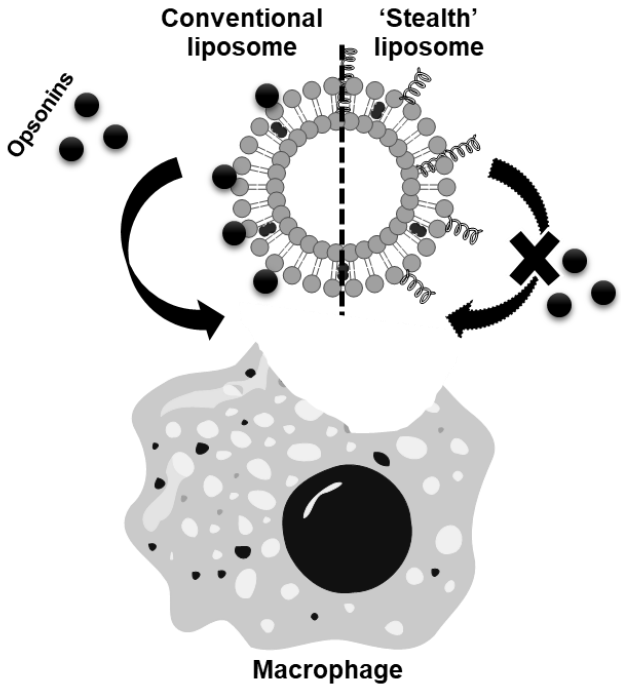

Figure 1.14. Illustration of conventional liposomes *vs.* 'stealth' liposomes. Conventional liposomes without PEGylation bind serum proteins (such as opsonins) that function as a signal for recognition of foreign bodies by the macrophage system. Liposomes are then quickly uptaken by these cells and rapidly cleared from circulation. In order to overcome this, the addition of PEG forms a hydrophilic surface that excludes binding of macromolecules. This steric hindrance inhibits macrophage uptake and significantly prolongs liposome circulation *in vivo*.

PEGylated liposomes at a 5–10 mol % PEG to total lipid are generally used to significantly enhance circulation time of the carrier [261]. This 'stealth' principle has led to the development of the first successful marketed Dox-loaded liposome product for cancer therapy, Doxil® (Janssen Biotech, Inc., Horsham, USA) or Caelyx® (Schering-Plough Corporation, Kenilworth, USA) [262] and is widely used in liposome production.

1.4.1.4. Preparation and characterisation

The preparation of liposomes is a spontaneous process that leads to the formation of lipid vesicles composed of a bilayer and self-enclosed aqueous core, stabilized by hydrogen bonding, van der Waals forces, and other electrostatic interactions [241,245]. These liposomal vesicles are highly attractive as they can encapsulate both lipophilic and hydrophilic drugs, of various chemical compositions [247,248]. In general, all methods used in liposomes preparation involve 4 main stages (**Figure 1.15**): 1) preparation of a dried lipid film, by evaporation of organic solvents used for lipid dispersion; 2) re-hydration of the film in an aqueous buffer, leading to the spontaneous self-assembly of vesicles; 3) purification of the resultant liposome population and 4) characterisation of the formed vesicles [244]. The method of preparation has pivotal role on size and structure of the liposomes, efficiency of drug loading and drug release. In turn, the lipid composition, drug's nature, optimum size, polydispersity, shelf-life, circulation *in vivo* and batch-to-batch reproducibility are parameters that should be taken into consideration when formulating a new liposomal system [263]. After preparation, drugs can be incorporated by two main strategies involving either a passive or remote loading method.

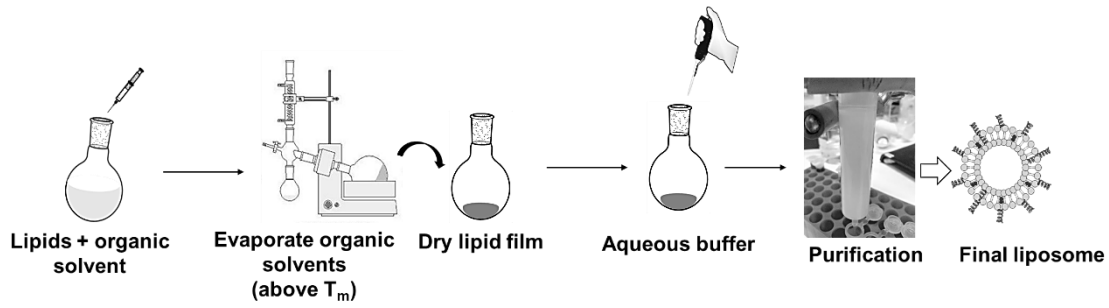

Figure 1.15. General schematics of liposome preparation.

The first method is often associated to the classical thin-film layer hydration method (TFH) or Bangham method, where drugs are added during the formation of the liposomal vesicles and rely on diffusion through the bilayer [244,248]. Passive loading often leads to poor drug loading, especially for water-soluble drugs, and can be modified, for improved drug encapsulation, using the following methods: ethanol injection [264], freeze-thaw cycling (FAT) steps [265,266], detergent dialysis [267], reverse-phase evaporation [268] and drugs in supersaturated state [269]. For remote or 'active loading', drugs are incorporated into preformed liposomes through generation of various gradients (salt, pH or metal-ion) that drive drug loading. pH mediated loading has been considered a milestone

in liposome preparation and led to the development of many marketed formulations [270]. This strategy is well-known for its excellent drug encapsulation, high drug-to-lipid ratios and improved retention through drug precipitation in the liposome core.

Furthermore, the use of metal-ion gradients and ion-complexes has also become an interesting and successful method that leads to excellent drug loading, retention and stability, with optimum drug release and therapeutic activity [271-273]. This strategy is exceptionally appealing, as it results in the preparation of stable drug-complex precipitates in the liposomal core, thus enhancing drug retention. More recently, methods such as microfluidics, the use of supercritical fluids and freeze-drying of double emulsions have been applied to the preparation of liposomes in order to potentiate batch-to-batch reproducibility and scale-up manufacture [274].

Following the formation of the lipid vesicles, reduction of size and lamellarity can be carried out using homogenization, sonication and extrusion [244]. Sonication is a widely used technique, as it is simple and quick to use, but can result in heterogeneously-sized populations [267]. On the other hand, the extrusion method yields controlled size reduction, aided by high temperature, but only allows small working volumes per extrusion cycle [275,276].

1.4.1.5. Conventional and targeted liposomes

Liposomes are well recognized for their vast application as carriers of drugs, peptides, genetic material (DNA, plasmids and siRNA) and their use in vaccine therapy, cosmetics and oral drug delivery [241]. Liposome bilayers protect the encapsulated compounds from hydrolysis or oxidative degradation and prolong circulation time in the body, therefore enhancing bioavailability at the selected target [247]. Many classical and commercially available liposomal anticancer drugs rely only on passive targeting to the tumour. This delivery method underlines transport of carriers through the leaky vasculature of tumours *via* EPR effect. This inherited feature of abnormal angiogenesis leads to leaky and heterogeneous nature of the tumour microvascularization, with impaired lymphatic circulation, that allows optimum accumulation of liposomes with sizes ranging *ca.*100 nm [277]. Passive targeting to the tumour is highly dependent on the physicochemical properties and surface characteristics of the nanocarriers. It is well established that liposome size has a detrimental role on circulation and tumour accumulation, especially *via* EPR effect. Studies have shown 10–50-fold higher accumulation of liposomes, compared to free drugs, at the tumour site, within 1–2 days after injection [236]. Additionally, analyses of tissue distribution and liposome circulation, confirmed that relatively small (< 200 nm) PEGylated-liposomes were poorly uptaken by macrophages, acquiring prolonged *in vivo* circulation [247]. The reduced size minimizes opsonin adherence and therefore, recognition by the reticuloendothelial system (RES) and complement activation. On the other hand, very large (> 200 nm) and very small (< 50 nm) liposomes, were either rapidly cleared by macrophages or showed elevated and rapid accumulation in the liver, respectively [278,279]. An

optimum size of 100 – 200 nm seems to satisfy the criteria for prolonged circulation and successful delivery to the tumour [278,279].

The overall net charge of liposomes, typically expressed as zeta-potential (ζ), also influences liposome uptake and delivery. According to their surface charge, liposomes can be classified as anionic, cationic or neutral [244]. Liposomes without charge have higher tendency to aggregate than those with net charge, which compromises stability and circulation. The nature and density of the surface charge has an impact on stability, PK, PD, cellular affinity and drug internalization [280]. Negatively charged liposomes are prone to opsonization, which leads to their rapid blood clearance. Nevertheless, negatively charged liposomes have shown to enhance cellular uptake through endocytosis at a faster rate and to a greater extent than neutral carriers [281,282]. On the contrary, net positively charged liposomes have a tendency to interact with serum proteins, which may lead to activation of complement system and trigger immune response, but can function as a targeting strategy to the angiogenic endothelium of tumours [283]. The overall charge of liposomes depends on their lipid head group composition, salt, and pH of the solution [281,282]. Surface modification of liposomes allows for modulation of their activity and tuning of their physicochemical properties. The EPR effect has become a standard in cancer-targeting drug designing and has been applied for almost all rapidly growing solid tumours. A significant number of non-targeted liposome formulations have been commercialized and are summarised in the next section.

The extensive research in cancer biology, has led to the discovery of new target receptors involving signalling pathways, microenvironment functions, angiogenesis and metastasis that resulted in the development of targeted liposome systems [284]. Active targeting is intended to deliver drugs exclusively to a specific tissue, cell, or intracellular organelle. This targeting scheme is known to enhance tumour cell inhibition, not necessarily by higher accumulation of the loaded liposomes at the target, but by increased receptor-mediated uptake of liposomes [241,285]. This strategy allows drugs, proteins, and nucleic acids to be introduced into target cells, while bypassing multi-drug resistance pathways and potentiating therapeutic action [286]. A variety of ligands or receptors, such as antibodies [284,287], peptides [288,289], cytokines [290,291], growth factors/internalized-based ligands [(folate, transferrin (Tf)] [292,293], sugar moieties [294,295], DNA/RNA aptamers/oligonucleotides [296,297] and lipoproteins [298] have been anchored and expressed on liposome surfaces. To date, there has been no approved ligand-targeted liposome for anti-cancer therapy [299]. However, recently, three main targeted liposome formulations have progressed to phase I and II clinical trials. A transferrin (Tf) targeted oxaliplatin liposome (MBP-426), a targeted anti-human epidermal growth factor receptor 2 (HER2) Dox formulation and a liposome with a conjugated antibody (SGT-53) [241]; which may well depict the potential of these systems in revolutionizing anti-cancer strategies.

1.4.1.6. Clinical translation and commercial application

Liposomes have evolved rapidly from conventional non-targeted or 1st generation vesicles to tunable 2nd generation 'stealth' systems and, more recently, complex functionalized hybrids to form effective targeting and/or 'theranostic' systems (3rd generation) [299]. Given their unique properties, about 15 liposome and lipid based-drug formulations have been approved for clinical use, seven of them intended for cancer therapy. A thorough summary of marketed liposomes and those in clinical trials was summarized in **table 1.4** [236,281]. Regarding cancer therapy, Doxil® [262] (1995), followed by Daunoxome® (1996) (PEGylated liposomes containing Dox and daunorubicin, respectively), were the firstly developed and FDA approved liposomes for the treatment of Kaposi's sarcoma and has rendered over 600 million dollars in annual sales, across all their markets. In Europe and Canada, Myocet®, a non-PEGylated liposome encapsulating Dox, has also been approved for the treatment of metastatic breast cancer in combination with cyclophosphamide [300]. The most recently marketed liposomal formulation (2012) is Mariqibo® (vincristine sulfate liposome injection), which has been licensed to treat acute lymphoblastic leukaemia [301]. This data has proven the efficacy of liposomal-based drug platforms. Future efforts to maintain such success, must rely on balancing high production cost, large-scale production and overcoming biological barriers for feasible clinical translation.

Table 1.4. Commercially available liposome-based drugs.

	Product	Manufacturer	Drug	Therapeutic Target	Year approved
Cytotoxic	**Doxil®/Caelyx®**	Johnson & Johnson	Doxorubicin	Kaposi's sarcoma, ovarian cancer, breast Cancer, multiple myeloma + Velcade	1995 1999 2003 (Europe, Canada)
	Daunoxome®	Gilead	Daunorubicin	Kaposi's sarcoma	1996 (Europe), 1996 (USA)
	Myocet ®	Zenus Pharma	Doxorubicin	Metastatic breast cancer + cyclophosphamide (combination therapy)	2000 (Europe)
	Depocyt®	Enzon Pharmaceuticals	Cytosine Arabinoside	Neoplastic meningitis and lymphomatous meningitis	1999
	Lipo-dox®	Sun Pharma	Doxorubicin	Kaposi's sarcoma, ovarian/breast cancer	2001 (Taiwan)
	Mepact®	Takeda	Muramyl tripeptide	Non-metastatic osteosarcoma	2009 (Europe)
	Mariqibo®	Talon	Vincristine sulfate	Acute lymphoblastic leukemia	2012 (USA)

Table 1.4. Commercially available liposome-based drugs (continued).

	Product	Manufacturer	Drug	Therapeutic Target	Year approved	
Vaccine		**Epaxal®**	Berna Biotech	Inactivated hepatitis A virus	Hepatitis A virus infections	1994 (Switzerland)
		Bio-Hep-B®	Biotechnology General	All three epitopes of hepatitis B surface antigen	Hepatitis B virus infections	2000 (marketed in Israel)
		Inflexal V®	Berna Biotech AG	Inactivated Influenza virus strains A and B	Influenza Virus	1997 (USA)
		FluMist®	MedImmune, LLC	Weakened live influenza viral particles	Influenza Virus	2003 (USA, Canada) 2011 (Europe)
Pain management		**DepoDur®**	Pacira Pharmaceuticals	Morphine sulfate	Postoperative pain following major surgery	2004 (USA)
		Exparel ™	Pacira Pharmaceuticals	bupivacaine	Management of postsurgical pain.	2011 (USA)
Fungicide		**Ambisome®**	Gilead	Amphotericin B	Several systemic fungal infections (Visceral leishmaniasis)	1990 (Europe) 1997 (USA)
Others		**Visudyne®**	Novartis	Verteporfin	Age-related macular degeneration, pathologic myopia and ocular histoplasmosis	2000 (USA) 2003 (Japan)

1.4.2. Nanomedicine, liposomes and PCa

Surgery followed by hormonal therapy are still the mainstay therapeutic options for treatment of non-metastatic PCa. However, most tumours become androgen resistant, leading to a more aggressive tumour phenotype. Nowadays, about 83% of patients with advanced PCa have a ten year survival rate estimate, due to the development of new adjuvant therapies including mono- or combined radiotherapy, immunotherapy and improved chemotherapy [302]. These treatments options, however, still present innumerous side-effects and lead to cancer recurrence, metastasis and development of drug resistance [303].

Different NP approaches have been developed for PCa [303,304]. In particular, a strategy where green tea extracts of epigallocatechin 3-gallate (EGCG) were used, displayed important chemoprevention effects on PCa [305]. Studies have been conducted using different NPs with EGCG *in vitro* and preclinical settings, where improved selective therapeutic effects were obtained via EGCG-carriers, compared to the compound alone [306,307]. Several other NPs have also been developed for PCa therapeutics: Au-NPs [308,309], polymeric [310,311] , quantum dots [312], micelles [313,314], hybrid lipid/polymer [315], gene delivery [316,317] and magnetic or metallic particles for adjuvant photothermal/hyperthermia therapies [318,319].

Treatment modalities of PCa patients include the use of several classical chemotherapeutics after androgen deprivation. Efforts have been made to develop non-targeted [315,320] and targeted NPs that deliver these drugs effectively to the tumour site, bypassing a high range of side-effects, leading to marked drug bioavailability. The main targeting moiety used in PCa nanomedicine is the surface functionalization of ligands and aptamers directed to a prostate specific membrane antigen (PSMA) that is highly expressed in advanced PCa [321]. This active targeting modality, led to the preparation of different NPs incorporating docetaxel [322], curcumin [323], gene delivery [324,325] or for theranostic purposes [326]. Other targeting moieties such as transferrin [327], cell-surface glycoprotein CD44 [328], mannose-6 [329], tumour-penetrating arginine-glycine-aspartic acid (RGD) peptide [330] and human epidermal growth factor receptor 2 (HER-2) [331] have also emerged as promising targets to enhance PCa therapeutics.

Despite the extensive research with liposomal anti-cancer therapies, few of these strategies have been applied to PCa. Nevertheless, these NPs have been given some thought particularly on their application for CRPC [332]. Liposomal formulations for PCa involve passive targeting [333,334], gene delivery [335,336], combinatorial therapies with radiation in hypoxia [337], ultrasound [338,339] (for improved uptake) and active targeting strategies [340,341], including PSA/PSMA [323,342] and TAMs [343,344].

The success of nanomedicine, as alternative therapies for PCa, was highlighted by the approval of 7 polymer-based formulations [303]. A promising targeted polymeric NP, BIND-014 prototype is now in Phase I and has shown to deliver up to 20 times more docetaxel to tumours than the equivalent free formulation [304]. In addition, liposomal Myocet® and Caelyx®, are also under clinical investigation for PCa [345], perpetuating the positive perspective of using these systems for PCa treatement.

1.5. Hypoxia-targeted nanomedicine

Research in nanomedicine has made tremendous progress, as reviewed in **table 1.4** [346]. More recently, the tumour microenvironment has been shown to contain several drug delivery barriers, but also a plethora of relevant new targets [347]. This tumour niche is now being exploited to develop new formulations that offer both single and combinatorial targeting systems, for selective anti-cancer therapy [348]. For the purposes of this work, the main focus will be put on targeting hypoxia *via* NPs that can provide beneficial selective targeting strategies with improved PK and PD.

Treatment of hypoxic cells using NPs has relied on several strategies [349], as follows: 1) leverageing hypoxia or reoxygenation; 2) preparation of hypoxia responsive linkers; 3) using small molecules that target the HIF-1 signalling pathway and 4) the use of cell-based macrophage carriers or encapsulated HAPs (**Figure 1.16**). To current knowledge, the latter is still poorly exploited.

Both radio- (RT) and photodynamic (PDT) therapies are widely used in cancer therapy. However, the presence of low oxygen levels has a negative impact on the therapeutic outcome of these treatment modalities, resulting in pronounced hypoxia-mediated resistance. Many strategies have been employed to either deliver oxygen directly by nanocarriers, use oxygen shuttles or even oxygen generating NPs. Huang *et al.* [350,351] developed two particularly interesting strategies to deliver oxygen and potentiate the activity of PDT post-hypoxia in prostate models. In the first strategy they used superparamagnetic iron oxide nanoparticles (SPION) oxygen-loaded polymer bubbles in monocyte-mediated delivery for co-transport of oxygen and a light activated photosensitizer, chlorin e6 (Ce6). The carrier exhibited a superior activity in inhibiting tumour growth in Tramp-C1 prostate tumour-bearing mice upon the treatment with magnetic field and light laser [351]. In the second study [350], the same principle was applied for the co-delivery of polymeric bubbles and doxorubicin-loaded polymeric vesicles to further enhance chemotherapy activity. Furthermore, other strategies using biomimetic artificial red blood cells [352] or NPs [353,354] have also allowed the efficient reoxygenation of hypoxic areas to synergistically enhance RT and PDT, or by mediating delivery of oxygen generators such as manganese (MnO_2) and hydrogen peroxide (H_2O_2) [355-357].

The most exploited strategy has been the development of carriers with specific linkers or hypoxia-responsive elements (mostly amine groups of nitro imidazole derivatives) that allow a selective activation of the NPs at the targeted tumour site. These NPs have been constructed as dual pH and hypoxic selective carriers [358,359] or to potentiate the activity of classical chemotherapeutics

[360,361], gene delivery [63,362] or PDT and RT [363,364]. Additionally, 'smart' carriers incorporating molecules that target or down-regulate HIF-1, or related hypoxia markers, have also shown promising results as specific anti-cancer therapies [62,365], as well as the use of anaerobes (*Bifidobacterium breve*, *Clostridium difficile* and *Magnetococcus marinus*) [366,367].

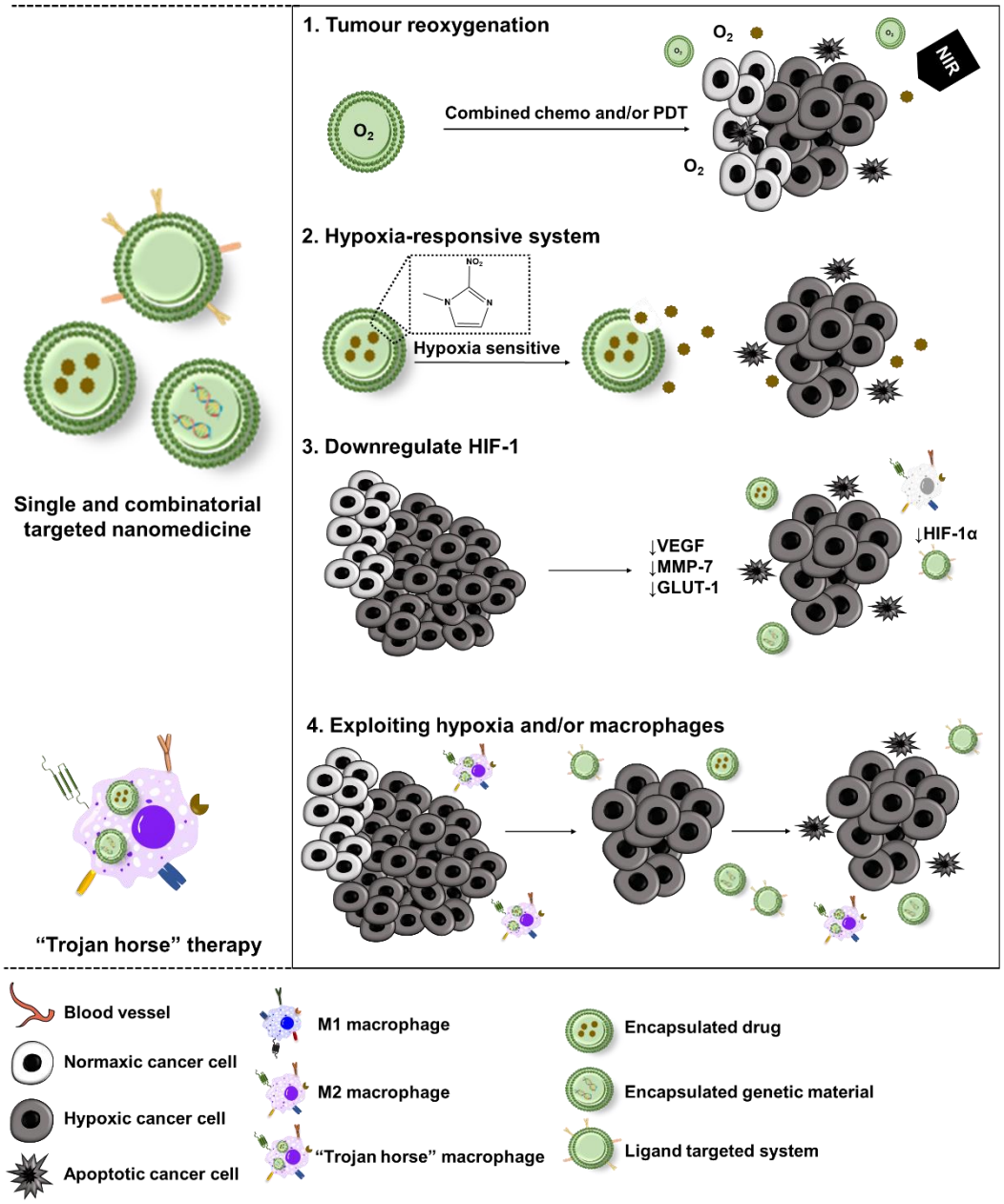

Figure 1.16. Nanoparticle-based therapeutics targeting/using hypoxia. DDS have shown great promises to inhibit the effect of hypoxia on cancer development. The main mechanisms that have been developed so far using nanoparticles to target hypoxic tumour microenvironment are: 1) Leverageing hypoxia or reoxygenating tumours to further potentiate photodynamic therapy and radiation, respectively; 2) developing hypoxia-responsive carriers that selectively release their cargo at hypoxic sites; 3) targeting and down-regulating HIF-1 or hypoxia related markers specific inhibitors/ligands, using specific small molecules; and 4) using macrophages as 'Trojan horses' to deliver DDS to the hypoxic regions of the tumour or via encapsulation of HAPs.

The pro-tumour effect exerted by the M2 macrophages (TAMs) and the high infiltration of these cells into hypoxic regions, has offered a potential combinatorial strategy to enhance nanoparticle (NP) penetration (>150 μm depth) [368]. Choi *et al.* [369] were the first to show the feasibility of a gold-laden cellular based therapy, where macrophages serve as 'Trojan horses' to effectively produce photo-induced cell death in hypoxic tumour spheroids. The Lewis' lab [370], previously used MACs to efficiently deliver oncolytic viruses to hypoxic prostate cancer tissues *in vivo.* One single systemic injection of the oncolytic virus-loaded MACs resulted in a marked inhibition of tumour growth and reduction of pulmonary metastases. This approach also enhanced the therapeutic efficacy of chemo- and radiotherapy in PCa models [371]. The data demonstrated the high potential of multifunctional NPs which target tumour hypoxia and MACs.

The final strategy, of most interest to this work, utilizes the encapsulation of HAPs within NPs and to current knowledge few studies have exploited this method. In 2017, Feng and co-workers [372] developed an interesting multipurpose PEGylated liposomal formulation that encapsulated the HAP Banoxantrone (AQ4N) and a photosensitizer (chlorin hCe6). The data showed marked tumour inhibition after PDT, which leveraged a severe hypoxia environment that simultaneously activated the HAP-liposomes. The liposomes were also fine-tuned with ^{64}Cu (AQ4N-^{64}Cu-hCe6-liposome) proving the versatile nature of these carriers for both therapeutic and *in vivo* PET-imaging purposes. Since then, further studies involving the encapsulation of AQ4N have been developed, mostly reliant on the same synergistic principles of PDT and chemotherapy. Two recent studies focused on the preparation of pH responsive polymeric [HA/AQ4N-Cu(II)-gossypol NPs] [373] or gold NPs [AQ4N-Cu(II)-AptCe6-GNPs] [374] for combinatorial hypoxia therapies with chemotherapy and PDT, respectively. Once again, these treatment modalities showed the superior activity of multimodal NPs within the hypoxia tumour environment, with remarkable anti-tumour efficacy *in vitro* and *in vivo*. An innovative liposomal plataform with AQ4N has also shown to potentiate hypoxia therapeutics through a 'smart' glucose/oxygen starvation strategy, where hypoxia is exacerbated and used to potentiate the activity of the HAP [375]. Aside from AQ4N, only TPZ has been used for alternative NP-HAP targeted therapies and these strategies will be discussed in the section below.

1.5.1. TPZ and drug delivery

Recent studies [230,236,346,349] have supported the notion that drug delivery is a key factor in altering drug PK and re-profiling "old" drugs into exciting anti-cancer therapies. TPZ is well known for its selective, moderate to severe, hypoxia activation [100,121], but requires reassessment and new strategies to improve on its clinical drawbacks. Wu *et al.* [376] were the first to attempt to the use of a carrier for TPZ, creating targeted delivery with transferrin (Tf-G-TPZ) conjugation and co-administered cisplatin. *In vitro* studies revealed that this combination induced substantially higher uptake and selective cytotoxicity, providing important evidence that TPZ mediated conjugation or encapsulation with NPs can markedly improve its PK and PD. More recently, innovative NPs, with either conjugation [376,377] or encapsulation strategies [378-383], have been synthesised to potentiate the efficacy of TPZ (**Figure 1.17**).

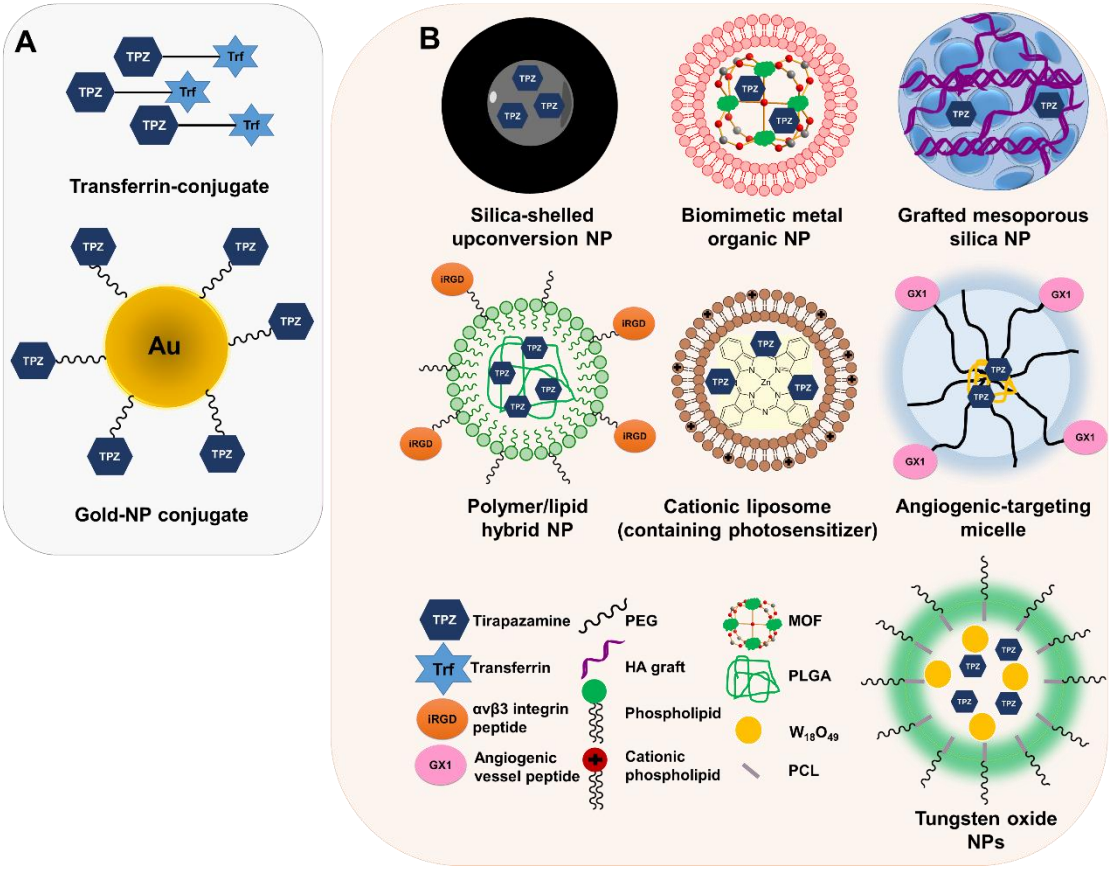

Figure 1.17. Schematic illustration of drug delivery strategies for TPZ. A) Conjugation strategies of TPZ delivery using transferrin and gold (**Au**) particles; B) encapsulation strategies of TPZ using different NPs. These particles were developed using silica, metal-organic frameworks (**MOF**), polymeric or lipid materials and tungsten oxide ($W_{18}O_{49}$). Other abbreviations: **αvβ3**, vascular integrin alpha v beta 3; **PEG**, Polyethylene glycol; **HA**, Hyaluronic acid; **PLGA**, Poly (lactic-co-glycolic acid); **PCL**, Polycaprolactone.

These studies mainly focused on combinatorial regimens of radiation or chemotherapy, used with small doses of TPZ and do not exploit the potential of TPZ carriers as a single treatment modality. Moreover, they depicted varying encapsulation efficiencies (EE) of the drug (2.4 – 77.41%), but generally resulted in loaded drug quantities <300 μM, where the best TPZ cargo was obtained via Tf conjugation [376]. In this study, a traditional bifunctional crosslinking method was employed to synthesize Tf-TPZ conjugates at a 6:1 molar ratio that proved to increase TPZ cellular uptake and bioavailability in vitro.

These NPs, along with their loading method, EE and main outcomes are thoroughly summarised in **table 1.5**. All these studies showed remarkable potentiation of TPZ activity, when used with other treatment modalities, proving the effective hypoxia potential of this drug. The main point of interest is the fact that the simple improvement on TPZ uptake mediated by a NP is enough to potentiate its biological activity. Increasing drug availability by minimizing non-targeted reduction is important to obtain significant hypoxia activity. However, many studies do report low encapsulated drug quantities, highlighting the need to develop stable formulations capable of maximizing TPZ loading so that pre-clinical testing and clinical translation may be an option. There is an unmet need for further research into improving TPZ encapsulation, especially with focus on liposomes and on potentiating its activity as a single agent. Nanomedicine could thus provide significant improvements on current TPZ therapies and repurpose this drug for hypoxia cancer therapy.

Table 1.5. Drug delivery strategies for TPZ.

DDS	Adjuvant	Loading Method	EE (%)/ [TPZ] (μM)[a]	Main findings	Ref.
Transferrin mediated (TPZ-Tf)	Cisplatin	Bifunctional crosslinking method with ester linkage	6:1 mol:mol (TPZ:Tf)/300	Conjugate is acid-sensitive, with endocytic-mediated uptake of NPs *In vitro* cytotoxicity: TPZ+ cisplatin (IC_{50} 139.7 μM ± 12.1 μM) *vs.* TPZ-Tf (IC_{50}, 25.7 μM ±4.2 μM) *In vivo*, i.v. injection of TPZ (20mg/kg) resulted in poor tumour targeting. In contrast, TPZ:Tf (combined with cisplatin) showed remarkable tumour accumulation, improved PK	[376]
Gold (Au) NPs (TPZ-Au)	Radiation	Conjugation *via* thiol of PEG-SH moiety	732:1 mol:mol (TPZ:Au)/134.9	Low toxicity of the system *Ca*. 20% radiation enhancement compared to control Higher uptake of TPZ intracellularly caused *in vitro* cell inhibition after exposure of 48 and 72h, with 3.1-fold increase in ROS production	[377]
Upconversion silica NPs (TPZ@UC/PS)	PDT and PET imaging to confirm hypoxia *in vivo*	Thermal decomposition method followed by oil-in-water emulsion (TPZ added to mixture)	6/168.4	TPZ release was accelerated under acidic conditions HeLa cells treated with TPZ@UC/PS + NIR resulted in 46.1% apoptosis) *In vivo*, TPZ@UC/PS (5.33 mg/mL), showed remarkable tumour growth inhibition, compared to other treatment groups and TUNEL assays confirmed significant apoptosis and synergistic effect of NP + PDT ($p<0.01$)	[378]
Cationic liposomes (ZnPC-ETLS/TPZ)	PDT (4^{th} generation photosensitizer)	Liposomes prepared by lipid film hydration (passive loading)	2.4/24	10-fold increase *in vitro* uptake of ZnPC-ETLS/TPZ, compared to TPZ, Neoadjuvant PDT effect - cell viability reduced to 67% (A431) and 63% (Sk-cha1) under normoxia; and 34% (A431) and 55% (Sk-cha1), under hypoxia	[384]
Micelles (AVT-NPs/TPZ)	PDT and angiogenesis vessel-targeting (AVT - GX1 peptide)	Amphiphilic conjugates that self-assembled into small micelles in aqueous solution	11.08 (Wt)/N.D.	GSH-responsive release (>50% release, after 20h); AVT-NPs/TPZ + irradiation, showed increased uptake, ROS production, and hypoxia cytotoxicity i.v. injection of AVT-NPs/TPZ (2 mg/Kg), *in vivo* led to selective accumulation at the tumour site, with longer circulation time (t ½ ca. 2.1h) *Ex vivo* IHC/western blot - increased angiogenesis and hypoxia in the tumour area	[380]

Table. 1.5. Drug delivery strategies for TPZ (continued).

DDS	Adjuvant	Loading method	EE(%)/ [TPZ](μM)	Main findings	Ref.
Mesoporous silica NPs (TPZ@MCMSN-Gd3$^+$)	PDT and magnetic resonance (MR) imaging agent gadolinium-III	Synthesis of NPs followed by overnight stirring with TPZ (passive loading)	3.9/218.4	HAase mediated release of TPZ HA caused selective CD44 uptake *via* endocytosis TPZ@MCMSN-Gd3$^+$ with PDT showed superior cell killing *in vitro* *In vivo*, TPZ@MCMSN-Gd3$^+$ (1.4 mg/Kg TPZ), showed substantial tumour accumulation and significantly increased tumour inhibition ($p<0.01$)	[379]
Porphyrinic MOF (TPZ@PCN@Mem)	PDT and 4T1 cancer cell membrane coating (biomimetic) for targeting	Synthesis of porous coordination network, + TPZ dissolution (passive loading)	9.8/274.4	Release was time and pH dependent, with increased TPZ in acidic conditions; Highly specific recognition of 4T1 cells IC_{50} *ca.* 5.6 μM, under hypoxia + PDT Injection of TPZ@PCN@Mem (2mg/kg) led to higher tumour accumulation, with improved therapeutic efficiency and evidence of apoptosis and necrosis of tumour tissue - histological analysis	[381]
Polymeric/lipid NP (co-encapsulation of ICG, NP/IT)	PDT and iRGD targeting	Single-step nanoprecipitation (passive loading)	37/N.D.	Rapid release of NP/IT within the first 12h (>40% TPZ) and increased uptake in 4T1 cells ($p<0.001$) Increased ROS production and hypoxia, upon light irradiation *in vitro*, with synergistic effect (IC_{50} under normoxia, 9.4 μg/mL *vs.* 3.7 μg/mL, under hypoxia) 7-fold increased uptake in 4T1 spheroid models with deeper penetration of NP/IT (89 um) i.v. of NP/IT (1.2 mg/kg) *in vivo*, resulted in enhanced tumour accumulation, with significant decrease ($p<0.001$) in tumour weight and volume, compared to control	[382]
Multifunctional tungsten oxide NPs ($W_{18}O_{49}$-TPZ)	Photothermal therapy (PTT)	Emulsion-solvent technique	77.41/*ca.*168	$W_{18}O_{49}$-TPZ + laser (808nm) resulted in temperature increase (25.4 °C to 63.6 °C) – promising PTT properties Laser-induced TPZ release (> 80% over 24h) *In vitro*, combination therapy resulted in 87% cell death with *ca.* 1.79 μM TPZ - superior synergistic treatment; i.v. injection of $W_{18}O_{49}$-TPZ NPs (50 mg/kg) led to increased tumour accumulation and decreased tumour growth ($p<0.01$)	[383]

[a] values calculated using information provided in each manuscript
N.D., information provided was insufficient to calculate encapsulated TPZ

Motivation, aims and objectives of the study

Hypoxia as emerged as a key factor to develop novel anti-cancer therapies. Despite the immense research and scientific know-how on the effectiveness of HAPs, most of these compounds have failed to translate to clinical application. The main issues underlying the current hypoxic modalities is their rapid metabolism, poor tumour penetration and also limited patient stratification that could blunt effective therapeutic outcome. Over the last years, nanocarriers have shown significant progress and also proved to be excellent targeting modalities for the tumour microenvironment, including hypoxia. However, there are still limited vehicles utilizing hypoxia as a target for cancer therapy, particularly in the liposome field.

Encouraged by the optimum hypoxia selectivity provided by TPZ and the growing evidence that repurposing of this drug may be key to its improved efficacy, there is an immense effort to develop nanocarriers for this HAP. The idea is to protect this compound from early non-targeted reduction and maximize its activity in the hypoxic cell. However, most of the developed NPs showing conjugation or encapsulation of TPZ have achieved rather low EE and focused on the activity of this drug in combination with other therapies. The same findings were drawn in a recent study showing the encapsulation of TPZ in cationic liposomes [384]. In addition, Lin *et al* [148] also highlighted the complexation of TPZ to copper (II) and how this metal complex could increase hypoxia selectivity; improving on TPZ activity. Given the strong redox activity of metal complexes a synergistic effect could be expected, after TPZ liberation from the copper complex. Therefore, developing a novel liposomal platform with improved TPZ encapsulation, may play a pivotal role on its cellular uptake, metabolism and overall therapeutic outcome. Taking into consideration the difficulty in encapsulating small drugs such as TPZ, it was sought to combine copper coordination as a strategy to effectively retain TPZ in liposomes. Moreover, given the emerging applications of copper (II) complexes in cancer therapy, this novel complex may well provide an alternative strategy to selectively target hypoxia in both free and liposomal form.

In this thesis, the synthesis and characterisation of cupric-TPZ complexes [$Cu(TPZ)_2$] was reported. Ideally, these $Cu(TPZ)_2$ complexes should maintain or improve TPZ hypoxia selectivity and potency, whilst providing an innovative metal-complex strategy for liposomal encapsulation of TPZ. The aim and main hypotheses of this work are depicted below.

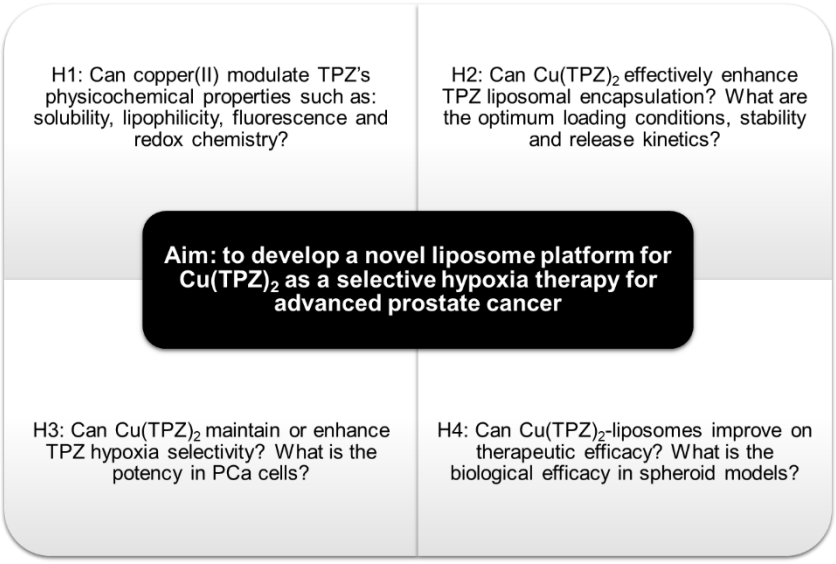

To exploit the above hypotheses, the following tasks were undertaken:

- Synthesise and validate TPZ complexation to copper;
- Investigate the physicochemical properties of $Cu(TPZ)_2$ using various characterisation techniques;
- Exploit TPZ and $Cu(TPZ)_2$ fluorescence for cellular uptake and *in vitro* imaging purposes;
- Prepare and characterise $Cu(TPZ)_2$-loaded liposomes with different lipid compositions, evaluating drug loading capacity, release and stability;
- *In vitro* analysis of free TPZ and $Cu(TPZ)_2$ cytotoxicity, determining hypoxia selectivity and potency in both 2D and 3D prostate cancer cell models;
- Investigate the biological potential of $Cu(TPZ)_2$-loaded liposomes in both 2D and 3D prostate cancer cell models.

Thesis overview

This thesis compromises six chapters, including a detailed summary and analysis of relevant literature reports, along with a discussion on the development and characterisation of both $Cu(TPZ)_2$ complexes and $Cu(TPZ)_2$-loaded liposomes. The project also aimed to investigate the biological applications and therapeutic potency of the free drugs [TPZ and $Cu(TPZ)_2$], and $Cu(TPZ)_2$-loaded liposomes in PCa, under hypoxia. Each chapter provides a summarised overview to focus relevant concepts and a thorough presentation and discussion of the results, ending with a general summary and conclusions. A brief description of each chapter is summarised below:

In **Chapter 1**, a general introduction is presented, providing essential concepts, facts and critical analysis, from current cancer/prostate cancer development to treatment modalities. An interesting summary and perspective on the role of hypoxia in cancer is given, as well as, its link to the development of advanced stage PCa and the need to develop improved nanomedicine platforms. In addition, the evolution of nanomedicine and liposomes is discussed, along with their current clinical status; and the importance of developing novel liposomal formulations for HAPs (particularly TPZ), to overcome their current biological limitations.

Chapter 2 summarises all relevant material and chemicals utilised throughout the project. A relevant theoretical summary of all techniques (chemical and analytical) used in the synthesis and characterisation of $Cu(TPZ)_2$ and $Cu(TPZ)_2$-loaded liposomes is provided. The methods used for *in vitro* uptake and evaluation of hypoxia activity of $Cu(TPZ)_2$ and $Cu(TPZ)_2$-loaded liposomes, in different PCa cell models, is also presented.

In **Chapter 3**, the preparation of $Cu(TPZ)_2$ is described, with further evaluation of its physicochemical properties, compared to TPZ alone. 2.3.1.2. Fourier transform infrared spectroscopy (FTIR), mass spectrometry (MS) and elemental analysis were used to validate copper-TPZ complexation. TEM was used to assess size and morphology, while UV/Vis and fluorescent spectroscopy were used to study compound stability in different buffers and pH environments. Other parameters such as solubility are also discussed, and a HPLC method was developed to accurately quantify TPZ and $Cu(TPZ)_2$. The data regarding simulation of important parameters such as Log P and reduction potential is also presented, given their important role in modulating cellular uptake and hypoxia selectivity.

Chapter 4 highlights the difficulty of encapsulating TPZ alone in liposomes. The chapter includes a detailed evaluation of different methods for TPZ loading in liposomes, along with a thorough discussion on its troubleshooting. Moreover, an alternative metal-complex remote loading method, using $Cu(TPZ)_2$, is proposed. An overview on the various parameters used to optimize its loading technique is presented, highlighting the negative impact of pH gradients on drug loading.

Furthermore, the developed novel $Cu(TPZ)_2$-loaded liposomes were characterised by DLS for size, ζ-potential and phospholipid content was determined by the Stewarts assay. TEM imaging provided the first evidence of encapsulation of $Cu(TPZ)_2$ in liposomes and HPLC was used to determine encapsulation efficiency (EE) and drug loading. This chapter also presents relevant data on liposome release kinetics *in vitro, via* size exclusion chromatography (SEC). To finalize, the short and long term stability of the newly developed liposomes is discussed, along with their drug retention, over time.

In **Chapter 5**, a novel fluorescent method is presented to determine the cellular uptake of TPZ and $Cu(TPZ)_2$ in PCa cells, under normoxia and hypoxia, over time. The biological activity of TPZ and $Cu(TPZ)_2$ was assessed in both 2D and 3D PCa cell models, using the resazurin assay. The data were used to determine hypoxia selectivity and potency under 1% hypoxia *vs.* normoxia (21% O_2). UV/Vis spectroscopy was also used to analyse DNA binding capacity of TPZ and $Cu(TPZ)_2$, providing insight on relevant intracellular targets for these drugs. The cytotoxicity of empty liposomes and $Cu(TPZ)_2$-loaded liposomes was further evaluated, following a similar method described for the free drugs. Fluorescence-activated cell sorting (FACs) was then used to perform cell cycle analysis in PCa spheroid models, as a complementary technique to evaluate cell death.

Finally, in **Chapter 6** all these findings are correlated and discussed within the wider content of the literature, highlighting the future directives and main conclusions of this work.

Chapter 2

Materials and methods

2.1. Materials

The following chapter includes a thorough description of all experimental apparatus, reagents and overall methods explored in this thesis. This section includes an overview on the handling of the hypoxic drug TPZ and the preparation of its cupric complex – $Cu(TPZ)_2$. Following this, their analytical characterisation by different chemical and optical analysis are also provided. A detailed section on the preparation and characterisation of different liposomal formulations used to encapsulate the aforementioned drugs is also described. To finalize, a biological section is also provided, where the hypoxic selectivity and potency of both free drugs was validated, as well as, their liposomal equivalents in different PCa models.

All chemicals were employed without further purification, unless specified. All materials and general reagents are summarised in the following table (**Table 2.1**).

Table 2.1. List of materials. Summarised materials and consumables used throughout this thesis, including their supplier, catalogue number and any extra information considered essential.

	Product	Supplier	Catalogue No.	Description
General materials	4-(2 Hydroxyethyl) piperazine-1-ethanesulfonic acid (HEPES)	Sigma-Aldrich	H3375	≥99.5% (titration)
	Ammonium sulphate [$(NH_4)_2SO_4$]	Sigma-Aldrich	A4418	≥99.0%, for molecular biology,
	Ammonium thiocyanate	Sigma-Aldrich	221988	≥97.5%, ACS reagent
	Copper(II) chloride	Sigma-Aldrich	222011	97%,
	Ethylenediaminetetraacetic acid - disodium salt dehydrate (EDTA-$Na_2 \cdot 2H_2O$)	Sigma-Aldrich	330507	97%
	Ferric chloride hexahydrate	Sigma-Aldrich	207926	≥98%, reagent grade
	Phosphate buffered saline tablets	Sigma-Aldrich	P4417	1 tablet in 200 ml ddH_2O (pH 7.4, 137 mM NaCl, 10 mM phosphate buffer, 2.7 mM KCl)
	Polyethylene glycol sorbitan monooleate (TWEEN® 20)	Sigma-Aldrich	P1754	Viscous liquid
	Sephadex™ G-25 (PD-10) desalting columns	Fisher Scientific	11768488	
	Sodium citrate tribasic dehydrate ($Na_3C_6H_5O_7$)	Sigma-Aldrich	S4641	≥99.0%, ACS reagent
	Sodium hydroxide (NaOH)	Sigma-Aldrich	S5881	Reagent grade, 98%, pellets (anhydrous)

Table 2.1. List of materials (continued).

	Product	Supplier	Catalogue No.	Description
	Tirapazamine	Sigma-Aldrich	SML0552	50 mg
	Triton-X 100	Sigma-Aldrich	X100	Laboratory grade
	Tris hydrochloride	Fisher Scientific	10316893	Small white flakes/molecular biology
	Universal MALDI Matrix	Sigma-Aldrich	50149-1G-F	1:1 v/v, [2,5-dihydroxybenzoic acid (DHB): α-cyano-4-hydrocinnamic acid (CHCA)]
Solvents	Acetic acid	Fisher Scientific	A/0400/PB15	Glacial, certified for analysis
	Acetone	VWR	20066.330	≥99.8% AnalaR NORMAPUR® ACS
	Chloroform ($CHCl_3$)	Fisher Scientific	C/4966/17	HPLC grade
	Dimethylsulfoxide (DMSO)	Fisher Scientific	10080110	≥99%
	Ethanol (EtOH)	VWR	20821.330	≥99.8% AnalaR NORMAPUR® ACS
	Hydrochloric acid (HCl)	Sigma-Aldrich	320331	37%
	Isopropanol	VWR	20842.330	≥99.7% AnalaR NORMAPUR® ACS
	Methanol (MeOH)	Fisher Scientific	34860	HPLC grade
Lipids	1,2-dioleoyl-sn-glycero-3-phosphocholine (DOPC)	Lipoid	556600-2140160-01/911	Kind gift
	1,2-dipalmitoyl-sn-glycero-3-phosphocholine (DPPC)	Lipoid	556300-2130125-01/046	Kind gift
	1,2-distearoyl-sn-glycero-3-phosphocholine (DSPC)	Lipoid	556500-213030301/917	Kind gift
	1,2-distearoyl-sn-glycero-3-phosphoethanolamine-N-[amino(polyethylene glycol)-2000] (DSPE-PEG_{2000})]	Lipoid	588200-2130052-01/908	Kind gift
	Cholestrol	Sigma-Aldrich	1001575618	

Table 2.1. List of materials (continued).

	Product	Supplier	Catalogue No.	Description
Biological assays	Agarose	Sigma-Aldrich	A9539	BioReagent, for molecular biology, low EEO
	CYTO-ID® Hypoxia/Oxidative Stress Detection kit	Enzo Life Sciences UK	ENZ-51042-0125	
	Deoxyribonucleic acid sodium salt from calf thymus	Sigma-Aldrich	D1501	CT-DNA
	Dimethylsulfoxide (DMSO) – Hybrimax	Sigma-Aldrich	D2650	≥99.7%, sterile-filtered, BioReagent
	FxCycle™ PI/RNase Staining Solution	Fisher Scientific	F10797	Cell cycle analysis DNA stain
	Gibco™ Advanced RPMI 1640 Medium	Fisher Scientific	11530446	
	Gibco™ Dulbecco's (DPBS, 1X)	Fisher Scientific	10593093	No calcium, no magnesium
	Gibco™ Fetal Bovine Serum	Fisher Scientific	11563397	Non-heat inactivated
	Gibco™ Penicillin-Streptomycin	Fisher Scientific	11548876	10000 units/ml
	Gibco™ Trypan Blue Solution	Fisher Scientific	10062742	0.4% in PBS
	Gibco™ Trypsin-EDTA	Fisher Scientific	11590626	0.05%, phenol red
	GlutaMAX™ supplement	Fisher Scientific	10388582	200 mM
	Heat inactivated newborn fetal bovine serum	First Link UK	08-05-850	Filtered through 0.22µm
	Hoechst 33258	Sigma-Aldrich	B1155	Powder, BioReagent
	Paraformaldehyde (PFA)	Sigma-Aldrich	158127	4% (w/v) - 8 g Paraformaldehyde 200 ml PBS pH 7.3 Note: *dissolve PFA in initial 150 ml PBS at 60°C in fume cupboard*
	Poly-D-lysine hydrobromide	Sigma-Aldrich	P6407	Mol wt 70,000-150,000, lyophilised powder, γ-irradiated, BioReagent
	ProLong™ Gold Antifade mounting media	Fisher Scientific	15222826	
	Resazurin sodium salt	Sigma-Aldrich	R7017	BioReagent, suitable for cell culture

2.2. Synthesis of cupric-tirapazamine complexes [$Cu(TPZ)_2$]

2.2.1. TPZ stock preparation

For characterisation purposes, TPZ (50 mg) was dissolved in either DMSO (56 mM) or ethanol (2.8 mM) and stored in darkness at -20°C. Standard solutions in PBS (pH 7.4), HBS (20 mM HEPES, 150 mM NaCl, pH 7.4) and water, were prepared on a daily basis for subsequent studies. For biological studies, TPZ was dissolved in NaCl 0.9% (4.5 mM).

2.2.2. Preparation of $Cu(TPZ)_2$ complexes

All starting materials were commercially available research grade chemicals and were used without further purification. The $Cu(TPZ)_2$ complexes were prepared, as described previously [168,385]. Two equivalents of TPZ (13.2 mg, 0.074 mmol) were added slowly to a stirred solution of $CuCl_2$ (5 mg, 0.0.037 mmol) in a total 5 mL of an ethanolic solution, resulting in the formation of a deep red precipitate. Following overnight stirring, the dark red precipitate was isolated and washed with small volumes of ethanol by centrifugation at 5000 x *g* for 10 min, until a colourless supernatant was obtained. The red complex was then left to dry under vacuum at room temperature and resuspended in DMSO until complete dissolution (*ca.*2.5 mM stock solution). The complex was then sterile-filtered through 0.2 µm membrane filter. The stoichiometry of the compound was [$Cu(TPZ)_2$] and the yield *ca.*70% (11 mg, 0.026 mmol). The results of the elemental analysis (%) obtained with a Carlo Erba EA 1108 analyser were: ($C_{14}H_{10}CuN_8O_4$) Found/Calcd.: C, 39.85/40.32; N, 25.66/26.87; H, 2.39/2.21. IR (ATR) analysis: (cm^{-1}) - ($\nu N–H_2$), 3360-3311; ($\delta N–H_2$), 1570, 1500 ($\nu N \rightarrow O$), 1358; ($\nu C\text{-}N/\nu C\text{-}C$), 1111, 1165, 1215. MALDI-MS: m/z (%) $[Cu(TPZ)_2\text{-}H]^+$, Found/Calcd (%): 418.0199/418.0202 (100).

2.3. Characterisation of TPZ and $Cu(TPZ)_2$

2.3.1. Chemical analysis and complexation validation

2.3.1.1. Carbon-Hydrogen-Nitrogen (CHN) elemental analysis

In analytical chemistry, quantitative elemental analysis by CHN automated analysers is still a reliable complimentary method to identify and ascertain the structure of a new compound. It is also the fastest and most inexpensive method to test the compound's purity [386].

The CHN content is quantified based on flash combustion of solid samples. The combustion device is normally linked to a gas chromatograph to separate the resulting combustion gases, which are then analysed by mass spectrometry or thermal conductivity. In particular, the Carlo Erba EA 1108 Elemental Analyser, analyses dried solid samples, which have been previously weighed and prepared in small tin foil capsules. These samples are then placed in an auto-sampler and are dropped into a combustion reactor, which is normally kept at a temperature of 904°C. The injection of excess O_2 generates flash combustion of the sample that produces one or more of the following gases: NO_x, CO_2 and H_2. These combustion gases then move through the system carried by a helium stream, where they are separated by gas chromatography and analysed by a thermal conductivity detector [387].

In this work, CHN analysis was performed for $Cu(TPZ)_2$ in order to validate the complexation and test the purity of the compound. Briefly, 5 samples containing an empty tin foil capsule and 7 known sulphanilamide (Sigma, UK) standards (weight ranging from 0.2 mg up to 2.0 mg) were carefully weighed by a 4 d.p. sartorius scale. All samples were prepared in tin foil capsules that were subsequently closed into a ball formation using tweezers. These samples were used for instrument calibration and generation of a standard curve for quantitative analysis. Furthermore, a known sample of $Cu(TPZ)_2$, within the range of the standard curve was also weighed out and prepared in triplicate. Analyses were performed using a Carlo Erba EA 1108 Elemental Analyser by technicians at the School of Environmental Sciences (University of East Anglia).

2.3.1.2. Fourier transform infrared spectroscopy (FTIR)

Infra-red spectroscopy is a standard method that can be used for both quantitative and qualitative purposes in analytical pharmacy and chemistry. It is based on the absorption spectra obtained from the transition between different vibrational modes and most molecules display infra-red bands in the so-called mid infra-red radiation (4000 cm^{-1} to 400 cm^{-1}). The position and frequency of such vibrational modes are characteristic of specific functional groups and their conformation, thus allowing a distinctive identification of spectral regions and further characterisation of the compound [388].

Furthermore, Attenuated Total Reflection-IR (ATR-FTIR) requires none or little sample preparation, given the high penetration of the IR light in the sample. This technique provides significant improvement in signal-to-noise ratio, by simply placing solid samples in contact with the diamond ATR crystal [389].

In this work, dried samples of TPZ and $Cu(TPZ)_2$ were analysed using a Perkin-Elmer BX ATR-FTIR spectrometer. The spectra were recorded in a range between 600 and 4000 cm^{-1} after 32 scans by correcting the background. Only diagnostic and/or intense peaks were reported.

2.3.1.3. Mass spectrometry (MS)

Mass spectrometry is a versatile analytical technique used to identify ionized biomolecules or pharmaceutical compounds, based on their mass to charge (m/z) ratio. The use of "soft ionization" techniques such as matrix-assisted laser desorption ionisation time-of-flight (MALDI-TOF), have been widely used, as they do not lead to sample fragmentation. In this method, the samples are mixed with an organic compound used as a matrix, that absorbs light and facilitates sample desorption and ionization [390]. Upon drying, this mixture leads to the formation of a co-crystal, where the sample is entrapped within the matrix. Short pulses of laser light are then focused on the sample, generating single protonated ions [391]. These ions are accelerated at a fixed voltage and separated based on their m/z ratio, where they are analysed by a TOF detector (**Figure 2.1**). The time required for an ion to travel towards the end of the flight tube is determined by its mass, allowing separation and identification of different analytes.

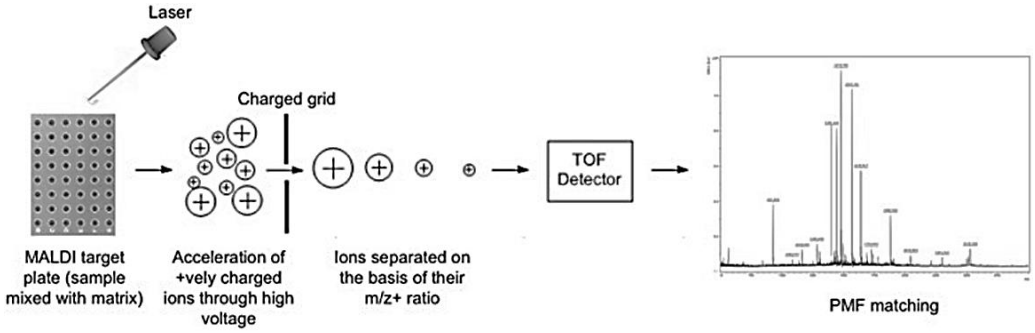

Figure 2.1. Schematic diagram illustrating the principle of MALDI-TOF MS [391].

In this work, MALDI-MS was used to validate the complexation of copper to the hypoxia prodrug TPZ. Samples of TPZ alone and the complex were mixed at 1:1 volume ratio, with a universal matrix [mixture of 2,5-dihydroxybenzoic acid (DHB) and α-cyano-4-hydrocinnamic acid (CHCA)]. The combined sample and matrix were dropped onto a metal target plate and dried before analysis. Analyses were recorded on a Shimadzu Axima CFR Plus Maldi TOF Mass Spectrometer, with a variable repetition rate 50 Hz N_2 laser with a wavelength of 337 nm. Data was obtained with the help of Dr. Ashkan Dehsorkhi (School of Pharmacy, University of East Anglia).

High resolution mass spectrometry was also used, in order to validate the results obtained above by MALDI-MS. High resolution MS was performed by the EPSRC Mass Spectrometry Unit at the University of Swansea.

2.3.2. Optical measurements

2.3.2.1. Ultraviolet-visible spectroscopy (UV/Vis)

Ultraviolet-Visible Spectroscopy (UV/Vis) refers to an optical spectroscopy method, which is routinely used in analytical chemistry for qualitative and quantitative analysis of molecular compounds. After a beam of light is applied to the sample, compounds containing π-electrons or non-bonding electrons (*n*-electrons) can absorb energy in the ultraviolet (200–400 nm) or visible light (400–800 nm) range and excited electrons transit from the ground state to a higher anti-bonding orbital or excited state. Absorption in the visible range reflects the colour of the test sample, yielding different information on the properties and energy state of the given compound [392]. The intensity of absorbed light is directly related to the concentration of the sample, as portrayed by the Beer-lambert law:

$$\mathbf{A = \varepsilon C l} \qquad \textbf{Equation 2.1}$$

Where **A** represents the absorbance, $\boldsymbol{\varepsilon}$ is the molar absorptivity, **l** is the path length of the sample and **C** is the concentration of the sample.

UV/Vis spectroscopy was used to identify the maximum absorbance of TPZ and $Cu(TPZ)_2$ and further used to evaluate stability and chemical changes. This method also corroborated previous methods to validate the complexation of TPZ to copper, by significant displacement of signature peaks.

UV/Vis measurements were performed using a Perkin Elmer Lambda 35 (Perkin Elmer, USA) double-beam spectrometer in a quartz cuvette (10×10 mm), at room temperature. A full absorption spectral scan (190-1100nm) was performed for an appropriate range of concentrations for TPZ (0-280 µM) and $Cu(TPZ)_2$ complexes (0-50 µM) in DMSO. All scans were performed in triplicate (Scan rates 240 nm/min, slit: 2.0 nm) and samples without drug were used for baseline reference, in accordance to each reading. Additionally, copper was used as a standard control for qualitative analysis. The results (mean ± SD) obtained were also plotted to generate standard curves for further quantitative analysis.

2.3.2.2. Fluorescence spectroscopy

Different molecules present different energy states and absorption of light (photons) by a population of molecules induces electrons to transit from the singlet ground electronic level S_0 to an excited state S_n (n > l). This process is quantifiable by absorbed energy, described above as the principle of UV/Vis spectroscopy. The excited molecule can then return to the ground state, after collision with other molecules, by two main successive steps: 1) the excited electron (S_n) dissipates part of its energy and returns to the lowest excited state S_1, a phenomenon designated internal conversion and 2) the excited electron (S_1) loses vibrational energy, and returns to the ground state (S_0), via different processes [393]. In the latter step, absorbed energy can be dissipated in the medium through heat, transit to an excited triplet state T_1 through intersystem crossing and generate phosphorescence, or spontaneously decay by relaxation through a process called fluorescence. The electronic states of a molecule and possible energy transitions described here, have been schematically illustrated in the Jablonski diagram (**Figure 2.2**) [394]. The advantage of fluorescence spectroscopy is that light can be detected with high sensitivity and nowadays, different instruments and set-ups can provide gain and amplification of fluorescent signals, even for nearly non-fluorescent samples. The choice of the ideal spectrophotometer depends on the experimental design and number of samples tested. At the present, high throughput screening is often associated to drug testing and a numerous amounts of samples. Such multi-sample fluorescent measurements can be performed by microplate readers, with reliable detailed information. Such method can provide analysis of emission and excitation spectrum profiles, quenching and also cell based and kinetics studies [395].

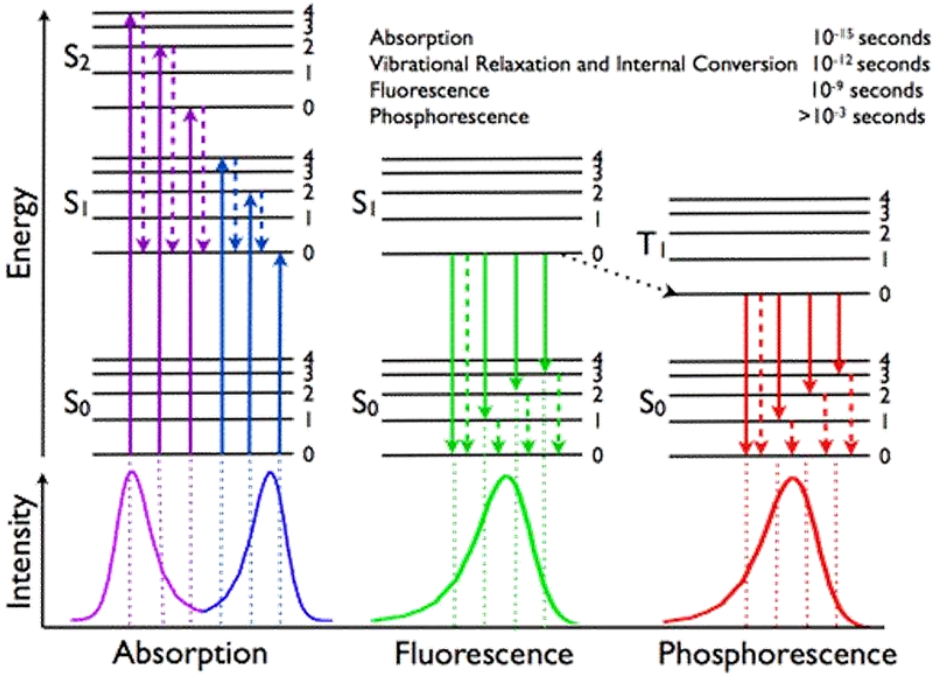

Figure 2.2. Schematic illustration of the Jablonski diagram, summarizing all main electronic states and possible energy transitions in a molecule [393].

In this study, it was of interest to assess the fluorescence spectrum of TPZ and any spectral differences resultant from its complexation to copper. The fluorescent profile for TPZ and $Cu(TPZ)_2$ was determined by testing a range of concentrations (up to 60 µM) in DMSO and HBS. A full fluorescence spectral scan, for both excitation (320 – 530 nm) and emission (540 – 700 nm), was performed by transferring 200 µL of samples to 96-flat bottom black well plates (Sterilin®, Fisher Scientific, UK). Fluorescence spectral analysis was performed using a CLARIOstar Omega microplate reader (BMG Lab Technologies) (filter, bandwidth 10 nm, focal height 8.7 mm and 154 wavelength scan-points) and gain adjustment for the maximum fluorescent sample at 25°C. The fluorescence from each well was captured, digitized, and stored on a computer using MARS data analysis software (Version 3.02). The analysis was performed with triplicate samples of two independent experiments (n=2) and All spectra were corrected by subtracting the background from the dispersing solvent. The results were expressed as mean ± SD in spectral diagrams for qualitative analysis and standard curve graphs were also generated to determine linear dependence for both drugs.

2.3.2.3. pH stability study

To complete drug characterisation and determine their stability in different buffers and pH, UV/Vis and fluorescence spectroscopy were used for spectral analysis, as described above. The spectra of both TPZ and $Cu(TPZ)_2$ was further analysed after dilution in PBS (10mM and 100mM, pH 7.4) and HBS (20mM HEPES, 150 mM NaCl, pH 7.4). To analyse pH dependent spectral differences, TPZ and $Cu(TPZ)_2$ were titrated in water at pH ranging from 1 up to 12.5. Solutions were adjusted to a basic pH with NaOH (aq) and to acidic pH with HCl (aq).

2.3.3. Size and morphology analysis

2.3.3.1. Transmission electron microscopy (TEM)

Transmission electron microscopy (TEM) is operated based on the same principal as optical light microscopes, but uses a beam of electrons as a light source. The discovery that small material particles such as electrons have a wavelike character designated Debroglie wavelength, led to the development of an electron-based microscopy with high resolution and important applications in the fields of material science, physics, chemistry, biology and nanotechnology. It was found that accelerating the beam of electrons at high potential of 50 kV up to 200 kV, led to the penetration of these high-energy electrons through solid specimens or suspensions on a grid. This interaction or more specifically, diffraction of electrons through the specimen generates a specific pattern, resulting in a contrast image, which is then focused and magnified onto an imaging device. With a modern TEM it is possible to obtain an image resolution of approximately 0.2 nm [396].

TEM imaging was performed with a JEOL, JEM 2010 microscope running a LaB6 (lanthanum hexaboride crystal) emitter at an accelerating voltage of 200 kV. TEM samples were prepared by drop-casting a dilute suspension of the $Cu(TPZ)_2$ sample (2 mM and 20 μM), dispersed in EtOH, onto a 200-mesh carbon-coated copper grid (Agar Scientific). The samples were left to dry for 30 s at room temperature, before the measurement. TEM micrographs were taken at different spots of grids, to ensure the imaging of a large number of particles. Images were kindly taken by Dr. Ashkan Dehsorkhi (School of Pharmacy, University of East Anglia).

2.3.4. High performance liquid chromatography (HPLC) quantification method

High performance liquid chromatography (HPLC) is a popular analytical technique used to separate, identify, purify and quantify different samples. It relies on a pressurized liquid solvent, which is flushed with the sample through a column that contains a solid adsorbent matrix. The components of the sample are then separated, based on their interaction with the column matrix and passed on to a detector (commonly UV/Vis). A signal is then generated, proportional to the amount of sample and further used for quantitative analysis. Additionally, HPLC columns possess smaller sorbent particles (2–50 μm in average particle size), giving this method a superior resolving power compared to other chromatographic techniques.

More specifically, reversed phase (RP)-HPLC has a non-polar adsorbent matrix (typically silica columns constituted of straight chain alkyl groups $C_{18}H_{37}$ or C_8H_{17}), formerly designated stationary phase and a moderately polar solvent is used as a mobile phase (water, acetonitrile and/or methanol). It operates on the principle that analytes with large hydrophobic areas will interact more strongly with the stationary phase and are eluted later. On the other hand, analytes that are more hydrophilic are easily eluted by the mobile phase. The time taken for a compound to pass through the column to the detector is known as the retention time. Factors such as the pressure of the system, the column (material used, length, pore size), composition of the solvent in the mobile phase, and the temperature of the column can then be fine-tuned in order to modulate and obtain an optimum retention time, better separation and quantification [397].

RP-HPLC chromatography was carried out using a modified protocol previously described for TPZ [398]. HPLC analysis was performed using a Phenomenex® Luna Phenyl-Hexyl column (100 mm x 4.60 mm, 5 μm beads), as it provides unique selectivity for aromatic and moderately polar analytes, such as TPZ. The analysis was performed using an Agilent 1200 series HPLC system, with a G1367B automated sample injector (20 μL sample). The mobile phase consisted of 22% methanol in water and was delivered isocratically at a flow-rate of 1.0 ml/min. Absorbance of the column effluent was monitored using a Diode Array Detectors (DAD G4212A/B) set at 270 nm.

Furthermore, this method was successfully adapted to indirectly quantify $Cu(TPZ)_2$ based on the premises of its 2:1 molar complexation to TPZ and dissociation at acidic pH. Serial dilution samples of $Cu(TPZ)_2$ were prepared in methanol:isopropanol (86:4, %v/v) adjusted to pH 2. HPLC analysis was performed as described above and standard curves were generated for both TPZ ($Y = 30.4x - 42.06$, $R^2=0.9957$) and $Cu(TPZ)_2$ ($Y = 58.33x + 55.15$, $R^2=0.9996$), validating the 2:1 molar complexation and the feasibility of this method for drug quantification. The protocol established here was chosen as the standard quantification method for all remaining studies in this thesis.

2.3.5. Energy minimization and Log P simulation

The structure of $Cu(TPZ)_2$ was initially drawn by ChemDraw (CambridgeSoft, Cambridge, MA) and "cleaned up" by the software. The 2D structure was then converted into a 3D structure by Chem3D (ChemOffice, CambridgeSoft, Cambridge, MA), followed by molecular mechanics' minimization (MM2) force field (minimum RMS gradient of 0.1). MM2 parameters used here are from the full MM2 Parameter Set including p-systems, as provided by N. L. Allinger and implemented in Chem3D. This system has an extended set of parameters and the ability to include centres with more than four bonds, such as metals. ChemOffice was also used to predict the Log P. The Log P value of a compound is estimated from the sum of the contribution of each fragment type, and the program accounts for steric, electronic and hydrogen bonding interactions, based on Hansch and Leo [399].

2.4. Liposome preparation and characterisation

In this work, three lipid compositions with different carbon chain length and saturation were chosen as candidate formulations. The composition of the lipid formulation influences the fluidity of the liposomes itself, which in turn modulates drug encapsulation, release and therapeutic activity. The lipid components chosen were: 1, 2 - dioleoyl-*sn*-glycero-3-phosphocholine (DOPC, 18:1 - Δ9 Cis, T_m=-20°C); 1, 2 - Dipalmitoyl-*sn*-glycero-3-phosphocholine (DPPC, 16:0, T_m=41°C) and 1, 2 - Distearoyl-*sn*-glycero-3-phosphocholine (DSPC, 18:0, T_m=55°C). All formulations were prepared with 50 mol% (total phospholipid, *ca.* 33% molar ratio total lipid) of cholesterol, to modulate membrane permeability [256,257] and 10 mol% 1,2-distearoyl-*sn*-glycero-3-phosphoethanolamine-*N*-[amino(polyethylene glycol)-2000] (DSPE-PEG_{2000}) to provide stability and enhanced circulation time, taking into consideration future biological applications.

2.4.1. Preparation of empty and TPZ-loaded liposomes

In this section a wide range of methods were used to study and achieve an acceptable encapsulation of TPZ in liposomes. Passive and active loading methods were compared, given the different success rates obtained by these methods. A summarised scheme of all methods exploited in this work to encapsulate TPZ are illustrated in **figure 2.3**.

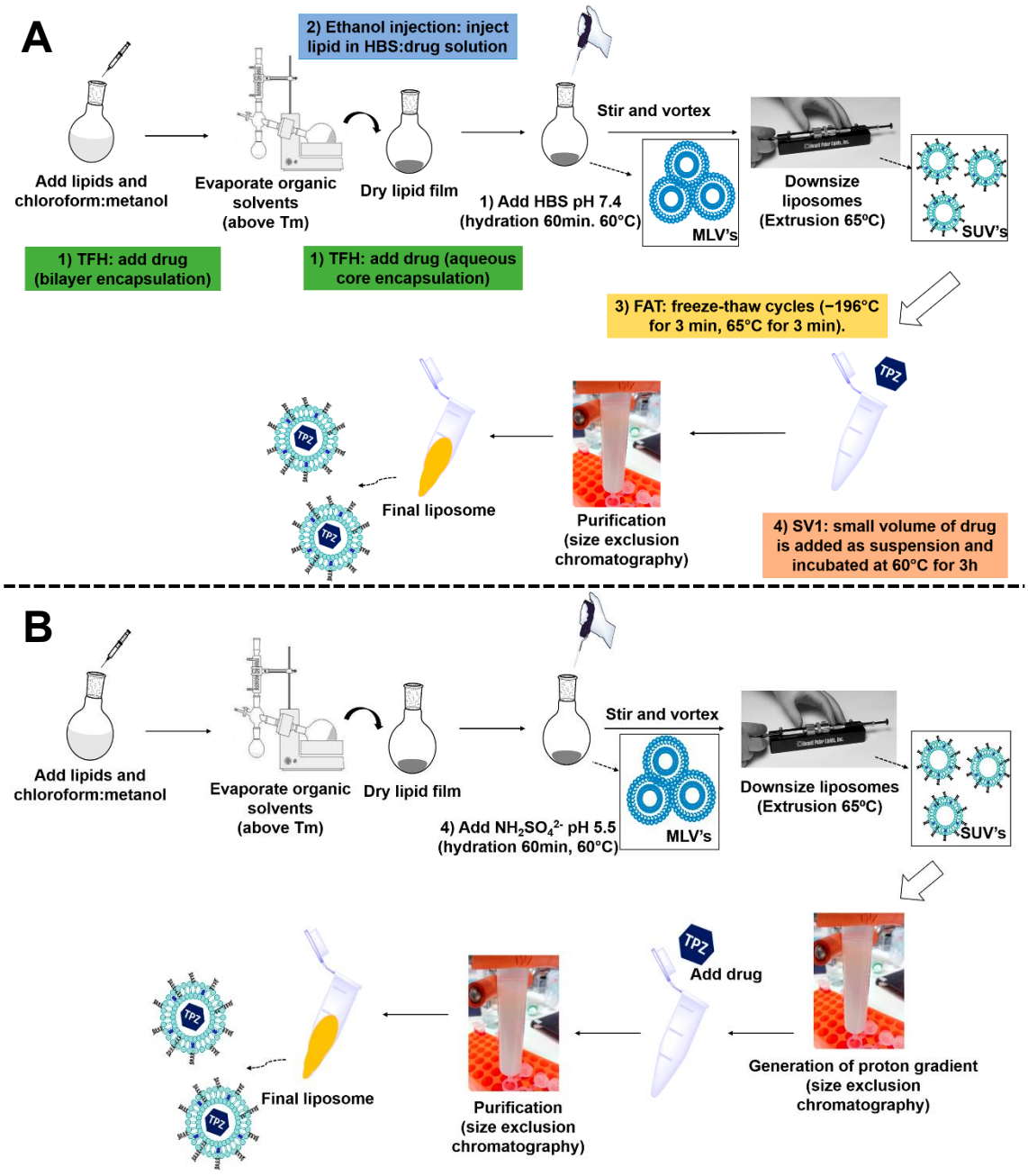

Figure 2.3. Summarised scheme of all loading methods tentatively used for TPZ encapsulation. A) Passive loading techniques including: 1) thin-film hydration (THF), 2) ethanol injection, 3) freeze-thaw cycling (FAT) and 4) small volume incubation (SVI) method. B) Remote or active loading method using ammonium sulphate proton gradient.

2.4.1.1. Passive loading

2.4.1.1.1. Thin-lipid film hydration (TFH) methods

TFH was chosen as the starting point of this work, as it is the simplest and quickest method used for liposome preparation. This technique relies on the preparation of a thin lipid film, which is subsequently hydrated with an aqueous buffer, where the lipids self-assemble into multillamelar vesicles (MLV's). The drug is then included either in the lipid film (lipophilic drugs) or during the hydration step (hydrophilic drugs). This method relies on passive diffusion of the drug either into the bilayer or the aqueous core and can have relatively poor EE.

Additionally, extrusion was the method chosen to down-size the prepared vesicles, in order to generate vesicles of desired uniform size (polydispersity – PDI, below 0.2) [400]. DOPC:Chol:DSPE-PEG_{2000} was prepared by dissolving the lipids in chloroform/methanol (4:1 v/v) in a 25 mL round bottom flask (Fisher Scientific, UK). The organic solvents were removed under vacuum for about 40 min at 45°C, while rotating at high speed (BÜCHI Labortechnik AG, Switzerland). The lipid film was then flushed with a gentle stream of N_2 to remove residual traces of organic solvent and hydrated with HBS (20 mM HEPES, 150 mM NaCl, pH 7.4), to maintain a final lipid concentration of 5 mM. The lipid solution was placed in a water bath for 40 min at 60°C, with subsequent vortex every 10 min, to ensure complete hydration of the lipid. In order to prepare small unilamellar vesicles (SUVs), liposomes were extruded through 800 nm, 200 nm and 100 nm, polycarbonate filters in 5, 15 and 11 time passes, respectively, using a mini-extruder at 60°C (Avanti Polar lipids, AL USA). Liposomes were left to stabilize and anneal overnight at 4°C.

For DPPC:Chol:DSPE-PEG_{2000} and DSPC:Chol:DSPE-PEG_{2000} liposomes, the previous method was adapted. The lipid solution was transferred to a 25 mL and 250 mL round bottom flask, respectively and evaporated under vacuum for about 40 min at 60°C, while rotating at low speed. The lipid film was then flushed with N_2 stream to remove residual traces of organic solvent and hydrated with HBS at 60°C to also achieve a final lipid concentration of 5 mM. Subsequent steps were as described in the previous protocol.

For TPZ loaded liposomes, encapsulation in the bilayer and aqueous core of liposomes was assessed. DOPC:Chol:DSPE-PEG_{2000} (5 mM phospholipid, 95:50:5 molar ratio) loaded liposomes were prepared by adding TPZ (10:1 and 20:1, lipid-to-drug molar ratio). For encapsulation in the bilayer the initial lipid solution was mixed with the appropriate concentration of TPZ, while for encapsulation in the aqueous core, the drug was only added during the hydration step, following the protocol described above. Liposomes were then purified as further described in **section 2.4.1.3**.

2.4.1.1.2. Ethanol injection

The ethanol injection technique has been shown to improve on the low EE obtained by the TFH method. With ethanol injection, the lipid components are dispersed in an ethanolic solution, which is rapidly injected, using a thin needle, into an excess solution containing the candidate drug. This causes the ethanol to rapidly dilute in the aqueous component, whilst the lipid molecules are dispersed evenly, with the drug molecules [254,264].

DOPC:Chol:DSPE-PEG_{2000} (5 mM phospholipid, 95:50:5 molar ratio) liposomes were prepared by the ethanol injection technique, in order to test the effect on liposome characteristics and drug encapsulation further on in this study [264]. Lipids were dissolved in chloroform/methanol (4:1 v/v), mixed in a 25 mL round bottom flask and organic solvents were evaporated under vacuum for about 40 min at 45°C, while rotating at high speed. The lipid film was flushed with N_2 stream and dissolved in 300 µL of ethanol. With a glass syringe, the lipid solution is quickly withdrawn and injected in 2 mL of HBS (20 mM HEPES, 150 mM NaCl, pH 7.4) in a different 25 mL round bottom flask. The ethanol was then evaporated under vacuum for about 20 min at 45°C, while rotating at high speed to allow vesicle formation. SUVs were prepared as mentioned above.

To prepare TPZ loaded liposomes, TPZ (10:1, lipid-to-drug molar ratio) was added to the HBS buffer prior to ethanol injection. Liposomes were then purified as further described in **section 2.4.1.3**.

2.4.1.1.3. Freeze-thaw cycling (FAT)

Repeated cycles of freeze-thaw have shown to significantly increase drug encapsulation in different liposomal formulations. This method produces physical disruption of the lipid bilayer, caused by formation of ice crystals during the freezing process. This causes the transient spacing of the closely compact lamellae of the lipid membrane, which in turn enhances drug penetration and increase in the aqueous to lipid ration. This phenomena results in increased liposome volume and enhanced EE [266].

DOPC:Chol:DSPE-PEG_{2000} (5mM phospholipid, 95:50:5 molar ratio) liposomes were prepared by freeze-thaw cycling [266]. Liposomes were firstly prepared by the TFH method. The solution was then transferred to a closed cap cryovial tube (Fisher Scientific, UK) and subjected to ten freeze-thaw cycles (−196°C for 3 min, 65°C for 3 min). The sample was equilibrated at 60°C for 10-20 min and stored at 4°C. Liposome extrusion was carried on as described throughout this section.

Loaded liposomes were prepared by adding TPZ during the hydration step, at a concentrated 2:1, lipid-to-drug molar ratio, to fully maximize TPZ content and explore the strength of this method. Liposomes were then purified as further described in **section 2.4.1.3.**

2.4.1.1.4. Small volume incubation (SVI) method and supersaturated TPZ

A novel method has been described to encapsulate small amphiphilic molecules with success. This SVI strategy allows a higher concentration of drug to be available in a small external volume, in order to achieve higher encapsulation. The minimized external volume allows the drug to passively load in the liposomal core, based on simple osmosis. Given this, buffer concentration must be cautiously determined in order not to create liposomal burst, due to high osmotic pressure created by the inflow of drug molecules [269]. Also, drugs in suspension have also shown to be an alternative strategy to further improve on drug loading, using this method, as the dissolution is fast enough to enhance drug loading.

In this work, a modified SVI method was used to tentatively encapsulate TPZ in DPPC:Chol:DSPE-PEG_{2000} (10 mg total lipid, 6:3:1 molar ratio) and DSPC:Chol:DSPE-PEG_{2000} liposomes (10 mg total lipid, 6:3:1 molar ratio). The lipid mixtures was dissolved in chloroform/methanol (4:1, v/v) and the lipid film was formed using the TFH-extrusion method, using either PBS (10 mM, pH 7) or Mili-Q water as hydrating buffer, depending on drug concentration used for loading[1]. Given that the solubility of TPZ in water is about 5.6 mM, a supersaturated suspension of TPZ was prepared, to minimize the drug volume added to the liposomal solution. A maximum solubility of about 22.4 mM TPZ in 0.9% NaCl, was obtained after slowly dispersing the drug and heating the solution to 70°C (**Figure 2.4**).

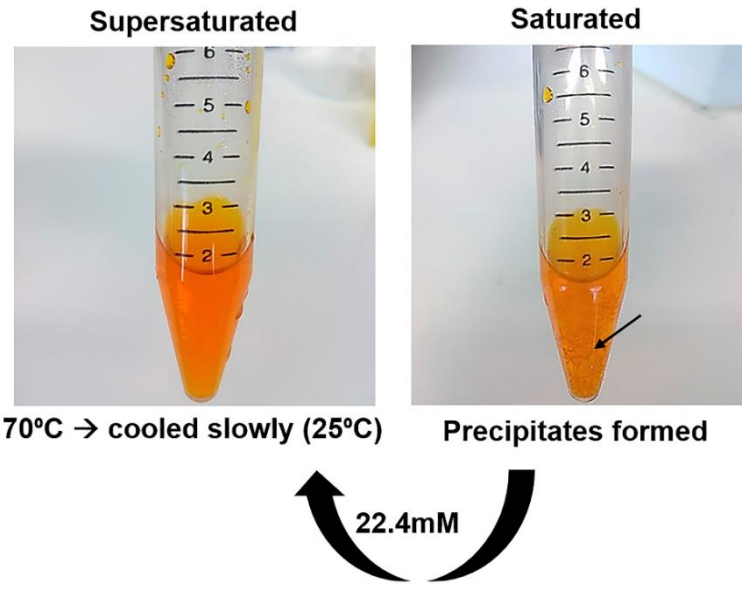

Figure 2.4. Supersaturated solution of TPZ. The drug (22.4mM) was added to 2mL of 0.9% NaCl at room temperature. The drug quickly precipitated, due to low solubility creating a saturated suspension. When heated at 70°C and cooled slowly, a supersaturated solution of TPZ was obtained, allowing a 4-fold increase in aqueous solubility.

[1] Optional remote loading with ammonium sulphate or freeze-thaw cycling was also used for comparison.

After total dissolution was obtained, the sample was allowed to cool slowly (no precipitation should be visible) and subsequently used for liposome loading. Liposomes were then concentrated to the desired column (0.5 mL) using a Vivaspin ultrafiltration spin column (GE Healthcare, Fisher Scientific, UK) with a cut-off of 100 kDa, after repeated centrifugation cycles (1000 x *g*, 4°C for 40 min). TPZ (0.48 mM and 2.4 mM) was then added to the liposomal solution, vortexed and incubated at 60°C for 3h. Finally, the final liposome solution was reconstituted to the initial lipid concentration and further purified, as discussed in **section 2.4.1.3**.

2.4.1.2. Remote loading

In addition to the various passive loading methods described above, the remote (or active) loading of drugs into liposomes, is one of the most successful methods to achieve high EE of weak base molecules [270,401]. The main principle of this loading method is creating a strong intra-liposomal proton gradient using hydrating buffers such as ammonium sulphate [$(NH_4)_2SO_4$]. The diffusion of ammonia generates an acidic internal pH, which is balanced by an external neutral pH environment. These conditions allow the unionized drug molecule to quickly diffuse through the lipid bilayer and once inside the liposomal core, retains the ionized form. When the drug concentration inside the liposomal space is maximum, the drug forms precipitates and is entrapped within the liposomes, yielding high drug loading. According to the literature, this method is most suitable for loading weak bases with pKa $\leq$ 11 and Log P value ranging from -2.5 to 2.0 [269]. These requirements seem to make TPZ (pKa 5.2, log P = -0.31) a good candidate for remote loading.

In order to determine the effect of a pH gradient on the encapsulation of TPZ, liposomes were prepared by a remote loading pH gradient method [401]. DOPC:Chol:DSPE-PEG_{2000} and DSPC:Chol:DSPE-PEG_{2000} (5 mM phospholipid, 95:50:5 molar ratio) were prepared by the TFH-extrusion method, using 250 mM $(NH_4)_2SO_4$ (pH adjusted to 5.5) as the hydrating buffer. Transmembrane pH gradients were then prepared, by passing liposomes through a Sephadex™ G-25 (PD-10) desalting column (Fisher Scientific, UK), pre-equilibrated with an external buffer of HBS (20 mM HEPES, 150 mM NaCl, pH 7.4). Three fractions were collected, taking into account sample turbidity, and liposome concentration was adjusted if any dilution was performed. These liposomes were further loaded with TPZ at a lipid-to-drug ratio of 10:1 and 20:1 (mol:mol) and incubated for 1h at 60°C. Liposomes were further purified as described below.

2.4.1.3. Purification and encapsulation efficiency (EE) of TPZ-loaded liposomes

In order to separate the loaded and free drug, size exclusion chromatography (SEC) was used. A Sephadex™ G-25 PD-10 desalting column (GE Healthcare Lifesciences, UK) was washed, equilibrated with HBS buffer (20 mM HEPES, 150 mM NaCl, pH=7.4) and 2 mL of the liposome solution was added to the column. The sample was then eluted with 1 mL of buffer (flow rate of 1.0 mL/min) and a total of 17 fractions (fraction size 1.0 mL) were collected in 1.5 mL amber microcentrifuge tubes (Starlab, UK). Lipid-containing fractions were identified macroscopically by higher turbidity of the sample and then pooled again, when necessary, to obtain the original lipid concentration. Free drug fractions were monitored due to the yellow colour of the compound TPZ. The total drug was determined after lysing the liposomes with 0.1% v/v Triton-X 100 solution (final concentration). Empty liposome fractions and 0.1% Triton-X 100 were used for baseline correction.

The free and total drug were then quantified by fluorescence spectral analysis, to obtain the purification and elution profile. Fluorescence was measure using a CLARIOstar Omega microplate reader (BMG labTechnologies), with emission/excitation of 490/570 nm (bandwidth 10 nm) and gain adjustment for the maximum fluorescent sample at 25°C. The fluorescence from each well was captured, digitized, and stored on a computer using MARS data analysis software (Version 3.02).

Furthermore, after liposome purification, drug quantification was carried out using an HPLC protocol described in **section 2.3.4**, for TPZ. Briefly, liposome samples before and after drug loading were diluted (1:10) in methanol and analysed using an Agilent 1200 series HPLC system. A previously generated standard curve for TPZ was used for drug quantification and the EE was determined as follows:

$$\mathbf{EE\ (\%)} = \frac{\textbf{Concentration of encapsulated TPZ}}{\textbf{Concentration of TPZ before purification}} \times \mathbf{100} \qquad \textbf{Equation 2.2}$$

2.4.2. Preparation of $Cu(TPZ)_2$-loaded liposomes

Previous studies have shown that ionophores or ion-mediated loading can be an alternative method to enhance the EE of drugs [270,402,403]. All methods exploited above for the encapsulation of TPZ provided extremely low or null drug loading (a fact further discussed in **chapter 4**). Therefore, an alternative method to successfully encapsulate TPZ was developed and exploited. This method relied on the pre-complexation of TPZ to Cu(II) in a 2:1 molar ratio and the protocol is described in the following sections.

2.4.2.1. Remote loading at pH 7.4

$Cu(TPZ)_2$ was encapsulated into liposomes using a remote loading procedure. DOPC:Chol:DSPE-PEG_{2000}, DPPC:Chol:DSPE-PEG_{2000} and DSPC:Chol:DSPE-PEG_{2000} (5mM phospholipid, 95:50:5 molar ratio) liposomes were prepared by TFH method and further extruded, as described above. The liposomes were then flushed with N_2 stream and allowed to anneal overnight at 4°C.

Preliminary studies showed high EE using this method, so further temperature and time-course studies were conducted to establish the optimum conditions for drug loading. Initially, a fixed 140:1 lipid-to-complex ratio was used to establish the optimum incubation time and temperature. $Cu(TPZ)_2$ (140:1 lipid-to-complex ratio) was then added to the liposomal solution and time-course studies up to 6h were undertaken and an incubation time of 30 min was considered optimal for drug loading. In addition, temperature studies were conducted at 20, 37 and 55°C for the pre-established optimum incubation time of 30 min. These studies led to the conclusion that an incubation of $Cu(TPZ)_2$ at 55°C for 30 min yielded good EE for all lipid formulations tested. The novel remote loading technique described in this work was summarised in **figure 2.5.** Finally, $Cu(TPZ)_2$ was added to liposomes at different lipid-to-complex ratios (mol:mol) at the optimized conditions, in order to establish the influence of different drug concentrations on EE.

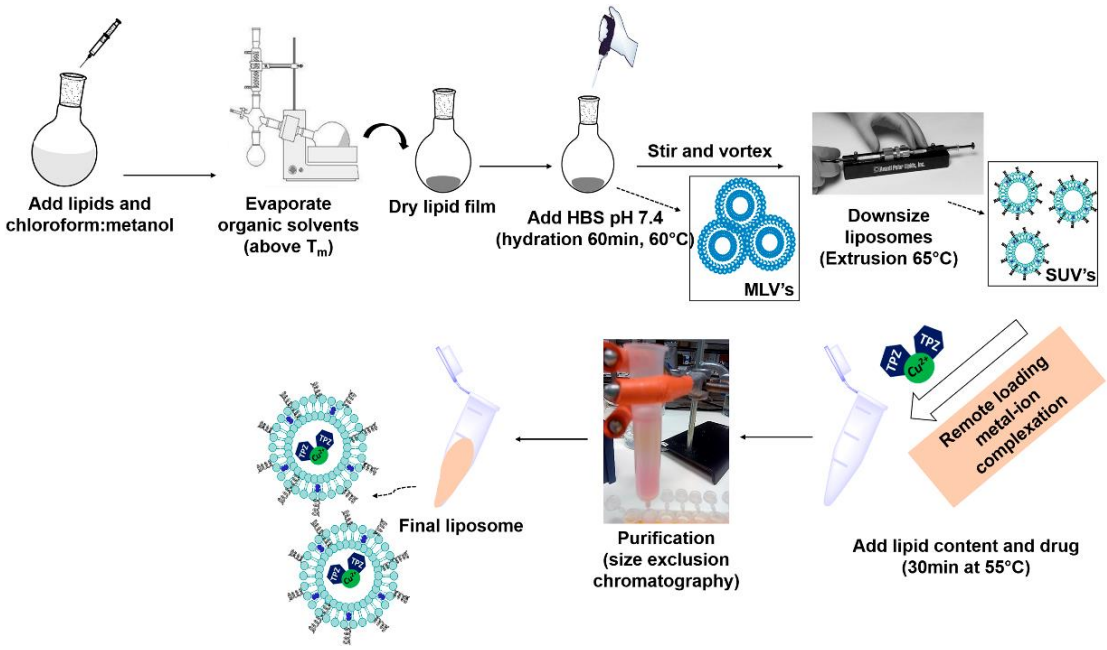

Figure 2.5. Optimized ion-mediated remote loading method for $Cu(TPZ)_2$-loaded liposomes.

2.4.2.2. Remote loading at pH 5.5

In order to determine the effect of a pH gradient on the encapsulation of $Cu(TPZ)_2$, liposomes were prepared by a remote loading pH gradient method [401]. DOPC:Chol:DSPE-PEG_{2000}, DPPC:Chol:DSPE-PEG_{2000} and DSPC:Chol:DSPE-PEG_{2000} (5 mM phospholipid, 95:50:5 molar ratio) were mixed and dissolved in chloroform/methanol (4:1 v/v) and the organic solvents were then removed under vacuum, as described previously. The lipid film was then hydrated with either 250 mM $(NH_4)_2SO_4$ (pH adjusted to 5.5) or 300 mM Na-citrate (pH adjusted to 5.5), to maintain a final lipid concentration of 5 mM and generate a proton gradient in the liposomal space. The lipid solution was placed in a water bath for 40 min at 55°C, with subsequent vortex every 10 min, to ensure complete hydration of the lipid film. The resulting preparation was extruded as detailed above. Transmembrane pH gradients were prepared, by passing liposomes down a Sephadex™ G-25 (PD-10) desalting column (Fisher Scientific, UK), pre-equilibrated with an external buffer of HBS (20 mM HEPES, 150 mM NaCl, pH 7.4). Three fractions were collected, taking into account sample turbidity, and liposome concentration was adjusted if any dilution was performed. These liposomes exhibited a proton gradient and were further loaded with $Cu(TPZ)_2$ at a lipid-to-complex ratio of 140:1 (mol:mol) and incubated at 55°C for time course studies up to 6 h.

2.4.2.3. Purification and encapsulation of $Cu(TPZ)_2$-loaded liposomes

Non-encapsulated $Cu(TPZ)_2$ was removed by SEC, using a Sephadex™ G-25 (PD-10) desalting column. 1.5mL of loaded liposomal solution was added to the desalting column and eluted with 1 mL HBS buffer. As determined before, fractions 2, 3 and 4 were collected, containing $Cu(TPZ)_2$-loaded liposomes. Due to the high lipophilic nature of the complex, any non-encapsulated $Cu(TPZ)_2$ was retained in the column, providing efficient purification of the liposomal fractions.

Liposome samples before and after purification were diluted (1:10) in methanol/isopropanol (80:10, %v/v) adjusted to pH 2. The quantification of $Cu(TPZ)_2$ was carried out by reverse phase chromatography using a modified protocol previously described in **section 2.3.4**, as described for the complex. $Cu(TPZ)_2$ concentrations, before and after purification, were corrected for any dilutions used and calculated using a pre-determined standard curve ($Y = 58.33x + 55.15$, $R^2=0.9996$). The EE was determined using **equation 2.2** and drug loading (**DL**) was calculated as follows:

$$\mathbf{L\ (\%) = \frac{Concentration\ (\mu M)\ of\ encapsulated\ Cu(TPZ)_2}{Total\ concentration\ of\ lipid\ (\mu M)} \times 100} \qquad \textbf{Equation 2.3}$$

For DL, lipid concentration was corrected according to the results obtained by Stewart assay (*ca.* 4.5 mM lipid).

2.4.2.4. Physicochemical characterisation

2.4.2.4.1. Dynamic light scattering (hydrodynamic size)

In order to determine the median hydrodynamic size of particles in solution, dynamic light scattering (DLS) also known as photon correlation spectroscopy (PCS) is widely used. This method is quite sensitive and allows the detection of particles sized from a few nanometers up to 3 µm [404]. This technique is based on the incidence of a helium-neon based laser (λ = 633 nm) on the sample with a predefined dispersion angle of 173º. The light is then scattered in all directions (Rayleigh scattering) and the intensity of the light scattered from a particle is proportional to the square of the particle mass (**Figure 2.6**) [405].

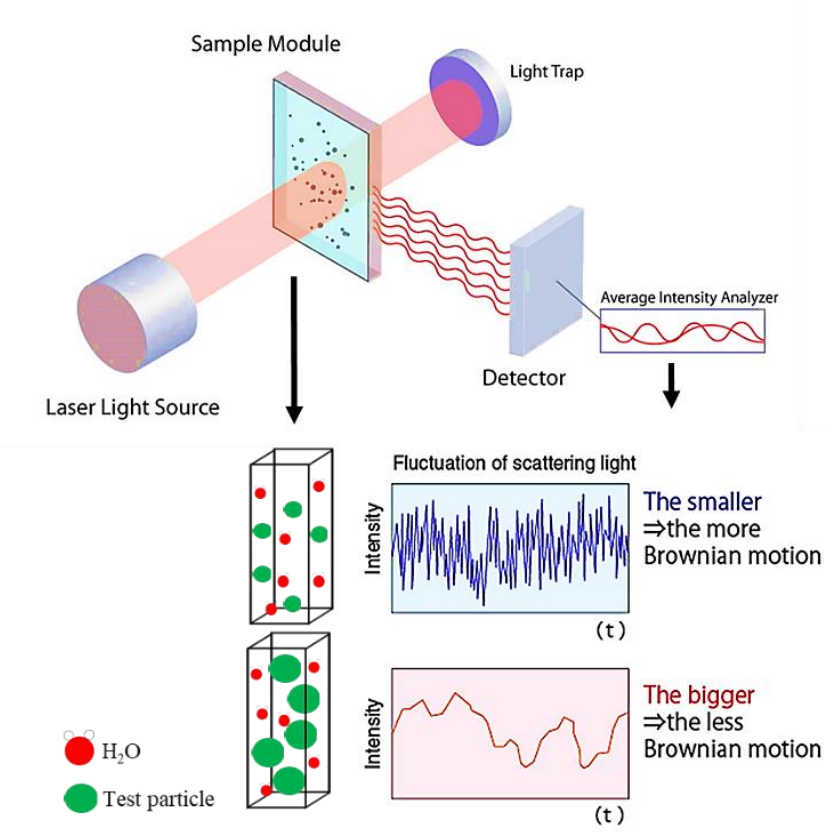

Figure 2.6. Schematic representation of the principle of Dynamic Light Scattering. After the incidence of light, different particle will scatter light in all directions, due to their Brownian motion. Analysis of the intensity fluctuations yields the particle hydrodynamic size.

Additionally, the scattering intensity is constantly changing over time, due to the Brownian or "zig-zag" motion of particles. Analysis of the intensity fluctuations yields the particle velocity and, thus, the particle size form the Stokes-Einstein relationship:

$$Dh = \frac{KbT}{6\pi\eta r}$$ **Equation 2.4**

Where $\mathbf{D_h}$ is the hydrodynamic diameter, $\mathbf{K_b}$ is Boltzmann's constant, **T** is absolute temperature, $\boldsymbol{\eta}$ is viscosity and **r** is the radius of the particle. DLS was used to measure the hydrodynamic mean diameter and the polydispersity index (PDI) of liposomal formulations (before and after $Cu(TPZ)_2$ loading). The scattered light intensity of the solution at 173° was determined using a Malvern Zetasizer Nano ZS (Malvern, UK, He-Ne laser). Samples were placed in plastic disposable cuvettes (Fisher Scientific, UK) and equilibrated at 25°C, after appropriate 1:100 dilutions in 0.2 μm filtered dH_2O. The PDI was used as a measurement of the distribution of size within a given population, where 0 represents a perfectly uniform/homogenous population of vesicles with similar size range; while 1 designates a highly polydisperse population with vesicles of multiple sizes [406]. For liposomes, a PDI below 0.3 is generally accepted [406]. The average of three measurements was used and results expressed as mean diameter (nm) ± SD.

2.4.2.4.2. Zeta-potential measurement (ζ-potential)

The surface charge of particles in solutions is an important property to regulate the stability of colloidal suspensions. A quantitative parameter used to assess the repulsive electrostatic interactions between the surface of a charged particle and its dispersing media is Zeta potential (ζ-potential) [405,407]. Particles with a ζ-potential of ± 15 mV are considered to be at the threshold for agglomeration, while large positive or negative values, higher than ± 30 mV, represent colloidal systems that are thoroughly stable.

In this work, ζ-potential was measured as particle electrophoretic mobility by means of laser microelectrophoresis in a thermostatic cell. Samples were prepared after appropriate dilution (1:10) in 0.2 μm filtered dH_2O. The average of three measurements was used and results expressed as mean ± SD.

2.4.2.4.3. Phospholipid quantification by Stewart assay

A simple colourimetric assay to determine phospholipid content and further assess lipid loss during liposomal preparations is the Stewart assay [408]. The protocol is based on the formation of a coloured complex between ammonium ferrothiocyanate and phospholipid. Briefly, ammonium ferrothiocyanate is a red inorganic compound that is insoluble in chloroform. However, when mixed with the pre-dissolved lipid samples in chloroform, it partitions into the chloroform phase, forming a deep red complex with the phospholipid content. After phase separation the red complex is recovered and quantified by UV/Vis spectroscopy at a maximum wavelength of 469 nm.

First, a solution of ammonium ferrothiocyanate [0.1 M, (27.03 g ferric chloride hexahydrate and 30.4 g ammonium thiocyanate /1L dH_2O)] was prepared and a standard curve of known concentrations of phospholipids or liposomes (0 – 100 μg/mL) was generated (**Table 2.2**).

Table 2.2. Lipid standard concentrations for determination of phospholipid concentration using the Stewart assay.

Sample lipid stock (µg/ml) / (µM)	Lipid (µl)	Chloroform (µl)	Ammonium ferrothiocyanate (µl)
0	0	2000	2000
5 (7.24)	5	1995	2000
10 (14.48)	10	1990	2000
25 (36.20)	25	1975	2000
50 (72.40)	50	1950	2000
75 (108.6)	75	1925	2000
100 (144.8)	100	1900	2000

2 mL of chloroform was transferred to 15 mL test tubes (Fisher Scientific, UK) and known amounts of lipid samples (stock: 2 mg/mL) were then added to this solvent. Finally, 2 mL of ammonium ferrothiocyanate was added and the components were vortexed vigorously. For phase separation, the mixture was centrifuged at 1000 x *g*, 10 min and the organic phase recovered by aspiration. The lipid absorption was then measured using a Lambda 35 spectrophotometer (Perkin Elmer, USA) at 469 nm. Subsequent analysis was done by preparing liposome samples with the previously described protocol and lipids before and after drug loading were quantified using the established standard curve. Triplicate samples were prepared for all measurements and reference blanks were used for baseline correction. The results were expressed as mean ± SD.

2.4.2.5. *In vitro* release kinetics

2.4.2.5.1. Release studies of free $Cu(TPZ)_2$

The *in vitro* release of $Cu(TPZ)_2$ was evaluated by dynamic dialysis method adapted from [409]. $Cu(TPZ)_2$ was diluted in HBS (20 mM HEPES, 150 mM NaCl, pH 7.4) to a final water soluble concentration of 10 µM $Cu(TPZ)_2$, equivalent to 20 µM TPZ content (3 mL). This solution was then placed into a pre-swelled Pur–A–Lyzer™ Maxi Dialysis tube (Fisher Scientific, UK) with 12 kDa molecular weight cut-off. The dialysis tube was incubated in 30 mL release media (HBS containing 1% Tween-80) at 37 ± 0.5 °C, with stirring at 100 rpm, at predetermined time intervals (up to 72h), triplicate 1 mL samples were taken and replaced with fresh media. The amount of $Cu(TPZ)_2$ in the samples was then determined by HPLC, as described before. Results were expressed as mean ± SD of cumulative release for triplicate samples of three independent experiments (n=3). Furthermore the same method was be used to determine the release profile in biological media (HBS:FBS, 1:1 v/v).

2.4.2.5.2. Release studies of $Cu(TPZ)_2$-loaded liposomes

Given the high lipophilicity and possible retention of the complex within the dialysis membrane, as well as difficulty in quantifying the overly diluted samples; an alternative indirect method to quantify the dynamic release of $Cu(TPZ)_2$ was adapted. The *in vitro* release of $Cu(TPZ)_2$ loaded liposomes was evaluated by incubating the liposomal fraction in either HBS or serum, at 37°C and purifying the withdrawn liposome samples. This allowed the separation of free/released drug from the remaining encapsulated liposomal fractions. Briefly, $Cu(TPZ)_2$ loaded liposomes at a 60:1 lipid-to-complex molar ratio (20 µM TPZ content = 10 µM $Cu(TPZ)_2$) were incubated in HBS or HBS:FBS (1:1, v/v) in a 15 mL centrifuge tube (Fisher Scientific, UK) at 37°C, with gentle stirring, up to 72h. At pre-determined time-points 0.5 mL samples were withdrawn and purified using a QeV size exclusion columns (iZon Science, UK), to ensure adequate separation of released drug, liposomal fractions and serum proteins. The column was eluted with 1 mL HBS and two liposomal fractions were collected and pooled. Liposome samples of the initial stock (0 min) and samples after purification were diluted (1:2) in methanol/isopropanol (80:10, %v/v) adjusted to pH 2. The quantification of encapsulated $Cu(TPZ)_2$ was carried out by RP-HPLC using a modified protocol previously described in **section 2.3.4**. $Cu(TPZ)_2$ concentrations, were corrected for any dilutions used and calculated using a pre-determined standard curve. The EE was determined for each time-point (**t**), and percentage of release was calculated as follows:

$$\mathbf{Release_t\ (\%) = 100 - EE_t\%} \qquad \textbf{Equation 2.5}$$

2.4.2.6. Size and morphology analysis by TEM

Transmission electron microscopy (TEM) was performed on empty and $Cu(TPZ)_2$ loaded liposomes at different lipid-to-complex molar ratios. TEM samples were prepared at 25˚C by drop-casting 1–2 µl of liposome sample onto a glow-discharged 200 mesh carbon-coated copper grid (Agar Scientific). Unstained and negative-stained samples with 2% uranyl-acetate (Sigma, UK) were used for comparison. Excess liquid was removed by blotting with filter paper, leaving a thin film of solution on the grid. TEM images were taken using a high resolution JEOL, JEM 2100 microscope running a LaB6 (lanthanum hexaboride crystal) emitter operated at 80 kV in the zero loss bright-field mode and analysis software JEOL TEMographyTM suite. An underfocus of 1–2 µm was used to enhance the image contrast. TEM micrographs were taken at different spots of grids with a total magnification of 100,000 up to 300,000 x. Images were kindly taken by Dr. Franklin Nóbrega (Delft University of Technology, Netherlands).

2.4.2.7. Stability of $Cu(TPZ)_2$ loaded liposomes

The physicochemical stability of the $Cu(TPZ)_2$-loaded liposomes prepared by a remote loading method was also investigated. Liposomes were stored in the form of suspension (in HBS buffer) at 4°C, away from light. Hydrodynamic size, PDI and EE of liposomes were monitored over 1 month. Samples were taken on a weekly basis.

2.5. Biological studies

In vitro cell culturing is one of the most common methods used for drug screening. The development of continuous or immortalized cell lines, capable of indefinitely expanding in culture, offered a rapid procedure for high-throughput analysis in many fields [410]. Culture conditions can vary widely for each cell type, but the basics rely on creating a general environment in a vessel in which essential nutrients (amino acids, carbohydrates, vitamins and minerals), growth factors, hormones, and gases (O_2, CO_2) are carefully provided as well as, the regulation of physicochemical properties such as pH, osmotic pressure and temperature.

In this particular study, the aim was to test a novel cupric-TPZ prodrug for PCa. This type of cancer is highly heterogeneous and its molecular and hormonal characteristic are quite complex. The main determinant in PCa is its behavioural dependence on androgen. Early stages of the disease are composed of cells, where growth is dependent on hormonal stimulation. As the disease progresses, cells become insensitive to androgen, they will respond to hormonal stimulation, but do not require it for growth. Finally, PCa cells can become androgen independent and therefore acquire high resistance to therapy and become metastatic. Many cell lines have been established depending on the disease stage, hormonal dependence and metastatic site of prostate cancer [411-413]. Four PCa cell lines were chosen to establish a thorough screening of early and late stage disease for this cancer model and the cell characteristics are summarised in **table 2.3**.

Table 2.3. Prostate cancer cell lines used in this work and their main molecular, hormonal and metastatic characteristics [412,413].

Cell line	Origin	Doubling time	PSA/PSMA	Androgen sensitivity	Tumorigenicity[a]	Bone Metastatic behaviour
LNCap	lymph node metastasis	60 h	+/+	Sensitive	Very low	N.A.
C4-2B	Osseus tumours	48 h	+/+	Insensitive	High	osteoblastic
DU145	Brain metastasis	34 h	-/-	Insensitive	Moderate	osteolytic
PC3	Bone metastasis of grade IV of prostate cancer	33 h	-/-	Insensitive	High	osteolytic

[a]**Tumorigenicity:** the ability of cultured cells to form malignant tumours in immunologically suppressed animals, overtime.

2.5.1. General cell culture conditions (normoxia)

The prostate cancer cell lines LNCap, PC3 and DU145 were obtained from American Type Culture Collection (ATCC). C4-2B cells were purchased from Dr. Leland Chung (MD Anderson Cancer Centre, Texas USA). All cell lines were maintained in Advanced RPMI-1640 (1x) medium supplemented with 10% heat inactivated FBS, 1% penicillin/streptomycin (10,000 units/mL) and 1% GlutaMax (200 mM). All cell lines were cultured as adherent monolayers. Briefly, PC3 and DU145 in tissue culture treated 75cm^3 canted-neck tissue culture flasks (Triplered, UK), while LNCap and C4-2B cells were maintained in Corning® CellBIND® 75cm^3 canted-neck tissue culture flasks (Fisher Scientific, UK) to enhance adherence. For general or normoxia (21% O_2) culture conditions, cells were maintained in a humidified chamber (BB15 CO_2 incubator, Thermo Fisher Scientific UK) at 37°C and 5% CO_2.

For sub-culturing, cells were gently passaged using 0.05% trypsin/EDTA at 70-80% cell confluency and media was replenished every two to three days, depending on growth. Cells were maintained up to 30 passage numbers, to avoid genetic drift and senescence.

2.5.1.1. Cell stock and storage

All cell lines were stored as a seed stock in sterile cryovials (Fisher Scientific, UK) in liquid nitrogen. Cell freezing and storage was achieved as described by ATCC. Approximately 1 x 10^6 cells/ml were suspended in FBS containing 5% DMSO, which is used as a cryoprotective agent. These agents reduce the freezing point of the medium and also allow a slower cooling rate, avoiding the formation of ice crystals in cell membranes, which can damage cells and cause cell death. Subsequent preservation and freezing of cells was done using in a Mr Frosty freezing container (Fisher Scientific, UK) containing 100% isopropanol and transferred to a -80 °C freezer to ensure cell freezing at an optimum rate. Next, the cryovials were transferred to the liquid nitrogen container for long-term storage.

Cell thawing was rapidly achieved by gently immersing the cryovials in a 37°C water bath. Once the cell suspension had thawed, 1 ml of appropriate growth media was added to dilute the DMSO and the cells were transferred into a cell culture flask. After the cells had adhered to the culture flask, the DMSO containing media was removed, the cells gently washed with 1x PBS, and fresh media was added.

2.5.2. Cell culture conditions (hypoxia)

To validate drug efficacy, *in vitro* hypoxic cell conditions were optimized and applied to the cell culturing conditions. All hypoxic protocols mentioned throughout this work were based on the culture conditions described here, adapted from [414]. Hypoxia was induced using a modular hypoxic incubator (Incubator chamber Billups Rothenberg Inc., MIC-101) which was sterilized using 70% EtOH followed by 15 min of UV light exposure. The two white plastic clamps located on the tubes attached to the chamber are used for the injection/ purging the hypoxic gas and a tray of sterile water is always placed inside the chamber to provide adequate humidification to the cultures (**Figure 2.7**). Furthermore, prior to hypoxia treatment studies the O_2 contained in the culture media was eliminated by degassing with a gas mixture of 1% O_2, 5% CO_2, and 94% N_2 (BOC, UK), using a sterile needle for about 1-2 h. Although different gas mixtures were tested prior to this, 1% O_2 was chosen for all main protocols in this work, because it adequately mimics the tumour biological environment [414].

For hypoxia treatment, cells were placed in culture plates inside the hypoxic incubator that was appropriately sealed. The chamber was then flushed by opening the gas tank (1% O_2, 5% CO_2, and 94% N_2) at a flow rate of 20 L/min for about 15 min (a flow meter incorporated in the regulator can be used to optimize this). The gas flow was then terminated by completely sealing the chamber by closing both white clamps. To ensure minimal oxygen fluctuations, the chamber was re-flushed twice a day and at every end-point of the experiment.

Figure 2.7. A modular hypoxic incubator and main set-up.

2.5.3. 2D *in vitro* models

2.5.3.1. Validation of hypoxia in cellular models

Nitromidazole containing molecules have emerged as the most prevalent type of probe for hypoxia imaging [415]. The CYTO-ID® Hypoxia/Oxidative Stress Detection kit (Enzo Life Sciences. UK) contains a weakly fluorescent aromatic compound containing a nitro (NO_2) moiety, which can be reduced by nitroreductases inside the cell. Under normoxia, the NO_2 anion radical is oxidized back to the original NO_2 group and the compound remains weakly fluorescent. On the other hand, in hypoxic conditions, the radical anion is stabilized and further reduced to NHOH and subsequently NH_2 degrading the original compound, thus releasing the active fluorescent probe.

Hypoxia was validated using C4-2B and LNCap, with the CYTO-ID® Hypoxia/Oxidative Stress Detection kit (Enzo Life Sciences. UK) according to the manufacturer manual [416]. Cells were harvested by trypsinization and seeded at 5×10^4 and 8×10^4 viable cells/well, respectively, onto pre-coated poly-D-lysine (100 µg/mL) sterile X100 Microscope Round Coverslips (Fisher Scientific, UK) in 24-well assay plates (Triplered, UK). The cells were allowed to adhere overnight under either normoxia or hypoxia, as mentioned in the previous section. The supernatant was then removed and replaced with the hypoxia detection mix. Cells were incubated with the hypoxia red probe (250 nM), while desferrioxamine (DFO, 200 µM) was used as a positive control and unstained cells were used as a negative control. Incubation was performed in normal conditions for 4h at 37°C. After 4h, the suspension was removed and the wells were washed 3x with cold PBS (1x). The nuclei were counter-stained by incubating with Hoechst 33258 (5 µg/mL) (Sigma, UK) for 30 min at 37°C. The cell monolayer was washed three times with 1x PBS and analysed immediately using an inverted Leica DMII fluorescence microscope (Leica, UK), equipped with 40x PHI objective and Texas red filter set (596/670 nm). Images were processed and analysed using ImageJ (NIH, Bethesda, MD, USA: http://imagej.nih.gov/ij).

2.5.3.2. Cellular uptake studies of TPZ and $Cu(TPZ)_2$

2.5.3.2.1. Quantitative uptake

Confluent C4-2B cells were harvested by trypsinization and seeded into 24 well assay plates (Triplered, UK), pre-coated with poly-D-lysine (100 µg/mL), at 5×10^4 viable cells/well. The cells were incubated overnight under either normoxia or hypoxia to allow adherence. Cells were subsequently incubated with 25 and 50 µM equivalent TPZ content in free and copper-complex form (12.5 and 25 µM) at 37 °C for 1, 4, 8 and 24h. At designated time periods, the suspension was removed and the wells were washed 3x with cold PBS (1x). After that, cells were harvested by trypsinization and pelleted by centrifugation (500 x *g*, 10 mins). The pellet was ressupended in 200 µL of DMSO (to guarantee solubility of released drug) and cells were then lysed by mechanical

disruption using a bath sonicator (Ultrasound cleaning baths, USC, VWR). This ensured full disruption of cell membrane and intercellular organelles. The fluorescence intensity (**FI)** of each sample well was measured using a BMG microplate reader (FLUOstar Omega, BMG Labtec) at 485 nm excitation and 590 nm emission and % uptake was calculated relative to initial feed solution and corrected for samples without drug.

2.5.3.2.2. Fluorescence microscopy

Confluent C4-2B cells were harvested by trypsinization and seeded at 5×10^4 viable cells/well, onto X100 Microscope Round Coverslips (Fisher Scientific, UK), pre-coated with poly-D-lysine (100 µg/mL), in 24 well assay plates (Triplered, UK). The cells were incubated overnight under normoxia or hypoxia, as mentioned in **sections 2.5.1** and **2.5.2**. The cells were then incubated with 100 µM equivalent TPZ content in free and copper-complex form at 37 °C for 1, 4, 8 and 24h. At designated time periods, the suspension was removed, and the wells were washed 3x with cold PBS (1x). The cells were then fixed with 4% PFA at room temperature for 20 min. Then, the cells were washed 3x with cold PBS (1x). The nuclei were stained by incubating with Hoechst 33258 (5 µg/mL) (Sigma, UK) for 30min at 37°C. The cell monolayer was washed 3x with PBS (1x) and mounted using ProLong™ gold antifade mounting media (Fisher Scientific, UK). Images were obtained using a Zeiss Axioplan 2 epifluorescence microscope (Carl Zeiss, UK) with a Plan-Apochromat 63x/1.4 Oil objective and Axiovision 4.1.8 software. Images were processed and analysed using ImageJ (NIH, Bethesda, MD, USA: http://imagej.nih.gov/ij). For each endpoint, duplicates of two independent experiments (n=2) resulted in the analysis of over 50 cells.

2.5.3.3. *In vitro* cytotoxicity

There are many cell viability assays that are routinely used to assess drug cytotoxicity. Given the high number of parameters that were tested in this work, a method that is simple, rapid, efficient, reliable, sensitive, safe and inexpensive would be the ideal choice to perform high-throughput drug analysis [417]. The resazurin assay, also known by its commercial name Alamer blue®, is a simple redox colourimetric assay used to evaluate cell viability [417,418]. This method, as other colourimetric assays, relies on the intracellular reduction of a blue weakly fluorescent dye (resazurin) into a highly fluorescent pink resorufin dye, which it then excreted into the cell media (**Figure 2.8**). The reduction is considered irreversible and is directly proportional to the number of viable cells, which allows a fluorimetric quantitative analysis of drug effect over time. The main advantages of this method is its non-toxicity, higher sensitivity (can detect as low as 50-80 cells) and its multiplex use with other methods. The disadvantages of the resazurin include the possibility of fluorescent interference from compounds being tested, which was considered irrelevant in this work after preliminary testing.

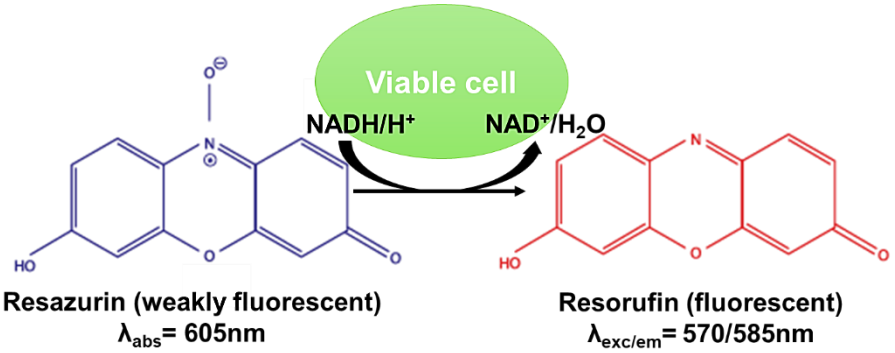

Figure 2.8. Mechanism of reduction of resazurin to the fluorescent compound resorufin by viable cells.

2.5.3.4. TPZ and $Cu(TPZ)_2$

In this work, the cytotoxicity of TPZ and $Cu(TPZ)_2$ was assessed using the resazurin assay, as previously described [419]. A 400 µM stock solution of resazurin sodium salt powder (Sigma Aldrich, UK) was prepared in 25mM NaCl/Pi buffer, sterilized by 0.2 um filtration, and stored at 4 °C (1 week) or at -20°C (6 months).

Cells were seeded at densities of $11x10^3$/well for DU145, PC3 and C4-2B and 15 $x10^3$/well for LNCap in 96-flat bottomed tissue culture well plates (Triplered, UK) and allowed to adhere for 24 h at 37°C in a humidified chamber. LNCap and C4-2B cells were seeded in pre-coated poly-D-lysine (100 µg/mL) plates to enhance adherence. Cell culture media and drug stock solutions were pre-purged with the latter gas mixture to minimize oxygen fluctuations and experiments under both normoxia and hypoxia (described in **sections 2.5.1** and **2.5.2**) were run simultaneously to avoid batch-to-batch variation.

Taking into account the 2:1 stoichiometry of the $Cu(TPZ)_2$ complex, various concentrations of the free ligands were tested, maintaining an equivalent copper and TPZ content as to the complex (TPZ content: 0.02 up to 100 µM). The cells were treated for 48, 72 and 96h using 10% DMSO as a positive control. 20 µl of resazurin solution (400 µM) was added to each well at the experiment endpoint and incubated for 4 h, at 37°C to determine cell viability. Fluorescence intensity **(FI)** was measured using a BMG microplate reader (FLUOstar Omega, BMG Labtec) at 544 nm excitation and 590 nm emission. Values were corrected by subtracting **FI** of the media alone. The average percentage cell viability for each drug concentration was expressed as mean ± SD of six replicates of three independent experiments (n=3) and calculated by normalizing the **FI** values to the untreated cells using the following formula:

$$\textbf{Cell Viability (\%)} = \frac{\mathbf{FI_{treated}}}{\mathbf{FI_{control}}} \times 100 \qquad \textbf{Equation 2.6}$$

Dose-response curves were then generated and the IC_{50} values for drug inhibition were determined by nonlinear regression analysis of the data fit to a four-parameter equation using GraphPad Prism version 7.0 (GraphPad Software Inc., La Jolla, CA, USA, www.graphpad.com). The hypoxia cytotoxicity ratio (HCR) was then determined as IC_{50} normoxia/IC_{50} hypoxia.

2.5.3.5. Empty and Cu(TPZ)$_2$-loaded liposomes

After determining the potency and selectivity of $Cu(TPZ)_2$ compared to TPZ alone for various prostate cancer cell lines, it was essential to test if the developed $Cu(TPZ)_2$-loaded liposomes maintained their activity *in vitro*. To this purpose C4-2B cells were used, given the higher hypoxia selectivity shown for this cell model. Cells were seeded at densities of 11×10^3/well in pre-coated poly-D-lysine (100 µg/mL), 96-flat bottomed tissue culture well plates (Triplered, UK) and allowed to adhere for 24h under normoxia or 1% hypoxia.

$Cu(TPZ)_2$-loaded liposomes at a 60:1 lipid-to-complex molar ratio were assessed, given its adequate drug loading and stability. These liposomes were purified in a sterile Sephadex™ G-25 (PD-10) desalting column inside a safety flow cabinet, prior to cell studies, to ensure aseptic conditions. Briefly, $Cu(TPZ)_2$-loaded liposomes were diluted in cell media at equivalent TPZ content, as to the complex (2:1 molar ratio, TPZ content: 0.02 up to 40 µM) and the cells were treated for 48, 72 and 96h using 10% DMSO as a positive control. Experiments under normoxia and hypoxia were run simultaneously and empty liposomes with equivalent lipid content were used as control. After treatment, the supernatant was removed, cells were gently washed with 1x PBS and 200 µL of fresh media was added. Washing out liposomes prior to incubation with resazurin was used to avoid any scattering or false positives, due to phospholipid content. Furthermore, 20 µl of resazurin solution (400 µM) was added to each well and incubated for 4 h, at 37°C to determine cell viability. The average percentage cell viability for each liposomal concentration was expressed as mean ± SD of six replicates for three independent experiments (n=3). Dose-response curves were generated and the IC_{50} values for drug inhibition were determined, as described in the previous section.

2.5.4. DNA binding studies

An interesting and classical target of metal-based anticancer compounds is DNA. Therefore, understanding how these drugs can interact with DNA, is of upmost importance to shed light on its mechanism of action (MoA). Using UV/Vis spectroscopy is a simple and reliable method to understand the possible interaction of copper (II) complexes with this biological target [420].

Small molecules such as metal complexes can bind to double stranded DNA in different ways. Intercalative binding between adjacent pairs, results in clear hypochromism, visible in the UV/Vis spectrum after complex/DNA titration. On the other hand, non-intercalating binding either through functional grooves of the major or minor groove, sugar-phosphate binding in the outside edge of the helix or covalent interactions at the nitrogen base pairs, result in hyperchromism [421,422].

In this study a simple titration between $Cu(TPZ)_2$ (25 µM) and calf-thymus DNA (CT-DNA) was performed and analysed by UV/Vis spectroscopy to understand if and how this particular complex can interact with DNA. The CT-DNA stock solutions was prepared in Tris-buffer (containing 5 mM Tris-HCl and 50 mM NaCl at pH 7.2). The UV absorbance at 260 and 280 nm of the CT-DNA gave a ratio of 1.84, indicating that DNA was sufficiently free of protein contamination. DNA stock concentration (8.71 mM) was determined spectrophotometrically at 260 nm, by using the molar extinction coefficient value of 6600 $M^{-1}cm^{-1}$ and the beer lambert-law [420].

$Cu(TPZ)_2$ (25 µM) solutions were also prepared in Tris-buffer and were highly soluble, showing the similar red colour to its solid phase, thus, suggesting the stability of the compound under these conditions. We further performed electronic absorption titrations, which were carried out with a constant concentration of the copper(II) complex (25 µM) and varying concentrations of CT-DNA (0–500 µM) in Tris-buffer. The complex and DNA solutions were incubated at 37 °C for 24 h. Subsequently, the spectra were recorded using a UV/Vis spectrophotometer at ambient temperature. To subtract the absorption due to the DNA itself (in each sample), solutions of free CT-DNA (namely in the absence of copper compound) at the corresponding concentrations (0–500 µM) were used as blanks before recording the absorption band of each sample. As a positive control, titrations of the corresponding concentration of TPZ (50 µM) were also performed, with varying concentrations of CT-DNA (0–500 µM). Solvent samples without DNA or drug were used as baseline reference and the results were presented as mean absorbance of triplicate samples of two independent experiments (n=2).

The intrinsic binding constant ($\mathbf{K_b}$) for the interaction of $Cu(TPZ)_2$ with CT-DNA was calculated using the following equation:

$$\frac{[\mathbf{DNA}]}{\varepsilon_a - \varepsilon_f} = \frac{[\mathbf{DNA}]}{\varepsilon_b - \varepsilon_f} + \frac{1}{\mathbf{K_b}\,(\varepsilon_b - \varepsilon_f)} \qquad \textbf{Equation 2.7}$$

where $\boldsymbol{\varepsilon_a}$ was calculated as $A_{obsd}/[Cu]$, $\boldsymbol{\varepsilon_f}$ is extinction coefficient for the free $Cu(TPZ)_2$ and $\boldsymbol{\varepsilon_b}$ the extinction coefficient for the $Cu(TPZ)_2$ in the fully bound form.

In the plot of $\mathbf{[DNA]/(\varepsilon_a - \varepsilon_f)}$ *vs.* **[DNA]**, $\mathbf{K_b}$ (M^{-1}) is then given by the ratio of the slope to intercept.

2.5.5. 3D *in vitro* models

For many years, anticancer drug screening relied on the simplified model of two-dimensional cultures, with indisputable advantages. However, the gap between *in vitro* testing and reliable *in vivo* and clinical outcome is limited by the loss of important cellular, molecular and genetic features, when cells are grown in a 2D model [423,424]. To overcome this, the development of tumour spheroids or three-dimensional models, has become a widely accepted concept in *in vitro* testing that may produce more reliable and translational results. 3D tumour spheroids, allow cells to grow in versatile self-assembled spheres or cell clusters. They are a more stringent and realistic model of tumour heterogeneity, possessing several *in vivo* features such as cell-cell interaction, hypoxia, quiescent cells, oxygen, nutrient and pH gradients and the possibility of production/deposition of extracellular matrix. All these features allow a thorough study of the dynamics of cancer biology, providing a more translatable outcome of drug penetration, response and more importantly, resistance [425].

In the research group, different PCa cells were optimized in their 3D cellular growth. Different cellular densities and growth rates were compared to obtain the desired hypoxic model. In this thesis, the C4-2B spheroid model was selected, as it showed higher drug sensitivity than the former 2D model and represents a late stage form of PCa, while adequately representing osteoblastic metastasis *in vivo*.

2.5.5.1. Preparation of C4-2B tumour spheroids – growth curves

C4-2B spheroids were cultured in 96-well flat-bottom plates (NuncTM Delta Surface plate) (Sigma-Aldrich, UK) using the liquid overlay technique [426], as it is an inexpensive, rapid and suitable method to grow reproducible 3D cell cultures of uniform well-defined circular shape for automated high-throughput screen. Briefly, 1% agarose (Sigma, UK) was dissolved in deionized water and autoclaved at 121°C, 15 PSI for 15 min (Systec DB-100). 100 μL of agarose solution was casted onto 96-well plates, gently shaken to ensure homogeneity, and allowed to solidify at room temperature. Plates were prepared prior to seeding, used fresh or stored in the fridge, up to 1 week.

C4-2B cells were detached using 0.05% trypsin/EDTA, counted and seeded (5000 cells/well) in the pre-coated 96-well flat-bottomed plates. Plates were gently shaken to bring the cells closer together and encourage the formation of a single spheroid. 3D cultures were maintained in normal culture conditions in a humidified chamber at 37°C and 5% CO_2. To maintain culture, the old media was replenished every two days by removing 100 μL and replacing it with fresh media, taking care not to disturb the spheroids. Spheroid growth was monitored over time and more than 30 spheroids were imaged on a daily basis, using light microscopy (Olympus CKX41 microscope with a 10x objective and an attached Micropublisher 3.3 RTVcamera). Images were analysed using the open source software ImageJ (NIH, Bethesda, MD, USA: http://imagej.nih.gov/ij), applying an image of known scale as calibration. In order to determine spheroid diameter and volume, a previously written macro (Macro S1) was used to automate the process [427] (**Figure 2.9**).

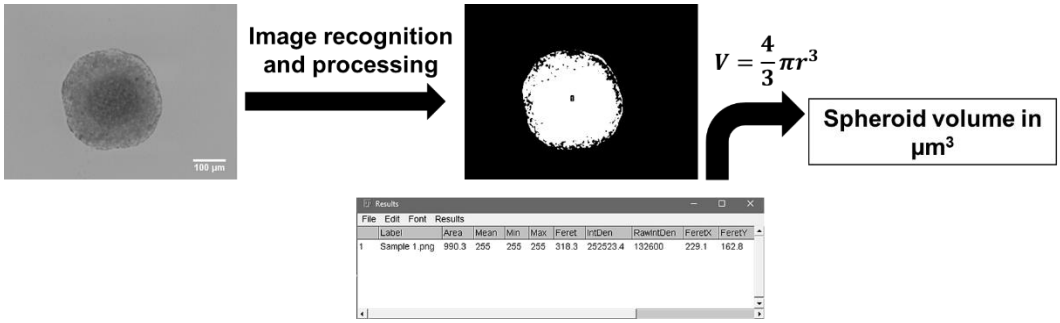

Figure 2.9. Scheme depicting the simplified image processing and analysis of the ImageJ automated spheroid macro. The macro allowed the determination of spheroid diameter and volume over time.

The macro allowed the analysis on whole folders of images. It initially converted the images to black and white and uses the Yen thresholding algorithm to generate a clean image, clear from all artefacts, holes and separates debris, allowing a reliable determination of the area Diameter and all shape parameters were analysed via ImageJ, then saved and analysed in Excel. The Ferret's diameter (**r**) was used in the estimation of the mean diameter of the spheroids and to determine their average volume (**V**) over time, as follows:

$$\mathbf{V=\frac{4}{3}\pi r^3} \qquad \textbf{Equation 2.8}$$

Moreover, the parameter "circularity" was used to determine the spheroid proximity to a circle (determining their regularity), while the "Solidity" function indicates the roughness of the spheroidal surface [428]. The final results were a good indicator of spheroid uniformity and experimental size reproducibility to ensure less variability during drug treatment studies. Data was produced together with Mr. Moustafa Abdelhamid and Mr. Duuamene Nyimanu (M.Sc. students, School of Pharmacy, University of East Anglia).

2.5.5.2. Hypoxia validation in C4-2B spheroid models

Hypoxia was validated for C4-2B spheroids using the CYTO-ID® Hypoxia/Oxidative Stress Detection kit (Enzo Life Sciences. UK). Cells were harvested by trypsinisation and seeded at 5×10^3 cells/well onto 1% agarose pre-coated 96 flat-bottom well assay plates (Triplered, UK). The cells were allowed to grow and were monitored up to 8 days of culture, for hypoxia assessment. 100 µL of the supernatant was then removed slowly and the spheroids were washed three times with cold PBS (1x), by gently removing and replenishing 100 µL of the supernatant. The spheroids were then incubated with the hypoxia red probe (500 nM), while DFO (200 µM) was used as a positive control and unstained cells were used as a negative control. Incubation was performed in normal conditions for 4h at 37°C. After 4h, the suspension was removed, and the wells were washed three times with cold PBS (1x), as described above. Spheroids at different days of culture were analysed immediately using an inverted Zeiss Axiovert 200M equipped with epifluorescence and a Zeiss ApoTome (Carl Zeiss, UK), Texas Red (596/670 nm) filter, to create optical sections free of scattered light. For

each spheroid a z-stack with 10 µm intervals was generated. Images were acquired with a 10x/0.45 air objective and Axiovision 4.1.8 software and were processed and analysed using ImageJ (NIH, Bethesda, MD, USA: http://imagej.nih.gov/ij). For each endpoint, three spheroids from two independent experiments (n=2) were analysed.

2.5.5.3. *In vitro* cytotoxicity of TPZ and $Cu(TPZ)_2$ complex

In this work, spheroids with diameters above 300 µm were used, to ensure adequate oxygen fluctuations and formation of hypoxic cells within the spheroids. This allowed a more reliable model to test the cytotoxic effects of the hypoxic prodrugs studied in this work. Unlike 2D cultures, ensuring a validated and reproducible method for determination of cell viability and drug cytotoxicity can be a tedious and difficult task. The aim was to establish a protocol that could be easily compared to our 2D culture results and allow high-throughput analysis. Given this, the continuous use of the resazurin assay was applied, which had been previously validated for use in 3D models [419]. However, this method must be used with caution, as spheroid size and compact pattern can limit the use of this colourimetric assay [427]. C4-2B spheroids generated herein were large in diameter and very compact in size thus, ensuring an adequate penetration and reduction of the resazurin dye is of upmost importance. For this purpose, the use of chelating agents such as EDTA can be used to disrupt the intercellular tight junctions, restoring the high reduction rates of the resazurin dye [419]. In summary, the resazurin assay was used in this work to estimate the cellular toxicity of TPZ and $Cu(TPZ)_2$ in C4-2B spheroids. The method was applied with and without EDTA, pre-treatment to assess method validation.

C4-2B tumour spheroids were treated on day 5 of culture growth, taking into consideration the spheroid size and hypoxia generation. 100 µL of media was then carefully removed and replaced with pre-diluted fixed concentrations of TPZ in free and complexed form (TPZ content: 0.002 up to 20 µM). Spheroids were treated for 48, 72 and 96h using 10% DMSO as a positive control. At the experiment endpoint, some plates were used with and without EDTA pre-treatment. Spheroids were carefully washed with 1x PBS and replenished with fresh media or pre-treated with EDTA (10 mM), for 30 min, with shaking (70 rpm). 20 µl of resazurin solution (400 µM) was then added to each well and the spheroids were further incubated overnight, at 37°C to determine cell viability. To complement this assay, spheroid images were taken at the specified endpoints to further evaluate spheroid volume and morphology change before and after treatment. The average percentage cell viability for each drug concentration was expressed as mean ± SD of six replicates of at least two independent experiments (≥18 spheroids, n≥2) and calculated by normalizing the **FI** values to the untreated cells. Dose-response curves were generated, where possible, and the IC_{50} values for drug inhibition were determined, as previously described.

2.5.5.4. *In vitro* cytotoxicity of $Cu(TPZ)_2$-loaded liposomes

The cytotoxicity of $Cu(TPZ)_2$-loaded liposomes at a 60:1 lipid-to-complex molar ratio was also assessed, given their adequate drug loading and stability. These liposomes were purified in a sterile Sephadex™ G-25 (PD-10) desalting column inside inside a safety flow cabinet to ensure aseptic conditions. The vesicles were then diluted in cell media at varying $Cu(TPZ)_2$ concentrations with equivalent TPZ content (2:1 molar ratio, TPZ content: 0.02 up to 20 μM). The spheroids were treated for 48, 72 and 96h, using 10% DMSO as a positive control. At the experiment endpoint, spheroids were gently washed with 1x PBS and pre-treated with EDTA (10 mM), 30 min, with shaking (70 rpm). 20 μl of resazurin solution (400 μM) was then added to each well and the spheroids were further incubated overnight, at 37°C to determine cell viability, as described previously. To complement the viability assay, spheroid images were taken at the specified endpoint to evaluate spheroid volume change, before and after treatment. The percentage cell viability for each liposomal concentration was expressed as mean ± SD of six replicates of at least two independent experiments ($n \geq 2$). Dose-response curves were generated, where possible, and the IC_{50} values for drug inhibition were determined, as previously described.

2.5.5.5. Cell cycle analysis using flow cytometry

Flow cytometry is a versatile laser-based technology used for a multiplexed analysis of cells or particles. It is predominantly used to detect fluorescence intensity allowing the characterisation, counting and sorting of cell populations or discrimination of the expression of several external and intracellular markers. This technology works on the basis of a fluorescent microscope, but instead of creating an image allows the high-throughput analysis and automated quantification of thousands of particles/cells per second [429]. This is achieved inside the flow cytometer, where the cell suspension is drawn into a laminar flow stream by the sheath or isotonic fluid. This allows each cell to pass individually through a point where a laser beam intersects a cell, allowing light to be deflected in all directions and directed to a series of filters and dichroic mirrors that isolate particular wavelength bands (**Figure 2.10**).

Light scattering can distinguish differences in size or dimeter (forward light scattering) and internal complexity or granularity (side scattering) of cells, for phenotypic characterisation and exclusion of debris. In addition, intensity of light emission allows the quantification and multi-parameter analysis of DNA or RNA content, and a wide range of membrane-bound and intracellular markers, based on the fluorescent label used.

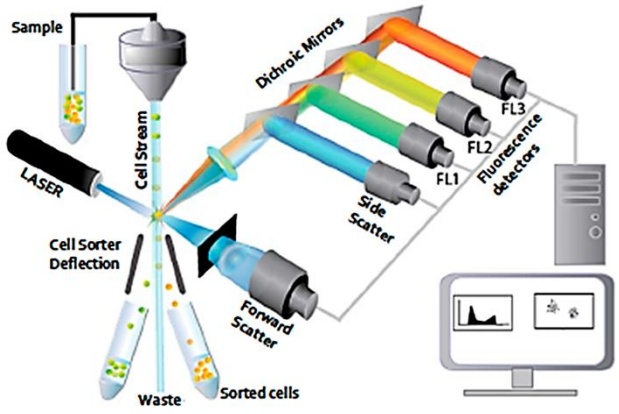

Figure 2.10. Flow cytometry fluidics set-up. The cell suspension is injected into the fluidics of the flow cytometer and directed into a single stream of cells via the sheath fluid, thus analysing single cells. Once the laser beam hits the cell, light is scattered in all directions, allowing analysis of forward and side scattering and/or detection of multiple fluorophores for multiparameter quantification. Image taken from [430].

One of the oldest and most popular applications of flow cytometry is the quantification of cell DNA content and cell cycle analysis [431]. Univariate analysis of cellular DNA is a simple and reliable method that allows the discrimination amongst cells in G0/1, S and G2/M phases. In this assay, cells are fixed or permeabilized and labelled with a nuclei dye, such as propidium iodide (PI) that intercalates into the DNA helical structure. In this particular assay, treatment with RNase is essential to exclude any PI binding to this nucleic acid. The principle is that the amount of incorporated PI will be directly proportional to the DNA concentration, allowing quantification of cell populations in different cell cycle points [432,433]. Cells in G1 phase will have DNA content equivalent to one unit, progressively increasing its content during the DNA synthesis S phase, until cells achieve twice the DNA content (two units) in the G2/M phase. To discriminate any cell aggregates or doublets and risk overestimation of valid events, the intensity of the staining measured as pulse-area (FL2A) and pulse-width (FL2W) of the samples, in a dot plot graph is analysed (**Figure 2.11**). A gate is set around the singlet population and then a histogram graph of this gated population shows the four distinct phases that can be further fitted to calculate percentage of cells in each phase.

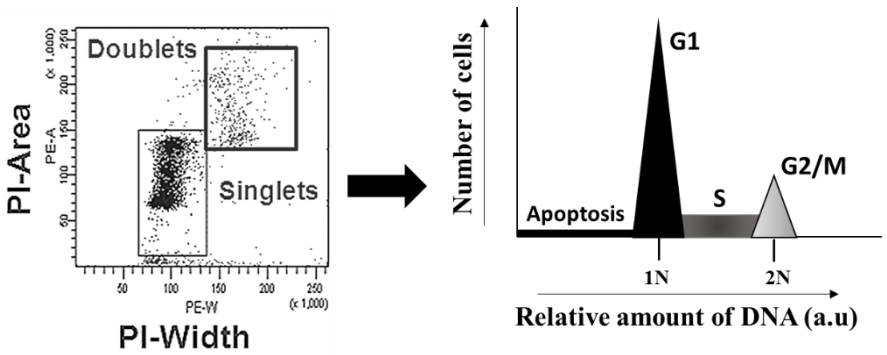

Figure 2.11. Cell cycle analysis. Dot plot of FL2W/FL2A for DNA content and doublet discrimination and typical histogram plot consisting of the discriminated cell cycle phases, plotted relatively to DNA content.

To complement the cell viability assays, the effect of TPZ and $Cu(TPZ)_2$ on the spheroid cell cycle progression was analysed. C4-2B spheroids were cultured at a density of 5×10^3cells/well and on day 5 of growth, were treated with 2 and 20 μM (equivalent TPZ content) in free and copper-complex form. After 72h, spheroids were harvested, using a 1 mL pre-cut micropipette tip, into 1.5 mL micro centrifuge tubes (Fisher Scientific, UK) and centrifuged at 500 × *g* for 5 min, to sediment the spheroids. The cells were then washed three times with cold PBS (1x), with repeated centrifugation and resuspended in 100 μL of PBS (1x). Thereafter, a single cell suspension was formed by mechanical dissociation, using a micropipette, and cells were fixed in 70% ethanol for at least 1h, on ice. To achieve this, 400 μL of ice-cold 70% ethanol was added dropwise to each sample, while vortexing, to ensure complete fixation and avoid cell clumping. Cells were then washed three times with PBS (first spin at 800 × g, 10 min, to recover all cells) and the cell pellet was resuspended in 0.5 mL of FxCycle™ PI/RNase staining solution (Molecular Probes, UK). The samples were incubated for 30 min at room temperature, protected from light and further analysed, without washing, by flow cytometry using a Becton Dickinson CytoFLEX (Beckman Coulter, UK). Cell doublets were separated from single cells in G2/M phase using pulse-width/pulse-area signal. At least 10,000 cells were acquired in a histogram and cell cycle data were exported as FSC files and analysed using FlowJo software. Each data measurement was made up from at least ten pooled spheroids, repeating the whole procedure independently two times (n=2). Results were expressed as mean ± SD, after population deconvolution, peak integration and calculation of population percentage.

2.6. Statistical analysis

Data was presented as mean ± SD Two-way Analysis of variance (ANOVA) followed by Bonferroni or Tukey multiple comparisons post-hoc tests were performed when three or more groups of data were analysed. P-values < 0.05 were considered significant and statistical differences amongst groups was estimated and appropriately denoted in text and figure captions. The IC_{50} values for inhibition were determined by nonlinear regression analysis of the data fit to a four-parameter equation. All analyses and graphs were generated using GraphPad Prism version 7.0 (GraphPad Software, La Jolla California USA, www.graphpad.com).

Chapter 3

Preparation and characterisation of cupric-TPZ [$Cu(TPZ)_2$] complexes

This chapter has been included in the following publication:

Silva, V.L, *et al*. Enhanced selectivity, cellular uptake, and *in vitro* toxicity of an intrinsically fluorescent copper-tirapazamine nanocomplex for hypoxia targeted therapy. *ACS Bioconjugate Chemistry* (under revision).

3.1. Overview

Previous studies have focused on analysing different physicochemical properties of TPZ, including solubility [434], Log P [434], redox potential [147,434], and extravascular diffusion [435]; and characterised using UV/Vis spectra [436,437], fluorescence [438], MS [439] and HPLC [440]. Several structure-activity relationship (SAR) studies focused on understanding the effect of 5, 6, 7 and 8 substituents on the solubility, redox potential and consequently, biological potency of different TPZ analogues [147,441]. Moreover, electron-withdrawing 3-substituents have also shown to greatly influence hypoxia selectivity [442]. Together, these findings were important to understand how modulating TPZ's chemical substituents and structure can help improve on its current *in vivo* limitations, designing new analogues that have improved PK. In line with this, the use of metal-complexes, has also emerged as an important strategy to modulate prodrug activity, due to their excellent anticancer properties [156,179]. The coordination of metal centres has shown to enhance stability and effectively modulate properties such as redox potential and lipophilicity, which play a detrimental role on cellular uptake, reduction and hypoxia selectivity [167,171]. To properly select the most appropriate metal centre one must take into consideration its affinity to the ligand, activity or selectivity under hypoxic conditions and the ability to undergo reduction by cellular reductases [443].

Copper(II) has attracted special attention over the last years as a potential metal coordinate to develop hypoxia selective complexes. To date, the coordination of TPZ with metal ions has been poorly investigated. Only one study showed the possible coordination of copper to TPZ and its potential use to treat hepatic tumours. Lin *et al.* [148] described the enhanced DNA damage potential of these complexes, compared to TPZ prodrug alone and their use as targeted radioisotopes for cancer therapy [193]. However, these studies lacked substantial information regarding the physicochemical characterisation of this complex, which in turn may be important to further elucidate its biological potential.

In this chapter, the synthesis and extensive characterisation of $Cu(TPZ)_2$ complexes was reported, with the aim of potentiating TPZ activity. A detailed description of the complexation procedure is provided, as well as, the analysis of the chemical and optical properties of the complex and its individual components. By developing such complexes, the unique hypoxia selectivity of TPZ was exploited, whilst taking advantage of the biocompatible reductive properties of copper (II).

First, the synthesis of $Cu(TPZ)_2$ is described along with the validation of its complexation and stoichiometry. These novel complexes were synthesised using inexpensive materials and could offer significant advantages over conventional chemotherapeutics. The remaining of the chapter focused on the optical properties of these complexes, in particular their intrinsic fluorescent properties, overall stability and morphology. A detailed method for quantification of both TPZ and its complex, using a simple HPLC method, was also provided.

In addition, the relevant physicochemical properties, such as lipophilicity and reduction potential were summarised and discussed, in order to support the findings obtained in **chapters 4 and 5.** The analysis emphasized the importance of understanding the analytical properties of this novel complex, to sustain its biological activity. Throughout the whole project, TPZ was maintained as an internal control in all analyses. The findings obtained in this chapter would further dictate its encapsulation in novel liposomal delivery systems (**chapter 4**) and provide insight on cellular uptake, localization and *in vitro* cytotoxicity (**chapter 5**).

3.2. Results and discussion

3.2.1. Synthesis of cupric-TPZ complexes

Similar to quinoxaline-*N*1-*N*4-oxide analogues, TPZ is a potential candidate for coordination to metal (II) centres (affinity to N and O atoms) [168]. In this study, $Cu(TPZ)_2$ complexes were prepared by mixing TPZ with $CuCl_2$ (2:1, molar ratio) in an ethanolic solution **(Figure 3.1),** as described in **chapter 2** and previously reported [148]. The mixture was stirred overnight in a centrifuge tube to maximize complexation of the components. The red precipitates were then collected and washed by multiple centrifugation steps to obtain purified $Cu(TPZ)_2$ complexes. $Cu(TPZ)_2$ was then solubilized in DMSO (stock solution *ca.* 2.5mM). Preliminary theoretical computational analysis indicated the formation of $Cu(TPZ)_2$ complexes in a *trans* square-planar structure.

Cu(II) complexes have been shown to be stabilized by both electrostatic and covalent interactions of the type Cu-N and Cu-π, but mostly self-assembled due to Van der Waals' interactions [184]. In addition, removal of H-bond donor of the $3NH_2$ group of TPZ has shown to have a marked effect on lipophilicity and tumour diffusion [73], as well as increasing hypoxia cytotoxicity [444]. Generation of this strong Cu-N bond may be important to define complex stability and therapeutic potency.

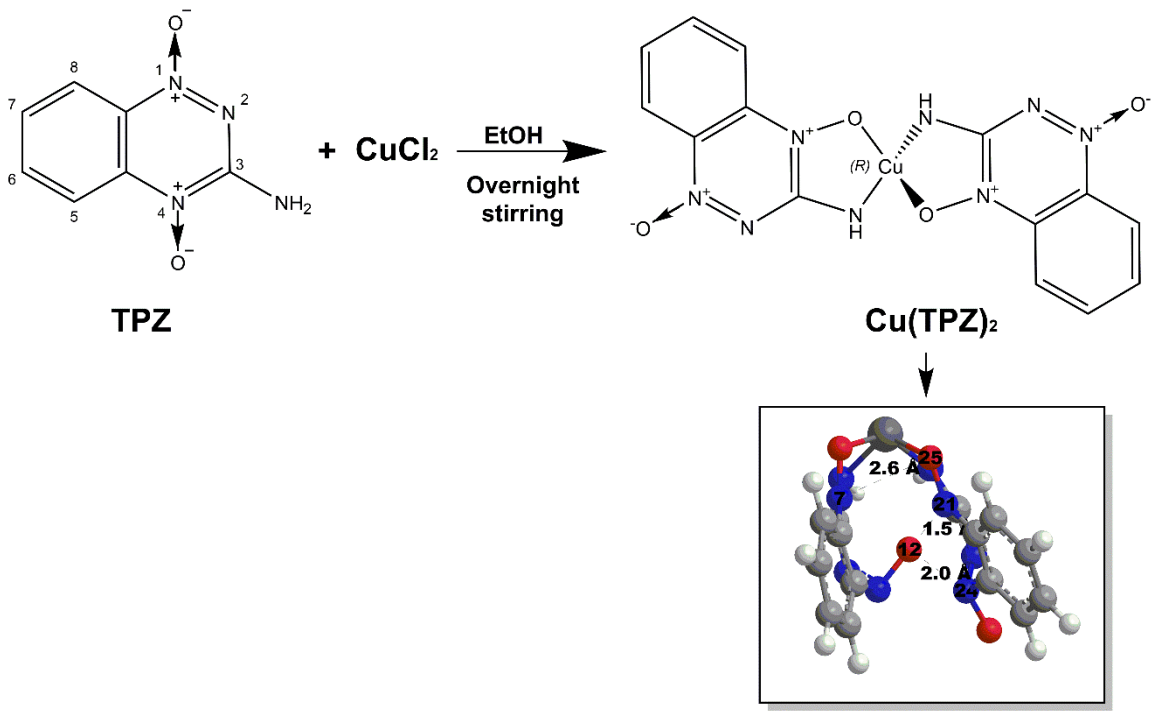

Figure 3.1. Synthesis and characterisation of $Cu(TPZ)_2$ complexes. Schematic representation of the synthesis protocol with proposed structure of $Cu(TPZ)_2$ complexes (Inset: MM2 minimized model using Chem3D 15.0, CambridgeSoft, MA).

Molecular modelling (MM2) was used to simulate a 3D structure for $Cu(TPZ)_2$ (Chem3D 15.0, CambridgeSoft, MA), resulting in a significantly distorted geometry, where electrostatic interactions between O(7)···N(25) (2.5Å), O(12)···N(21) (1.5Å) and O(12)···N(24) (2.0Å), seem to stabilize and tilt the plane enough to facilitate π- π interaction between the benzene aromatic rings **(Figure 3.1, inset)**. Although outside the scope of this work, future analysis using X-ray crystallography and , electronic paramagnetic resonance (EPR) spectroscopy can be used to determine the exact chemical structure and geometry of this complex and initiate SAR studies [181].

3.2.2. Chemical analysis and complexation validation

3.2.2.1. CHN elemental analysis

Elemental analysis of $Cu(TPZ)_2$ complexes was performed using a CHN automated analyser and the results are summarised in **Table 3.1.** Known samples of sulphanilamide were used as internal standards for a reliable quantification. The analysis clearly indicated the presence of $Cu(TPZ)_2$ elements, that appeared in the expected ratios. Overall these results were complementary to other analytical techniques, discussed next, allowing to ascertain the structure of the new compound and its purity.

Table 3.1. CHN elemental analysis of calculated/found atom percentage.

Atom	% Calculated	% Measured
C	**40.32**	**39.85**
N	**26.87**	**25.66**
H	**2.21**	**2.39**

3.2.2.2. Chemical bonding by FTIR

FTIR was used to confirm copper-complexation and compare spectra of both compounds **(Figure 3.2)**. TPZ showed ligand bands corresponding to ν_{as} (NH_2) (3409 cm^{-1}) and ν_s (NH_2) (3258 cm^{-1}) that upon coordination were displaced significantly (3360, 3311 cm^{-1}), resulting from deprotonation and formation of a secondary amine, upon complexation to the copper ion [168,169]. The displaced frequency could be attributed to some residual weak protonation, where the electron density of the nitrogen being directed to the metal ion, leaving the amine protons less tightly bound to the nitrogen [445]. Furthermore, the strong vibrational frequency assigned to the N-O stretch for TPZ (1345 cm^{-1}) turned to weak upon complexation, indicating the coordination of only one of the N → O groups per ligand molecule, with decreasing π character of the *N*-oxide bond [168].

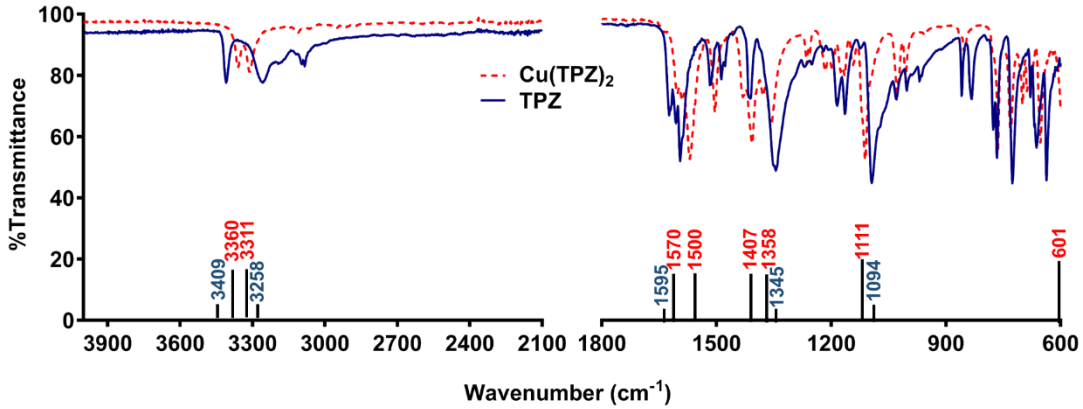

Figure 3.2. ATR-FTIR spectra of TPZ (solid line) and Cu(TPZ)$_2$ (dashed line). IR spectra were obtained in the range between 600 and 4000 cm^{-1} and only diagnostic and/or intense peaks are highlighted.

Additionally, bands at 1500 cm^{-1} and 1570 cm^{-1} from νN=N and νC=N → O, further confirm involvement of the *N*-oxide group in complexation. Additionally, aromatic in plane bending modes can be attributed for TPZ (1094 cm^{-1}) and aromatic out of plane bending modes of the complex (1111 cm^{-1}), suggesting reorientation of the TPZ molecules upon complexation, and possibly originating a distorted geometry. Although poorly resolved, the Cu-NO bending peak can be assigned at 601 cm^{-1}. These results confirm the successful complexation of TPZ to copper and validate previous tentative assignment of TPZ-Cu(II) binding sites at the 3NH$_2$ and 4NO positions [148]. Future studies utilizing thermal analysis, conductivity measurements, EPR and X-ray crystallography can provide additional details on the stability and structure of these complexes, in both solution and solid-state [168,169].

3.2.2.3. Complexation by mass spectrometry

The formation of Cu(TPZ)$_2$ was also confirmed using high resolution MS analysis. For the free ligand, the molecular ion sodium species [L–Na]$^+$ (*m/z* 201.0382) was observed as the base peak **(Figure 3.3A)**. The presence of a peak at *m/z* 162.0533 was a likely a result of thermal decomposition of TPZ, induced by the heated probe or the ion source of the mass spectrometer, originating the corresponding 1-oxide species.

The results were in good agreement with previous fragmentation patterns obtained with ESI-MS [439], where the recovery signal at *m/z* 179 was reported, demonstrating a neutral protonated TPZ as a stable species in the gas phase. This was consistent with the notion that it could form this neutral form in aqueous solution [439]. Moreover, the data was a good indicator of the fragmentation patterns generated for TPZ *in vitro* (**Figure 3.4**), with two typical TPZ metabolites, the TPZ benzotriazine radical and mono-N-oxide (SR4317) (*m/z* 162.0533).

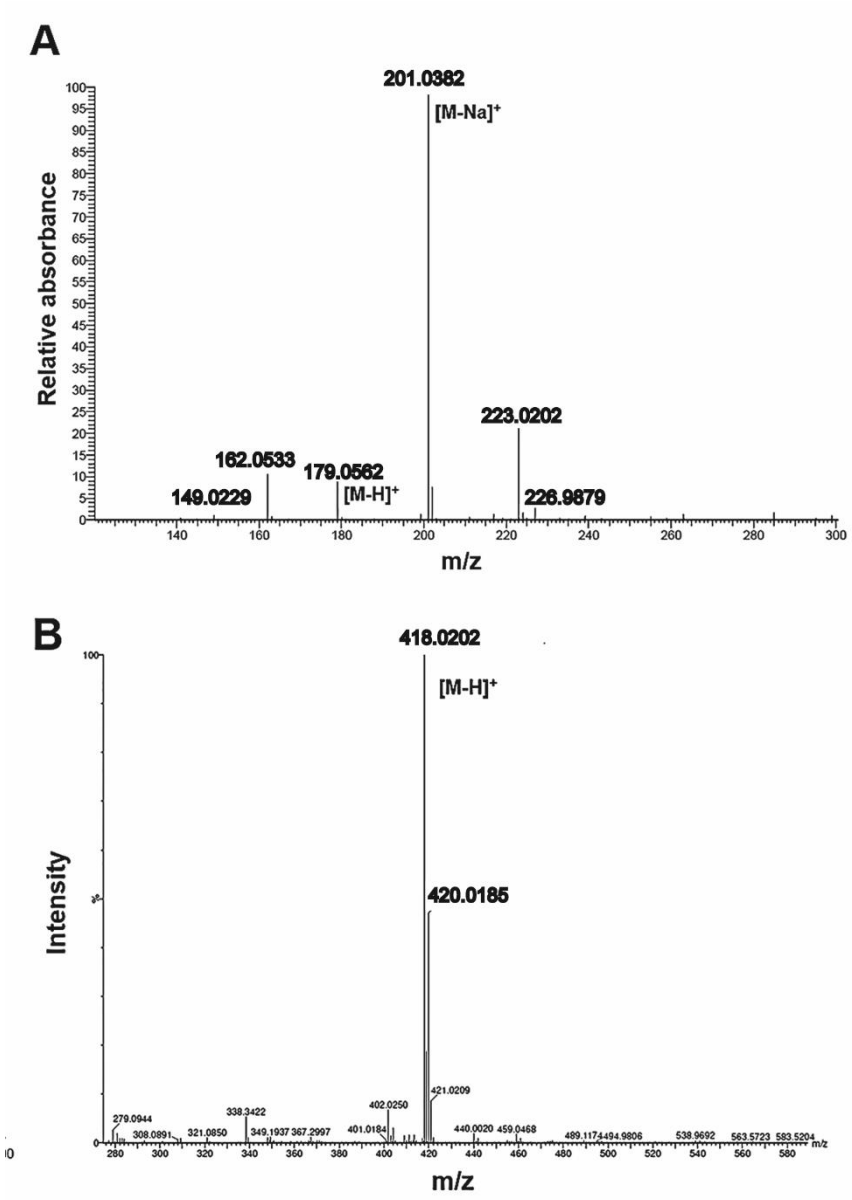

Figure 3.3. High resolution mass spectrometry analysis. A) FTMS (Fourier Transform Mass Spectrometry) spectrum of protonated 3-amino-1,2,4-benzotriazine 1,4-dioxide, TPZ and B) MALDI-MS (Matrix-assisted Laser Desorption/Ionization Spectrum Mass Spectrometry) of Cu(TPZ)$_2$ complex. The data was provided by the EPSRC Mass Spectrometry Unit at the University of Wales, Swansea.

The complex presented an intense base peak that corresponded to one copper coordinated to two deprotonated TPZ ligand molecules [Cu(L–H]$^+$ (*m/z* 418.0202), which agreed very well with the formula weight (Wt) of the complex (Wt = 417.83 g/mol); thus confirming complexation in a 2:1 coordination ratio **(Figure 3.3B)**. These results, together with those obtained by FTIR and elemental analysis, resulted in the proposed structure presented in **figure 3.1.**

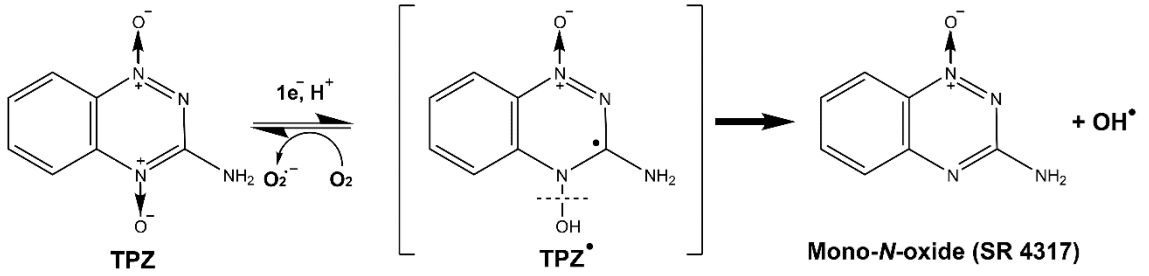

Figure 3.4. TPZ bioreduction. Schematic depicting fragmentation of TPZ (*m/z* 179) in an intermediate TPZ radical, finally generating a stable mono-*N*-oxide derivative (*m/z* 162) and the DNA-damaging hydroxyl radical.

3.2.3. Optical properties of TPZ and Cu(TPZ)$_2$

3.2.3.1. UV/Vis absorption spectrum analysis

The absorption spectra of free TPZ in different solvents was evaluated, along with the spectral differences obtained after complexation (**Figure 3.5**). Given the high solubility of the complex in DMSO, the spectral properties in this solvent and in aqueous buffers (*e.g.* HBS, relevant for *in vitro* purposes) were evaluated and compared between TPZ and Cu(TPZ)$_2$. TPZ was initially reconstituted in DMSO (56 mM) or ethanol (2.8 mM) and further dispersed in HBS. The UV/Vis spectral analysis was performed within a linear concentration range. In DMSO, TPZ presented two typical bands, one in the UV region of the spectra (λ_{max} 280 nm) and a less intense band at λ_{max} 500 nm (**Figure 3.5A, blue line**). In ethanol (EtOH) (**Figure 3.5A, turquoise line**) and in HBS (**Figure 3.5A, purple line**), TPZ presented a spectral blue-shift with split bands at λ_{max} 260 nm and a more intense band at λ_{max} 472 nm (EtOH) and λ_{max} 462 nm (HBS). The first peak is attributed to the $\pi \rightarrow \pi^*$ transitions in the phenyl group and the second one to $\pi \rightarrow \pi^*$ transitions from the pyridine-*N*-Oxide that is highly sensitive to the environment polarity [446]. The findings obtained in this work were in agreement with a previous study [436], where a correlation between absorption band maximum and the Dimroth solvatochromic parameter (ET30) was established for TPZ in a range of different solvents.

Cu(TPZ)$_2$ complexes were synthesised, completely solubilized in DMSO and their absorption spectra was analysed and compared to that of TPZ. Both compounds showed similar optical properties in DMSO (**Figure 3.5B**), with two characteristic absorption peaks at λ_{max} 280 nm and 500 nm. The intense UV band (λ_{max} at 280 nm) was assigned to intraligand (IL) transitions. In EtOH (**Figure 3.5C**) a similar spectrum was obtained for Cu(TPZ)$_2$. In contrast, TPZ showed a marked blue-shift (λ_{max} 500 nm to 472 nm), confirming the sensitivity of this drug to solvent polarity and the involvement of the pyridine-*N*-Oxide group in complexation. In HBS (**Figure 3.5D**), Cu(TPZ)$_2$ maintained a ligand centered band at λ_{max} 280 nm and a broad absorption band in the visible region at 500-600 nm, which is characteristic of copper (II) d-d transition bands (band I: $d_{xy,yz} \rightarrow d_{x2-y2}$) [447].

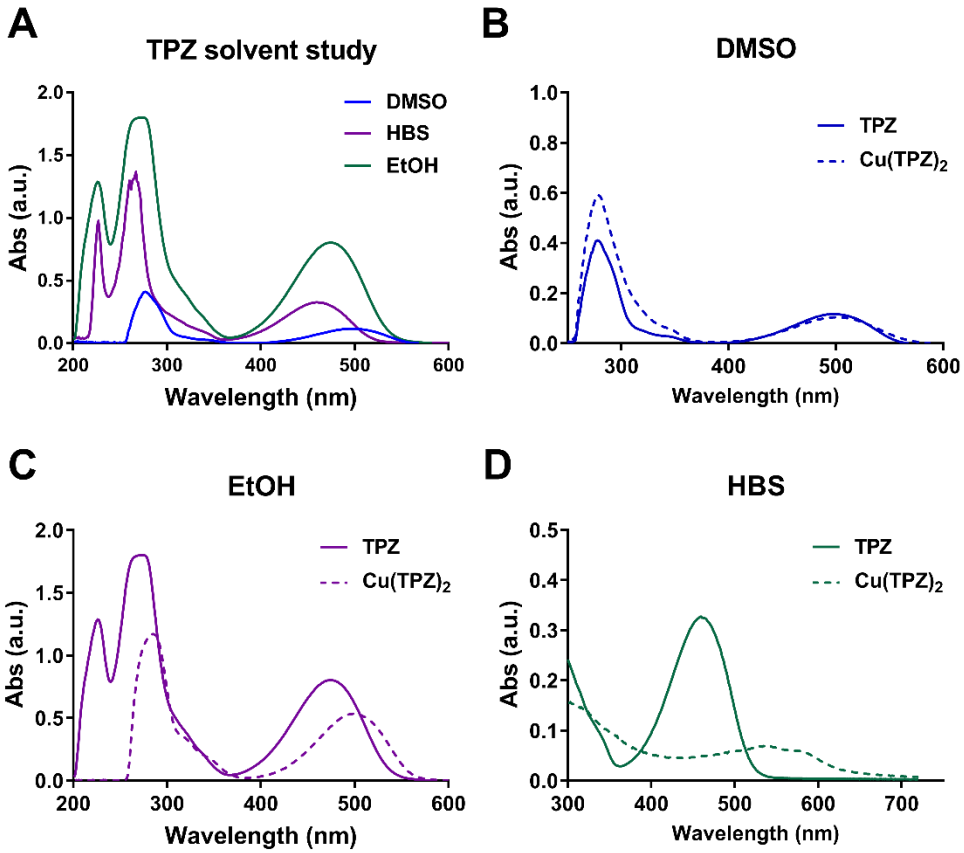

Figure 3.5. UV/Vis spectral analysis of free TPZ and copper-complexed TPZ. Absorption spectra of A) TPZ in different solutions; Absorption spectra of TPZ and $Cu(TPZ)_2$ in B) DMSO; C) dispersed in ethanol (EtOH) and D) dispersed in HBS (20 mM HEPES, 150mM NaCl, pH 7.4). Upon complexation, bands are overall shifted to higher wavelengths resulting from an increase in the system conjugation. Blank solvents were used for baseline corrections and spectrums were expressed as mean of triplicate samples.

Once again, TPZ displayed the typical polarity shift to shorter wavelengths. Overall, upon coordination to copper (II), the spectrum bands for TPZ were shifted to longer wavelengths, because of a larger conjugated system [445], thus supporting complexation.

Motivated by a previous study [148], the solubility of the complex was enhanced by adjusting the solution to lower pH. Surprisingly, these conditions did not yield a higher solubility of the complex and resulted in dissociation and release of uncoordinated TPZ. This finding is depicted in **figure 3.6A**, where a clear differentiation of the spectral changes from complexed and free TPZ forms are observed. A significant bathochromatic shift (λmax 410 nm to 500 nm) was observed when TPZ is coordinated to copper (II), due to ligand-metal charge transfer upon complexation. In contrast, the 500 nm metal-transfer band is shifted to lower wavelengths, upon dissociation of TPZ. This spectral shift was further accompanied by a solution colour change from dark red (complex) to yellow (free TPZ) (**Figure 3.6B**). The results obtained here have demonstrate impact on the stability of the complex under different pH conditions, which may be important in the context of the tumour microenvironment and consequently on the biological activity and/or stability of the complex.

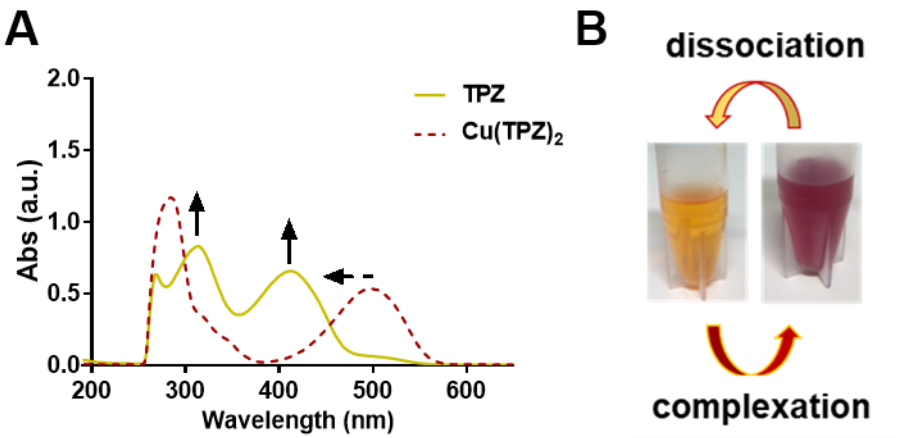

Figure 3.6. UV/Vis spectral analysis of synthesis and dissociation of Cu(TPZ)2. A) Absorbance spectra of TPZ and Cu(TPZ)2 confirming complexation. Spectral changes (indicated by the arrows) confirm dissociation of the complex, which is pH dependent. B) Image depicting solution colour change of TPZ (yellow) to a dark red solution, upon complexation and/or dissociation of the complex (Red) to free (yellow) TPZ in acidic conditions (pH <5). Ethanol was used for baseline corrections and spectrums were expressed as mean of triplicate samples.

3.2.3.1.1. Stability in buffers

Following the evaluation of the spectral characteristics intrinsic to TPZ and its cupric complex in DMSO, the effect of different aqueous buffers on the stability/solubility of both drugs was also determined. The results depicted in **figure 3.7A** confirmed the stability of TPZ, in both PBS and HBS solutions, where the absorbance spectrum at λ_{max} 462 nm, remained relatively unchanged. In addition, Cu(TPZ)2 (**Figure 3.7B**) presented the typical d-d transitions (band I: $d_{xy,yz} \rightarrow d_{x2-y2}$), as shown before in HBS, suggesting a distorted octahedral geometry (when coordinated in aqueous solution); characteristic of Cu(II) complexes [168,169].

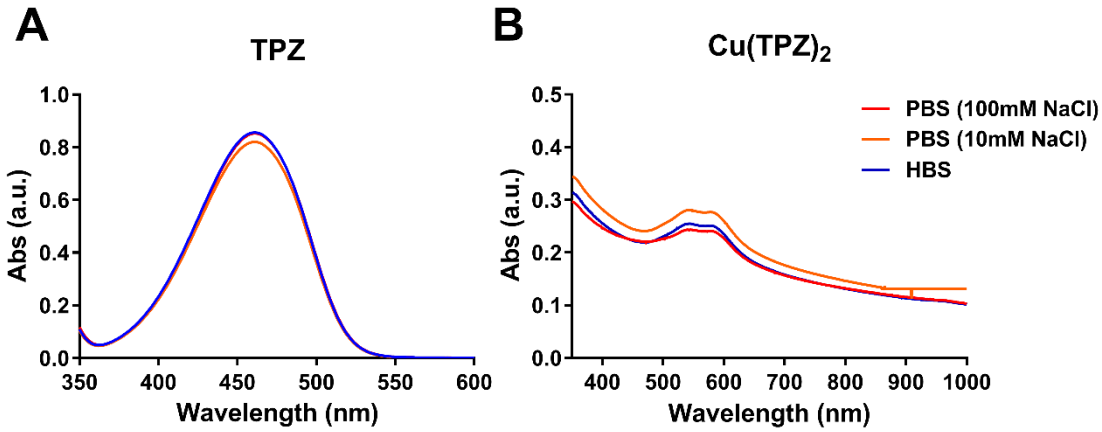

Figure 3.7. UV/Vis characterisation in different aqueous solutions. Absorption spectra of A) TPZ and B) Cu(TPZ)2, further diluted in PBS (10 mM NaCl, pH 7.4), PBS (100 mM NaCl, pH 7.4) and HBS (20 mM HEPES, 150 mM NaCl, pH 7.4). Appropriate blank solvents were used for baseline corrections and spectrums were expressed as mean of triplicate samples.

3.2.3.1.2. Effect of pH on compound stability, determined by UV/Vis

To complement the data obtained in different aqueous buffers, the effect of pH on both compounds was evaluated, given the aforementioned pH dependent dissociation of Cu(TPZ)$_2$. As depicted in **figure 3.8A**, the overall absorbance of TPZ at different pH values (pH from 2 to 12.5) remained mostly unchanged, until up to pH 11. Moreover, at pH 12.5, a significant red-shift (λ_{max} 474 nm to 540 nm) and decrease in absorbance intensity occurred, attributed to deprotonation of the amine group [436]. Together, these results confirmed good stability of the drug over a wide range of pH conditions. To fully understand the dissociation mechanistics of Cu(TPZ)$_2$, this compound was subjected to different pH environments and its aborbance spectra analysed. As shown in **figure 3.8B**, when the pH decreases, the absorbance at 535 nm decreases, whilst the absorbance at 462 nm increases, thus indicating the presence of uncoordinated TPZ

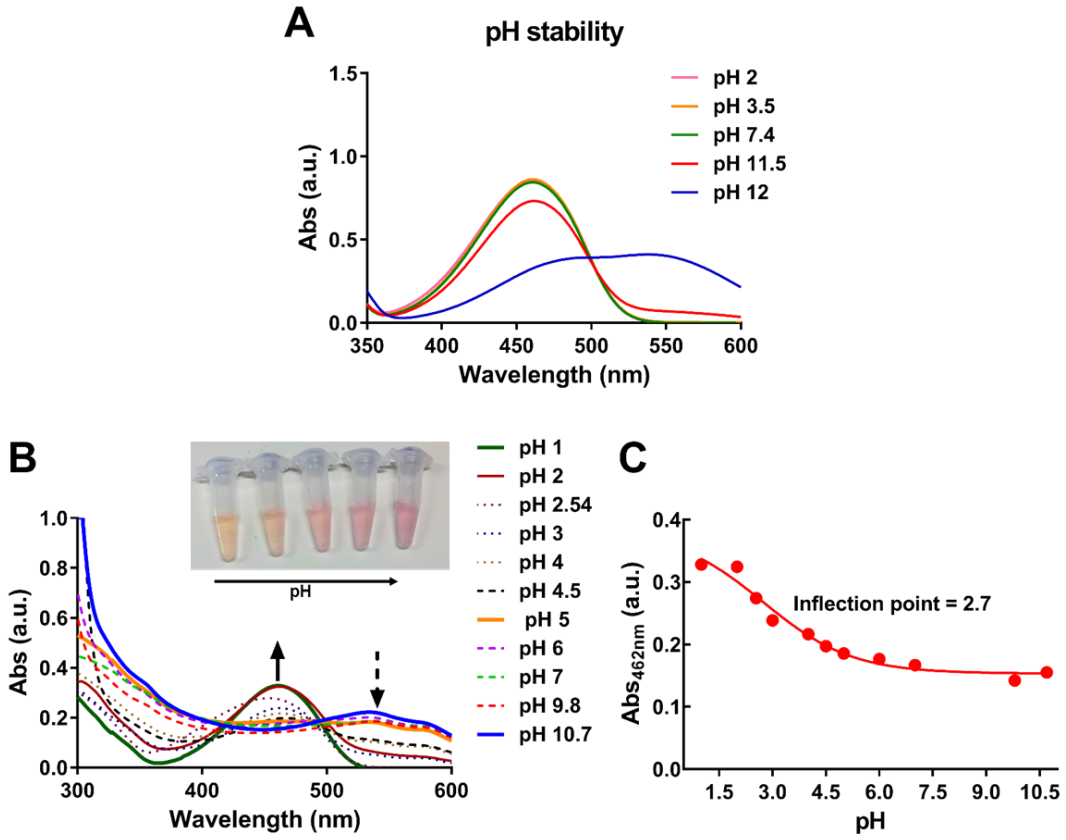

Figure 3.8. TPZ and Cu(TPZ)$_2$ stability in different pH conditions and dissociation mechanistic. UV/Vis spectra at varying pH values of A) TPZ (pH 2, 3.8, 7.4, 11.5 and 12.5); B) Cu(TPZ)$_2$ (pH range from 1-10.7). Inset shows colour change of Cu(TPZ)$_2$ from dark red to yellow (free TPZ) with decreasing pH; and C) absorbance spectra of Cu(TPZ)$_2$ at 462 nm, plotted against pH in water. The calculated inflection point for the fitted sigmoidal curve was 2.7. Appropriate blank solvents were used for baseline corrections.

A single sigmoidal curve was fitted to the absorbance at 462 nm and plotted against pH, providing a pK_a value of 2.7 (**Figure 3.8C**), in agreement with a previous study involving TPZ [385]. The analysis of the pH-dependent behaviour of copper-complexes becomes relevant due to acidified enviroment of tumour cells. Partial dissociation was already observed at pH<5 (**Figure 3.8C, orange solid line**), where a significant increase of free TPZ was present at pH<3 (**Figure 3.8C, dashed blue line**). This can render promising applications for tumour therapy and marked stability of $Cu(TPZ)_2$. This data agreed well with a study by Kheirolomoom *et al.* [448], where copper-Dox complexes exhibited good stability under a range of pH conditions. Dissociation was low at physiological pH and rapid at pH below 5. Likewise, a water-soluble HAP (KS119W) [449], also displayed marked pH stability, which played a pivotal role on it's hypoxia selectivity. Within the tumours pH range (pH 5.5 -7) compound stability is important for hypoxia effectivness *in vivo* and to minimize some side-effects, as explained below.

TPZ has been shown to possess a pH-dependent cytotoxicity [450], where the slightly acidic tumour microenviornment (pH 6.0) dramatically increased its aerobic cytotoxicity, thus contributing to the observed clinical side-effects (muscle cramping, peripheral neuropathy, and GI symptoms) [99,100]. These studies proved that this pH stability contributed to minimize systemic toxicity, enhance complex bioavailibility in tumours and increase hypoxia selectivity. The results obtained here indicated that $Cu(TPZ)_2$ showed overall good stability witihin different conditons. Aside from their pH-dependent stability, the reductive hypoxic environment determines the dissociation rate of metal-complexes. Previous reports have showed that copper trans-chelation can occur with serum albumin [448], but also thiol-rich molecules (glutathione, cysteine and ascorbate), which are capable of reducing these complexes intracellularly [385]. Albumin or amino-acid binding can displace copper from these complexes, therefore accelerating dissociation and compound activity. Furthermore, previous data [148] showed that TPZ can compete with glutathione for copper, but not EDTA, which can be important for $Cu(TPZ)_2$ stability in experimental and biological conditions. Together these findings are important from a biological point of view, suggesting that $Cu(TPZ)_2$ may be dissociated *via* a pH-dependent mechanism, thiol-mediated reduction or albumin trans-chelation.

3.2.3.2. Fluorescence excitation and emission profile

In this section, the fluorescence properties of the developed complex were investigated. Aside from its well-defined UV/Vis spectra, the presence of a phenyl group in the structure of TPZ, may give the compound fluorescence properties. Previous reports have described the fluorescence efficiency of TPZ [436,437]. Laser flash photolysis indicated that the excited state for TPZ was not an efficient process, resulting in a low quantum yield (0.002 in water) and very short fluorescence life-time (98.5 ± 2 ps) in water [436]. Further analysis revealed the difficulty in detecting the triplet state of this compound and no phosphorescence was observed upon excitation [437]. They observed that the S1 state of TPZ chould readily cyclize to from an oxaziridine, which resulted in a low

fluorescence quantum yield and a short fluorescence lifetime. In line with these findings, it was important to analyse the fluorescence efficiency of TPZ upon coordination to copper.

Herein, the complexation of TPZ to copper(II) resulted in a similar fluorescence profile, with no significant changes in the emission intensity in DMSO (**Figure 3.9A,** TPZ/$Cu(TPZ)_2$: $\lambda_{exc}/\lambda_{em}$ 490/600nm). Although the Dimroth solvatochromic correlation with the emission spectra was considered poor, compared to that of the absorbance spectra [436], it is still noticeable that solvent solute transfer influences the excitation and emission profile. This was particularly relevant for TPZ, where the excitation and emission profiles were λ_{exc} 490 nm/λ_{em} 600 nm in DMSO **(Figure 3.9A, solid line)** and λ_{exc} 450 nm/λ_{em} 570 nm in HBS **(Figure 3.9B, solid line)**.

Copper is a strong fluorescence quencher, but attempts to develop efficient copper-based fluorescent probes have been successful, as well as their application for bioimaging purposes [451,452]. Interestingly, the data obtained here clearly showed that TPZ fluorescence was not decreased upon complexation, and no copper-induced quenching was observed. Also, a marked increase in fluorescence intensity was observed in HBS for the complex (**Figure 3.9B, dashed line**), compared to TPZ (**Figure 3.9B, solid line**), accompanied by a *ca.* 50 nm bathocromatic shift between the fluorescence excitation/emission spectra of TPZ and $Cu(TPZ)_2$. This effect was possibly due to a shift in energy states upon coordination to the metal centre. This agrees well with previous proposals that argued on metal binding altering the fluorescence intensity (intensiometric sensors), the wavelength of excitation or emission (ratiometric sensors), or the fluorescence lifetime of the free ligand [453]. This enhancement or changes in fluorescence lifetime can result from metal-induced changes in the geometry or flexibility of the ligand [454], as proposed in **figure 3.1**. The calculation of the quantum yield may provide quantitative data on the fluorescent induction of $Cu(TPZ)_2$.

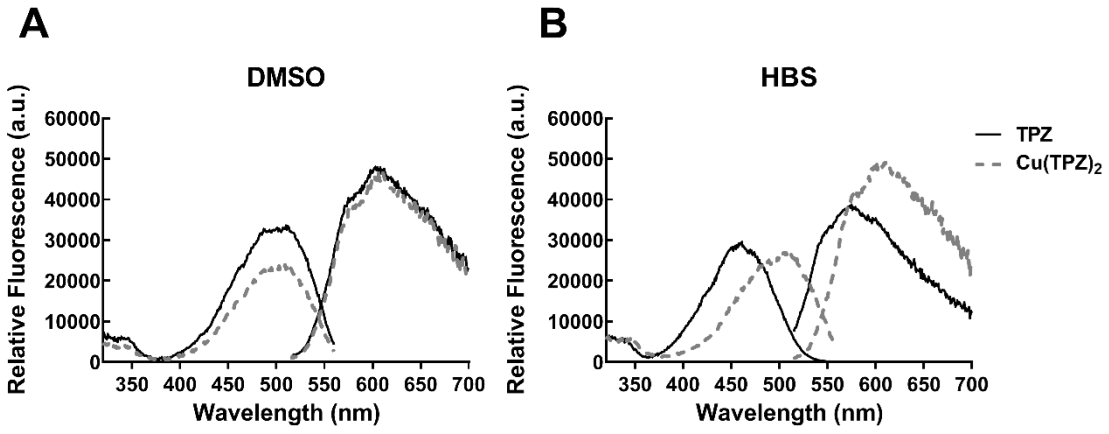

Figure 3.9. Excitation and emission spectra of TPZ and $Cu(TPZ)_2$. A) Fluorescent spectra of both TPZ and $Cu(TPZ)_2$ diluted in DMSO (TPZ/$Cu(TPZ)_2$: $\lambda_{exc}/\lambda_{em}$ 490/600nm) and B) HBS (TPZ: $\lambda_{exc}/\lambda_{em}$ 450/570nm, $Cu(TPZ)_2$: $\lambda_{exc}/\lambda_{em}$ 500/600nm). Appropriate blank solvents were used for baseline corrections and spectrums were plotted from mean of triplicate samples.

3.2.3.2.1. Effect of buffer and pH, determined by fluorescent analysis

In order to fully establish the fluorescent properties of TPZ and Cu(TPZ)$_2$, their stability in different aqueous buffers and pH conditions was assessed. Like the UV-Vis spectra, TPZ maintained its fluorescence intensity in different buffers (**Figure 3.10A**) and showed slightly higher emission intensities in solutions with higher ionic strength. TPZ fluorescence was also maintained at different pH values, except at pH (12.5). Here, the emission decreased in intensity, due to amine deprotonation, in accordance to its UV/Vis spectra (**Figure 3.10B**). The results indicated good compound stability for TPZ in different experimental conditions.

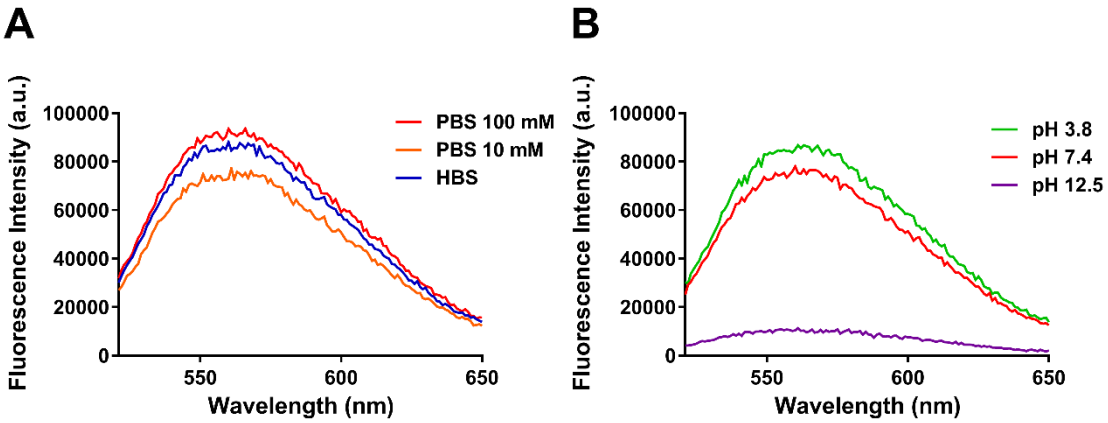

Figure 3.10. Fluorescent characterisation and stability of TPZ. Fluorescence spectrum of A) TPZ diluted in PBS (10mM, pH 7.4), PBS (100 mM, pH 7.4) and HBS (20mM HEPES, 150mM NaCl, pH 7.4); and B) TPZ further diluted in aqueous buffer at pH 3.8, pH 7.4 and pH 12.5. Appropriate blank solvents were used for baseline corrections and spectrums were plotted as mean of triplicate samples**.**

Next, the fluorescent intensity of TPZ and Cu(TPZ)$_2$ at varying concentrations was determined. As shown in **Figure 3.11A, left panel**, the fluorescent intensity is linear for TPZ at all concentrations tested in DMSO, but initiated a plateau phase at 40 µM for Cu(TPZ)$_2$. This can be attributed to stacking or aggregation of the complex, with increasing concentrations, resulting in fluorescence quenching; or simple saturation of emitted photons which can cause reabsorption. Similar results were observed when the drugs were solubilized in HBS (**Figure 3.11B, left panel**), but due to the low solubility of the complex in aqueous buffers (formation of small precipitates), a plateau phase is observed from 15 µM. Additionally, linear plots were generated for both TPZ and Cu(TPZ)$_2$. This method was applied for quantification of the intracellular uptake of both TPZ and Cu(TPZ)$_2$ *in vitro* (**chapter 5).** DMSO was used as a solvent to guarantee solubility even at higher concentrations, and the standard curves generated here used to calculate the amount of internalized pro-drugs, normalized to an initial feed-solution. The data obtained here showed enhancement in emission intensity for Cu(TPZ)$_2$ in DMSO (**Figure 3.11A, right panel**), that was intensified in HBS (**Figure 3.11B, right panel**).

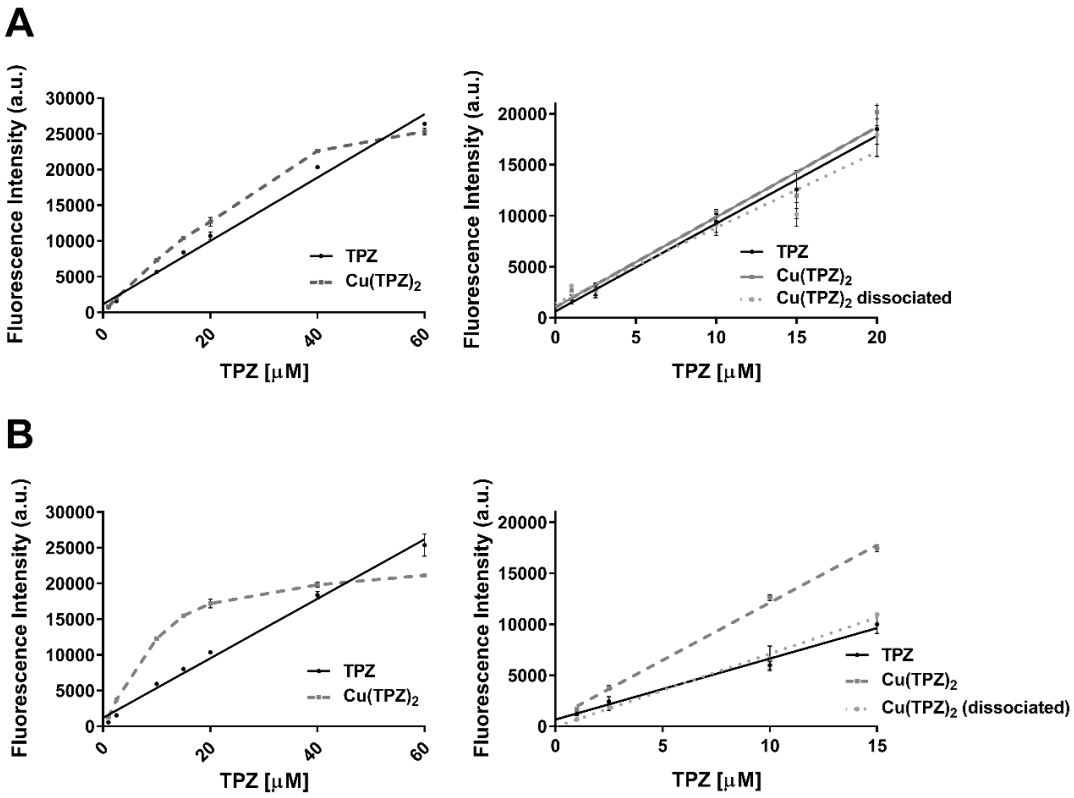

Figure 3.11. Fluorescent intensity and linear regression of TPZ and Cu(TPZ)$_2$ at varying concentrations. Fluorescent intensity of TPZ and Cu(TPZ)$_2$ at different concentrations in A) DMSO (left panel) and the linear range determined to generate a fitted standard curve (right panel); and B) HBS (left panel) and the fitted standard curve (right panel). pH mediated dissociation of the complex was used as an internal standard for fluorescence comparison. Appropriate blank solvents were used for baseline corrections of all spectra's and data was expressed as mean ± SD of triplicate samples.

More interestingly, after pH-mediated dissociation of the complex (pH=2), a strong decrease in the emission intensity was observed in HBS. This decrease in fluorescence overlapped with the emission intensity obtained for TPZ, strongly indicating that fluorescent enhancement is metal-induced and is markedly decreased upon ligand dissociation. These results agree with those described before, suggesting that copper (II) stabilizes the fluorescence intensity of TPZ, thus providing an interesting bioimaging tool that was exploited in **chapter 5.**

3.2.4. Purification and quantification by HPLC

Although previously published data describing the separation of TPZ and its metabolites reported a good separation of these compounds on hydrophobic C_{18} based columns [440], this method proved unreliable in this study. The elution of TPZ was concurrent with the solvent injection peak, hampering an adequate peak integration and compound quantification. Given this, a phenyl-hexyl column, which maximized the interaction with the aromatic rings of TPZ, yielded good separation with an isocratic gradient of 22% methanol in water and a retention time of *ca.* 5.6 min (**Figure 3.12A**). The wavelength was set at a detection of 270 nm, as this resulted in the highest absorbance intensity (**Figure 3.7**) and was in agreement with previously published data [398].

To note, it was also found that the use of acetonitrile did contribute to better peak resolution, but with significantly lower retention time, therefore methanol was used for all subsequent HPLC experiments.

After complexation, different protocols with both C_{18} and phenyl-hexyl based columns were attempted but all failed to show adequate elution of the complex. This could be due to a strong interaction of the lipophilic complex with the solid phase or co-elution with the injection peak due to limited solubility in methanol and pre-dissolution in DMSO. Taking into consideration the dissociation of the complex in acidic environments, HPLC samples for complex quantitation were prepared in methanol at pH 2 and sonicated. HPLC analysis therefore involved the quantification of TPZ in both non-complexed and complexed form. After colour change from dark red [$(Cu(TPZ)_2$] to yellow (free TPZ), dissociation was confirmed and the protocol was adapted for a direct quantification of TPZ. The calculations were adapted, using the theoretical 2:1 stoichiometry of preparation, previously confirmed by MS. Furthermore, standard curves were generated for both compounds by plotting the equivalent TPZ content in both free and complexed form (TPZ, $Y = 30.4x - 42.06$, $R^2=0.9957$ and $Cu(TPZ)_2$, $Y = 58.33x + 55.15$, $R^2=0.9996$). The overlapped linear regression (TPZ, $Y = 30.4x - 42.06$; $R^2=0.9957$ and $Cu(TPZ)_2$, $Y = 30.73x + 18.74$; $R^2=0.9996$) confirmed the 2:1 molar ratio and proved the feasibility of this method for $Cu(TPZ)_2$ quantification, using TPZ content (**Figure 3.12B**).

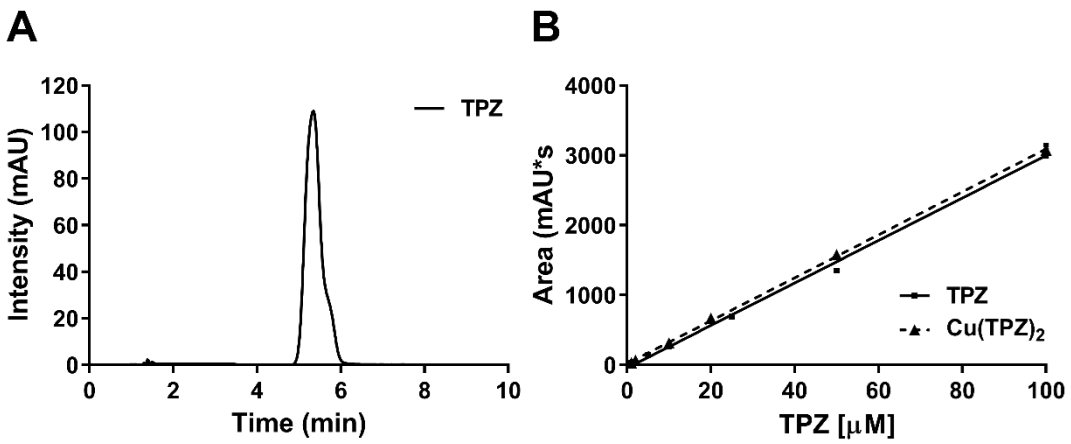

Figure 3.12. HPLC analysis of TPZ and $Cu(TPZ)_2$ after dissociation. A) HPLC chromatogram of TPZ. The chromatographic conditions were 22% methanol in water at a flow rate of 1mL/min with a detection wavelength of 270 nm. TPZ was eluted at *ca*.5.6 min; B) HPLC standard curve obtained for TPZ alone and upon dissociation of $Cu(TPZ)_2$, with comparable TPZ content. The results confirm the 2:1 molar ratio used in preparation of complexed TPZ and further validated the dissociation method for complex quantification. The results were expressed as mean ± SD for triplicate samples of two independent experiments (n=2). Where error bars are invisible, the error is smaller than the symbol used.

3.2.5. Solubility, simulation of log P and analysis of reduction potential

Within this chapter, elemental and spectroscopic data was obtained, which allowed validation of the empirical formula, weight and pH behaviour of TPZ, as a free ligand and copper-complex. Moreover, when considering hypoxia applications of this metal-complex it is important to consider other physicochemical properties such as solubility, lipophilicity and redox chemistry. The main properties of both TPZ and $Cu(TPZ)_2$ are summarised in **table 3.2**.

The solubility of both compounds was evaluated throughout the extensive analytical studies. TPZ was soluble in polar solvents, such as DMSO, methanol and ethanol; and moderately soluble in aqueous buffers (up to 5.6 mM).

Table 3.2. Physicochemical properties of TPZ and $Cu(TPZ)_2$.

Property	TPZ	$Cu(TPZ)_2$
MW (g/mol)	179.15	417.83
pKa	5.6 [a]	2.7
Log P	-0.31[a]	2.88[*]
E_{red} (1) (V)[**]	-0.65[a]	-0.75[b]

[a]from reference [147]
[b]from reference [385]
***predicted using Chemdraw 3D 15.0**
****reference electrode Ag/AgCl, converted where necessary**

On the other hand, $Cu(TPZ)_2$ complexes were soluble in DMSO (up to *ca.* 2.5 mM), but only partially soluble in other polar solvents, such as ethanol, methanol and poorly soluble in aqueous buffers. Also, the complexes were completely insoluble in nonpolar organic solvents, such as octanol, which proved difficult to conduct lipophilicity studies. Therefore, determination of octanol/water partition coefficients were performed, but without success. The use of alternative delivery strategies, such as liposomes, may help improve on solubility of this complex (**chapter 4**).

It is well acknowledged that the increased lipophilicity of metal-complexes plays a role on membrane permeability and, consequently, cellular uptake efficiency [181,455,456]. Log P is an established parameter to determine the lipophilicity of a given compound. This value has already been measured for TPZ (log P = -0.31, **Table 3.2**), consistent with the amphiphilic nature of the drug. Given the difficulty encountered in determining the log P value for $Cu(TPZ)_2$, ChemOffice (a user-friendly software) was used to predict this value, using the fragmental method based on Hansch and Leo [399]. This methodology relies on algorithms built from full compounds, or fragments, rather than per atom. When using whole fragments, electronic and intramolecular interactions may be better modeled (which is essential for metal-complexes and compounds with complex aromaticity), and after application of correction factors a better prediction may be obtained.

Previous reports have validated that using such *in silico* screening methods can provide a reliable preliminary Log P indicator and the fragment method has indeed generated the lowest error and better correlation with experimental data [457,458]. TPZ was used as a control and the Log P value obtained was -0.58, which is in line with that reported previously [147]. After running the simulation, a Log P of 2.88 was obtained for the cupric-complex, evidencing its increased lipophilic nature. This result is in line with previous reports [147,447], which have shown a good correlation between the enhanced lipophilic nature of a cupric complex, after coordination of copper (II) to the N_3 position of the ligand. Additionally, removal of this H-bond donor 3-NH_2 group has also shown to be a major determinant in improving the diffusion rate of TPZ analogues in tumour spheroid models [73]. The results obtained herein, indicated that $Cu(TPZ)_2$ may improve on TPZ's current biological drawbacks, enhancing its cellular uptake and tissue diffusion. Nevertheless, studies using reversed-phase thin-layer chromatography (TLC) would provide an experimental value of Log P [169] and should be considered in future experiments.

The inter-relationship between structure, lipophilicity and redox potential of copper (II) complexes is a strong predictor of hypoxia selectivity and *in vitro* activity [182,186,189,421,459]. As discussed, the lipophilic character is presumably necessary for improved cellular uptake, but the nature of the redox chemistry reaction has a strong correlation with the hypoxia potency. Together with the results discussed here, these reports prompted a detailed summary and discussion on the one-electron reduction potentials, determined by cyclic voltammetry, for TPZ and $Cu(TPZ)_2$ (**Table 3.2**). The measurements indicated a significantly lower $E°(1)$ reductive potential for $Cu(TPZ)_2$ (-0.75 V) [385], compared to the free ligand (-0.65 V) [147]. According to J. Dearling *et al.* [181,455], studies with [Cu(ATSM)] have suggested a Cu(II/I) redox potential more negative than -0.57 V *vs.* Ag/AgCl, for adequate hypoxia selectivity. On the basis of this notion, it would be expected that $Cu(TPZ)_2$ would show greater hypoxia selectivity, compared to its ligand TPZ. It is noteworthy that this trend can support the rational design of hypoxia selective complexes, but shifting the redox potential to much more negative values, may also hinder the hypoxic cells capacity to reduce these compounds [151,176,456,460]. The chemical properties discussed herein contributed to a better understanding of $Cu(TPZ)_2$'s biological activity in **chapter 5**.

3.2.6. Morphology and size measurement of $Cu(TPZ)_2$ by TEM

The morphology and size of $Cu(TPZ)_2$ complexes were analysed by TEM imaging (**Figure 3.13**). The sample morphology was concentration dependent, constituting large smooth needle like shape particles (300-400 nm in length) at high concentrations (2 mM) and small spherical nanoparticles (3-4 nm in diameter) at lower concentrations (20 µM). PDI analysis could be a complementary experiment to determine the size of these particles.

Cu(II) complexes have shown different structures in solid and solution state [169]. Under the dehydrated TEM conditions, a solid dimeric form of $Cu(TPZ)_2$ could be present, which concurrently forms intermolecular bonding with neighbouring molecules, *via* the uncoordinated 1-*N*-oxide group.

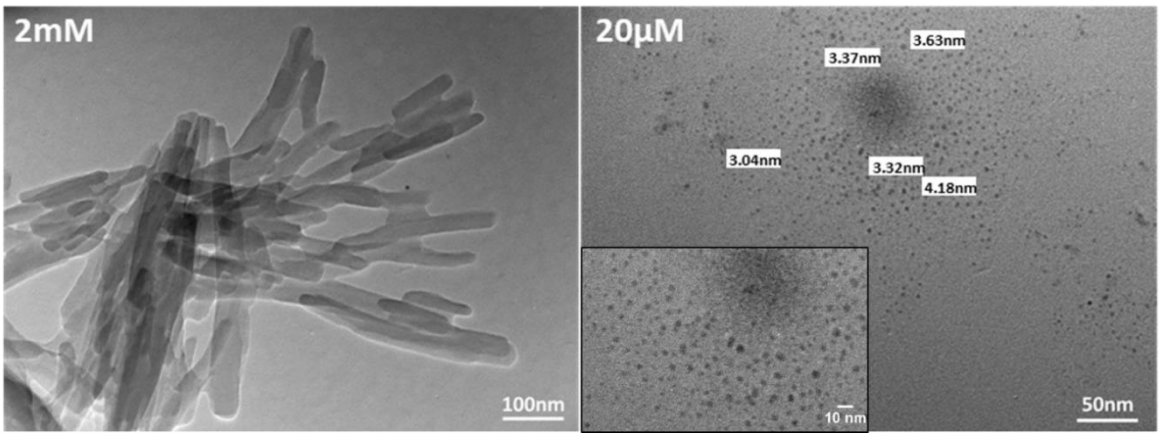

Figure 3.13. Morphology and size analysis by TEM. Images represent Cu(TPZ)$_2$ at high (2mM) and low (20µM) concentrations, depicting concentration dependent self-aggregation of the complex. The inset shows an enlarged high-resolution image of an area of small complex particles (3-4 nm in size).

This can lead to the formation of multi-copper crystalline structures, possibly resulting from π→π stacking and van der Waals interaction between molecules that resemble the large needle structures [461]. These higher concentrations (> 2 mM) are not therapeutically relevant and therefore the large structures do not compromise further usage of this compound for hypoxia therapy. X-ray diffraction applied to these crystals can help elucidate the structure and morphology of Cu(TPZ)$_2$. Furthermore, the small NP shaped particles obtained at lower concentrations are therapeutically relevant and become important during liposomal encapsulation. This will be discussed in more detail in **chapters 4 and 5.**

3.3. Summary and conclusions

Metal-ion complexes have been widely exploited for anti-cancer therapy [161,167,171,179]. Particular attention has been drawn to copper (II) complexes with coordination to pyridine-*N*-oxides (similar to TPZ), and their ability to induce DNA damage [156,167,179]. Interestingly, due to the unique biocompatible reductive properties of copper (II), this ion has also been described as an important metal centre to develop novel hypoxic selective compounds. As a result, Lin *et al.*[148], were the first to propose the complexation of TPZ to copper (II), and other copper(II)-*N*-oxides have shown ability to maintain their potent and selective activity in hypoxia [168,169]. Although the latter studies contained preliminary *in vitro* data, establishing the potency of this complex, it was necessary to validate copper-TPZ complexation and understand how this metal-complex could modulate relevant properties such as fluorescence, lipophilicity, solubility, redox-potential and overall stability.

In this chapter, a simple and inexpensive method was used to synthesise $Cu(TPZ)_2$ complexes, and different analytical techniques were used for characterisation. Overall, the results obtained proposed that complexation can induce cellular uptake, given the higher lipophilic nature of the complex, and potentiate hypoxia selectivity by hindering metabolic reduction under normoxic conditions. This work led to the development and characterisation of a small, planar, lipophilic complex with encouraging fluorescent properties that can possibly improve on TPZ's cellular uptake, diffusion and hypoxia selectivity.

The following conclusions were drawn from this chapter:

- $Cu(TPZ)_2$ complexes presented a 2:1 stoichiometry, where TPZ is coordinated through the $3NH_2$ and 4NO positions
- UV/Vis spectral analysis confirmed complexation of TPZ and established the stability of this drug and $Cu(TPZ)_2$ over a wide range of solvents, aqueous buffers and different pH conditions
- $Cu(TPZ)_2$ showed pH-dependent dissociation (pKa 2.7), which can confer stability in the acidic hypoxic tumour microenvironment
- $Cu(TPZ)_2$ exhibited intrinsic fluorescent properties which can be exploited in cellular uptake and localization assays
- Upon complexation the lipophilicity of TPZ was significantly increased (Log P 2.88), in addition to the one electron redox-potential, which was substantially shifted to a more electronegative value [E(1) -0.75 V]. These properties may well determine hypoxia selectivity and provide substantial improvement on therapeutic outcome.

Chapter 4

Development and characterisation of $Cu(TPZ)_2$-loaded liposomes

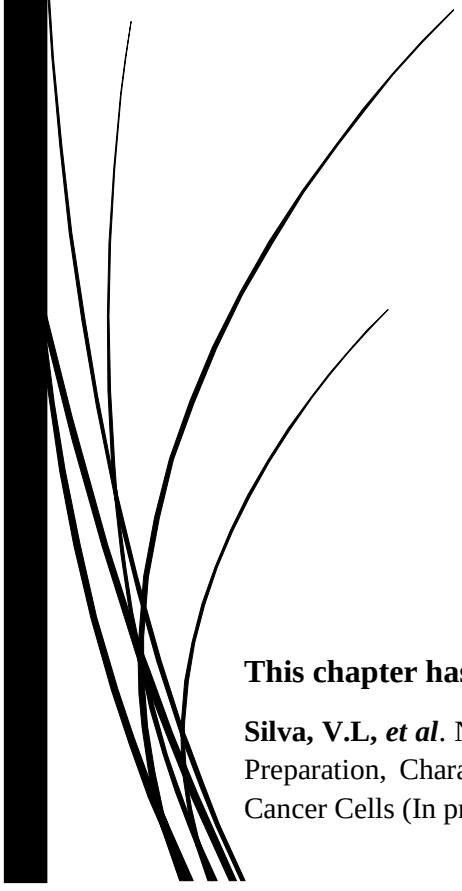

This chapter has been included in the following publication:

Silva, V.L*, et al*. Novel Hypoxia Selective Cupric-Tirapazamine Liposomes: Preparation, Characterisation and *In vitro* Activity in 2D and 3D Prostate Cancer Cells (In preparation).

4.1. Overview

TPZ has been thoroughly investigated, due to its potent selective activity under hypoxia [99,100]. However, both pre-clinical and clinical studies have shown that TPZ's activity is limited by poor extravascular diffusion [376,462], short blood half-life [73,129], instability and rapid metabolism [107], while diffusing the tumour tissue; compromising its translational potential [72,136,138]. The development of novel drug carriers for TPZ [26], may well improve on its current biological drawbacks and potentiate its efficacy.

Nano vehicles have offered significant improvement over conventional hypoxia therapies [26], but these systems have mainly focused on synthesising hypoxia responsive moieties [64,361], enhancing the effect of classical chemotherapeutics (*e.g.* Dox) [463] or used in combination with PDT [382,464]. Few strategies have focused on potentiating the efficacy of existing HAPs [372-375,465], including TPZ. In 2012, Wu *et al.* [376] were the first to attempt the use of a carrier for TPZ, creating targeted delivery with transferrin (Tf-G-TPZ) conjugation and co-administered cisplatin. *In vitro* studies revealed substantially higher uptake and selective hypoxia cytotoxicity, providing important proof that TPZ mediated conjugation or encapsulation with NPs can markedly improve on its PK and PD. More recently, innovative NPs, with either conjugation [376,377] or encapsulation strategies [378-380,382,383], have been synthesised to potentiate the efficacy of TPZ. These studies mainly highlighted the synergistic effect when using TPZ as a pre-sensitizer for radio- and chemotherapy [376,377] or by potentiating its effect under hypoxic conditions, after exposure to PDT [378-380,382,383]. Although these systems offered significant therapeutic improvement over TPZ alone, they all report rather low loading capacity of TPZ, with the best results, to date, obtained using Tf conjugation (*ca.* 300 μM TPZ content) [376]. In addition, only one study has shown the successful loading of TPZ into liposomes, but with a low EE (2.4%) [384]. In order to increase TPZ liposomal loading and potentiate its delivery and therapeutic activity, different loading strategies and lipid formulations were evaluated in this work.

This chapter presents the development of three liposomal formulations that differed in the length of the phospholipid and saturation of their carbon chain, which were initially characterised, prior to drug loading. Furthermore, TPZ was loaded in these liposomes, using different passive and remote loading methods. An extensive discussion on the preparation and characterisation of these TPZ-loaded liposomes, as well as their loading efficiency, is presented. Unfortunately, the methods exploited, failed to show any relevant drug loading or resulted in low encapsulation ($\leq 6\%$) which was not reproducible. Experiments regarding the encapsulation of TPZ alone were abandoned and alternative successful strategies were employed.

Taking into consideration the TPZ-cupric complexes developed in **chapter 3**, it was proposed that TPZ encapsulation *via* copper-complexation could provide an alternative modality for liposomal loading. Therefore, the rest of this chapter focuses on discussing the preparation and characterisation (hydrodynamic size, zeta-potential and stability) of these liposomes, before and after drug loading. The distinct remote loading methods that successfully resulted in $Cu(TPZ)_2$ encapsulation, were analysed, by comparison of different lipid formulations and also the effect of liposome size, pH, temperature, and incubation time on EE. This work led to the development of a simple remote loading method (in HBS, pH 7.4) that provided high EE with good drug retention. TEM was also used to analyse liposome morphology, validate $Cu(TPZ)_2$ encapsulation and gain preliminary insight on the distribution of $Cu(TPZ)_2$, within the liposomal vesicles. To finalize, the *in vitro* release kinetics of the optimized formulations was studied, as well as their long-term stability; which can provide supportive evidence on their potential biological activity. In summary, this chapter reports important findings that can draw a bridge between **chapters 3** and **5**, prompting the use of $Cu(TPZ)_2$ complexes to increase TPZ liposomal loading and their application as novel nanocarriers for hypoxia-targeted therapy.

4.2. Results and discussion

In this project, three different liposomal formulations were developed for applied hypoxia PCa therapy. DOPC (18:1 - Δ9 Cis, T_m = -20°C), DPPC (16:0, T_m = 41°C) and DSPC (18:0, T_m = 55°C) were the main phospholipid constituents of the liposomal vesicles. These lipids differ in the length and degree of saturation of their hydrocarbon chain, which in turn accounts for significantly different phase transition temperatures. Properties such as length of the hydrocarbon chain, degree of saturation and temperature greatly influence T_m and define the overall fluidity of the bilayer [249]. Generally, unsaturated lipids with low T_m (*e.g.* DOPC) provide more permeable and fluid bilayers, while saturated lipids (*e.g.* DSPC) with long acyl chains and high T_m, form more rigid, compact and impermeable structures [253,254,466]. Additionally, cholesterol was added at an equimolar to phospholipid concentration (*ca.* 33 % molar ratio, total lipid), due to its key role in membrane organization, dynamics and function, as well as its capacity to minimize destabilization from plasma lipoproteins [467]. Chol reduces the rotational freedom of the hydrocarbon chains and acts as a 'buffer' in the lipid bilayer, by modulating the T_m [256,257]. The inclusion of Chol has shown to increase fluidity of bilayers at low temperatures, while decreasing fluidity at high temperatures (**Figure 4.1**), and is therefore a determinant factor on membrane stability and permeability [249].

Moreover, to obtain sterically stabilized liposomes, DSPE-PEG$_{2000}$ (10 % molar ratio) was also included. The addition of PEG (2000 Da), reduces the interaction with serum proteins, minimizing macrophage clearance, prolonging plasma half-life [467]. Both PEG and Chol are essential for increasing carrier stability and significantly prolonging circulation time *in vivo*.

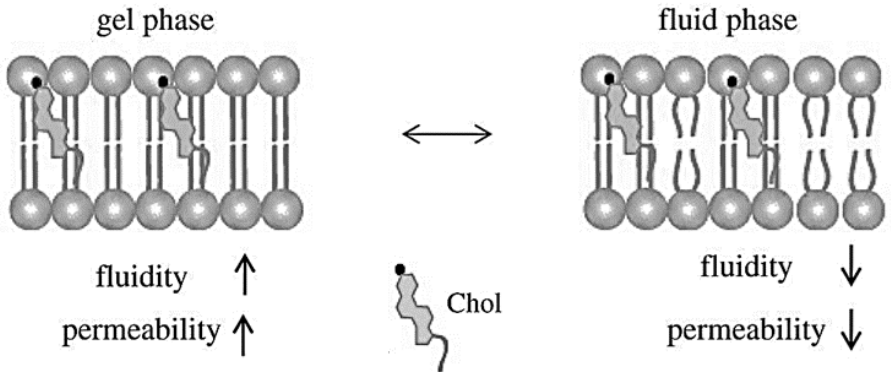

Figure 4.1. Effect of Chol on phospholipid bilayer permeability. Chol's steroid rings are dense, allowing this molecule to pack well between the phospholipid fatty acid chains. At low temperatures (below T_m), Chol increases the distance between the tightly packed phospholipids in the gel phase, increasing lipid mobility and consequently fluidity and permeability. In contrast, at temperatures above T_m (liquid/fluid phase), Chol decreases the surrounding lipid mobility and enhances rigidity, decreasing fluidity and permeability of the lipid bilayer. Chol acts as a membrane 'buffer' by modulating T_m at different temperatures. Adapted from [249].

In this thesis, different lipid compositions were tested in order to assess the best liposomal formulations to achieve maximum encapsulation [255]. The inclusion of appropriate ratios of Chol and PEG were essential to undermine the *in vitro* application in **chapters 5 and 6**, or the future translation to *in vivo* models.

4.2.1. Preparation and characterisation of empty liposomes

Empty liposomes, DOPC:Chol:DSPE-PEG_{2000} (5mM phospholipid, 95:50:5 molar ratio), DPPC:Chol:DSPE-PEG_{2000} (5mM phospholipid, 95:50:5 molar ratio) and DSPC:Chol:DSPE-PEG_{2000} (5mM phospholipid, 95:50:5 molar ratio) were initially prepared using the well-established lipid-film hydration method (TFH), as outlined in **chapter 2** (**section 2.4.1.1.1**). Briefly, lipid mixtures were evaporated under vacuum, subsequently hydrated in HBS buffer, pH 7.4, to form large lipid vesicles and downsized using the extrusion method [275,276]. This method relies on forcing the passage of liposomes, under pressure, through filters with defined pore sizes, to obtain liposomes of desired uniform size (PDI below 0.2). The liposome formulations were then allowed to anneal, stored overnight at 4°C and were purified using SEC.

4.2.1.1. Hydrodynamic size by DLS

DLS was used to measure the hydrodynamic size (*Z*-Ave) of the prepared empty liposomes. DOPC:Chol:DSPE-PEG_{2000} liposomes presented an average size of 129.6 ± 2.33 nm and polydispersity (PDI) of 0.053 ± 0.04 (**Figure 4.2A**). These results confirmed the formation of monodisperse vesicles, with narrow size distribution. Similar results were obtained for DPPC:Chol:DSPE-PEG_{2000} liposomes (**Figure 4.2B**), with slightly increased hydrodynamic size (*Z*-Ave, 139.4 ± 3.25 nm and PDI, 0.070 ± 0.014). In contrast, DSPC:Chol:DSPE-PEG_{2000} liposomes were prepared in a 250 mL round bottom flask to ensure the formation of a thin uniform lipid film. This method led to the formation of small liposomes with exceptional homogeneity (*Z*-Ave, 139.9 ± 2.92, PDI, 0.029 ± 0.004) (**Figure 4.2C**).

The mean hydrodynamic diameter of liposomes is a determinant factor, when considering the *in vitro* application, *in vivo* circulation and passive tumour targeting *via* EPR effect. Overall, different studies have shown that very large (>200 nm) and very small (<50 nm) liposomes are either rapidly cleared by macrophages or show elevated and rapid accumulation in the liver, respectively [278]. On the other hand, liposomes with sizes ranging *ca.* 100 nm [247] are considered ideal for prolonged circulation, penetration and passive accumulation into the intratumoural space (EPR effect) [277]. Together, this evidence supported the notion that the liposomes developed herein, showed excellent size range for biological applications.

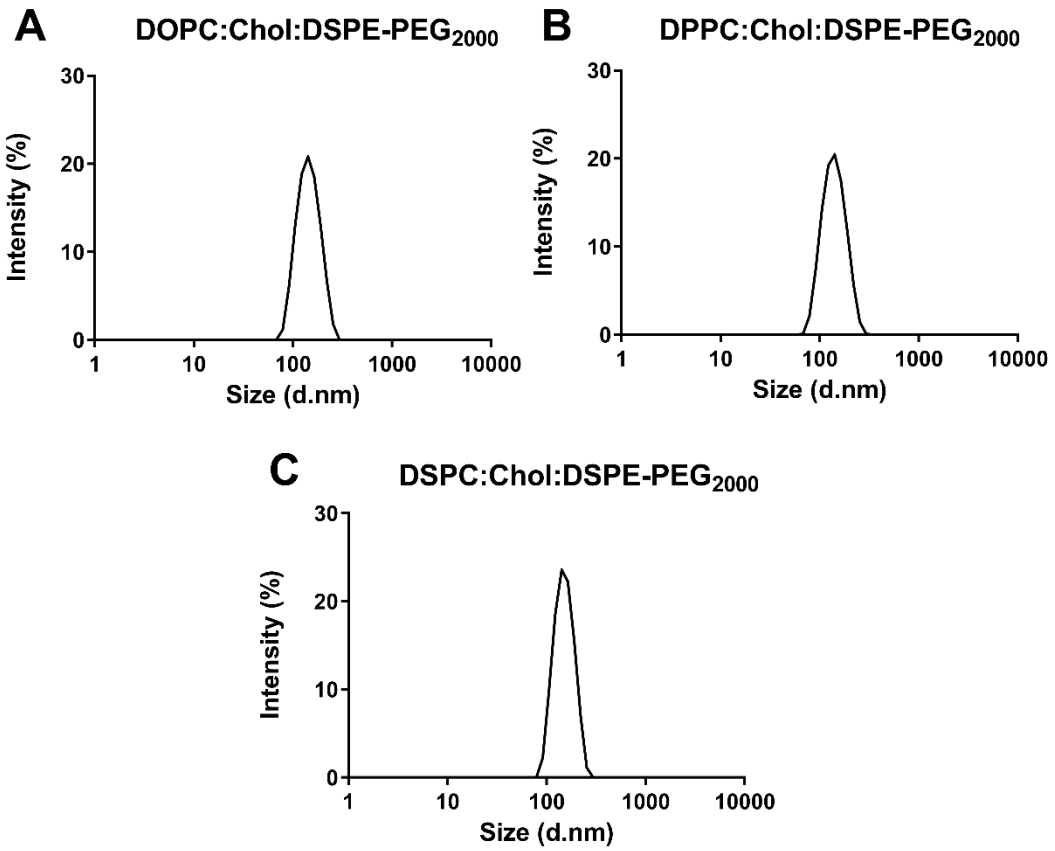

Figure 4.2. DLS spectra of small unilamellar liposomes prepared by lipid film hydration after purification. A) DOPC:Chol:DSPE-PEG$_{2000}$ empty liposomes, prepared in a 25 mL round bottom flask at 45°C (*Z*-Ave, 129.6 ± 2.33 nm; PDI, 0.053 ± 0.04); B) DPPC:Chol:DSPE-PEG$_{2000}$ empty liposomes, prepared in a 25 mL round bottom flask at 60°C (*Z*-Ave, 139.4 ± 3.25 nm; PDI, 0.070 ± 0.014); and C) DSPC:Chol:DSPE-PEG$_{2000}$ empty liposomes, prepared in a 250 mL round bottom flask at 60°C (*Z*-Ave, 139.9 ± 2.92, PDI, 0.029 ± 0.004). Data was expressed as mean (nm) ± SD (n≥3), for a total of three measurements per sample, at 25°C.

4.2.1.2. Influence of extrusion cycles on hydrodynamic size

In line with the previous results, it was interesting to analyse how different extrusion cycles can influence the hydrodynamic size of liposomes. This study can be fundamental to guarantee that the prepared vesicles sustain batch-to-batch reproducibility and are within the biological size window, even if drug loading causes increase in liposome size. Therefore, DOPC and DSPC liposomes were prepared and size was reduced using the following conditions: 1) 15 extrusion cycles through 200 nm polycarbonate membrane filters and 2) 11, 15 and 21 extrusion cycles through 100 nm polycarbonate filters. The final liposomal solutions were then characterised by DLS and the results are summarised in **table 4.1**. DOPC liposomes showed and average size of 136.7 ± 5.61 nm, after extrusion through 200 nm membrane filters, which decreased after subsequent extrusion through smaller sized pore membranes and increasing extrusion cycles (21x, 100 nm: 120.5 ± 13.15). On the other hand, DSPC liposomes were larger in size compared to DOPC, when extruded through 200 nm membrane filters (165.5 ± 2.4 nm), possibly due to its more rigid nature.

Table 4.1. Effect of extrusion on the average size of empty liposomes. DOPC:Chol:DSPE-PEG$_{2000}$ and DSPC:Chol:DSPE-PEG$_{2000}$ liposomes (5mM phospholipids, 95:50:5 molar ratio) were prepared in HBS (pH 7.4). The average hydrodynamic size and PDI of liposomes was determined by DLS after 15 extrusion cycles through 200 nm membranes and 11, 15 and 21-time passage through a 100 nm polycarbonate extrusion membranes). The hydrodynamic size and polydispersity (PDI) values were measured. Data was expressed as mean ± SD for triplicate samples of two independent experiments (n=2).

Formulation	Extrusion cycles (pore size, nm)	Z-Ave (nm)	PDI
DOPC:Chol:DSPE-PEG$_{2000}$	15x (200)	136.7 ± 5.61	0.080 ± 0.006
	11x (100)	133.4 ± 2.90	0.034 ± 0.015
	15x (100)	124.7 ± 13.93	0.054 ± 0.020
	21x (100)	120.5 ± 13.15	0.062 ± 0.022
DSPC:Chol:DSPE-PEG$_{2000}$	15x (200)	165.5 ± 2.40	0.040 ± 0.012
	11x (100)	133.2 ± 4.26	0.019 ± 0.015
	15x (100)	130.5 ± 0.15	0.074 ± 0.020
	21x (100)	136.4 ± 2.79	0.082 ± 0.016

In addition, a size decrease was observed, when the liposomes were further passed through 100 nm membrane filters (133.2 ± 4.26 nm), but increasing extrusion cycles, did not affect the size (136.4 ± 2.79). Moreover, the overall PDI (<0.1), confirmed excellent uniformity of the liposomal populations. These results suggested that extrusion is a quick and reliable method to modulate liposome size. However, parameters such as size and PDI are highly dependent on the lipid composition [400].

4.2.1.3. Zeta-potential measurement

In addition to the liposome hydrodynamic size, zeta-potential is an important analytical measurement for liposome surface characterisation. This value represents the potential charge between the liposome surface and the immediate surrounding environment, designated as the slipping plane [468]. It is highly dependent on factors such as temperature, pH and ionic strength and provides useful predictions on liposome stability, circulation times and cellular uptake [469]. In this work DLS was used to determine the zeta-potential of the engineered formulations (**Figure 4.3**). The measurements showed a ζ-Ave of -11.7 ± 0.69 mV for DOPC, ζ-Ave of -10.2 ± 0.84 mV for DPPC and ζ-Ave, -8.7 ± 0.47 mV for DSPC empty liposomes. The lipid-PEG containing neutral liposomes all presented zeta-potential values within the neutral range (-10mV to +10mV) [244]. These findings indicate the successful incorporation of PEG (10% molar ratio), with the formation of stable liposomes that retain enough electrostatic stabilization to prevent aggregation in solution [280].

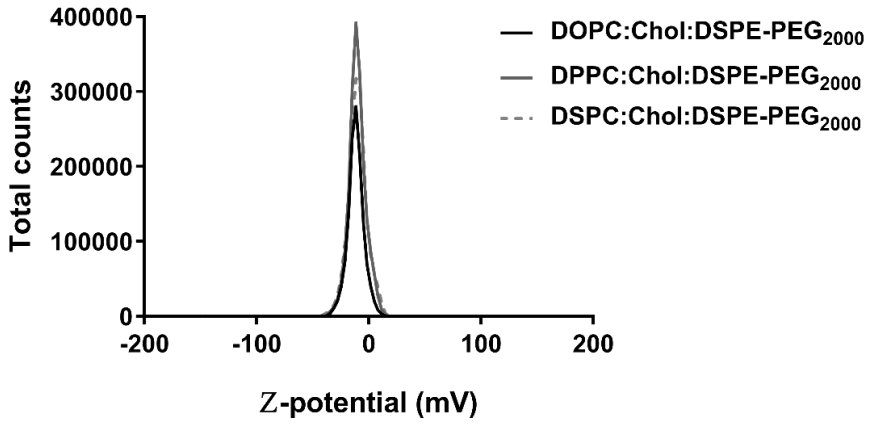

Figure 4.3. Zeta-potential for small unilamellar liposomes prepared by lipid film hydration after purification. A) DOPC:Chol:DSPE-PEG_{2000} empty liposomes, prepared in a 25 mL round bottom flask at 45°C (ζ-Ave, -11.7 ± 0.69 mV); B) DPPC:Chol:DSPE-PEG_{2000} empty liposomes, prepared in a 25 mL round bottom flask at 60°C (ζ-Ave, -10.2 ± 0.84 mV); C) DSPC:Chol:DSPE-PEG_{2000} empty liposomes, prepared in a 250 mL round bottom flask at 60°C (ζ-Ave, -8.7 ± 0.47 mV). Data was expressed as mean (mV) ± SD (n≥3), for a total of six measurements per sample, at 25°C.

4.2.1.4. Phospholipid quantification: evaluation of lipid loss during extrusion

In order to evaluate overall lipid loss (% lipid from liposomes) through extrusion, quantitation of phospholipids was carried out by the Stewart assay [408], as previously described in **section 2.4.2.4.3**.This assay is an inexpensive and moderately rapid colourimetric method, based on the ability of phospholipids to form complexes with ammonium ferrothiocyanate, where the absorbance (measured at 469 nm) is proportional to the lipid concentration in the samples. Also, it has the advantage of showing no interference from inorganic phosphate in solution [408]. In this work, standard curves for individual DOPC and DSPC lipids, as well as their lipid mixtures (incorporation of Chol and DSPE-PEG_{2000}) were generated (**Figure 4.4A**) to accurately determine the appropriate reference spectra. The results showed similar absorbance values between the free lipids (**Figure 4.4A, solid lines)**, but decreased absorbance when the lipids were quantified as a mixture (**Figure 4.4A, dashed lines)**.

This method was thus reevaluated and the preformed liposome vesicles (before extrusion) were chosen as the standard reference to guarantee a reliable phospholipid quantification. The data obtained accounted for an average lipid loss, after extrusion, of 12.29 ± 2.02 % for DOPC liposomes (**Figure 4.4B)** and 13.05 ± 0.41 % for DSPC liposomes (**Figure 4.4C)**. These values were in good agreement with the expected lipid loss during the extrusion process [470] and were further taken into consideration when calculating drug loading (**Chapter 2, section 2.4.2.3**).

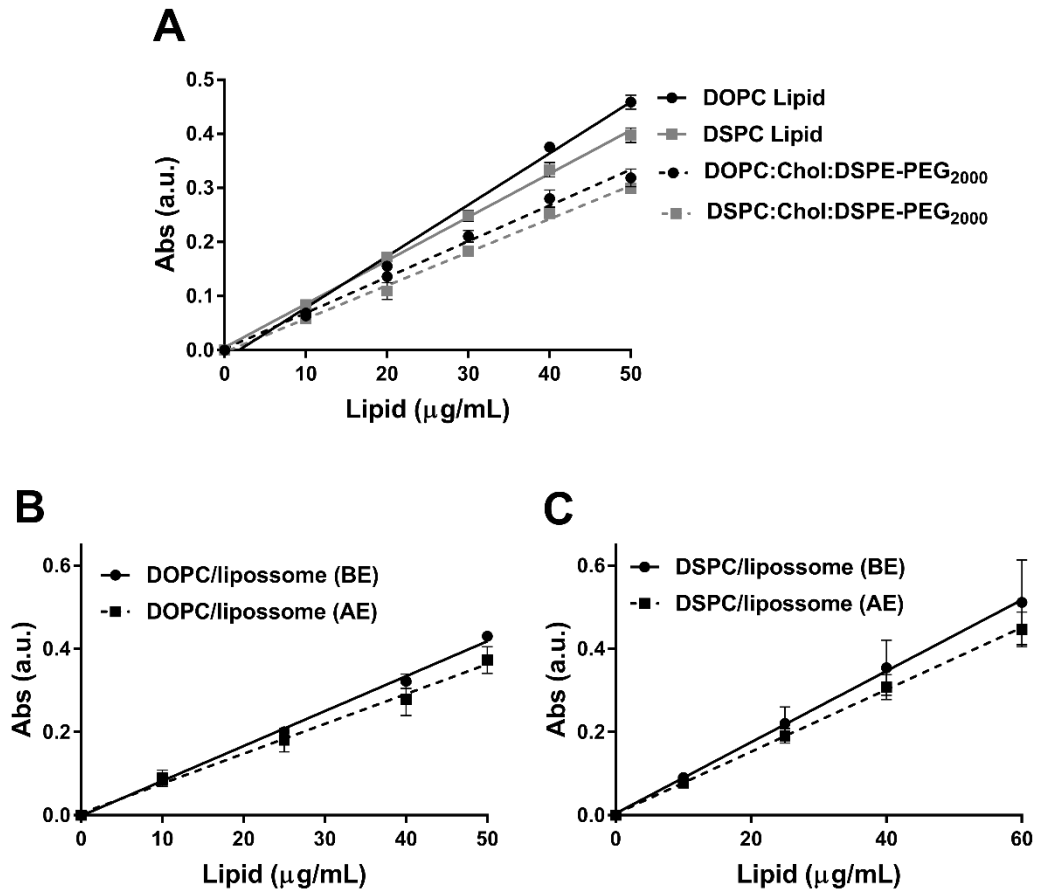

Figure 4.4. Standard curves for phospholipid quantification via Stewart assay. Absorbance values *vs.* lipid content, obtained for A) DOPC:Chol:DSPE-PEG$_{2000}$ liposomes, before (BE) and after extrusion (AE) and B) DSPC:Chol:DSPE-PEG$_{2000}$ liposomes BE and AE. Lipid loss % was calculated from the curve deviation and absorbance values between 20 and 50 μg/mL. Absorbance was measured at λ_{max}= 469 nm) for triplicate samples and data was expressed as mean ± SD of three independent experiments (n=3). Error bars smaller than the symbols are not visible.

4.2.2. Preparation and characterisation of TPZ-loaded liposomes

One of the aims of this project was to encapsulate TPZ in a liposomal delivery system, thus improving on its current *in vivo* limitations. When this project was initiated, there were no studies showing the encapsulation of TPZ in DDS, leading to the development and exploitation of different loading methods for this HAP.

TPZ loaded-liposomes were prepared by the lipid film hydration method, as described in **section 2.4.1.1.1** (**chapter 2**). To separate encapsulated TPZ from the free drug, liposomes were purified by SEC. A total of 15 fractions (1 mL each) were collected and liposomes were eluted in fractions 2, 3 and 4, confirmed by the macroscopic turbidity of these samples. Phospholipid content was determined using the Stewart assay, as discussed above. Moreover, in fractions 7 to 15, a yellow-coloured solution was visible, attributed to free TPZ. Preliminary studies were first conducted to assess the purified elution profile of the free drug to adequately adapt this method to the liposomal formulations.

All samples were quantified using fluorescence and the elution profile obtained was depicted in **figure 4.5**. The results clearly indicated that free TPZ is easily eluted throughout the size-exclusion matrix and is recovered in fractions 7 to 15. Therefore, any non-encapsulated drug will be efficiently separated from the loaded-liposomes fractions and drug loading is easily quantified. For all methods exploited in this section, liposomes before and after purification were lysed with Triton-X 100 (0.1%) and fluorescence was measured to quantify drug EE, based on a previously generated standard curve. However, it was found that only background fluorescence was detected in the corresponding liposome fractions (2,3 and 4), justifying the lack of differences between samples non-treated and treated with triton-X 100. Although this method confirmed he elution profile of the drug it was not used in this work for further quantification of EE:

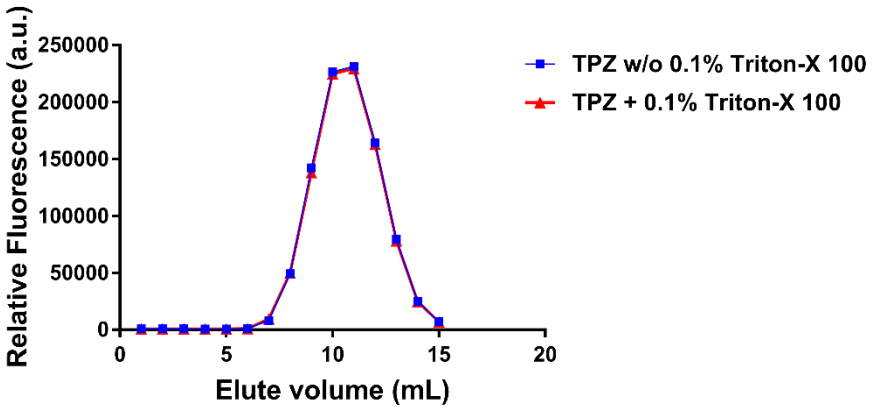

Figure 4.5. Elution profile of purified TPZ-loaded liposomes by size-exclusion chromatography. A total of 15 (1 mL) fractions were collected. Fractions 2, 3 and 4 contained the liposomal solutions, while free drug eluted from fractions 7 to 15. Triton-X 100 (0.1%) was used for baseline correction and the results are expressed as mean fluorescence values.

A series of experiments to exploit various liposomal loading methods for TPZ encapsulation were then conducted. All liposomes, before and after loading, were characterised by DLS and the drug EE was quantified using HPLC. All formulations, loading methods and liposomal properties were summarised in **table 4.2**. Firstly, a passive loading method (TFH) was tested using both DOPC (T_m=-20°C) and DSPC (T_m=-55°C) liposomes for direct comparison of lipid composition. Given the amphiphilic nature of TPZ liposomal bilayer and aqueous loading were simultaneously evaluated. TPZ (10:1 and 20:1, lipid-to-drug molar ratio) was then added either during the lipid film preparation to promote incorporation in the hydrophobic bilayer, or during rehydration step for encapsulation in the aqueous core. Liposomes were then extruded, purified and the Z-Ave, PDI, and EE were determined, before and after loading. For DOPC-TPZ the Z-Ave, after encapsulation, was 139.4 ± 1.45 nm (PDI, 0.04 ± 0.009) for both loading techniques. These results did not differ significantly from those obtained for empty liposomes (Z-ave: 138.1 ± 0.15 nm, PDI: 0.054 ± 0.016). The ζ-potential was also determined and did not differ between any of the formulations/conditions tested and was excluded from the result panel.

Table 4.2. Proposed loading methods and characterisation of TPZ-loaded liposomes. Liposomes were prepared in different conditions and denoted as follows: A: DOPC:Chol:DSPE-PEG$_{2000}$ (5 mM phospholipid, 95:50:5 molar ratio); B: DPPC:Chol:DSPE-PEG$_{2000}$ (10 mM phospholipid, 6:3:1 molar ratio); C: DSPC:Chol:DSPE-PEG$_{2000}$ (5 mM phospholipid, 95:50:5 molar ratio) and D: DSPC:Chol:DSPE-PEG2000 (10 mM phospholipid, 6:3:1 molar ratio). The hydrodynamic size (Z-Ave), polydispersity, ζ-potential values, and EE were determined for both empty (1:0) and TPZ-loaded liposomes. Data was expressed as mean ± SD for triplicate samples of at least two independent (n≥2).

Formulation	Loading method	Lipid:drug (mol:mol)	Z-Ave (d.nm)	PDI	EE (%)
A	Passive loading (TFH) bilayer and aqueous core loading	1:0	138.1 ± 0.15	0.054 ± 0.016	N.A.
		20:1	139.4 ± 1.45	0.040 ± 0.009	0
		10:1			
	Remote loading (pH gradient) $(NH_4)_2SO_4$ (pH 5.5)	1:0	102.5 ± 1.13	0.057 ± 0.018	N.A.
		20:1	105.6 ± 0.78	0.070 ± 0.013	0
	Passive loading EtOH injection	1:0	76.12 ± 0.04	0.090 ± 0.048	N.A.
		20:1	73.95 ± 0.06	0.050 ± 0.018	0
		10:1			
	Passive loading Freeze-thaw cycling	1:0	71.26 ± 0.97	0.139 ± 0.031	N.A.
		2:1	69.57 ± 0.09	0.090 ± 0.013	0
		20:1			
B	SVI method	1:0	107.9 ± 0.45	0.104 ± 0.030	N.A.
		18:1	108.6 ± 0.21	0.063 ± 0.040	6.04
		4.5:1			1.12
		ca.2.3:1			1.45
	SVI method $(NH_4)_2SO_4$ (pH 5.5) (optional FAT)	1:0	132.0 ± 0.02	0.106 ± 0.050	N.A.
		4.5:1	131.4 ± 0.67	0.131 ± 0.091	0.84
		3.6:1			0.81
C	Passive loading (TFH) bilayer and aqueous core loading	1:0	146.4 ± 1.06	0.016 ± 0.001	N.A.
		20:1	139.5 ± 1.27	0.090 ± 0.010	0
		10:1			
	Passive loading FAT	1:0	131.4 ± 1.82	0.042 ± 0.006	N.A.
		2:1	133.2 ± 4.27	0.020 ± 0.020	0
		20:1			
D	SVI method	1:0	141.1± 2.23	0.086 ± 0.078	N.A.
		18:1	142.6 ± 1.18	0.120 ± 0.051	0
		4.5:1			0
		ca.2.3:1			1.47
	SVI method $(NH_4)_2SO_4$ (pH 5.5) (optional FAT)	1:0	141.1 ± 2.23	0.086 ± 0.078	N.A.
		4.5:1	142.6 ± 1.18	0.120 ± 0.021	1.45
		3.6:1			0.83

N.A., Not applicable

A similar trend was obtained for DSPC-TPZ liposomes, suggesting that drug loading did not have a significant impact on the vesicles' physicochemical properties. More importantly, fluorescent quantification did not reveal any drug encapsulation in the liposomal fractions (EE=0%), but recovery of non-encapsulated TPZ was calculated to be between 87-94%. This data suggested that the remaining drug was either lost during the extrusion process, or the loaded quantity was too low to be detected thus, drug loading was not successful at this point.

One of the main drawbacks for liposomal loading of small drugs is their low EE, especially when using passive loading methods. However, modifications of this protocol have been suggested to slightly improve on EE. Xu *et al.* [471] proposed the ethanol injection [254,264] and freeze-thaw cycling (FAT) [265,266] methods as interesting modifications of the TLH to improve drug loading of small molecules. DOPC-TPZ liposomes were prepared by ethanol injection at 10:1 and 20:1 lipid-to-drug molar ratios, with the purpose of obtaining improved drug encapsulation. A small volume of ethanol (300 µL) containing the lipid film was injected into an HBS solution containing TPZ allowing rapid dilution of ethanol in the aqueous environment while drug molecules could be incorporated in the spontaneously formed lipid vesicles [472]. The liposomes were then extruded, purified and characterised. As summarised in **table 4.2**, the loaded liposomes showed significant size decrease, compared to other methods (Z-ave: 73.95 ± 0.06 nm, PDI: 0.050 ± 0.018), but did not differ from its empty lipid counterparts indicating, once again, that drug loading did not affect vesicle preparation. This was not surprising given the lack of drug loading and maximum recovery (99.5%) for non-encapsulated TPZ, after purification. This method relies on the rapid injection of small volumes of lipid-ethanol into an excess solution of the drug, which may preclude drug retention or lead to liposome dilution (and decrease in vesicle size) that compromised the aqueous volume available for drug encapsulation [473].

Alternatively, pre-formed DOPC and DSPC liposomes prepared by TLH were subjected to 10 cycles of freezing (-193°C, 3 min) and thawing (60°C, 3min) and incubated with 20:1 (lipid-to-drug) and a 2:1 (lipid-to-drug) ratio to fully exploit the encapsulation capacity of this method. Repeated cycles of freeze-thawing should produce physical disruption of the liposomal phospholipid bilayers due to the formation of ice crystals during the freezing process, thus increasing the ratio of aqueous solute to lipid and drug permeation/retention [266]. Following purification, samples were characterised and quantified by fluorescence. For this method, small liposomes with excellent homogeneity were also obtained, and did not differ from those shown before loading. Nevertheless, no drug loading was obtained and the maximum total drug recovery was only of 31.7%. The remaining drug might have been lost during the extrusion process or FAT might have compromised drug stability and, consequently EE. Although this method has been somewhat successful in increasing drug loading, the transient deformation of the vesicles during repeated FAT may have induced drug leakage and compromised TPZ-liposome retention [270]. Disappointingly, these methods did not improve on TPZ encapsulation.

Next, a remote loading strategy with a pre-established pH gradient, was also developed. This method has been very successful in terms of high drug loading in liposomal vesicles, particularly using Dox [401,474]. In line with this, some structural characteristics have been suggested as necessary criteria to allow drugs to permeate and accumulate within the liposomal core, *via* remote loading. Optimal loading has been achieved for molecules that present a Log P value in the range between -2.5 and 2.0, $pK_a < 11$ and moderate solubility in water [475]. TPZ seemed to meet the eligible criteria (log P = -0.31 and pKa 5.6) and was therefore loaded after preparing liposomes with a pre-established pH gradient to generate an acidic aqueous core. Empty DOPC:Chol:DSPE-PEG_{2000} were used as a template formulation, giving their high fluidity and were first hydrated in ammonium sulphate [$(NH_4)_2SO_4$, 240mM, pH 5.5]. The liposomes were further purified using HBS (pH 7.4) to establish a proton gradient and incubated with TPZ at 10:1 and 20:1 lipid-to-drug ratios. Unfortunately, once again, it was not possible to obtain any drug loading and free TPZ recovery was close to 100%, after purification. The protocol was then modified using higher concentrations of ammonium sulphate, lower pH buffered solutions and overnight dialysis (*data not shown*) to generate steeper proton gradients, but also without successful drug loading. The great advantage of this method is the possibility of drugs (*e.g.* Dox) in non-ionising forms (at extra-liposomal physiological pH) to translocate the lipid bilayer, which are then trapped after forming an ionized (positively charged) drug form, incapable of passing through the bilayer [401]. Moreover, Dox has also shown to form precipitate fibre bundles with ammonium, citrate and sulphate that also promoted drug retention [401]. The absence of TPZ ionizaton under such pH conditions (amine pK_a=12.5), precipitation, along with its low solubility in aqueous buffers (*ca.* 1 mg/mL, 5.6 mM), may have accounted for its poor liposome retention.

The last method evaluated to incorporate TPZ in liposomes, was a modified protocol based on drug supersaturation and small volume incubation (SVI) that was efficient in encapsulating small drugs, such as gemcitabine [269]. Significantly improved EE was obtained for this drug (30-37%), compared to other passive or remote loading methods (5.7% and 12.4%, respectively). With this strategy concentrated stock solutions of TPZ (25 mM, supersaturated state) were prepared, in aqueous buffers, which rendered the possibility of concentrating the drug in small hydration volumes (20 and 100 µL). This small volume should allow rapid dissolution of the drug suspension for complete drug loading, dependent on the osmotic pressure generated during liposome formation [476]. The loaded liposomes were then purified, characterised and EE was determined. Surprisingly, DPPC-TPZ liposomes yielded EE values ranging from 1.12 to 6.04%, which were significantly decreased (*ca.* 0.8%) when FAT or pH gradients steps were incorporated into the original SVI method. Moreover, liposome size and PDI were not altered with drug loading. In addition, DSPC-TPZ liposomes maintained their physicochemical properties, with EE ranging from 0 to.1.47%. Once again, FAT or pH gradient steps did not seem improve drug loading. Also, the values obtained were lower, compared to DPPC-TPZ, possibly due to lower permeation of the drug. Encouraged by these

results, this protocol was adapted for further studies, using the same conditions, as well as, simultaneously testing other lipid-to-drug conditions and liposomal formulations, but failed to show batch-to-batch reproducibility and high drug loading.

Several experimental designs for TPZ loading were evaluated, but a reliable method showing adequate and most importantly repeated drug loading, could not be achieved. It is difficult to establish one reason for which all these methods failed, but increased drug leakage, followed by the drug's unique chemistry may have made it a poor candidate for the protocols developed. Wu, *et al.* [376], achieved a good TPZ-NP cargo (*ca.* 300 µM TPZ), by establishing a covalent conjugation of TPZ to transferrin. This study suggested that chemical conjugation or modification of TPZ's chemical structure may aid with the development of new DDS for this drug, without compromising its hypoxia selectivity. In addition, a recent study by Broekgaarden and co-workers [384], published after the data gathered in this chapter, showed the encapsulation of TPZ in endothelium targeted liposomes composed of cationic lipids. Their results seemed to suggest that cationic formulations may promote drug loading by non-covalent interaction of TPZ with the lipid formulation. However, their loading method resulted in an extremely low EE (2.4%) of TPZ.

The synthesis of a cupric-TPZ complexes was hypothesized to be a good strategy to develop a novel metal-complex loading method for liposomal TPZ. The developed protocols and experimental outcome are thoroughly discussed in the following sections. The results obtained were promising and proved that modulation of TPZ's chemistry may be an important factor to consider, when encapsulating this HAP.

4.2.3. Preparation and characterisation of $Cu(TPZ)_2$-loaded liposomes

4.2.3.1. Remote loading of $Cu(TPZ)_2$ into preformed liposomes: effect of buffer pH

The use of metal-drug complexation has been exploited to enhance drug encapsulation. This method is based on the complexation of several difficult-to-retain molecules, such as topotecan [403,477], irinotecan [478,479] and mitoxantrone [402] to different metal-ions (*e.g.* copper, zinc, nickel), leading to the development of stable liposomes with increased drug loading. However, this method has mainly focused on complexation occurring inside the liposome core. For instance, cupric ions were encapsulated into liposomes to increase Dox [448], topotecan [477] and mitoxantrone [402] loading. Copper ions were also successful in permeating the lipid bilayer and remotely loaded into chelator-containing liposomes [480,481]. In this work, it was hypothesized that the pre-complexation of TPZ to copper (discussed in **chapter 3**), could aid with its liposomal encapsulation, thus driving TPZ loading *via* a novel method.

Initially, the lipid formulations prepared in **section 4.2.1** were used to analyse the effect of pH on the EE of $Cu(TPZ)_2$. First, empty liposomes were prepared in either HBS, at pH 7.4, or in acidic conditions (pH 5.5), using both ammonium sulphate [$(NH_4)_2SO_4$,] and sodium citrate ($Na_3C_6H_5O_7$)

as hydration buffers. The external buffer was then exchanged with HBS, to enable the remote loading of the $Cu(TPZ)_2$ complex. These aqueous media allowed the simultaneous analysis of different remote loading conditions (detailed in **section 2.4.2** of **chapter 2**) to address the effect of pH on liposome properties and drug encapsulation. Empty liposomes were then characterised by DLS for hydrodynamic size, PDI and zeta-potential and the results are summarised by loading condition in **table 4.3**.

The results showed that all prepared liposomes, regardless of the lipid composition and hydration buffer, showed small hydrodynamic sizes (150-190 nm), low PDI (<0.1) and slightly negative zeta-potential (*ca*. -13 mV). The data confirmed, once again, the formation of biologically compatible liposomes with good size range and uniform population size.

Next, $Cu(TPZ)_2$-loaded lipid vesicles were prepared and denoted as DOPC-$Cu(TPZ)_2$, DPPC-$Cu(TPZ)_2$, and DSPC-$Cu(TPZ)_2$. Briefly, liposomes were hydrated with HBS (pH 7.4), 250 mM $(NH_4)_2SO_4$ (pH 5.5) or 300 mM $Na_3C_6H_5O_7$ (pH 5.5), followed by incubation with $Cu(TPZ)_2$ at a fixed 140:1 lipid-to-complex molar ratio (at 55 °C, between 30 min to 6 h).

Table 4.3. Physicochemical properties of empty PEGylated liposomes. DOPC:Chol:DSPE-PEG_{2000}, DPPC:Chol:DSPE-PEG_{2000} and DSPC:Chol:DSPE-PEG_{2000} liposomes (5mM phospholipids, 95:50:5 molar ratio) were prepared in HBS (pH 7.4), 250 mM $(NH_4)_2SO_4$ (pH 5.5), or 300 mM $Na_3C_6H_5O_7$ (pH 5.5). The hydrodynamic size (Z-Ave), polydispersity and ζ-potential values were determined. Data was expressed as mean ± SD for triplicate samples of three independent experiments (n=3).

Formulation	Hydration conditions	Z-Ave (d.nm)	PDI	ζ- potential (mV)
DOPC:Chol:DSPE-PEG_{2000}	HBS (pH 7.4)	165.3 ± 7.07	0.072 ± 0.040	-10.1 ± 0.84
DPPC:Chol:DSPE-PEG_{2000}		171.5 ± 3.51	0.048 ± 0.010	-11.2 ± 0.49
DSPC:Chol:DSPE-PEG_{2000}		169.4 ± 1.33	0.061 ± 0.020	-9.25 ± 0.79
DOPC:Chol:DSPE-PEG_{2000}	$(NH_4)_2SO_4$, (pH 5.5)	149.2 ± 0.70	0. 097 ± 0.009	-12.1 ± 0.64
DPPC:Chol:DSPE-PEG_{2000}		162.8 ± 2.20	0.074 ± 0.030	-12.2 ± 0.71
DSPC:Chol:DSPE-PEG_{2000}		166.4 ± 0.85	0.093 ± 0.006	-11.7 ± 0.50
DOPC:Chol:DSPE-PEG_{2000}	$Na_3C_6H_5O_7$ (pH 5.5)	157.3 ± 1.84	0.094 ± 0.005	-6.9 ± 0.781
DPPC:Chol:DSPE-PEG_{2000}		180.1 ± 0.44	0.105 ± 0.001	-11.2 ± 0.49
DSPC:Chol:DSPE-PEG_{2000}		189.5 ± 4.03	0.042 ± 0.020	-9.25 ± 0.80

The results did not show any significant changes in the physicochemical properties of the liposomal formulations throughout the 6h time-course studies. The data was then averaged and expressed as representative of the whole study (**Table 4.4**). When hydrated in neutral HBS, the $Cu(TPZ)_2$-loaded liposomes showed an average size of 164.8 ± 2.60 nm (DOPC), 171.9 ± 3.78 nm (DPPC) and 170.3 ± 3.65 nm (DSPC), which was similar to the corresponding empty formulations (**Table 4.3**).

Table 4.4. Physicochemical properties of $Cu(TPZ)_2$-loaded liposomes prepared using different remote loading conditions. DOPC:Chol:DSPE-PEG_{2000}, DPPC:Chol:DSPE-PEG_{2000} and DSPC:Chol:DSPE-PEG_{2000} (5mM phospholipid, 95:50:5 molar ratio) liposomes were prepared in HBS (pH 7.4), $(NH_4)_2SO_4$ (pH 5.5) or $Na_3C_6H_5O_7$ (pH 5.5). In all cases, the external buffer was exchanged with HBS (pH 7.4), using column chromatography to create a transmembrane pH gradient. The liposomes were then incubated with $Cu(TPZ)_2$ at 140:1 lipid-to-complex molar ratio at 55 ºC up to 6h, followed by purification. The hydrodynamic size (Z-Ave), PDI and ζ-potential values were determined for $Cu(TPZ)_2$-loaded liposomes [DOPC-$Cu(TPZ)_2$, DPPC-$Cu(TPZ)_2$, and DSPC-$Cu(TPZ)_2$] and averaged over all time-points. Data was expressed as mean ± SD for triplicate samples of three independent experiments (n=3).

Formulation	Loading conditions	Z-Ave (d.nm)	PDI	ζ- potential (mV)
DOPC-$Cu(TPZ)_2$	HBS (pH 7.4) 55°C	164.8 ± 2.60	0.098 ± 0.010	-7.43 ± 0.33
DPPC-$Cu(TPZ)_2$		171.9 ± 3.78	0.089 ± 0.040	-6.95 ± 0.27
DSPC-$Cu(TPZ)_2$		170.3 ± 3.65	0.079 ± 0.030	-9.85 ± 0.75
DOPC-$Cu(TPZ)_2$	$(NH_4)_2SO_4$ (pH 5.5) 55°C	161.5 ± 4.25	0.140 ± 0.040	-12.95 ± 0.90
DPPC-$Cu(TPZ)_2$		166.3 ± 2.87	0.108 ± 0.020	-11.75 ± 0.58
DSPC-$Cu(TPZ)_2$		171.6 ± 2.03	0.070 ± 0.008	-11.38 ± 0.84
DOPC-$Cu(TPZ)_2$	$Na_3C_6H_5O_7$ (pH 5.5) 55°C	165.5 ± 2.44	0.113 ± 0.020	-10.53 ± 0.30
DPPC-$Cu(TPZ)_2$		175.3 ± 1.81	0.097 ± 0.020	-10.21 ± 0.45
DSPC-$Cu(TPZ)_2$		178.9 ± 2.24	0.093 ± 0.020	-10.18 ± 0.59

The formulations were also hydrated at pH 5.5 with either $(NH_4)_2SO_4$ (pH 5.5) or $Na_3C_6H_5O_7$ (pH 5.5), to evaluate drug encapsulation *via* pH mediated remote loading. When prepared in $(NH_4)_2SO_4$, $Cu(TPZ)_2$-loaded liposomes presented an average size of 161.5 ± 4.25 nm (DOPC), 166.3 ± 2.87(DPPC) nm and 171.6 ± 2.03 nm (DSPC), which did not differ from their respective empty control formulation (**Table 4.3**). Additionally, after preparation in $Na_3C_6H_5O_7$, loaded liposomes also showed a similar size trend, 165.5 ± 2.44 nm (DOPC), 175.3 ± 1.81 nm (DPPC) and 178.9 nm ± 2.24 (DSPC). Moreover, the PDI values in all conditions were lower than 0.1, consistent with the formation of a monodisperse population of liposomes, even after complex loading, suggesting no further aggregation in all condition tested. The zeta-potential values obtained were consistent with those for neutral liposomal formulations [244]. It was thus concluded that at a 140:1 lipid-to-complex molar ratio, liposomal properties were not significantly affected by either drug loading or the aqueous medium used for hydration. This method may then offer an effective approach to encapsulate $Cu(TPZ)_2$ in liposomes, while maintaining biocompatible physicochemical properties [277,278].

Next the EE of $Cu(TPZ)_2$-loaded liposomes was evaluated, in order to assess the best loading conditions. As depicted in **figure 4.6A**, successful loading of the complex in neutral conditions (HBS, pH 7.4) was achieved for all lipid formulations, over a time-course of 6 h and an overall EE above 75% was obtained.

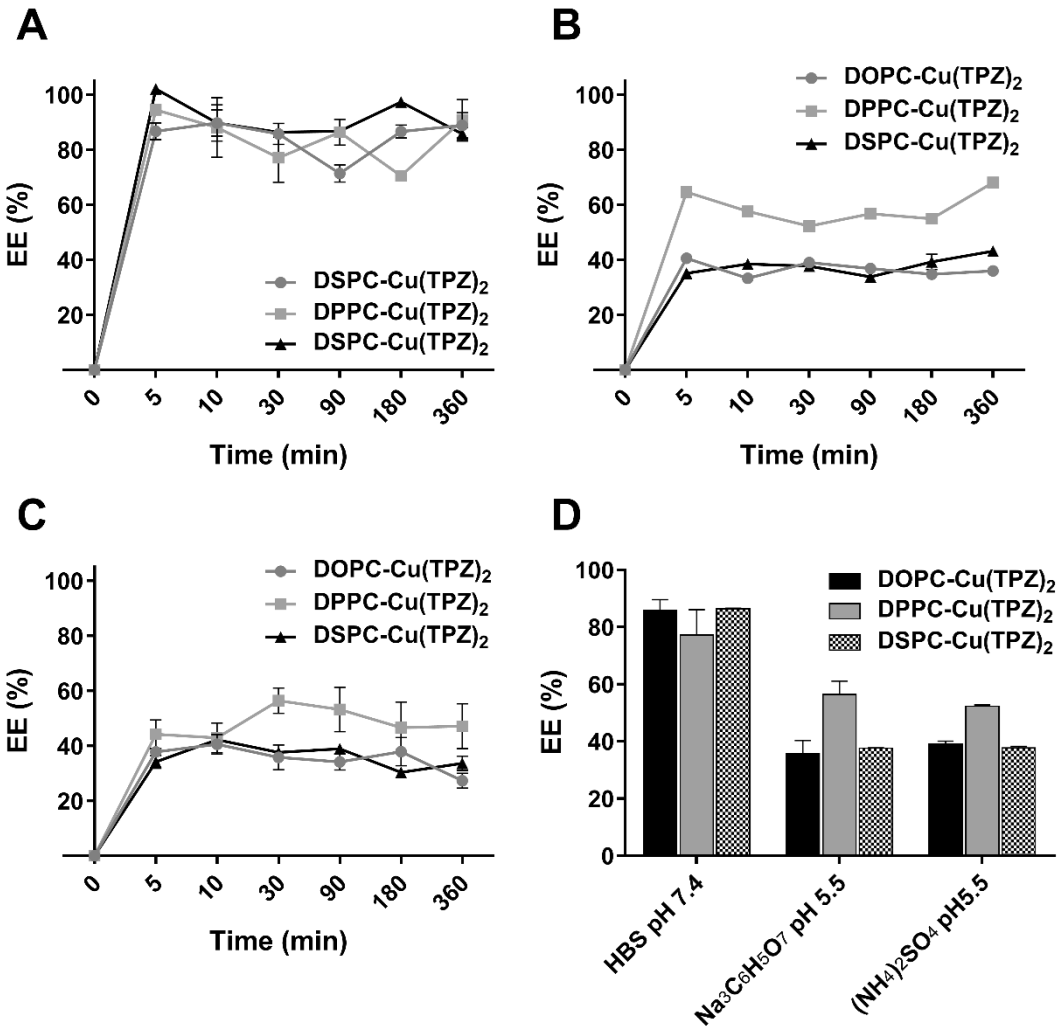

Figure 4.6. Liposomal encapsulation of Cu(TPZ)$_2$ using three remote loading procedures. Encapsulation efficiency over time in A) HBS. pH 7.4; B) $(NH_4)_2SO_4$, pH 5.5 and C) $Na_3C_6H_5O_7$ pH 5.5. D) Representative EE, in all conditions, at the optimized 30 min incubation time-point for Cu(TPZ)$_2$ loading. Lipid formulations of DOPC:Chol:DSPE-PEG$_{2000}$, DPPC:Chol:DSPE-PEG$_{2000}$, DSPC:Chol:DSPE-PEG$_{2000}$ (5mM, 95:50:5 molar ratio) were incubated with Cu(TPZ)$_2$ at a 140: lipid-to-complex molar ratio, at 55ºC up to 360 min. The loaded liposomes were abbreviated as DOPC-Cu(TPZ)$_2$, DPPC-Cu(TPZ)$_2$, DSPC-Cu(TPZ)$_2$. In all cases except A, the external buffers were exchanged with HBS, pH 7.4., using column chromatography to create a transmembrane pH gradient. At specified time-points, the EE was determined by HPLC as described in chapter 2. Data was expressed as mean ± SD for triplicate samples of two independent experiments (n=2). Error bars smaller than the symbols are not visible.

This high yield is in good agreement with previous studies, which showed EE of 95% of both radioactive copper and copper-complexed drugs, even after incubation periods as short as 5 min, at temperatures above 50°C [402,481]. Interestingly, although no significant changes were observed in liposomal size, PDI or ζ-potential, between all conditions tested, the pH gradient had a significant impact on the EE of Cu(TPZ)$_2$. When hydrated in $(NH_4)_2SO_4$ **(Figure 4.6B)** or $Na_3C_6H_5O_7$ **(Figure 4.6C)**, the EE significantly dropped to an average value of *ca.* 60% for DPPC formulations and *ca.* 40% for DOPC and DSPC. These differences strongly suggested that liposomal preparation in neutral HBS is more suitable to effectively load Cu(TPZ)$_2$, avoiding the need to use extra pH gradients to drive complex loading. For all further experiments, Cu(TPZ)$_2$-loaded liposomes were

prepared by hydrating the lipid film with HBS (pH 7.4), followed by 30 min incubation at 55°C with $Cu(TPZ)_2$. The EE results at 30 min were then averaged, summarised in **figure 4.6D** and clearly highlight the effect of pH on the encapsulation of this complex. The generation of a proton gradient had a detrimental effect on the loading efficiency of the complex, resulting in a 1.5 up to 2.5-fold decrease in encapsulation efficiency of $Cu(TPZ)_2$, compared to the remote loading method in HBS at pH 7.4.

The above result was surprising at the time but agreed well with the pH-mediated dissociation of the complex, discussed in **chapter 3**. This decreased loading was due, not to a lower encapsulation of the complex itself, but to dissociation of $Cu(TPZ)_2$ in free Cu^{2+} and TPZ under acidic conditions. This finding was consistent with a study by Kheirolomoom *et al.* [448] where a copper-Dox complex (1:2, molar ratio) showed good stability at neutral pH, but high dissociation in acidic conditions (>75% dissociation at pH<5). This pH-dependent stability compromised $Cu(TPZ)_2$ loading and consequently TPZ liposomal retention. It is plausible that after complex dissociation free TPZ diffused out of the liposomal bilayer, leading to marked decrease in EE, which is in accordance with the results obtained previously (**section 4.2.2**). This result was further confirmed by the observation of a strong yellow elute collected during the purification step (**Figure 4.7**), consistent with the presence of free TPZ. In conclusion, $Cu(TPZ)_2$, and consequently TPZ, can be successfully loaded in various liposomal formulations using a simple remote loading method in HBS, at pH 7.4. The method developed herein relied on the pre-complexation of copper to TPZ but was not dependent on the use of transmembrane proton gradients or ionophores. The enhanced lipophilicity of the complex (log P = 2.88) compared to that of TPZ (log P = -0.31) could have played an important role on promoting liposome encapsulation, as well as TPZ retention within the liposome core. This hypothesis will be discussed in **chapter 6**.

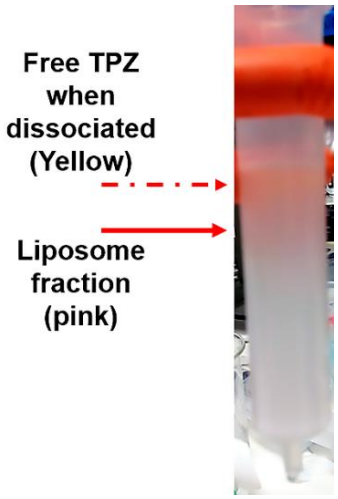

Figure 4.7. Representative image of a size exclusion chromatography column following $Cu(TPZ)_2$-loaded liposomes purification. DOPC:Chol:DSPE-PEG_{2000} liposomes hydrated with $(NH_4)_2SO_4$ (pH 5.5), and incubated with $Cu(TPZ)_2$, as described in the chapter 2. To remove the free complex, the liposomes were loaded into a PD-10 SEC column and eluted using HBS buffer. The top yellow band represents free TPZ (from dissociated complex), while the lower pink band represents the $Cu(TPZ)_2$-loaded liposomes band.

4.2.3.1.1. Stability of $Cu(TPZ)_2$-loaded liposomes

The liposomes prepared and loaded using the optimized remote loading method in HBS were stored at 4°C. To evaluate their short-term stability over 9 days, liposomes were characterised by DLS to assess any changes in size, PDI and zeta-potential. As shown in **table 4.5**, DOPC formulations showed a slight increase in PDI at day 9 (0.203 ± 0.006), indicating possible aggregation, possibly due to the lower T_m of these vesicles that can be prone to higher drug leakage [482]. On the other hand, DPPC and DSPC liposomal formulations remained stable over a period of 9 days, stored at 4°C, with no significant change in size or zeta-potential. Moreover, PDI values were ≤ 0.1, suggesting no aggregation during this period of storage. Overall, longer and/or saturated lipid chains, particularly DSPC, result in more stable vesicles due to greater van deer Waals interactions [482]. This allows stronger cohesion and less drug leakage, over time [483].

Table 4.5. Stability of PEGylated $Cu(TPZ)_2$-loaded liposomes. DOPC:Chol:DSPE-PEG_{2000}, DPPC:Chol:DSPE-PEG_{2000} and DSPC:Chol:DSPE-PEG_{2000} (5mM phospholipid, 95:50:5, molar ratio) liposomes were prepared in HBS (pH 7.4) and incubated with $Cu(TPZ)_2$ at 140:1 lipid-to-complex molar ratio at 55 ºC for 30 min. The purified loaded liposomes (DOPC-$Cu(TPZ)_2$, DPPC-$Cu(TPZ)_2$, and DOPC-$Cu(TPZ)_2$) were stored at 4 ºC. The hydrodynamic size (Z-Ave), polydispersity, and ζ-potential values were determined immediately after preparation (day 0) and after 9 days. Data was expressed as mean ± SD for triplicate samples of three independent experiments (n=3).

Formulation	Day	Z-Ave (nm)	PDI	ζ-potential (mV)
DOPC-$Cu(TPZ)_2$	0	164.8 ± 2.60	0.098 ± 0.010	-7.43 ± 0.33
	9	169.7 ± 1.93	0.203 ± 0.006	-9.39 ± 0.889
DPPC-$Cu(TPZ)_2$	0	171.9 ± 3.78	0.089 ± 0.040	-6.95 ± 0.27
	9	172.6 ± 0.61	0.103 ± 0.007	-9.20 ± 0.392
DSPC-$Cu(TPZ)_2$	0	170.3 ± 3.65	0.079 ± 0.030	-9.85 ± 0.75
	9	169.9 ± 2.27	0.092 ± 0.013	-10.4 ± 0.394

4.2.3.2. Remote loading of $Cu(TPZ)_2$: effect of temperature on EE

Given the successful loading of the complex at neutral pH it was important to analyse the effect of other parameters such as temperature, liposome size and PEGylation on the EE of $Cu(TPZ)_2$. Previously there were no significant variations in EE found between the different lipid formulations tested, which may be due, in part, to the use of an incubation temperature above the T_m (55 °C). It was hypothesized that lower temperatures may influence the loading capacity and give insight on whether complexation and, consequently complex-mediated diffusion, is the main driving force that promotes encapsulation. Therefore, the remote loading method in HBS, pH 7.4 was performed by incubating $Cu(TPZ)_2$ (140:1 lipid-to-complex molar ratio) for 30 min at 20, 37 and 55°C (**Figure 4.8)**.

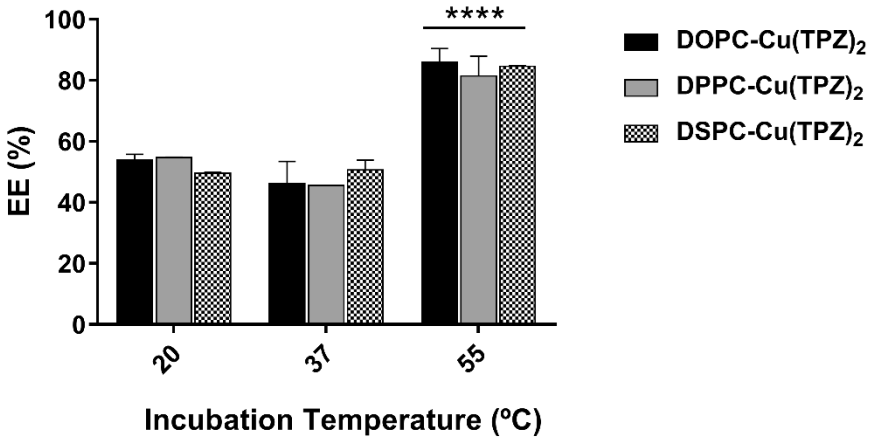

Figure 4.8. Effect of incubation temperature on the liposomal encapsulation of $Cu(TPZ)_2$. DOPC:Chol:DSPE-PEG_{2000}, DPPC:Chol:DSPE-PEG_{2000} and DSPC:Chol:DSPE-PEG_{2000} (5mM phospholipid, 95:50:5, molar ratio) liposomes were prepared in HBS (pH 7.4) and incubated with $Cu(TPZ)_2$ at 140:1 lipid-to-complex molar ratio at 20, 37 and 55 ºC, for 30 min. The loaded liposomes are abbreviated as DOPC-$Cu(TPZ)_2$, DPPC-$Cu(TPZ)_2$, DSPC-$Cu(TPZ)_2$, respectively. The EE was determined by HPLC as described in chapter 2. Data was expressed as mean ± SD for triplicate samples of two independent experiments (n=2). Statistical analysis: Two-way ANOVA multiple comparison with Tukey Post-test ($^{****}p$ <0.0001, compared to 20 and 37ºC). Error bars smaller than the symbols are not visible.

The results showed no significant difference in the obtained EE between all three liposomal formulations. The highest loading was obtained at 55°C (EE>80%), compared to 20 and 37°C (EE<60%). The temperature was a determinant factor on EE statistically accounting for over 87% of the total variation of the experiment, while lipid composition had negligible effect.

At 55°C EE showed an extremely significant increase ($p<0.0001$), for all formulations, compared to other temperatures. This finding was supported by previous results [480], which showed excellent loading (>90%) even for high phase transition liposomes (*e.g.* DSPC). This was shown for temperatures as low as 20°C, but for incubation periods above 60 min. The findings indicated a positive correlation between temperature, incubation period and assisted or unassisted loading (with/without ionophores) on the encapsulation of copper-complexes. The reports on the unassisted loading showed that an increase from 30 to 40°C, resulted in a remarkable loading efficiency increase from 47 to 97% for longer lipid chain lipids (DSPC) after 1h incubation [480,481]. Assuming $Cu(TPZ)_2$ is loaded due to its increased membrane permeability (Log P = 2.88) it is possible that temperature/time are important parameters determining its rate of internalization (as shown for the unassisted loading methods). In summary, the complex lipophilicity may play a detrimental role on bilayer permeation and consequently drug loading. Therefore, higher temperatures may aid in obtaining increased, but also quicker drug encapsulation.

The method developed here is versatile and can yield high drug loading (above 60%), even at different incubation temperatures. Future work using differential scanning calorimetry (DSC) could provide complementary information regarding the effect of $Cu(TPZ)_2$ on the bilayer T_m to better understand the effect of temperature on the loading mechanism.

4.2.3.3. Remote loading of Cu(TPZ)$_2$: effect of liposome size on EE

Until this point, only larger sized liposomes (extruded up to 200 nm) were characterised. The effect of liposome size on the EE of Cu(TPZ)$_2$ was also evaluated for smaller PEGylated liposomes (*ca.* 100 nm), given their application for *in vitro* and *in vivo* experiments. Extrusion through 100 nm membranes resulted in smaller liposomes with an average size of 138.4 ± 7.47 nm (DOPC), 131.7 ± 7.19 nm (DPPC) and 137.9 ± 2.72 nm (DSPC). Liposome size was an important factor to consider during drug loading (**Figure 4.9**). For the 140:1 lipid-to-complex molar ratio, a non-significant decrease in EE was observed for both DOPC (85.9%) and DPPC (64.7%), compared to their 200 nm extruded counterpart formulations (64.7% for DOPC and 65.65% for DPPC). In contrast, a *ca.* 1.5 fold decrease in EE was observed for DSPC (84.6% to 56.3%, $p<0.01$).

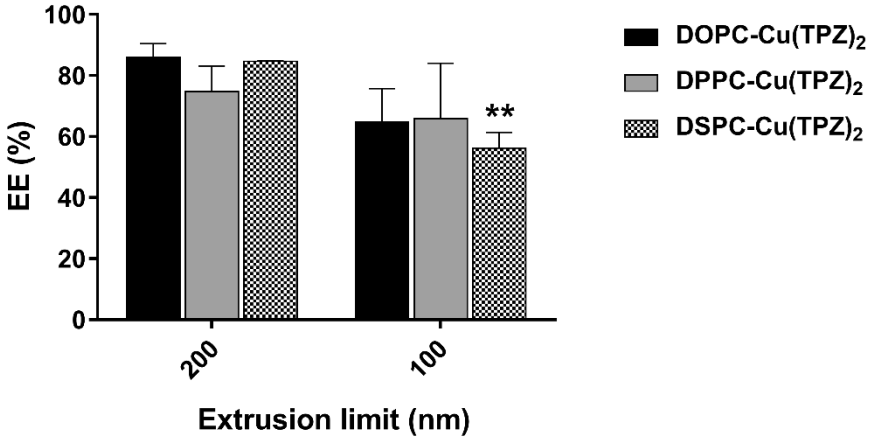

Figure 4.9. Effect of extrusion limit on the liposomal encapsulation of Cu(TPZ)$_2$ by remote loading. DOPC:Chol:DSPE-PEG$_{2000}$, DPPC:Chol:DSPE-PEG$_{2000}$ and DSPC:Chol:DSPE-PEG$_{2000}$ (5mM phospholipid, 95:50:5, molar ratio) liposomes were prepared in HBS (pH 7.4) and incubated with Cu(TPZ)$_2$ at 140:1 lipid-to-complex molar ratio at 55 ºC, for 30 min. Liposomes were then extruded 15× through 200 nm or 21× through 100 nm membrane filter and further loaded with Cu(TPZ)$_2$ to establish the effect of liposome size on drug encapsulation. The loaded liposomes are abbreviated as DOPC-Cu(TPZ)$_2$, DPPC-Cu(TPZ)$_2$, DSPC-Cu(TPZ)$_2$, respectively. The EE was determined by HPLC as described in chapter 2. Data was expressed as mean ± SD for triplicate samples of two independent experiments (n=2). Statistical analysis: Two-way ANOVA multiple comparison with Tukey Post-test ($^{**}p < 0.01$, compared to 200 nm extrusion). Error bars smaller than the symbols are not visible.

This led to the conclusion that the liposomal size may also determine EE, particularly for long saturated lipid chains, such as DSPC. Previous studies have shown that small liposomes may compromise drug incorporation, compared to larger ones, which yield higher drug encapsulation [484]. The analysis of different lipid-to-complex ratios may elucidate the encapsulation mechanism in smaller liposomes, which will be discussed later in this chapter.

4.2.3.4. Remote loading of Cu(TPZ)$_2$: effect of PEGylation on EE

PEGylation is known for its primary role in increasing stability and circulation time *in vivo* [485], as detailed in **chapter 1**. It was important to analyse if the addition of PEG was having a negative effect on drug loading. Interestingly, PEGylation yielded increased Cu(TPZ)$_2$ loading, between all formulations, compared to their non-PEGylated counterparts **(Figure 4.10)**. EE was significantly decreased upon removal of PEG for both DOPC ($p<0.01$) and DPPC ($p<0.05$). This result was particularly prominent, once again, for the more rigid formulation DSPC. A *ca.* 2-fold decrease in EE was observed ($p<0.0001$) when using non-pegylated formulations of this lipid. Research performed by Rissanen *et al.*[259], and Dzieciuch *et al.*[486], provided more information on the role of PEG and drug partitioning in lipid bilayers, including liposomes. Their atomic-scale molecular dynamic simulation studies showed that PEG can have both an entropic barrier effect [259] to some drugs, or improve drug loading [486]. The latter study showed that PEG is able to eliminate water from the lipid head group region of the lipids, aiding with solubility of hydrophobic compounds.

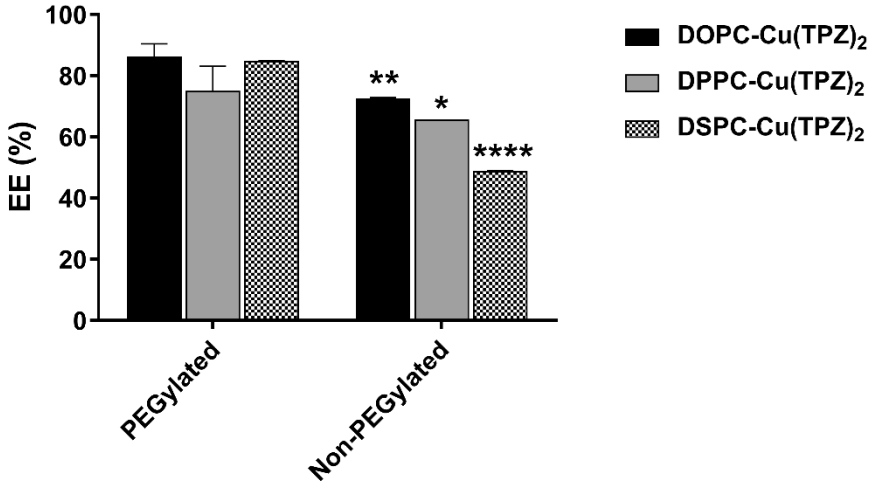

Figure 4.10. Effect of PEGylation on the liposomal encapsulation of Cu(TPZ)$_2$ by remote loading. PEGylated lipid formulations of DOPC:Chol:DSPE-PEG, DPPC:Chol:DSPE-PEG, DSPC:Chol:DSPE-PEG (5mM, 95:50:5 molar ratio) and non-PEGylated DOPC:Chol, DPPC:Chol, DSPC:Chol: (5mM, 100:50 molar ratio) were incubated with Cu(TPZ)$_2$ at 140:1 lipid-to-complex molar ratio at 55ºC, for 30 min. The loaded liposomes are abbreviated as DOPC-Cu(TPZ)$_2$, DPPC-Cu(TPZ)$_2$, DSPC-Cu(TPZ)$_2$, respectively. The EE was determined by HPLC, as described in chapter 2. Data was expressed as mean ± SD for triplicate samples of two independent experiments (n=2). Statistical analysis: Two-way ANOVA multiple comparison with Tukey Post-test ($^{*}p<0.05$, $^{**}p<0.01$ and $^{****}p<0.0001$, compared to the PEGylated formulation). Error bars smaller than the symbols are not visible.

More importantly, it increased the bilayer partitioning coefficient of such drugs, which resulted in improved drug-loading. Such findings led to the hypothesis that Cu(TPZ)$_2$ may form non-covalent interactions with PEG [487], which then aids with the complexes' solubility, but also bilayer permeation. This was particularly relevant for more rigid lipid structures in DSPC liposomes. Cu(TPZ)$_2$ may then permeate easily through the bilayer, promoting aqueous encapsulation. On the other hand, noncovalent adduct interaction between a metallic complex and the polymer cannot be excluded, justifying the decreased loading in non-Pegylated formulations. A more detailed discussion on this is provided in **chapter 6** (**section 6.1.2.2**).

4.2.3.5. Remote loading of Cu(TPZ)$_2$: effect of lipid-to-complex ratio on EE

The effect of increasing complex-to-lipid molar ratios on the liposomal EE of Cu(TPZ)$_2$, was also studied. DOPC:Chol:DSPE-PEG$_{2000}$, DPPC:Chol:DSPE-PEG$_{2000}$ and DSPC:Chol:DSPE-PEG$_{2000}$ liposomes, now extruded up to 100 nm, were incubated with varying molar ratios of lipid:Cu(TPZ)$_2$ (200:1 to 20:1) and purified using SEC. After liposome purification it was interesting to observe an increase in the eluted fraction's colour (pink), attributed to a marked increase of encapsulated liposomal Cu(TPZ)$_2$, with decreasing lipid-to-complex molar ratios **(Figure 4.11)**.

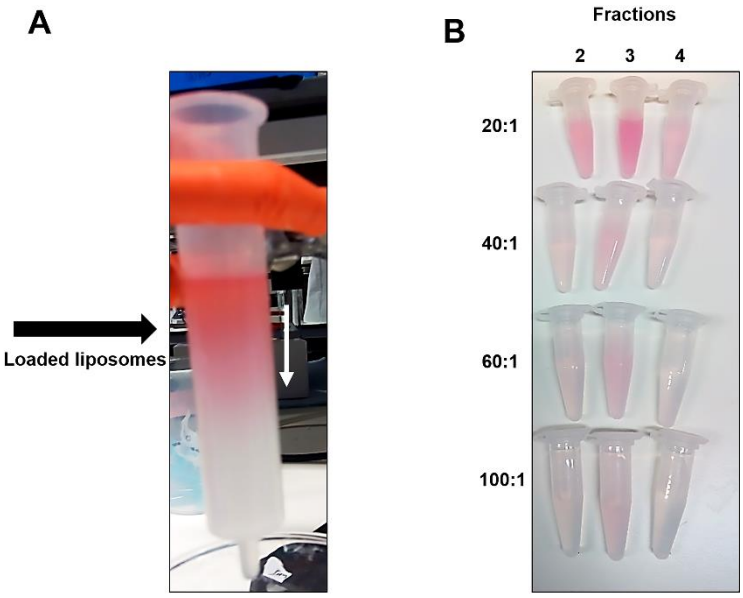

Figure 4.11. Representative image of size exclusion purification of Cu(TPZ)$_2$-loaded liposomes, and the effect of varying lipid-to-complex molar ratios on drug loading. DOPC:Chol:DSPE-PEG$_{2000}$ liposomes hydrated with HBS (pH 7.4), and incubated with Cu(TPZ)$_2$. A) The loaded liposomes were purified using a PD-10 SEC column. The pink band corresponds to the liposomal Cu(TPZ)$_2$, which was eluted through the column and collected in B) fractions 2, 3 and 4 (1 mL fraction); while the free complex was retained in the column. Decreasing lipid-to-complex molar ratios resulted in higher drug loading, as depicted with darker colour of the collected liposomal fractions.

Next, all formulations, prepared simultaneously, were characterised by DLS to analyse the physicochemical changes accompanied by varying lipid-to-complex ratios. The results were summarised in **table 4.6**. Interestingly, although good EE (>65%) was observed throughout the panel of formulations and conditions tested, there was an effect on liposome size, which was formulation dependent.

Empty DOPC liposomes presented an average size of 126.9 ± 8.08 nm, with the expected slightly negative zeta-potential (- 11.3 ± 0.91 mV), as discussed before, and narrow PDI (0.096 ± 0.02). For DOPC-Cu(TPZ)$_2$ liposomes, a slight increase in size was observed, up to 60:1 lipid-to-complex molar ratio (140.3.9 ± 2.71 nm). The PDI also increased to 0.23 ± 0.033. At lower lipid-to-complex ratios, the liposome size and PDI continued to increase, reaching the highest values at 20:1 lipid-to-complex ratio, with a Z-Ave of 181.8 ± 4.64 nm, and PDI of 0.35 ± 0.37. This data suggested liposome aggregation and instability with high drug content that can be associated to the lower T_m

and increased fluidity of DOPC [466]. The latter assumption was later confirmed by TEM, depicted in **appendix 1 (Figure A1**). For all ratios tested, no significant change in zeta-potential was observed. More promisingly, EE was not adversely affected (>65%), with maximum efficiency achieved at 60:1 lipid-to-complex molar ratio (84.53 ± 9.22 %). Empty DPPC liposomes presented a Z-Ave of 136.2 ± 7.19 nm with good PDI (0.041 ± 0.008), which was maintained up to 60:1 lipid-to-complex ratio, like DOPC. However, for the more rigid DPPC-$Cu(TPZ)_2$ liposomes, the size increase was subtler, reaching a Z-Ave of 150.9 ± 7.90 nm, and highest PDI of 0.35 ± 0.086 at 20:1 lipid-to-complex ratio; and the EE ranged between 70-87%.

Table 4.6. Physicochemical properties of $Cu(TPZ)_2$-loaded liposomes prepared at different lipid-to-complex molar ratios. DOPC:Chol:DSPE-PEG_{2000}, DPPC:Chol:DSPE-PEG_{2000} and DSPC:Chol:DSPE-PEG_{2000} (5mM phospholipid, 95:50:5 molar ratio) liposomes were prepared in HBS (pH 7.4), and incubated with varying lipid-to-complex molar ratios (200:1 – 20:1) at 55 °C, for 30 min. The hydrodynamic size (Z-Ave), polydispersity, ζ-potential values, and EE were determined for both empty (1:0) and $Cu(TPZ)_2$-loaded liposomes (DOPC-$Cu(TPZ)_2$, DPPC-$Cu(TPZ)_2$, and DSPC-$Cu(TPZ)_2$. Data was expressed as mean ± SD for triplicate samples of three independent experiments (n=3).

Formulation	Lipid:drug (mol:mol)	Z-Ave (nm)	PDI	ζ-potential (mV)	EE
DOPC:Chol:DSPE-PEG_{2000}	1:0	126.9 ± 8.08	0.09 ± 0.020	- 11.3 ± 0.91	N.A.
	200:1	129.0 ± 5.35	0.13 ± 0.008	- 11.6 ± 0.24	68.39 ± 6.26
	140:1	131.8 ± 3.47	0.15 ± 0.024	- 10.9 ± 0.42	70.05 ± 5.82
	100:1	136.4 ± 6.34	0.15 ± 0.026	- 11.7 ± 0.77	67.93 ± 5.69
	60:1	140.3 ± 2.71	0.23 ± 0.033	- 10.9 ± 0.61	84.53 ± 9.22
	40:1	147.4 ± 2.86	0.25 ± 0.031	- 11.2 ± 0.54	76.04 ± 2.71
	20:1	181.8 ± 4.64	0.35 ± 0.037	- 13.4 ± 0.63	70.61 ± 10.39
DPPC:Chol:DSPE-PEG_{2000}	1:0	136.2 ± 7.19	0.04 ± 0.008	- 9.69 ± 0.74	N.A.
	200:1	138.4 ± 5.99	0.07 ± 0.030	- 10.2 ± 0.81	75.14 ± 11.10
	140:1	138.3 ± 7.23	0.06 ± 0.024	- 10.3 ± 0.28	70.48 ± 8.08
	100:1	139.1 ± 5.79	0.07 ± 0.020	- 10.7 ± 0.57	72.96 ± 11.76
	60:1	135.5 ± 2.38	0.19 ± 0.029	- 9.69 ± 0.74	70.52 ± 9.26
	40:1	149.7 ± 6.30	0.26 ± 0.016	- 9.81 ± 0.51	78.84 ± 8.44
	20:1	150.9 ± 7.90	0.35 ± 0.086	- 12.5 ± 0.76	87.41 ± 2.04
DSPC:Chol:DSPE-PEG_{2000}	1:0	136.9 ± 5.03	0.05 ± 0.013	-8.25 ± 0.32	N.A.
	200:1	137.3 ± 3.73	0.07 ± 0.024	- 9.91 ± 0.49	67.16 ± 3.10
	140:1	137.9 ± 2.72	0.05 ± 0.011	- 8.66 ± 0.43	59.60 ± 1.34
	100:1	139.3 ± 3.81	0.07 ± 0.017	- 10.2 ± 0.44	68.83 ± 2.19
	60:1	140.7 ± 1.92	0.11 ± 0.020	- 10.3 ± 0.70	71.13 ± 5.21
	40:1	145.9 ± 8.74	0.21 ± 0.037	- 10.7 ± 0.55	85.23 ± 9.18
	20:1	165.0 ± 6.88	0.29 ± 0.067	- 10.7 ± 0.58	81.45 ± 3.57

Empty DSPC liposomes had a Z-Ave (136.9 ± 5.03 nm) and PDI (0.048 ± 0.013) like those obtained for DOPC and DPPC. Finally, after loading, DSPC-Cu(TPZ)$_2$, showed similar results to DPPC-Cu(TPZ)$_2$, with the smallest increase in size, up to 20:1 lipid-to-complex ratio, with a Z-Ave and PDI of 165.0 ± 6.88 and 0.289 ± 0.067, respectively. Once again, no significant changes in zeta-potential values were observed, confirming that the complex does not seem to affect liposomal surface charge. This formulation not only presented excellent EE values ranging from *ca.* 60% up to 85%, but maintained appropriate physicochemical properties for *in vitro* application [488], throughout all ratios tested. Moreover, DSPC is a good option for further exploration, if higher drug content is needed, particularly when considering future *in vivo* applications; given its improved stability over the other formulations shown here. In conclusion, the composition of the lipid bilayer did not affect the complex loading significantly but influenced liposome size and stability, which could ultimately affect the carriers' therapeutic efficacy. Although the 20:1 ratio presented the highest EE, liposome size and PDI were dramatically increased. Therefore, a lipid-to-complex ratio of 60:1 ratio presented a good combination between size, PDI and high EE, for all formulations, and was chosen for the *in vitro* studies conducted in **chapter 5**.

The remote loading method developed in this work, offered an interesting alternative to increase TPZ liposomal encapsulation. Despite the similarity between EE for all formulations, the drug content and/or drug loading at decreasing lipid-to-complex ratios was increased. This quantitative measurement of drug content per lipid (detailed in **chapter 2, section 2.4.2.3**) is important to assess the efficiency of the carrier. Decreasing the lipid-to-complex ratios (200:1 down to 20:1) resulted in increased complex loading efficiency **(Figure 4.12A)** and encapsulated drug content **(Figure 4.12B)**, with no significant differences between the formulations tested.

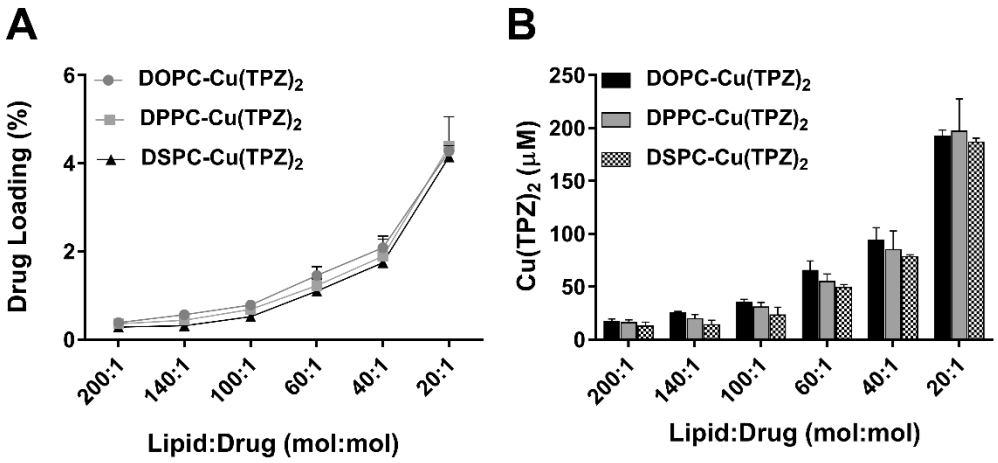

Figure 4.12. Liposomal drug loading of Cu(TPZ)$_2$ at various lipid-to-complex molar ratios. A) Drug loading of Cu(TPZ)$_2$, and B) concentration of encapsulated Cu(TPZ)$_2$ at various lipid-to-complex molar ratios. DOPC:Chol:DSPE-PEG$_{2000}$, DPPC:Chol:DSPE-PEG$_{2000}$ and DSPC:Chol:DSPE-PEG$_{2000}$ liposomes (5mM. 95:50:5 molar ratio) were incubated with Cu(TPZ)$_2$ at different lipid-to-complex molar ratio for 30 min at 55 ºC, followed by purification. The loaded liposomes are abbreviated as DOPC-Cu(TPZ)$_2$, DPPC-Cu(TPZ)$_2$, DSPC-Cu(TPZ)$_2$, respectively. At specified time-points drug loading and complex content was determined by HPLC, as described in chapter 2. Data was expressed as mean ± SD for triplicate samples of three independent experiments (n=3). Error bars smaller than the symbols are not visible.

In **figure 4.12A**, drug loading efficiencies vary from 0.38 ± 0.05 % (DOPC-$Cu(TPZ)_2$), 0.37 ± 0.07 % (DPPC-$Cu(TPZ)_2$) and 0.28 ± 0.08 % (DSPC-$Cu(TPZ)_2$), at 200:1 lipid-to-complex ratio; up to 4.27 ± 0.13 % (DOPC-$Cu(TPZ)_2$), 4.41 ± 0.65 % (DPPC-$Cu(TPZ)_2$) and 4.15 ± 0.08 % (DSPC-$Cu(TPZ)_2$), at 20:1 lipid-to-complex ratio. Additionally, and in line with this increased drug loading, **figure 4.12B** shows higher drug encapsulation with decreasing lipid-to-complex ratios. Maximum $(CuTPZ)_2$ encapsulation values of 192.31 ± 5.82 µM (DOPC-$Cu(TPZ)_2$) , 197.04 ± 30.39 µM (DPPC-$Cu(TPZ)_2$) and 186.58 ± 3.65 µM (DSPC-$Cu(TPZ)_2$) were obtained at 20:1 lipid-to-complex ratios.

More recently, different approaches have been developed to deliver TPZ, combined with other therapeutics, using covalent conjugation [376,377] or NP encapsulation strategies [378-383]. In these studies, TPZ EE varied (2.4 – 77.41%) [376-379,383,384], but generally resulted in loaded drug quantities <300 µM, with the best results obtained using Tf-TPZ (1:6) chemical conjugate (*ca.* 300 µM TPZ) [376]. Despite the apparent low drug cargo, all these studies showed remarkable potentiation of TPZ activity when used with other treatment modalities proving encapsulation was enough for positive therapeutic outcome. In the present work, marked improvement in liposomal-TPZ encapsulation was shown using copper-complexation compared to the aforementioned studies. Liposomal EE was consistently high (>60%) with all prepared formulations. Also, at the maximum 20:1 lipid-to-complex molar ratio tested $Cu(TPZ)_2$ resulted in liposomal loading quantities of 192.3 ± 5.8 µM (384.6 µM TPZ equivalent) for DOPC-$Cu(TPZ)_2$, 197.04 ± 30.3 µM (394.0 µM TPZ equivalent) for DPPC-$Cu(TPZ)_2$ and 186.5 ± 3.65 µM (373.1 µM TPZ equivalent) for DSPC-$Cu(TPZ)_2$, which were considerably higher than that obtained in the literature, even when compared to cationic TPZ-liposomes [384]. Broekgaarden and co-workers (2017) [384], reported the only other study regarding encapsulation of TPZ in liposomes, as a co-adjuvant therapy for PDT. The results showed an overall EE of 2.4% for TPZ in cationic liposomes, which resulted in *ca.* 24 µM of encapsulated drug. In this work, copper-complexation followed by encapsulation at 20:1 lipid-to-complex ratio resulted in a *ca.* 33-fold increase in TPZ encapsulation (16-fold increase in the amount of encapsulated TPZ), compared to the work by Broekgaarden *et al*. These results were very promising in terms of achieving a higher TPZ payload within liposomes, using $Cu(TPZ)_2$.

4.2.3.6. Structural elucidation of $Cu(TPZ)_2$ loaded liposomes by TEM

Metal-drug complexation has been established as a successful strategy to encapsulate different drugs within liposomal delivery systems. Many of these studies have proposed that the advantage of such complexation is developing stable liposomes capable of achieving high complex-to-lipid ratios, with excellent complex retention [402,489]. In turn, the solubility of these metal-drug complexes and the nature of their precipitation has shown to govern their kinetics of release and overall therapeutic efficacy. However, high drug loading may also compromise drug release and therefore the *in vivo* therapeutic activity of liposomes. It is important to balance complex loading, retention, stability and

release and maximizing complex encapsulation to a certain limit may have its downfalls. A particular study using copper-vincristine [489] showed an outstanding loading efficiency (5:1, lipid-to-complex molar ratio), which resulted in enhanced complex precipitation within the liposome core but compromised drug release. Another interesting example of this paradox was stated by Li *et al.* [402], where, once again, the nature of the drug-complex influenced liposomal drug-release and consequently the overall anti-tumour activity. In line with this, and with the data obtained in this thesis (EE markedly increasing with higher complex-to-lipid molar ratios) it was essential to question how this complex was encapsulated inside the liposomal vesicles and if it led to the formation of stable drug precipitates that compromised liposomal activity. To assess this, liposome morphology was evaluated using TEM with and without negative staining (2% uranyl acetate). The negative staining experiment was used as an internal control to confirm that electron density derived from $Cu(TPZ)_2$ encapsulation within the liposomal vesicles (**Appendix, Figure A1**). Moreover, free $Cu(TPZ)_2$ complexes (**Figure 4.13A**) were imaged at a concentration comparable to that of the loaded liposomes for comparison of morphology and size.

Empty DOPC liposomes (**Figure 4.13B**) without staining appeared spherical in shape with no apparent electron density; where size was in good agreement with previous DLS results (*ca.*100 nm). $Cu(TPZ)_2$ loading into liposomes was further confirmed, illustrated by the high electron density observed inside the liposomes at both 140:1 (**Figure 4.13C**) and 60:1 (**Figure 4.13D**) lipid-to-complex ratios. Even at a lower ratio of 140:1, liposomes already exhibited increased intra-vesicular density. The encapsulated complex appeared as a diffuse and small bundled fibre-like structure (**Figure 4.13C, inset)**, which can derive from precipitation of the small particle complexes (*ca.* 4-5 nm) observed for the free complex (**Figure 4.13A)**. At 60:1 lipid-to-complex ratio (**Figure 4.13D)** a large proportion of the liposomes contains electron dense precipitation as a dotted, granular and diffused structure of the complex possibly due to increased precipitation of the complex (**Figure 4.13D, inset)**. These structures are unlike the more linear precipitates observed for other drugs such as topotecan [403], but similar to that reported for copper-vincristine [489] and copper-Dox [448] and appeared to precipitate at a much faster rate and lower drug ratios than previously reported [273,477,490].

Furthermore, this increase in electron density could represent an amorphous or gel-like precipitate at the lower $Cu(TPZ)_2$ contents that becomes more prominent with higher drug contents. The precipitate formed can be dense (single crystal appearence) or diffused as separate fibres, but the physical state may be difficult to resolve at high densities using TEM [491]. Cryo-electron microscopy (cryo-EM) and even small-angle X-ray scattering (SAXS) or X-ray diffraction studies [403] could help to elucidate the structure of this complex within the liposome core.

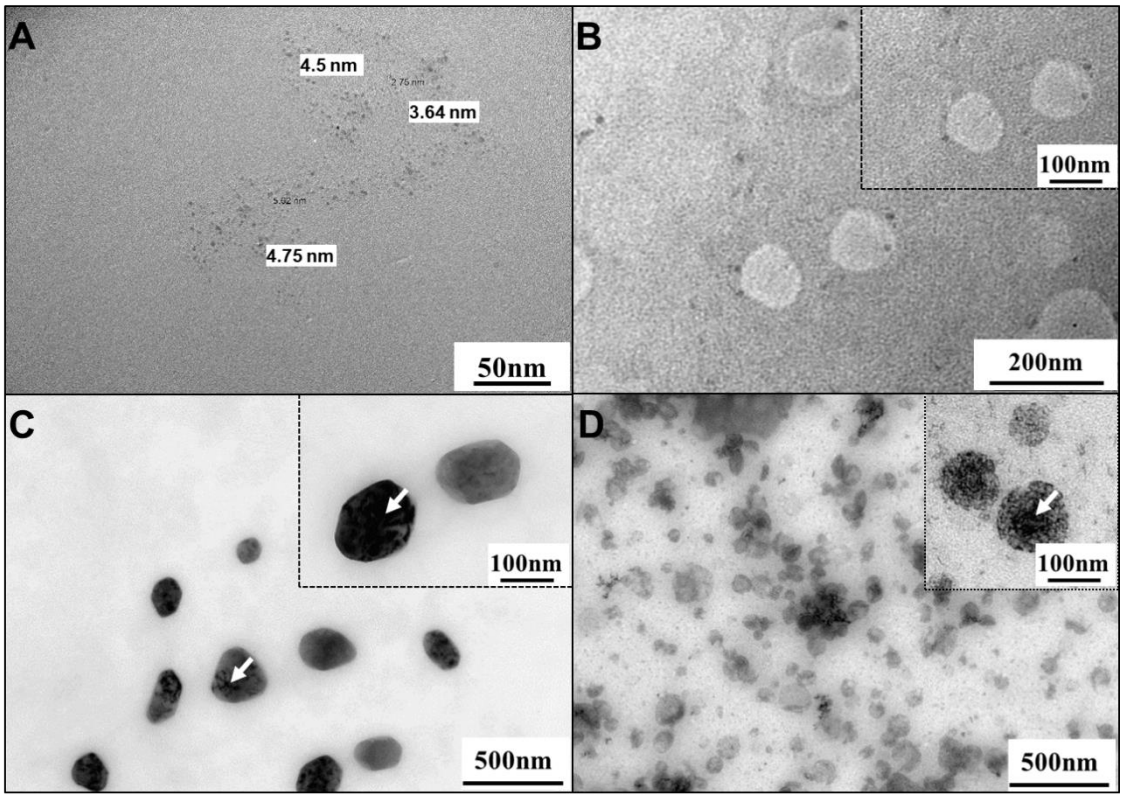

Figure 4.13. Structural elucidation of Cu(TPZ)$_2$-loaded liposomes. Transmission electron microscopy images of A) Cu(TPZ)$_2$ (20 µM) and unstained purified DOPC-Cu(TPZ)$_2$ liposomes at varying lipid-to-complex molar ratios of B) 1:0, (empty); C) 140:1 and D) 60:1. White arrows depict small precipitated bundles and dotted/diffused structures of Cu(TPZ)$_2$. Each panel is representative of at least 5 images per condition.

Cryo-EM is a versatile imaging technique that maintains liposomes in their native state and allows high resolution of drug precipitates and polymorphs, within nano-systems. In fact previous studies with copper-doxorubicin complexes showed the presence of precipitation as a dotted and diffused structures using cryo-EM, which were uniformly distributed inside the liposomes [448]. These structures are like those obtained herein and should be validated using alternative methods. Understanding the true physical-state of the encapsulated complex is an interesting link to its release mechanism and consequently to its biological activity. Imaging at 20:1 lipid-to-complex ratio was performed and aggregation and even fused vesicle structures were observed (**Appendix, Figure A2**) further complementing the higher PDI values obtained by DLS; and the adequate choice of 60:1 lipid-to-complex ratio as the optimum drug loaded formulation.

In conclusion, Cu(TPZ)$_2$ was efficiently encapsulated in the liposomal core, but its presence in the lipid bilayer cannot be ruled out. Furthermore, the increasing electron density with increasing complex-to-lipid ratio is preliminary evidence for drug precipitation within the liposomal core. Such findings led to the hypothesis that the main driving force for Cu(TPZ)$_2$ encapsulation is its high lipid permeability and low solubility.

4.2.3.7. *In vitro* release studies of $Cu(TPZ)_2$ and $Cu(TPZ)_2$-loaded liposomes

To fully exploit the potential of the novel liposomes prepared in this work, it is important to understand their ability to enhance or attenuate drug release over time and how this can complement their biological outcome. Initially, a dynamic dialysis method was used to evaluate the solubility, stability and diffusion (indicated as cumulative release) of free $Cu(TPZ)_2$. Complex stocks in DMSO were then diluted to 10 and 100 µM of $Cu(TPZ)_2$ and placed into a pre-swelled Pur–A–Lyzer™ Maxi Dialysis tube (12 kDa molecular weight cut-off). The dialysis tube was incubated in 30 mL release media (HBS containing 1% Tween-80), where the use of this surfactant aided with solubility and generated the most reliable sink conditions (sheer volume needed to provide complete dissolution of the drug in context). After taking 1 mL samples at specified time-points, the cumulative release % or diffusion of free $Cu(TPZ)_2$ was determined (**Figure 4.14**) and values were normalized taking into account drug/volume withdrawal, with respect to dilution factors.

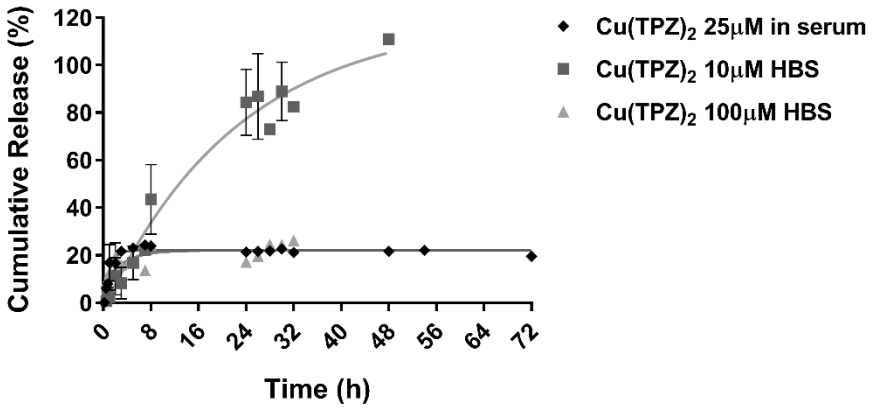

Figure 4.14. *In vitro* release profile of free $Cu(TPZ)_2$ in saline and serum conditions. Dynamic dialysis was used to analyse the diffusion or cumulative drug release over 72h. Release % was determined by HPLC and corrected for volume and drug withdrawal. Data was expressed as mean ± SD for triplicate samples of three independent experiments (n=3).

The results showed a quick release of $Cu(TPZ)_2$ (10 µM), where over 80% of the drug was released in the first 24h. In contrast, $Cu(TPZ)_2$ (100 µM), showed a steady release around 20% with no further differences in drug release, over a period of 72 h. Although dynamic dialysis or dissolution tests are the gold standard to evaluate release kinetics for drug carriers, it is essential to assume that the method complies with the sink conditions. By definition, these conditions are satisfied upon usage of a release medium which is at least three times the volume needed to form a saturated solution of the drug [470,492]. This makes any back diffusion to the donor compartment negligible, thus allowing complete solubility of the drug and adequately reflecting the release performance of the drug carrier in biological conditions [470,492]. Nevertheless, satisfying these conditions is quite challenging for poorly-water soluble drugs such as $Cu(TPZ)_2$, therefore the concentration dependent release profile discussed above was not surprising. These results are in agreement with those obtained

previously for other drugs [493], where concentrations above the solubility limit created supersaturated solutions that clearly underestimated the release profile. At 100 µM $Cu(TPZ)_2$, small drug precipitates were observed inside the dialysis membrane, from very early on in the experiment. This indicated that only a small portion of the dissolved $Cu(TPZ)_2$ in HBS could pass the membrane and became diluted in the release medium resulting in a low quantity of released drug. This result was counteracted when only 10 µM $Cu(TPZ)_2$ was used, but high variability was observed in the experiment as many samples collected in the release medium were below the detection limit for HPLC analysis. In addition, when serum conditions were used, the drug solubility was somewhat increased (25 µM $Cu(TPZ)_2$ was used), possibly complying with sink conditions and mimicking *in vitro* milieu. However, the release kinetics was also compromised, perhaps due to the interaction of the complex with serum proteins [494] limiting the methods applicability to liposomal release. In summary, the findings call for alternative methods to evaluate the release profile of $Cu(TPZ)_2$ that do not lead to underestimation of the released drug. Therefore, a different method relying on SEC was adapted to determine liposomal drug release.

4.2.3.7.1. *In vitro* release studies of $Cu(TPZ)_2$-loaded liposomes

Given the poor solubility, precipitation and possible interaction of the complex with the dialysis membrane, an alternative indirect method to quantify the dynamic release of $Cu(TPZ)_2$ from liposomes was developed. The premises of this strategy relied on the fact that non-encapsulated/released complex can be retained in the SEC matrix (possibly due to some metal-resin interaction), as depicted in **figure 4.15**. Based on the initial drug loading, the release kinetics can be easily determined by quantifying the remaining drug encapsulation over time after sample withdrawal and purification. $Cu(TPZ)_2$-loaded liposomes at 60:1 lipid-to-complex ratio, were chosen due to their excellent drug encapsulation and stability.

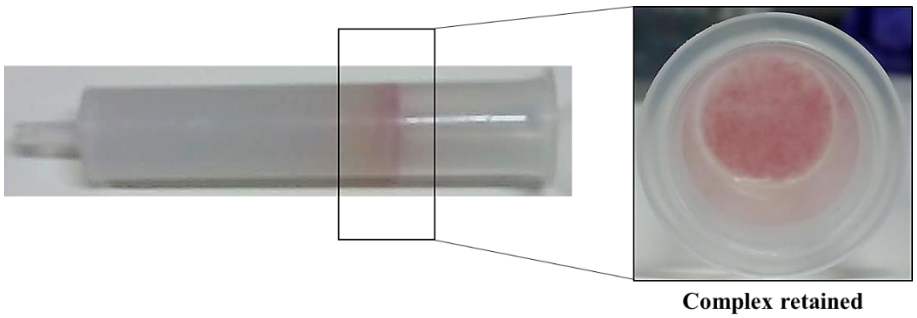

Figure 4.15. Illustration of free $Cu(TPZ)_2$ retention in the size exclusion chromatography matrix. This characteristic allowed the adequate separation of non-encapsulated complex from loaded liposomes.

The samples were further diluted in release conditions and, at specified time-points, the withdrawn solutions were purified by SEC and EE was determined by HPLC to evaluate drug loss. In HBS, there was an initial burst release of Cu(TPZ)$_2$ at 37 °C, for DOPC-Cu(TPZ)$_2$ (30.79 ± 5.44 %), DPPC-Cu(TPZ)$_2$ (21.13 ±8.89%) and DSPC-Cu(TPZ)$_2$ (31.31 ± 6.43%) (**Figure 4.16A**). This was then followed by sustained release kinetics [< 40% of Cu(TPZ)$_2$], over a period of 48h; indicating good stability of the drug carriers in these conditions, with no statistically significant differences between the formulations tested. The initial drug loss observed could be attributed to Cu(TPZ)$_2$ that is poorly adsorbed at the liposomal surface or encapsulated in the bilayer. Despite the presence of drug precipitation, suggested by TEM imaging of Cu-(TPZ)$_2$-liposomes, drug release did not seem to be compromised.

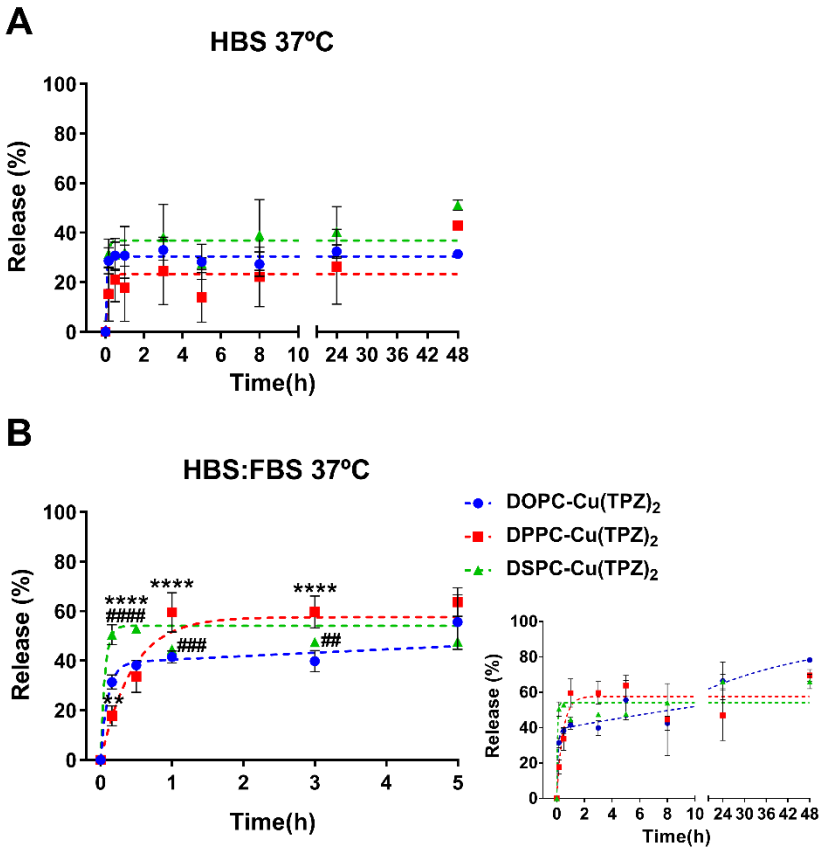

Figure 4.16. ***In vitro*** **release profile of Cu(TPZ)$_2$-loaded into different liposomes.** DOPC:Chol:DSPE-PEG$_{2000}$, DPPC:Chol:DSPE-PEG$_{2000}$ and DSPC:Chol:DSPE-PEG$_{2000}$ (5mM. 95:50:5 molar ratio) liposomes were incubated with Cu(TPZ)$_2$ at 60:1 lipid-to-complex molar ratio for 30 min at 55 ºC, followed by purification. The loaded liposomes are abbreviated as DOPC-Cu(TPZ)$_2$, DPPC-Cu(TPZ)$_2$, DSPC-Cu(TPZ)$_2$, respectively. The release kinetics of Cu(TPZ)$_2$-loaded liposomes incubated at 37 ºC in A) HBS buffer pH 7.4 up to 48 h , and B) 50% serum up to 5 h. Inset: continuous release in serum, over 48 h. The release % was determined by HPLC, after liposome purification. Data was expressed as mean ± SD for triplicate samples of two independent experiments (n=2) and were fitted to a two-phase kinetics association model. Statistical analysis: Two-way ANOVA multiple comparison with Tukey Post-test was performed to compare groups within the same time-point (**p <0.01 and ****p <0.0001, compared to DOPC; $^{\#\#}$p <0.01, $^{\#\#\#}$p <0.001 and $^{\#\#\#\#}$p <0.0001, compared to DSPC).

However, the release profile of $Cu(TPZ)_2$-liposomes seemed to reveal slightly slower-release kinetics (< 50% release, over 48 h), compared to other TPZ-NPs (*ca*. 20-40% released drug in the first 5-10h, followed by continuously increased TPZ release) [378,380,382,383], possibly due to complex precipitation, which conferred stability to the system [489]. Also, none of these studies evaluated serum-mediated release and relied on other stimuli such as pH [75,376,378], chemical cleavage [379,380] or irradiation [383] to induce TPZ leakage. Herein, the release profile in HBS:FBS (1:1, v/v) (**Figure 4.16B**) was also analysed in order to mimic the biological milieu. Interestingly, these results supported the previous assumption in HBS where an initial burst release of the drug was obtained for all formulations but at higher levels due the destabilizing effect of the serum proteins [495-497]. Unexpectedly, the most rigid DSPC-$Cu(TPZ)_2$ formulation exhibited the fastest burst complex release (*ca.* 50% in the first 1 h) compared to DPPC- $Cu(TPZ)_2$ (17.79%, $p<0.0001$), and DOPC-$Cu(TPZ)_2$ (31.49%, $p <0.0001$).

In contrast, the fluid DOPC-$Cu(TPZ)_2$ liposomes showed the slowest release (*ca.*40% in the first 1 h). This sustained release profile of DOPC-$Cu(TPZ)_2$ was maintained over the initial 5h of release and DPPC-$Cu(TPZ)_2$ surpassed the other formulations showing the highest drug release at 1h and 3 h ($p < 0.0001$). Furthermore, a more sustained release profile was observed with all formulations (60-80% drug release over 48 h). In conclusion, the complex release in serum was highly influenced by the composition of the liposomes, which proved to play a role on the *in vitro* activity under hypoxia in both 2D and 3D PCa models (discussed in **chapter 5**) and does not disregard possible modulation of their therapeutic efficiency *in vivo*. Future work comparing different lipid-to-complex ratios, complemented by cryo-TEM imaging may, give further insight on the release mechanism.

4.2.3.8. Long term stability of $Cu(TPZ)_2$ loaded liposomes

After the successful preparation and characterisation of novel $Cu(TPZ)_2$ liposomes it was important to assess their long term stability at 4°C storage conditions. Loaded $Cu(TPZ)_2$ liposomes were analysed by DLS on a weekly basis and repurified using SEC to quantify any drug leakage. As depicted in **table 4.7**, DOPC-$Cu(TPZ)_2$ liposomes showed marked increase in size (140.3 ± 2.72 nm to 178.9 ± 4.63 nm) and PDI (0.139 ± 0.03 to 0.349 ± 0.107), with about 30% reduction in encapsulated drug (week 0: EE=83.39 ± 1.56 %, week 4: DR=53.95 ± 0.71 %) after 1 month. This data correlated well with previous stability studies (**section 4.2.3.1.1**), suggesting aggregation and instability of this formulation over time. Following a similar trend, DPPC-$Cu(TPZ)_2$ liposomes exhibited increased size (171.8 ± 0.89 nm), narrow PDI (0.137 ± 0.02), and displayed good drug retention (week 0: EE= 80.32 ± 3.71 %, week 4: DR=54.19 ± 2.02%). In contrast, DSPC-$Cu(TPZ)_2$ liposomes maintained an acceptable size (147.2 ± 1.45 nm) and narrow PDI (0.132 ± 0.05), with improved drug retention (week 0: EE=85.47 ± 1.40%, week 4: DR=69.96 ± 1.36 %), compared to other formulations.

Table 4.7. Stability of Cu(TPZ)$_2$-loaded liposomes over 1 month. DOPC:Chol:DSPE-PEG$_{2000}$, DPPC:Chol:DSPE-PEG$_{2000}$ and DSPC:Chol:DSPE-PEG$_{2000}$ (5mM phospholipid, 95:50:5, molar ratio) liposomes were prepared in HBS (pH 7.4) and incubated with Cu(TPZ)$_2$ at 60:1 lipid-to-complex molar ratio at 55 ºC for 30 min. The purified liposomes (DOPC-Cu(TPZ)$_2$, DPPC-Cu(TPZ)$_2$, and DOPC-Cu(TPZ)$_2$) were stored at 4 ºC for 4 weeks. The hydrodynamic size (Z-ave), polydispersity (PDI) and EE were determined immediately after preparation (week 0) and DR (drug retention) at 4 weeks of storage. Data was expressed as mean ± SD for triplicate samples of three independent experiments (n=3).

	Week 0			Week 4		
Formulation	**Z-ave (nm)**	**PDI**	**EE (%)**	**Z-ave (nm)**	**PDI**	**DR (%)**
DOPC-Cu(TPZ)$_2$	140.3 ± 2.72	0.139 ± 0.03	83.39 ± 1.56	178.9 ± 4.63	0.35 ± 0.107	53.95 ± 0.71
DPPC-Cu(TPZ)$_2$	130.3 ± 1.02	0.02 ±0.005	80.32 ± 3.71	171.8 ± 0.89	0.14 ± 0.02	54.19 ± 2.02
DSPC-Cu(TPZ)$_2$	156.2 ± 3.00	0.07 ± 2.91	85.47 ± 1.40	147.2 ± 1.45	0.13 ± 0.05	69.96 ± 1.36

This data was in good agreement with the preliminary stability studies performed previously and with literature reports discussing the high stability and reduced drug leakage of DSPC-Chol liposomes [257,483,488]. In summary, all formulations depicted excellent EE, but lipid composition is an essential parameter to consider in terms of long-term drug retention and stability, despite the inclusion of Chol. Previous studies have suggested lyophilisation or increased lipid content <100 mM as alternative strategies to overcome drug leakage in liposomal formulations [498], which will be an interesting approach for future optimization of the developed protocol.

4.3. Summary and conclusions

TPZ is a well-established HAP that has shown excellent hypoxia selectivity. Recently, the development of nanocarriers has been proposed as a good strategy to modulate TPZs PK and toxicity hurdles, while improving its biological efficacy. Both conjugation [376,377] or encapsulation strategies [75,378-380,382,383] have been employed to deliver TPZ *via* NPs. These studies showed rather limited drug cargo and have been mostly exploited as combinatorial treatment modalities.

Liposomes are the most widely described and clinically accepted drug delivery systems and their dual capacity in encapsulating both hydrophilic and hydrophobic compounds [248,499] make them versatile candidates to load TPZ. To date, only one study has shown the encapsulation of TPZ in a liposomal system, which showed good synergistic effect with post-PDT hypoxia [384] but limited EE (2.4%). Further improvements on TPZ loading efficiency are warranted, as well as improvement on TPZ-NP efficacy as a monotherapy.

In this chapter, the encapsulation of TPZ in different liposomal formulations was explored by designing both passive and remote loading strategies. Unfortunately, all attempts to show an efficient encapsulation of this drug in various liposomal formulations failed or were unsuccessfully reproducible (SVI method). It seemed that drug leakage was difficult to prevent, limiting TPZ liposomal loading, which is common for small amphiphilic molecules. Alternatively, $Cu(TPZ)_2$ was used as a metal-drug complex with the aim of increasing liposomal-TPZ loading.

The pre-complexation of TPZ to copper led to the development of a successful remote loading method in physiological HBS without the need for pH gradients or ionophores. This metal-drug complex yielded high EE (>70%) of TPZ in all conditions tested and in three different liposomal formulations. This work established a new loading method, which substantially improved TPZ liposome loading [384] using copper complexation. Moreover, a particular 60:1 lipid-to-complex molar ratio displayed biocompatible size, PDI, ζ-potential, good drug loading, sustained release profile and adequate long-term stability; which made them ideal for *in vitro* applications.

The following conclusions were drawn from this chapter:

- TPZ was difficult to encapsulate in liposomes. Conjugation or modulation of its chemical structure may be important factors to consider, when developing new NP's for TPZ loading;
- TPZ-copper complexation was an interesting strategy to develop a new metal-drug complex with increased lipophilicity and MW, which seemed to promote TPZ liposomal retention;
- The metal-TPZ loading method allowed high encapsulation of TPZ in different lipid compositions, at varying incubation temperatures and smaller sized vesicles;

- In acidic pH, $Cu(TPZ)_2$ loading is compromised by complex dissociation, leading to TPZ liposomal leakage and decreased EE. Loading in physiological HBS yielded high EE and stable liposomes;
- Different liposomal formulations were successfully developed with increased TPZ loading, due to precipitation and 'trapping' of liposomal-$Cu(TPZ)_2$. The complexes' limited solubility and lipophilicity may be the main driving forces that enhance TPZ loading.
- Complex precipitation did not compromise liposomal drug release, maintaining a sustained release kinetics in both HBS and serum conditions;
- High $Cu(TPZ)_2$ EE was achieved up to a 20:1 lipid-to-complex molar ratio, but formulations displaying a 60:1 ratio maintained biocompatible size, PDI and ζ-potential. The latter formulations were chosen for biological applications.

Chapter 5

Biological activity of $Cu(TPZ)_2$ and $Cu(TPZ)_2$-loaded liposomes

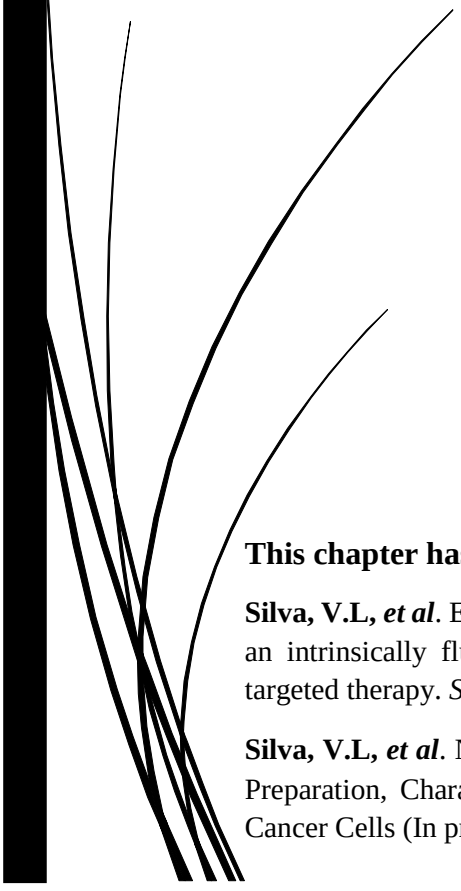

This chapter has been included in the following publications:

Silva, V.L, *et al*. Enhanced selectivity, cellular uptake, and *in vitro* toxicity of an intrinsically fluorescent copper-tirapazamine nanocomplex for hypoxia targeted therapy. *Submitted to* ACS *Bioconjugate Chemistry* (under revision).

Silva, V.L, *et al*. Novel Hypoxia Selective Cupric-Tirapazamine Liposomes: Preparation, Characterisation and *In vitro* Activity in 2D and 3D Prostate Cancer Cells (In preparation).

5.1. Overview

PCa is the second most common cancer in men and the fifth leading cause of death by cancer worldwide [195]. Disease progression from primary hormone-responsive lesions into CRPC has been associated to high mortality rates, poor clinical outcome and resistance to current treatments [202]. Moreover, hypoxia has shown to play a detrimental role in androgen signalling, which concurrently drives PCa progression and aggressiveness [219,226]. A previous study using TPZ and castration therapy in the Dunning H rat prostate cancer model provided first-line evidence of promising synergy between the use of HAPs and classical PCa treatments [228]. However, despite its promising cytotoxicity *in vitro*, TPZ's translational activity has been limited by its poor cellular uptake and rapid consumption while diffusing through the tumour tissue. Overcoming these limitations has warranted the synthesis of new analogues, TPZ-metal complexes and/or the development of novel DDS.

Many promising HAPs and hypoxia targeted nano-systems have shown controversial results in mouse models and humans. Many of these hypoxic therapies show promising activity *in vivo* but failed to translate their efficacy to a clinical set-up. Substantial efforts have been made to develop more reliable *in vitro* methods that can then be successfully translated to *in vivo* and clinical set-up [60]. 2D cell culture on synthetic plastic surface has been a mainstay model system for preliminary drug screening since the 1970's. Although this method continues to offer a convenient, cost-effective, rapid and reproducible means of testing new drug platforms in a high-throughput way it does not effectively mimic the complexity and heterogeneity of tumours [425,500]. It is now a well-established concept that tumours are not flat. Therefore, cell adherence and a restricted 2D space, causes severe limitations that improperly representing the tumour geometry and microenvironment [500]. Multicellular tumour spheroids (MCTS) or 3D tumour models are considered better cancer models that could aid with improving clinical drug predictions [501,502]. MCTS are self-assembled spherical cell clusters easily formed *in vitro* by a variety of methods and constitute a versatile drug screening platform [423,426]. Kemlin *et al.* [503], reported the importance of the unique tumour architecture that 3D cultures provide, evidencing the following *in vivo* features (**Figure 5.1**): 1) formation of cell-cell interactions; 2) cell stratification including proliferating and quiescent cells in the outer and inner spheroid shell, respectively; 3) possibility of producing extracellular matrix; 4) generation of nutrient, ATP and oxygen gradients; 5) development of hypoxia and necrosis; 6) reduced drug penetration and response with augmented treatment resistance and 7) modulation of protein expression and DNA repair mechanisms [425]. Spheroids with size of about 200-300 μm are known to have zones of both proliferating and quiescent cells, thus establishing physiological gradients leading to cell heterogeneity [501]. Larger spheroids (>400 μm) present a well-defined proliferating outer-shell with hypoxic mid-region and central necrotic core, representing poorly vascularized tumours and micro-metastasis [504]. These MCTS have shown to be an interesting

model to assess the efficacy and resistance to HAPs such as TPZ [505]. Spheroids can thus provide an optimised tool to possibly predict *in vivo* drug response, while potentially bridging the gap between preclinical and clinical models, as well as overcoming limitations of inter-species variations. It is not surprising to conclude that NPs will interact differently with 2D and 3D cell models given the more realistic diffusion gradient and treatment resistance conferred by the latter [500]. Also, the physicochemical properties of NPs will directly influence their interaction with biological systems. Parameters such as size, surface charge, bilayer fluidity and composition, lipid-spheroid interaction and steric hindrance (PEGylation) have been shown to influence the efficacy of liposomal systems in spheroid models and their penetration. It is therefore expected that the standard biological assays constitute a paradigm shift, where 2D and 3D complementary models are used to assess both free drugs and liposomal delivery systems [501].

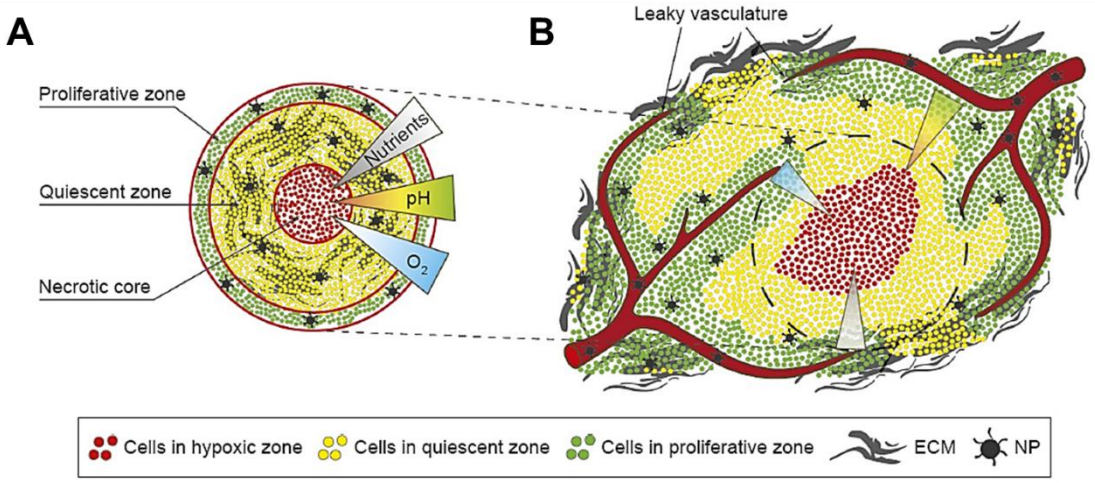

Figure 5.1. Schematic representation of the well-established similarity between spheroid models and *in vivo* tumour environment. A) Spheroid model illustrating generation of nutrient, energy and oxygen gradients, as well as, cell heterogeneity, where the outer shell composes proliferating cells encompassing a core of hypoxic and necrotic cells. These features will be relevant for the biological efficacy of nanoparticles (NPs). B) *In vivo* tumour model displaying similar characteristics to *in vitro* spheroids, proving the adequate representation of these models for avascular tumours and *in vivo* milieu, including the extracellular matrix (ECM) [506].

In this chapter, the biological activity of TPZ and $Cu(TPZ)_2$ was evaluated against a panel of 4 different PCa cell lines (LNCap, C4-2B, DU145 and PC3) cultivated in monolayer. The resazurin assay was used to assess cell viability over time while cultivating cells under different oxygen conditions, thus determining drug efficacy. These data provided significant knowledge on the hypoxia selectivity and potency of this complex compared to TPZ alone, using cell lines representing different metabolic/hypoxic profiles and disease stage. Furthermore, based on the data obtained, C4-2B was selected and used for the remainder of the project. The fluorescent properties of $Cu(TPZ)_2$ discussed in **chapter 3** provided an interesting tool to assess the cellular uptake and localization of these complexes over a period of 24h in C4-2B cells under normoxia and hypoxia. Moreover, it was possible to quantitatively assess the uptake efficiency of both drugs in this cell line, which could be

easily correlated to their physicochemical properties (*e.g.* lipophilicity and redox potential) analysed in **chapter 3**. In addition, given the previously reported DNA damaging effects of TPZ and of similar cupric-complexes, DNA binding studies were also conducted. Together, these results provided first-line evidence on the cellular uptake and activity of $Cu(TPZ)_2$ against PCa highlighting the biological potency and relevance of this work in the context of the field.

Additionally, the data presented in **chapter 4** showed that $Cu(TPZ)_2$ was important in enhancing TPZ-liposomal encapsulation. Biological studies were also conducted by treating C4-2B cells with $Cu(TPZ)_2$-loaded liposomes (60:1 lipid-to-drug molar ratio), comparing their therapeutic outcome to the complex and TPZ alone. The remainder of the chapter focussed on applying these assays in 3D models of C4-2B. The growth and morphological characterisation of these spheroids were assessed over a period of 14 days, as well as their hypoxic profile to further establish treatment modality. Discussion on the optimization and application of the resazurin assay for these models was provided allowing a detailed analysis of the cytotoxicity of TPZ, $Cu(TPZ)_2$ and $Cu(TPZ)_2$-loaded liposomes. The results proved relevant in distinguishing drug activity in a complex 3D environment compared to the previous monolayer counterparts suggesting differences in redox activity, toxicity/resistance, drug penetration and liposomal interaction. Finally, analysis on cell cycle progression provided data that were correlated with toxicity and DNA binding profiles. In several respects, these findings can be pave the way to further establish drug regimens using $Cu(TPZ)_2$ *in vivo*, and understand the advantage of using liposomal systems to significantly improve TPZ based hypoxic treatments in PCa.

5.2. Results and discussion

5.2.1. Part I: biological assays conducted in 2D PCa models

5.2.1.1. *In vitro* hypoxia validation

Hypoxia, was confirmed using a commercially available Cyto-ID® Hypoxia Detection Kit, where a substrate probe becomes fluorescent upon reduction by hypoxia-induced cellular nitroreductases [416]. **Figure 5.2** displays representative fluorescent images of both C4-2B and LNCap cells cultivated under normoxia (21% O_2) and hypoxic conditions (1% O_2) using a modular hypoxia chamber as specified in section **2.5.3.1** (**chapter 2**). Compared to normoxia, both cell lines exhibited strong red fluorescence upon treatment with desferrioxamine (DFO, 200 µM), a hypoxia biomimetic agent, for 4 h, validating the experimental set-up. Furthermore, cells cultivated under 1% hypoxia also exhibited strong red fluorescence compared to the normoxia, confirming the establishment of hypoxia *in vitro*. The data verified that degassing of the modular chamber induced a metabolic shift, with up-regulation of intracellular nitroreductases, under hypoxia. This then led to the reduction of the amine-based hypoxia probe and consequently to the production of a strong red fluorescent cell signal. These results were as expected [416] and agreed with previous studies exploiting this probe [507,508].

5.2.1.2. *In vitro* cytotoxicity and hypoxia selectivity of TPZ and $Cu(TPZ)_2$ complexes

Hypoxia is an early on-set feature of PCa, thus screening different PCa models may hinder valuable data on hypoxic drug regimens and cell sensitivity. Continuous advancement in PCa research has now established over 200 cell lines and derived sublines isolated form primary, metastatic and normal prostate tissue [509-511]. LNCap, PC3 and DU145 still remain the gold standard triad of PCa *in vitro* cell models, due to their common use in mouse xenografts [411]. LNCap cells were isolated from lymph node metastasis [512] and constitute an important cell model that responds to androgen stimulation (despite the already mutated AR receptor) and expresses high levels of PSA. Given its low tumourigenicity in athymic mouse models, different sublines of LNCap have been developed to increase its proliferative and metastatic capability. The androgen-independent subline, LNCap C4-2 was developed by Thalmann and co-workers after subcutaneously co-injecting LNCap and human osteosarcoma MS cells in castrated mice, to drive androgen insensitivity [513]. This model also led to the development of different metastatic sites, including osteoblastic lesions (common in human PCa) that allowed the isolation and establishment of the highly tumourigenic, metastatic and androgen insensitive C4-2B cell line [514]. In contrast, PC3 and DU145 were isolated from vertebral [515] and brain [516] metastatic sites, respectively, and do not present AR or express PSA. These two cell lines display high tumourigenicity, androgen-independence and chemo-resistance, similar to LNCap C4-2, and are frequently referred to as CRPC cell models, despite the fact that they do not possess AR [413].

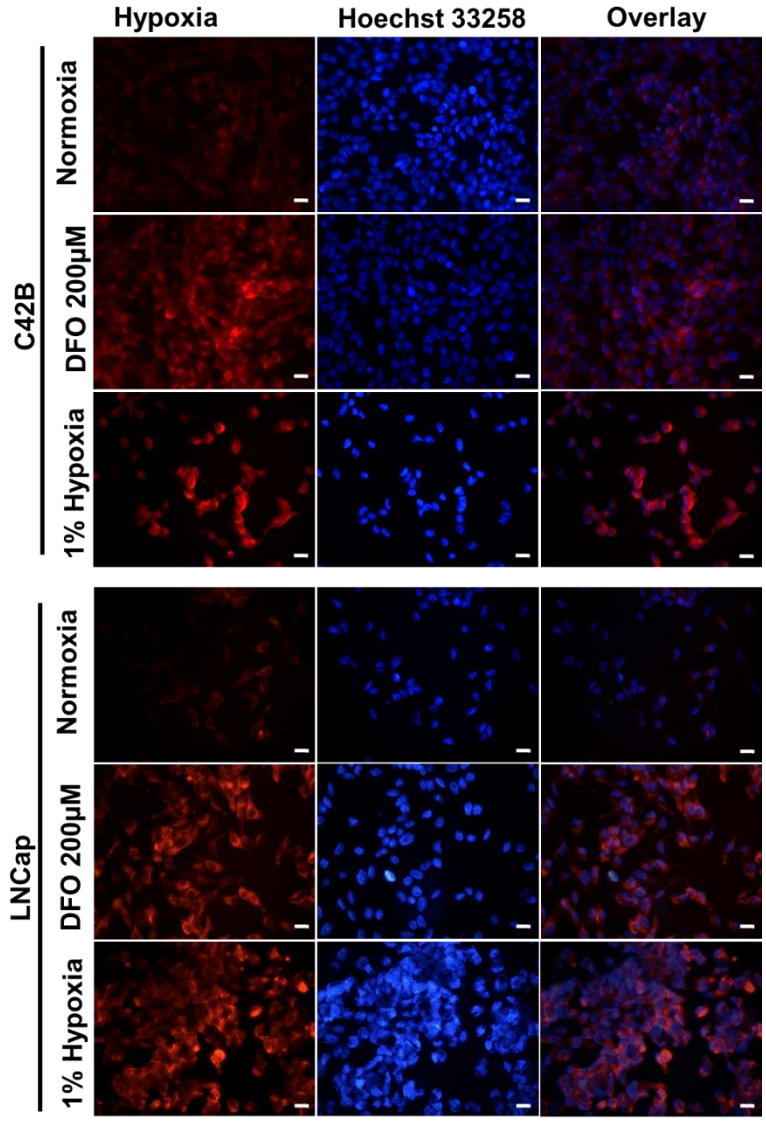

Figure 5.2. Hypoxia validation in C4-2B and LNCap prostate cancer cells. C4-2B (Top) and LNCap (bottom) cells were incubated under either normoxic (21% O_2, top panels) or hypoxic (1% O_2, bottom panels) conditions. Desferrioxamine (DFO) (200 μM) was used as a chemical inducer of hypoxia (positive control) (middle panels). Cyto-ID® Hypoxia detection kit was used to validate hypoxia, following the manufacture's protocol. Fluorescent images are representative of two independent experiments (n=2) and cells were stained with hypoxia probe (red channel) and Hoechst 33258 for nuclei staining (blue channel), scale bar 20 μm.

After validating the experimental hypoxia set-up, the selectivity and potency of free TPZ and $Cu(TPZ)_2$ complexes were analysed under normoxia (21% O_2) and 1% hypoxia in 4 different PCa cell lines. As discussed above, these cell lines were chosen according to their representation of earlier (LNCap) and late stage PCa. This analysis provided a first-line screening of the effect of TPZ and $Cu(TPZ)_2$ for hypoxic PCa. Furthermore, the inhibitory effect (IC_{50}) was calculated in all conditions and used to assess the hypoxia cytotoxicity ratio (HCR, IC_{50} normoxia/IC_{50} hypoxia), which expressed the selectivity of the compounds under hypoxic conditions. The potency (IC_{50}) and selectivity of TPZ and its complex were taken as measurements of hypoxia efficacy. It is expected that lower IC_{50} values correlate with improved drug activity.

However, in terms of selectivity it is expected that the IC_{50} values are increased under normoxia compared to hypoxia, proving that the compounds function as hypoxia-sensitive pro-drugs. Overall, the results demonstrated that cytotoxicity was cell-line, time and drug-dependent.

5.2.1.2.1. LNCap

LNCap has been reported as androgen-dependent [512] and possess wild-type p53 [511,517] representing an early onset of PCa. Studies have also shown a concomitant shift in its metabolism and overall phenotype, upon exposure to low oxygenated environments [518]. After continuous exposure to TPZ and $Cu(TPZ)_2$, LNCap showed pronounced sensitivity to both drugs. There was a significant decrease in cell viability under 1% hypoxia, depicted by a decrease in IC_{50} dose at 48, 72 and 96h (**Figure 5.3**). This shift was accompanied by increased hypoxia selectivity (HCR) (higher IC_{50} value under normoxia), over time, for both TPZ (**Figure 5.3, top panel**) and $Cu(TPZ)_2$ (**Figure 5.3, bottom panel**). LNCap cells have been shown to readapt under hypoxia, through a metabolic shift, which may sensitize these cells to hypoxia-selective treatments [518,519].

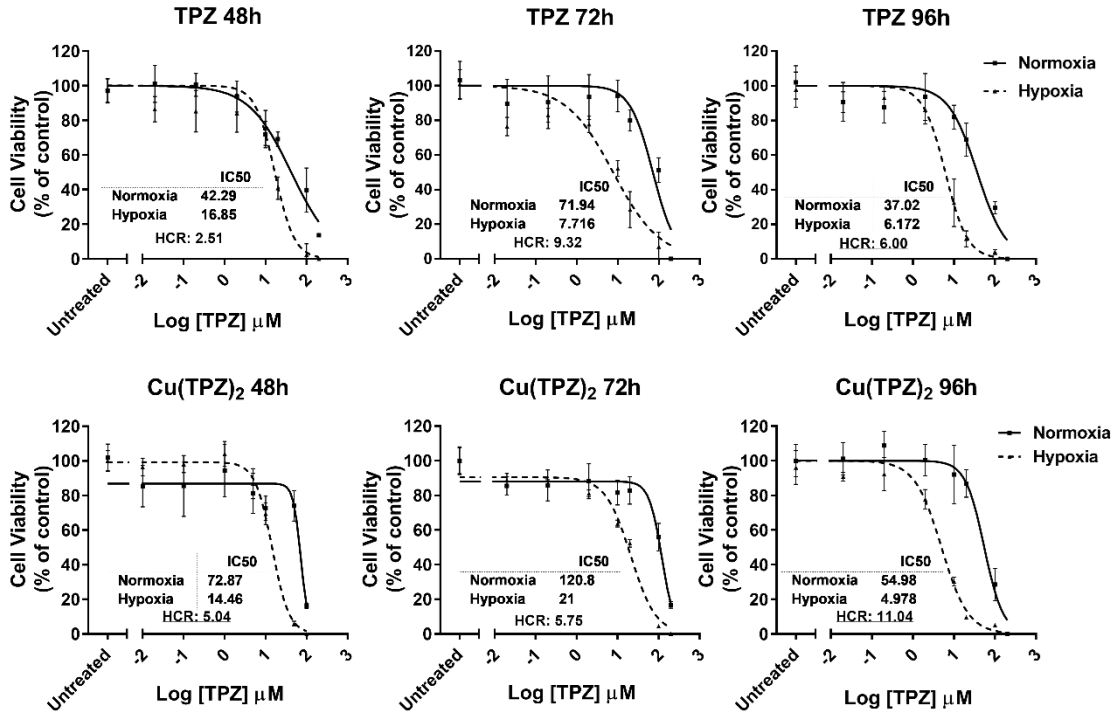

Figure 5.3. Analysis of cell viability in LNCap prostate cancer cells incubated with TPZ and $Cu(TPZ)_2$ under normoxia and 1% hypoxia. LNCap cells were incubated under both conditions with equivalent doses of TPZ (top panel) and $Cu(TPZ)_2$ (bottom panel) for 48, 72, and 96h. Cell viability was assessed by the resazurin assay, normalized to untreated and data was expressed as mean ± SD for six replicates of three independent experiments (n=3). The IC_{50} (μM) and HCR values were also presented (inset).

After determining the IC_{50}, it was evidenced that both agents exhibited extremely significant potentiation of their cytotoxicity under 1% hypoxia, even after 96h ($p<0.0001$) (**Figure 5.4**). At 48h, $Cu(TPZ)_2$ presented a 1.72 fold-increase in selectivity, compared to TPZ ($p<0.0001$) marked by a significant increase in IC_{50} under normoxia [$Cu(TPZ)_2$: IC_{50}, 72.87 ± 1.78 µM; TPZ: IC_{50}, 42.29 ± 1.09 µM]; while both agents showed similar potency under 1% hypoxia [$Cu(TPZ)_2$: IC_{50}, 14.46 ± 1.05 µM; TPZ: IC_{50}, 16.85 ± 1.02 µM]. Moreover, at 72h, $Cu(TPZ)_2$ still maintained pronounced hypoxia selectivity ($p<0.0001$), but TPZ was 3.5-fold more potent than $Cu(TPZ)_2$ ($p<0.001$). Finally, at 96h $Cu(TPZ)_2$ (IC_{50}, 4.98 ± 1.02 µM) surpassed TPZ activity (IC_{50}, 6.17 ± 1.03 µM; $p<0.05$). This data indicated overall improvement in hypoxia selectivity of $Cu(TPZ)_2$, compared to TPZ ($p<0.0001$).

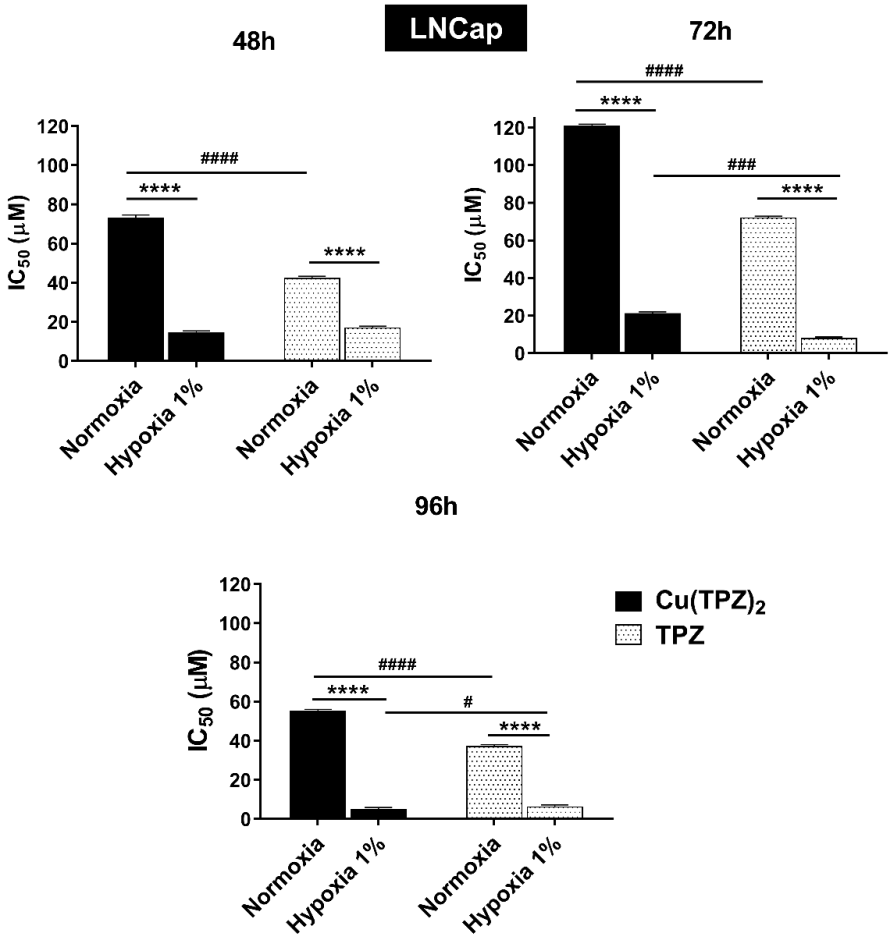

Figure 5.4. IC_{50} values to determine potency and selectivity of TPZ *vs*. $Cu(TPZ)_2$ under normoxia and 1% hypoxia, after continuous drug exposure in LNCap prostate cancer cell line. Cells were incubated with equivalent doses of TPZ in free and complex. IC_{50} values were determined at 48, 72 and 96h, The IC_{50} values for inhibition were assessed by the resazurin assay. Data was expressed as mean ± SD for six replicates of at least three independent experiments (n>3). Statistical analysis: Two-way ANOVA multiple comparison Bonferroni Post-test ($^{****}p<0.0001$, comparing normoxia to hypoxia; $^{\#}p<0.05$, $^{\#\#\#}p<0.001$ and $^{\#\#\#\#}p<0.0001$ comparing $Cu(TPZ)_2$ to TPZ).

5.2.1.2.2. C4-2B

Unlike LNCap, C4-2B is a derived bone metastatic PCa cell model. It espresses low levels of p53 and has been described as androgen-independent [520], with tumourigenic phenotype [411,413]. This cell line is a particularly relevant CRPC model due to its capacity to form osteoblastic PCa-induced bone metastasis *in vivo* [520] C4-2B could provide interesting pre-clinical data in terms of sensitivity to HAPs as both primary and metastatic tumour model.

Like LNCap, C4-2B was sensitive to both drugs, with clear dose-response shifts to the left under 1% hypoxia (**Figure 5.5**). The effect was especially pronounced in terms of hypoxia selectivity, confirmed by the overall decreased HCR values of TPZ (**Figure 5.5, Top panel**) compared to $Cu(TPZ)_2$ (**Figure 5.5, bottom panel**). The HCR values were consistently higher for the complex, compared to TPZ and achieved exceptional selectivity at 72h post-treatment, marked by a significantly low IC_{50} value under hypoxia, compared to normoxia (HCR: $Cu(TPZ)_2$, 69.66; TPZ, 19.26).

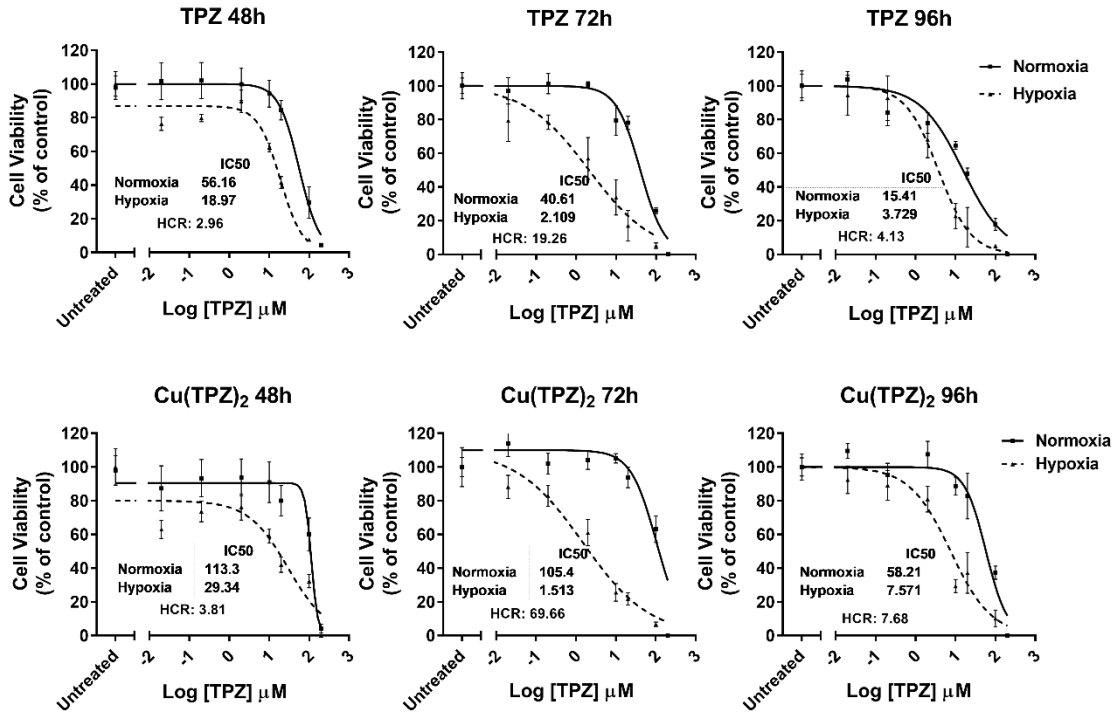

Figure 5.5. Analysis of cell viability in C4-2B prostate cancer cells incubated with TPZ and $Cu(TPZ)_2$ under normoxia and 1% hypoxia. C4-2B cells were incubated under both conditions with equivalent doses of TPZ (top panel) and $Cu(TPZ)_2$ (bottom panel) for 48, 72, and 96h. Cell viability was assessed by the resazurin assay, normalized to untreated and data was expressed as mean ± SD for six replicates of three independent experiments (n=3). The IC_{50} (μM) and HCR values were also presented (inset).

Furthermore, the cytotoxic effects under normoxia revealed a 2.03, 2.61 and 3.78-fold increase in IC_{50} (at 48, 72 and 96h, respectively) for $Cu(TPZ)_2$ compared to TPZ alone ($p<0.0001$) (**Figure 5.6**). Surprisingly, for this cell line, potentiation of the complex under hypoxia (IC_{50}: 1.51 ± 1.0 µM), compared to TPZ (IC_{50}: 2.831 ± 1.04 µM, $p<0.05$) was also obtained at 72h time-point. However, potency was lost after long exposure periods (96h, TPZ: IC_{50}: 3.79 ± 1.02 and $Cu(TPZ)_2$: 7.57 ± 1.03 µM). Nonetheless, selectivity under hypoxia was obtained throughout the whole time-course indicating that $Cu(TPZ)_2$ may function as a metal-HAP, with additional improved hypoxia selectivity compared to TPZ. These findings can be therapeutically relevant in tumour models and prompt further investigation in an *in vivo* set-up. The data also correlated well with the selective hypoxia uptake of $Cu(TPZ)_2$ obtained in C4-2B cells (discussed in **section 5.2.1.3**), which can be correlated to the lipophilic nature of this complex, compared to TPZ **(chapter 3)**. Furthermore, the increased expression of hypoxia markers in this cell line can also contribute to its enhanced selectivity and sensitivity to these hypoxic agents [521].

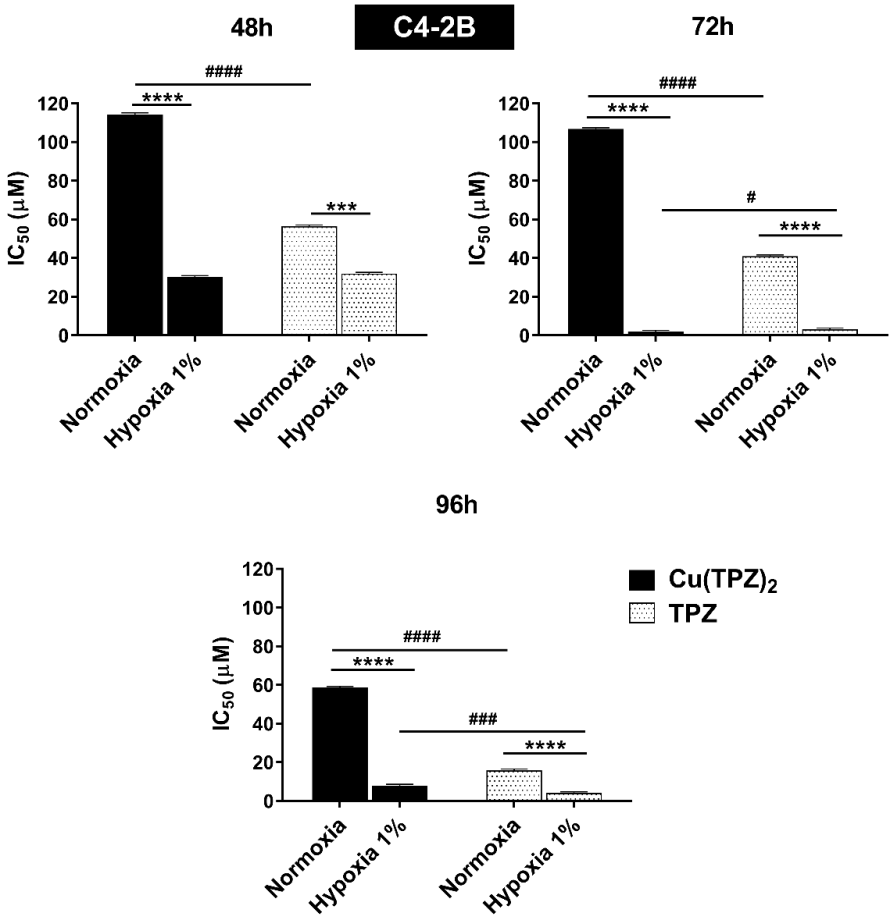

Figure 5.6. IC_{50} values to determine potency and selectivity of TPZ *vs.* $Cu(TPZ)_2$ under normoxia and 1% hypoxia, after continuous drug exposure in C4-2B prostate cancer cell line. Cells were incubated with equivalent doses of TPZ in free and complex. IC_{50} values were determined at 48, 72 and 96h, The IC_{50} values for inhibition were assessed by the resazurin assay. Data was expressed as mean ± SD for six replicates of at least three independent experiments (n>3). Statistical analysis: Two-way ANOVA multiple comparison Bonferroni Post-test ($^{***}p<0.001$, $^{****}p<0.0001$, comparing normoxia to hypoxia; $^{\#}p<0.05$, $^{\#\#\#}p<0.001$ and $^{\#\#\#\#}p<0.0001$ comparing $Cu(TPZ)_2$ to TPZ).

5.2.1.2.3. DU145

The cytotoxicity of the drugs was also assessed against the CRPC tumourigenic DU145 cell line, which possesses mutated p53 [411,516]. Contrary to both LNCap and C4-2B there was a less prominent left shift in the dose response curves for the two drugs (**Figure 5.7**), indicative of lower response to treatment by DU145. This was further underpinned by lower HCR values exhibited by TPZ (**Figure 5.7, top panel**) and Cu(TPZ)$_2$ (**Figure 5.7, bottom panel**), compared to the previous cell lines. Nevertheless, despite the decreased HCR values, it was still encouraging to observe that the prodrugs exhibited enhancement of cytotoxicity at 1% hypoxia ($p<0.0001$).

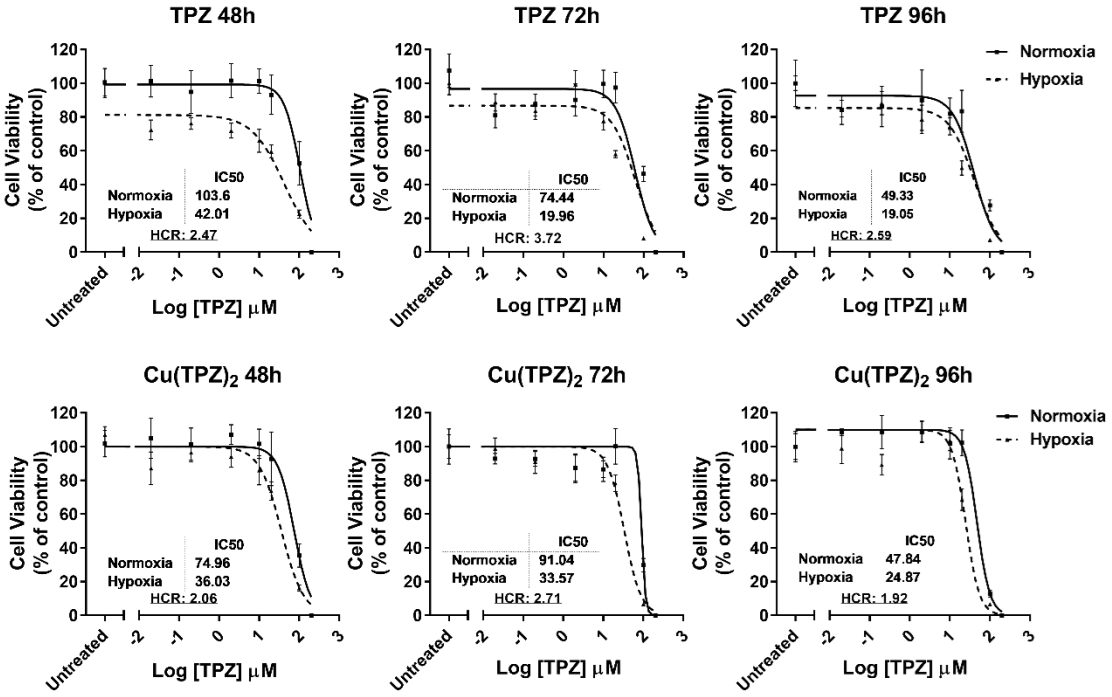

Figure 5.7. Analysis of cell viability in DU145 prostate cancer cells incubated with TPZ and Cu(TPZ)$_2$ under normoxia and 1% hypoxia. DU145 cells were incubated under both conditions with equivalent doses of TPZ (top panel) and Cu(TPZ)$_2$ (bottom panel) for 48, 72, and 96h. Cell viability was assessed by the resazurin assay, normalized to untreated and data was expressed as mean ± SD for six replicates of three independent experiments (n=3). The IC$_{50}$ (µM) and HCR values were also presented (inset).

DU145 presented a variable response to treatment (**Figure 5.8**), with less sensitivity to the HAPs, compared to LNCap and C4-2B. At 48h, TPZ IC$_{50}$ under normoxia (IC$_{50}$: 103.6 ± 1.02) resulted in higher selectivity compared to Cu(TPZ)$_2$ (IC$_{50}$: 74.96 ± 1.02 µM, $p<0.0001$), but with similar IC$_{50}$ values under hypoxia. At 72h, higher selectivity was obtained for Cu(TPZ)$_2$ (IC$_{50}$: 91.04 ± 2.43 µM) under normoxia, compared to TPZ (IC$_{50}$: 74.44 ± 1.08 µM, $p<0.0001$). However, both drugs had higher potency under 1% hypoxia ($p<0.0001$). Finally, at 96h, this cell line exhibited similar sensitivity to both drugs, under both oxygenated conditions.

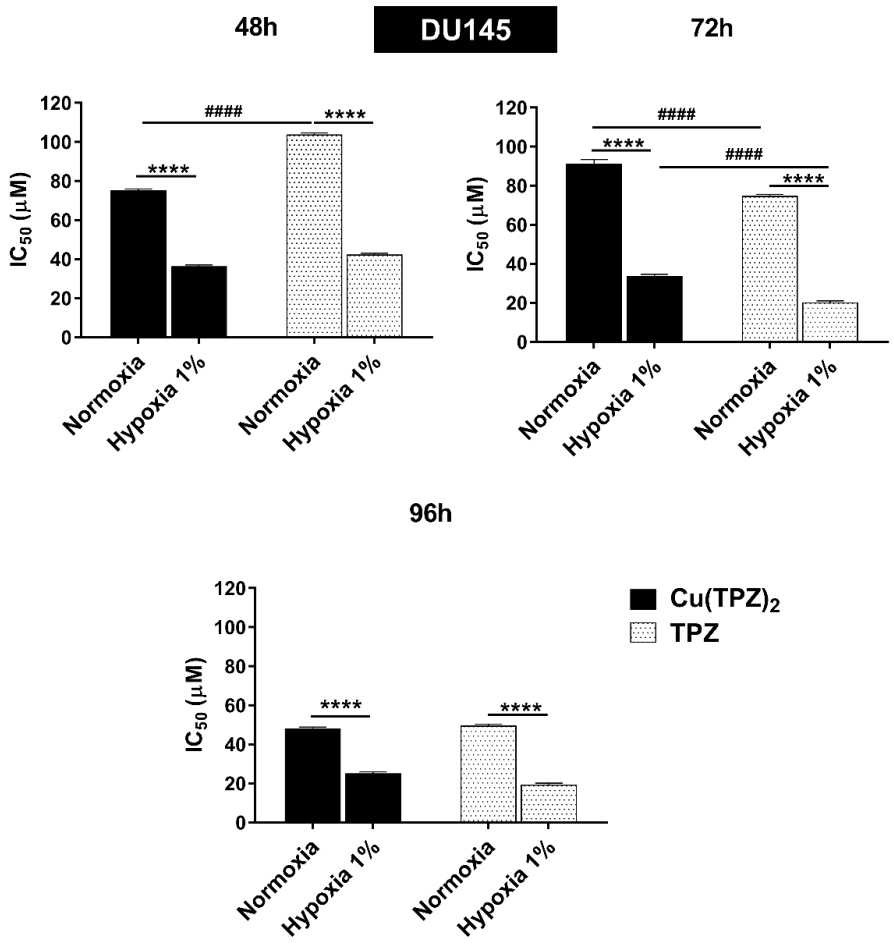

Figure 5.8. IC_{50} values to determine potency and selectivity of TPZ *vs.* $Cu(TPZ)_2$ under normoxia and 1% hypoxia, after continuous drug exposure in DU145 prostate cancer cell line. Cells were incubated with equivalent doses of TPZ in free and complex. IC_{50} values were determined at 48, 72 and 96h, The IC_{50} values for inhibition were assessed by the resazurin assay. Data was expressed as mean ± SD for six replicates of at least three independent experiments (n>3). Statistical analysis: Two-way ANOVA multiple comparison Bonferroni Post-test ($^{****}p<0.0001$, comparing normoxia to hypoxia; $^{####}p<0.0001$ comparing $Cu(TPZ)_2$ to TPZ).

In a more general analysis, DU145 showed a 2.49, 2.56 and 3.08-fold decrease in potency under hypoxia for TPZ; and 2.49, 1.59 and 4.99-fold decrease for $Cu(TPZ)_2$, at 48, 72 and 96h respectively, compared to LNCap. This effect was more pronounced compared to C4-2B, where IC_{50} values under hypoxia were 1.32, 7.05 and 5.10-fold lower for TPZ and 1.26, 20.81 and 3.28-fold lower for $Cu(TPZ)_2$, at 48, 72 and 96h respectively. This confirms the lower therapeutic sensitivity of this cell line, whilst selectivity was still maintained, but to a lesser extent (HCR>2). The aggressive phenotype of DU145 and its rapid adaptation to hypoxia made it refractory to treatment [518,522].

5.2.1.2.4. PC3

The final cytotoxicity screening was performed against the CRPC cell line PC3, which has been established as p53 deficient [511,515], to possess defects in cytochrome c oxidase (COX) [518], which modulates copper transport and metabolism and express higher basal levels of HIF-1α in both normoxia and hypoxia [226]. PC3 showed higher resistance to treatment compared to the previous cell lines, well represented by the overlap of the dose-response curves obtained under normoxia and hypoxia, over 96h (**Figure 5.9**).

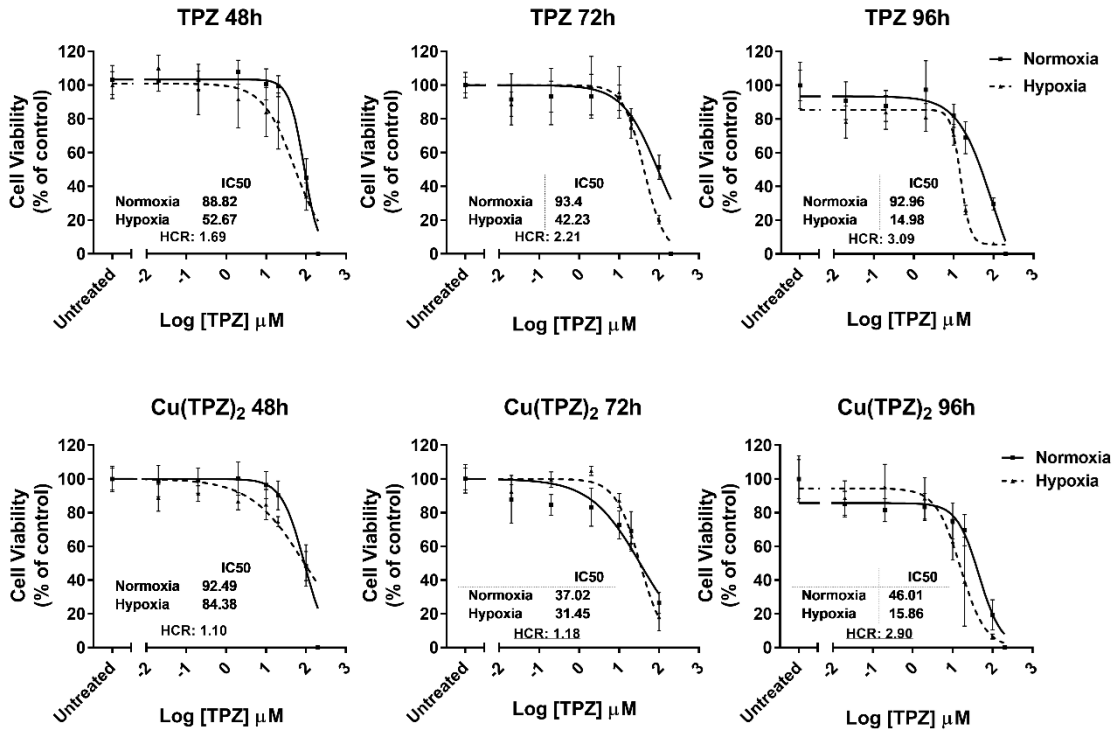

Figure 5.9. Analysis of cell viability in PC3 prostate cancer cells incubated with TPZ and Cu(TPZ)$_2$ under normoxia and 1% hypoxia. PC3 cells were incubated under both conditions with equivalent doses of TPZ (top panel) and Cu(TPZ)$_2$ (bottom panel) for 48, 72, and 96h. Cell viability was assessed by the resazurin assay, normalized to untreated and data was expressed as mean ± SD for six replicates of three independent experiments (n=3). The IC$_{50}$ (µM) and HCR values were also presented (inset).

This cell line exhibited the lowest HCR values of the PCa screening panel for both TPZ (**Figure 5.9, top panel**) and Cu(TPZ)$_2$ (**Figure 5.9, bottom panel**), showing no selectivity or potency of the drugs under hypoxia, especially for the TPZ-complex.

The resistance of PC3 to the prodrug action was further confirmed by the reported IC$_{50}$ values under normoxia and hypoxia (**Figure 5.10**). At 48h, PC3 was not sensitive to Cu(TPZ)$_2$ in either normoxia (IC$_{50}$: 92.49 ± 1.02 µM) or hypoxia (IC$_{50}$: 84.38 ± 1.07 µM), whilst selectivity and potency of TPZ was significantly maintained under 1% O_2, compared to normoxia ($p<0.001$). Significant loss of selectivity was also observed for Cu(TPZ)$_2$ (normoxia, IC$_{50}$: 37.02 ± 1.06 µM; hypoxia, IC$_{50}$: 31.45 ± 1.02 µM), compared to TPZ alone ($p<0.0001$).

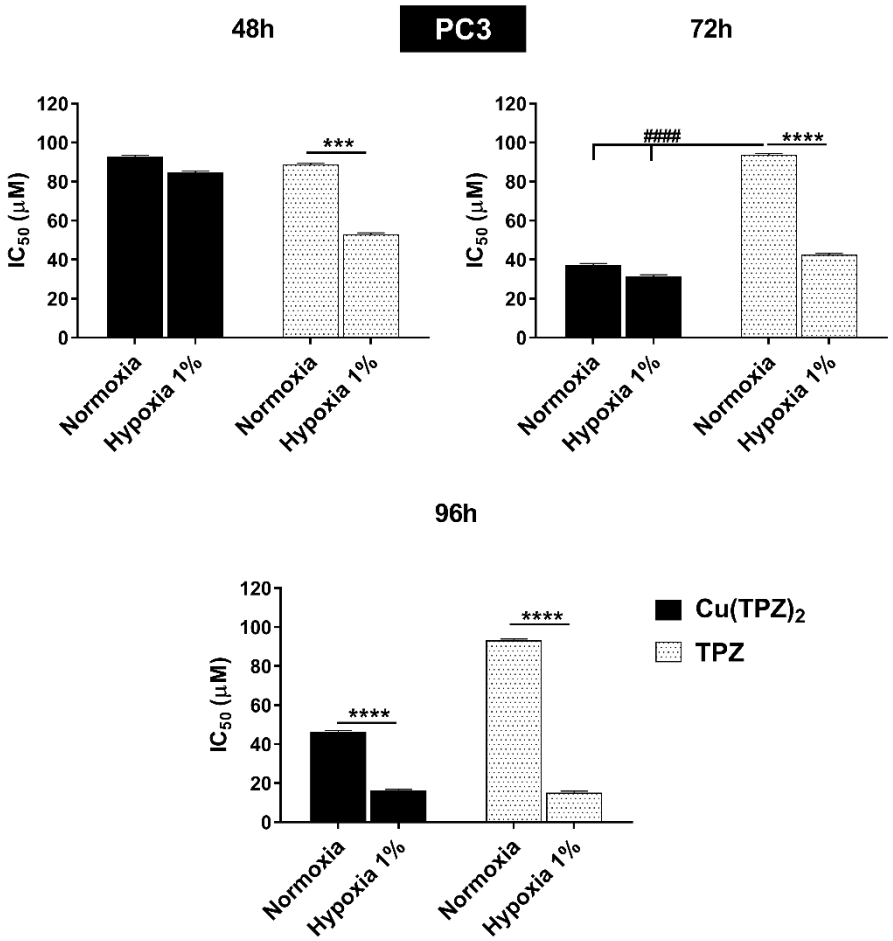

Figure 5.10. IC_{50} values to determine potency and selectivity of TPZ *vs.* $Cu(TPZ)_2$ under normoxia and 1% hypoxia, after continuous drug exposure in PC3 prostate cancer cell line. Cells were incubated with equivalent doses of TPZ in free and complex. IC_{50} values were determined at 48, 72 and 96h, The IC_{50} values for inhibition were assessed by the resazurin assay. Data was expressed as mean ± SD for six replicates of at least three independent experiments (n>3). Statistical analysis: Two-way ANOVA multiple comparison Bonferroni Post-test ($^{***}p<0.0001$ and $^{****}p<0.0001$, comparing normoxia to hypoxia; $^{####}p<0.0001$ comparing $Cu(TPZ)_2$ to TPZ).

At 96h, both drugs exhibited similar potency under both normoxia and hypoxia, but hypoxia selectivity was better for TPZ. The data obtained herein showed that PC3 is the most resistant of the PCa panel analysed in this work and, more importantly, showed loss of hypoxia selectivity for $Cu(TPZ)_2$. A previous report examined a series of cell lines (PC3 included), determining the IC_{50} and HCR of a HAP (PR104) using TPZ as a positive control [523]. In this report PC3 exhibited good therapeutic response to TPZ treatment (IC_{50} *ca.* 20 μM and HCR *ca.* 90), but, to note, cell proliferation was evaluated under extreme hypoxic conditions (anoxia, $O_2<0.1\%$) and over 5 days' post-treatment, *via* sulforhodamine B (SRB) and clonogenic assays. In line with these findings it is reasonable to argue that PC3 cells, along with DU145, may require more aggressive hypoxic/anoxic conditions to establish prodrug sensitivity. In addition, the diminished selectivity and effectiveness may have arisen from the augmented basal levels of HIF-1α under normoxia, previously reported in both CRPC cell lines [226,524].

In turn, this can cause overexpression of reductive nitroreductases and increased ROS activity (shifting the redox paradigm), which can intensify HAP activity even under normoxia [522]. Elevated basal oxidative stress and diminished GSH-mediated antioxidant capacity can hamper copper detoxification, potentiating $Cu(TPZ)_2$ cytotoxicity under normoxia [165,518].

5.2.1.2.5. General discussion

Two different studies evaluated the potency of TPZ and several of its analogues *in vitro* using clonogenic and SRB assays [147,460]. The data showed an IC_{50} of 30 µM for TPZ under severe hypoxia, achieving HCR of 75 compared to other analogues (potency between 1-30 µM and HCR values 10-150) in Chinese hamster lung fibroblasts (V79 cells) [147]. Moreover, similar results were obtained for SCC and colorectal cancer [460]. Furthermore, an MTT assay in nasopharyngeal cancer cells revealed the efficacy of TPZ at 48 h post-treatment, with an IC_{50} of 54.73 µM (normoxia) *vs.* 6.18 µM (hypoxia) [115]. Together, these findings are in good agreement with the results obtained herein for PCa cancer models, confirming the efficacy of TPZ under 1% hypoxia. The efficacy of this drug is well-known to be cell-line dependent [102,103,115]. It is noteworthy that most studies were performed over several days of treatment, under strict hypoxia conditions, and cytotoxicity was then evaluated using time-consuming, but sensitive techniques, such as clonogenic assays. These experiments can show prodrug efficacy over multiple cloning generations due to extreme DNA damaging, establishing higher HCR values for TPZ compared to other viability assays (resazurin, MTT, SRB, etc.). Future experiments using clonogenic assays could provide detailed complimentary data regarding TPZ and $Cu(TPZ)_2$ *in vitro* activity.

A detailed evaluation on the structure-activity relationship of TPZ analogues has been conducted, correlating their redox potential [E°(1)] with their hypoxia selectivity [147,460]. The main conclusions were that the *N*-oxide group is essential for TPZ selectivity and that $E^0(1)$ values ranging from -0.45 to -0.51 V resulted in maximum HCR due to decreased reduction of the drug under normoxia. This resulted in augmented hypoxia selectivity, with improved therapeutic outcomes for prodrugs exhibiting more electronegative redox potentials (*e.g.* metal-complex derived prodrugs) [174,181,455]. Accordingly, it was encouraging to observe that $Cu(TPZ)_2$ [$E^0(1)$, -0.75 V] (**chapter 3**) [385], caused an increase of hypoxia selectivity preferentially in LNCap and C4-2b cells, compared to TPZ alone [$E^0(1)$, -0.65 V] [147]. Also, improved hypoxia potency was obtained, in C4-2B, and IC_{50} value (1.51 ± 1.0 µM) resulted in superior hypoxia efficacy compared to other copper-complexes (IC_{50} 10-20 µM) [168,169]. Taking into consideration the differential biological activity obtained across the PCa panel assessed in this work, it is reasonable to conclude that cell oxygenation may not be the only parameter affecting prodrug reduction. These findings clearly call for caution when analysing *in vitro* toxicity and that the effect is marked by different factors, beyond oxygenation.

Numerous reports found that factors such as p53 status [525-527], expression of reductive enzymes (*e.g.* cytochrome c P450) [108,111,528], CA-IX [78], acidic microenvironment [529] and expression of homologues recombination proteins (XRCC2, Rad51D, BRCA1 and BRCA2) [530] could influence TPZ sensitivity by modulating DNA repair. Future analysis regarding gene and protein expression in these PCa cell lines could help elucidate the MoA of both TPZ and $Cu(TPZ)_2$.

TPZ cytotoxicity has been correlated to p53 status, which is cell-line dependent. TPZ-induced cell death has been shown to be p53-dependent in neuroblastoma cells [525] and p53-independent in NSLC and SCC [526,527]. The findings from the current work suggest a p53-dependent mechanism of cell death because both LNCap (wild-type p53) and C4-2B (expresses p53) were highly sensitive to treatment [517]. In contrast, p53 mutant or deficient cell lines, DU145 and PC3 respectively, showed reduced sensitivity to both TPZ and $Cu(TPZ)_2$.

Furthermore, the distinct metabolic profile under hypoxia and tumour aggressiveness is marked by defects in DNA repair mechanisms and increased basal ROS levels [518,531]. LNCap is particularly responsive to hypoxia, dramatically shifting its metabolic response and decreasing ATP levels, with augmented lactate production and increased external pH [518]. This can explain the increased sensitivity to treatment, where decreased efflux of the drugs can increase their hypoxia accumulation [518,519]. Furthermore, augmented basal levels of HIF-1α under normoxia present in DU145 and PC3 cells, along with their well-described genetic instability and defects in DNA repair mechanisms, may have instigated their resistance to treatment. Moreover, PC3 presents a peculiar hypoxia phenotype, even under well oxygenated conditions [518]. Compared to DU145, PC3 appeared to have elevated basal levels of HIF-1α, ROS and GSH, creating a more reductive intracellular environment [518]. Therefore, exposure to $Cu(TPZ)_2$ could have led to elevated copper pools that diminished the cell capacity to handle ROS induced damage, leading to cell apoptosis even under normoxia contributing to loss of selectivity [165,522].

In conclusion, the most promising results were obtained at 72h post-treatment, where hypoxia selectivity of $Cu(TPZ)_2$, was improved in the following order, compared to TPZ: C4-2B>LNCap>DU145>PC3. All IC_{50} and HCR values obtained in this work have been summarised in **table 5.1**.

Table 5.1. IC_{50} values and hypoxia cytotoxicity ratio (HCR) in 4 different prostate cancer cell lines, following continuous drug exposure under aerobic or different hypoxic conditions. Values represent mean ± SD of six replicates of at least two independent experiments ($n \geq 2$). IC_{50} values were determined by nonlinear regression analysis of the data fit to a four-parameter equation (GraphPad Prism version 7).

IC_{50} (μM)						
Cell line	**TPZ**			**$Cu(TPZ)_2$**		
LNCap	Normoxia	Hypoxia 1%	HCR	Normoxia	Hypoxia 1%	HCR
48h	42.29 ± 1.09	16.85 ± 1.02	1.77	72.87 ± 1.78	14.46 ± 1.03	5.04
72h	71.94 ± 1.06	7.71 ± 1.04	14.34	120.8 ± 1.09	21.00 ± 1.04	5.75
96h	37.02 ± 1.05	6.17 ± 1.04	4.13	54.98 ± 1.04	4.98 ± 1.02	11.04
C4-2B	Normoxia	Hypoxia 1%	HCR	Normoxia	Hypoxia 1%	HCR
48h	56.16 ± 1.03	18.97 ± 1.02	2.96	113.3 ± 1.01	29.92 ± 1.06	3.81
72h	40.61 ± 1.04	2.81 ± 1.04	19.26	105.4 ± 1.09	1.51 ± 1.04	69.66
96h	15.41 ± 1.14	3.72 ± 1.04	4.13	58.21 ± 1.05	7.57 ± 1.03	7.68
DU145	Normoxia	Hypoxia 1%	HCR	Normoxia	Hypoxia 1%	HCR
48h	103.6 ± 1.02	42.01 ± 1.07	2.47	74.96 ± 1.02	36.03 ± 1.04	2.06
72h	74.44 ± 1.08	19.96 ± 1.06	3.72	91.04 ± 2.43	33.57 ± 1.04	2.71
96h	49.33 ± 1.07	19.05 ± 1.05	2.59	47.84 ± 1.04	24.87 ± 1.05	1.92
PC3	Normoxia	Hypoxia 1%	HCR	Normoxia	Hypoxia 1%	HCR
48h	88.82 ± 1.02	52.67 ± 1.06	1.69	92.49 ± 1.02	84.38 ± 1.07	1.10
72h	93.40 ± 1.06	42.24 ± 1.04	2.21	37.02 ± 1.06	31.45 ± 1.02	1.18
96h	92.96 ± 1.05	14.97 ± 1.05	6.2	46.01 ± 1.04	15.86 ± 1.04	2.90

5.2.1.3. Cellular uptake and localization of $Cu(TPZ)_2$ complexes in C4-2B

5.2.1.3.1. Fluorescence microscopy

Development and application of copper mediated cell sensors has proven difficult due to the general quenching properties of this metal upon coordination [453]. However, attempts to develop efficient copper-based fluorescent probes have been successful and used for bioimaging purposes [451,452]. Surprisingly, the findings presented in **chapter 3** regarding the fluorescent properties of $Cu(TPZ)_2$, allowed the use of this complex as an imaging tool for cellular uptake and localization. Different fluorescent-based techniques have been widely exploited to assess uptake and localisation of fluorescent compounds both qualitatively (fluorescence microscopy) and quantitatively (fluorimetry, FACs).

Encouraged by the stable fluorescent properties of the complex, the cellular localization and accumulation of $Cu(TPZ)_2$ was monitored. Fluorescence microscopy provided direct observation of the uptake and intracellular localization of the complex, and further complimented by the quantitative analysis discussed below. In **figure 5.11**, representative images taken at 1, 4, 8 and 24h, showed the cellular accumulation of $Cu(TPZ)_2$ (green fluorescence) in C4-2B cells, with counterstained nuclei (blue fluorescence) to further assess cell localization.

The results depicted a rapid uptake of the complex, with a strong green fluorescent intensity in the cytosol and perinuclear region even after 1h of incubation under both normoxia and 1% hypoxia. Cellular uptake gradually increased over time and at 4h, the appearance of bright green punctate structures (**figure 5.11,** white arrows) particularly in hypoxic conditions, suggested that copper complexes can also accumulate in lysosomal compartments or autophagic structures.

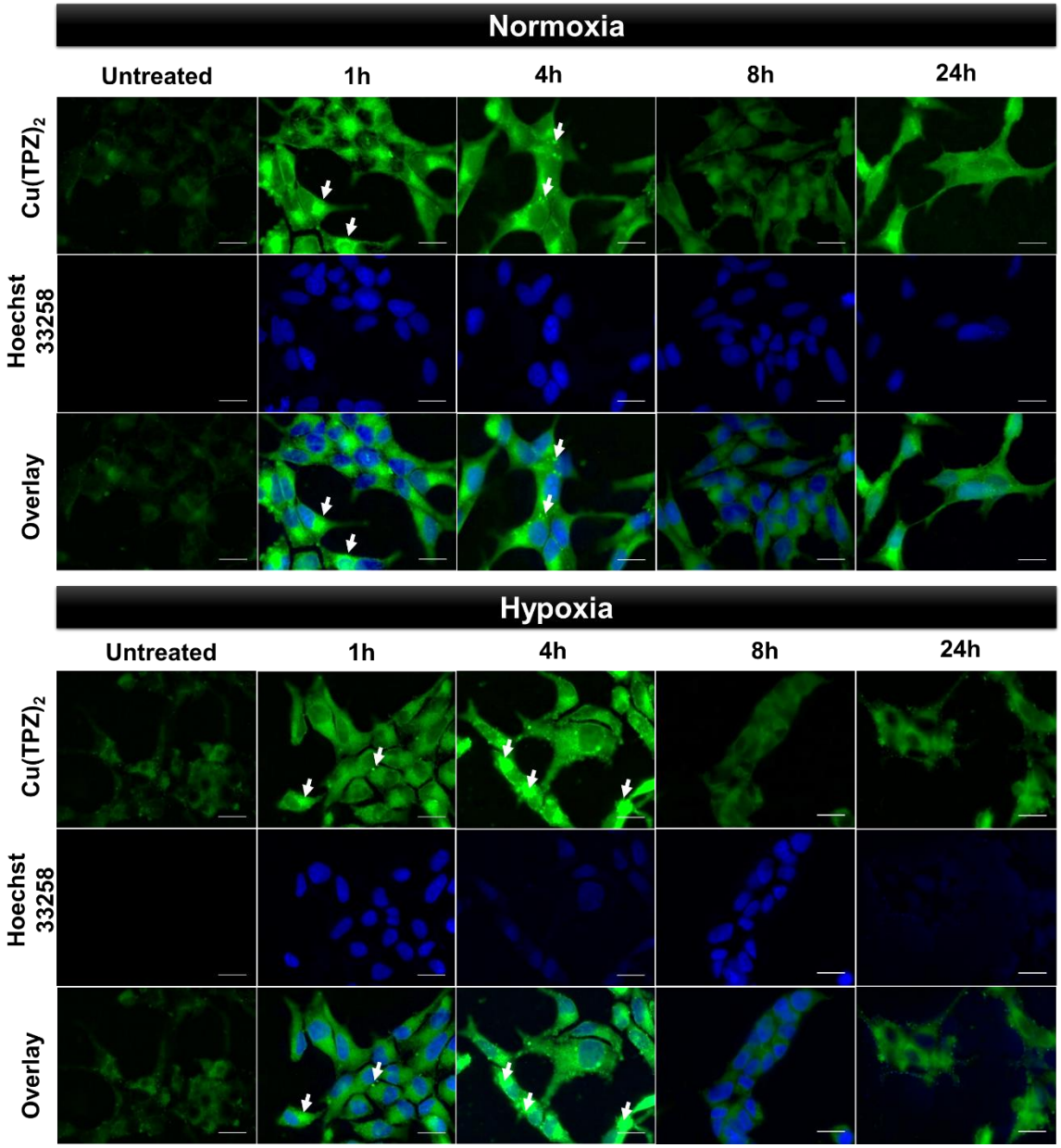

Figure 5.11. Cellular uptake and localization of $Cu(TPZ)_2$ in C4-2B prostate cancer cells. $Cu(TPZ)_2$ (50 μM) at 1, 4, 8 and 24h under normoxia and 1% hypoxia. The white arrows depict intense green puncta signals, suggesting accumulation of the complex in intracellular vesicles. The signals were more prominent under hypoxic conditions and in the perinuclear area. Images are representative of at least 50 cells of two independent experiments (n=2). Green channel: $Cu(TPZ)_2$ treated cells; Blue channel: nuclei stained with Hoechst 33258. Scale bars, 20 μm.

These findings agreed well with previous studies [174,181,182,456,459], where both passive and facilitated diffusion can be involved in the uptake of these metal-complexes. These results can be further validated by co-localization studies with endosomal markers, previously shown for similar complexes [456,533]. After 8 and 24h, the fluorescent signals were clearly lower, suggesting efflux or dissociation of the complex. Some images also evidenced nuclear localization of the complex however, the lack of fluorescence in the nucleus does not completely preclude this finding as the fluorescence of the complex can be quenched upon interaction with DNA [533].

TPZ was used as an internal control, but the weak fluorescent intensity of this drug did not allow reliable observation of its cellular localization under the same conditions (**Figure 5.12**).

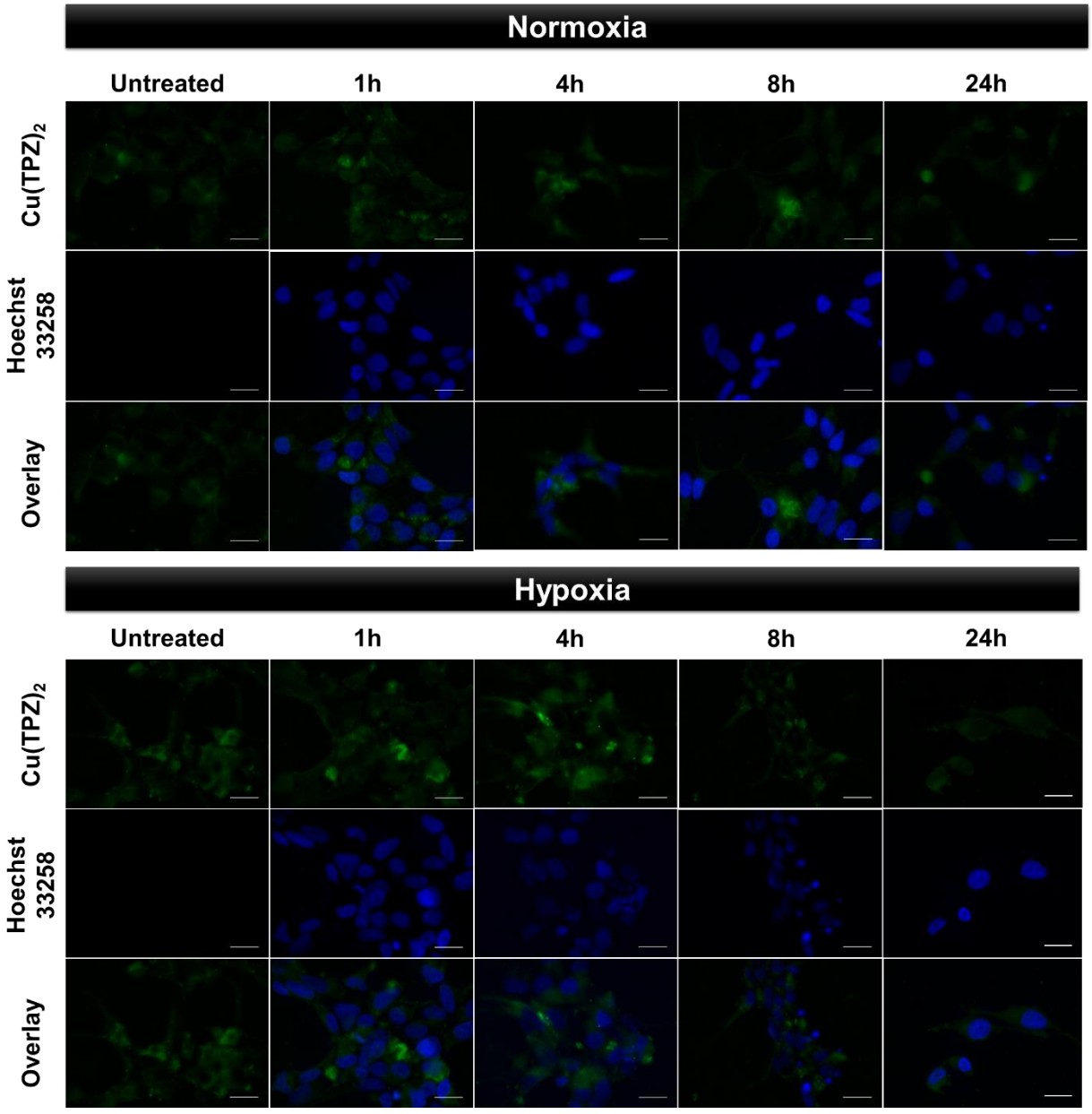

Figure 5.12. Cellular uptake of TPZ in C4-2B prostate cancer cells. Qualitative uptake of TPZ (100 µM) was assessed at 1, 4, 8 and 24h under normoxia and 1% hypoxia. Images are representative of at least 50 cells of two independent experiments (n=2). Green channel: TPZ treated cells; Blue channel: nuclei stained with Hoechst 33258. Scale bar, 20 µm.

However, these findings did confirm that the bright fluorescent green signal obtained previously originated from the intact complex. Any decrease in fluorescence may be attributed to complex dissociation to free Cu^{2+} and TPZ [534], suggesting this complex can function as a redox-sensitive probe. Further studies using live cell confocal imaging and co-localization markers could provide additional data on precise organelle biodistribution as well as copper release in the cell.

5.2.1.3.2. Quantitative uptake (microplate reader)

Fluorescence-activated cell sorting (FACs) is a highly sensitive technique that enables rapid and significant quantification of internalized compounds. However, previous studies have shown significant differences in fluorescence intensity between intact and lysed cells, compromising the results obtained by this method [535]. Florescence signals can be quenched intracellularly in intact cells yielding low signal, a finding we also observed. Therefore, fluorescence reading using a plate reader allowed a rapid and reliable method to detect total uptake of both TPZ and $Cu(TPZ)_2$, even for the weakly fluorescent TPZ [536].

The total uptake of TPZ and $Cu(TPZ)_2$ at fixed concentrations of 25 (**Figure 5.13**, **top left**), 50 (**Figure 5.13A**, top right) and 100 µM (**Figure 5.13A, bottom**) equivalent TPZ content, was determined over 24 h, under normoxia or 1% hypoxia. The cells were washed, lysed using DMSO, and sonicated to ensure complete cell rupture (including organelles). The percentage of cell uptake was calculated based on the initial fluorescence intensity of each compound.

As evidenced before [100] TPZ showed low cellular uptake, with no significant differences under both normoxia and hypoxia. On the other hand, $Cu(TPZ)_2$ (25 µM equivalent TPZ content) showed a significant improvement in cellular uptake, under normoxia (4h, $p<0.001$; 8h, $p<0.01$ and 24h, $p<0.0001$) and hypoxia (4h, $p<0.0001$; 8h, $p<0.05$ and 24h, $p<0.0001$), compared to TPZ (**Figure 5.13**, **top left**). These results could be correlated to the enhanced lipophilic nature of $Cu(TPZ)_2$ (detailed in **chapter 3**), after coordination of copper (II) to the N3 position of the ligand [39, 53] leading to increased uptake of the complex. Additionally, removal of this H-bond donor 3-NH_2 group, has also shown to be a major determinant in improving TPZ cellular uptake and the diffusion rate in tumour spheroid models [16]. A similar trend was observed using $Cu(TPZ)_2$ (50 µM equivalent TPZ content), with accelerated cellular uptake under hypoxia at 1h, compared to TPZ ($p<0.01$) (**Figure 5.13**, **top right**). Higher uptake was maintained under both conditions as discussed but the uptake efficiency, was slightly lower than 12.5 µM $Cu(TPZ)_2$ (25 µM equivalent TPZ content). More importantly and in line with previous reports [174,177,180,182], the complex demonstrated selective hypoxia uptake at 4h with increased uptake efficiency compared to normoxia at both concentrations ($p<0.001$).

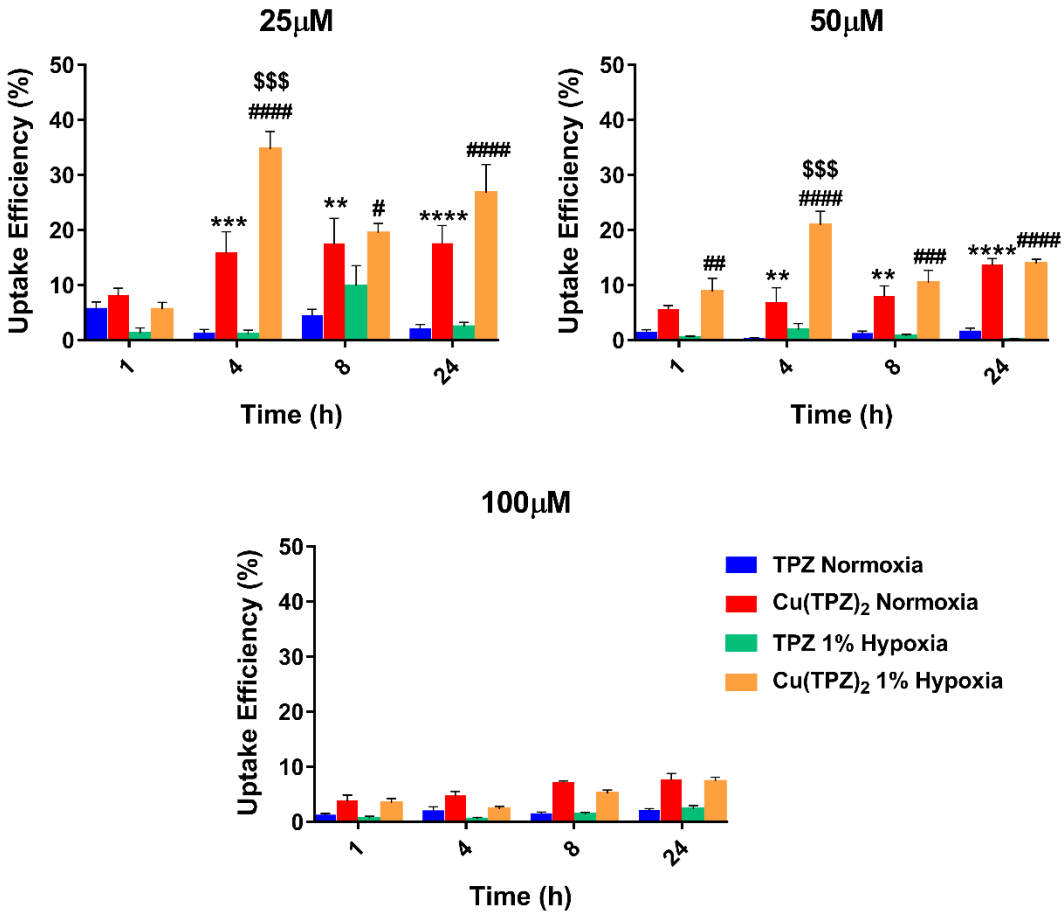

Figure 5.13. Quantitative uptake of TPZ and Cu(TPZ)$_2$ in C4-2B cells. Cells were incubated with 25 (top left), 50 (top right) and 100 μM (bottom) equivalent TPZ, and the cellular uptake was determined at 1, 4, 8 and 24h under normoxia and 1% hypoxia. Fluorescence was measured at $\lambda_{exc}/\lambda_{em}$ 485/590 nm in DMSO. Data was expressed as mean ± SD for triplicates of three independent experiments (n=3). Statistical analysis: Two-way ANOVA multiple comparison with Bonferroni Post-test (GraphPad Prism version 7.0, GraphPad Software Inc., La Jolla, CA, USA) was performed to compare uptake of TPZ *vs.* Cu(TPZ)$_2$: (**p<0.01, ***p<0.001 and ****p<0.0001, comparing drugs under normoxia; $^{\#}$p<0.05, $^{\#\#}$p<0.01, $^{\#\#\#}$p<0.001 and $^{\#\#\#\#}$p<0.0001, comparing drugs under hypoxia; and $^{\$\$\$}$p<0.001, comparing Cu(TPZ)$_2$ under hypoxia *vs.* normoxia.

The bioreductive cycle in the lysosome (E_{red} -0.75) could be responsible for this high intracellular accumulation, with lower complex efflux under hypoxia [183]. Furthermore, the slight decrease in cell uptake at 8h, could be attributed to complex dissociation in acidic compartments, such as lysosomes, with consequent loss of fluorescence intensity, which agrees with the fluorescent imaging.

Increasing concentrations of Cu(TPZ)$_2$ may have also intensified cellular reduction of the complex or led to loss of hypoxia selectivity, thus resulting in decreased fluorescence. This hypothesis agrees well with the results depicted in **figure 5.13 (bottom)**, where uptake of Cu(TPZ)$_2$ (100 μM equivalent TPZ) showed significantly decreased uptake (<10%) under normoxia and hypoxia. These higher drug quantities may then lead to increased retention of the complex in the membrane or even higher 'washout' of the non-entrapped Cu(TPZ)$_2$, eventually resulting in decreased uptake [183].

In summary, these findings highlight that $Cu(TPZ)_2$ uptake is concentration-dependent. Up to *ca.* 50 µM equivalent TPZ, increased accumulation of $Cu(TPZ)_2$ in PCa was observed, resulting in enhanced selectivity and accumulation under hypoxia. These results may justify the pronounced cytotoxic potency observed in C4-2B (**section 5.2.1.2.2**).

5.2.1.4. *In vitro* DNA binding studies of TPZ and $Cu(TPZ)_2$ complexes in C4-2B

Given that DNA is the main intracellular target of copper-complexes [171] studies were conducted to understand if $Cu(TPZ)_2$ could also interact with DNA. UV/Vis absorption spectroscopy has been routinely used to analyse the binding interactions of small molecules with DNA. Here, the absorption spectrum of $Cu(TPZ)_2$ (fixed at 25 µM) was monitored in the absence and presence of increasing concentrations of CT-DNA in Tris/HCl buffer solution (**Figure 5.14A**).

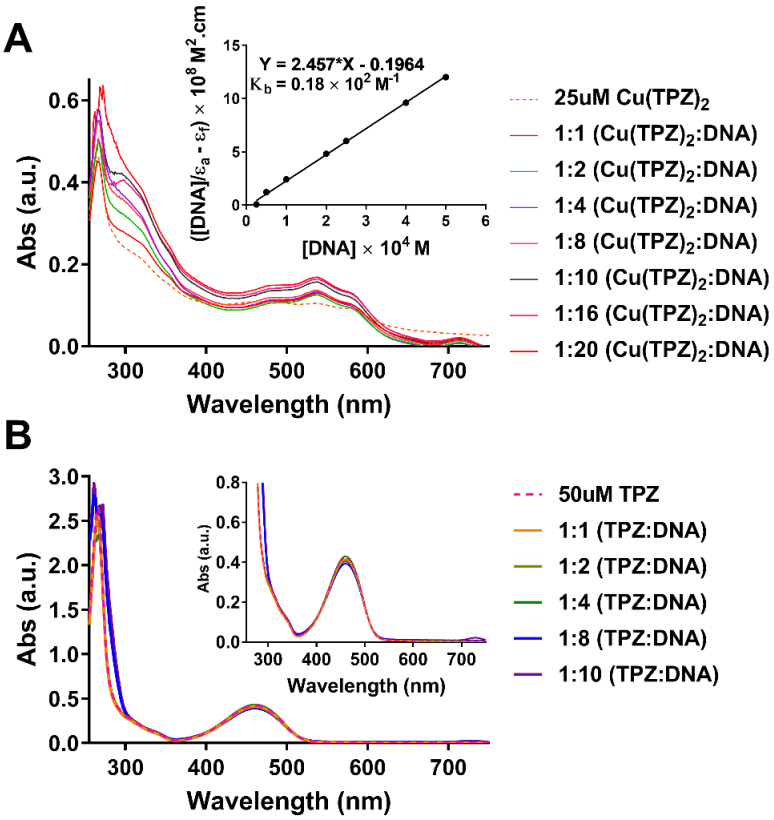

Figure 5.14. Interaction of $Cu(TPZ)_2$ and TPZ with CT-DNA. Absorption spectra of A) $Cu(TPZ)_2$ (25 µM) in the absence (dashed line) and presence (solid line) of increasing amounts of CT-DNA at room temperature in 5 mM Tris/HCl/50 mM NaCl buffer, PH 7.2. The arrow depicts the absorbance changes on increasing CT-DNA concentration. Inset shows the plot of $[DNA]/(\varepsilon_a-\varepsilon_f) / (\varepsilon_b-\varepsilon_f)$ *vs.* [DNA] and derived K_b value; and B) TPZ (50 µM) in the absence (dashed line) and presence (solid line) of increasing amounts of CT-DNA at room temperature in 5 mM Tris/HCl/50 mM NaCl buffer, PH 7.2. DNA only samples were used as baseline reference, as described in **section 2.5.4 of chapter 2**. Inset shows a zoom in of the visible spectral region, displaying no changes in the spectrum.

The results showed a significant hyperchromic effect at λ=530 nm, with a small bathocromatic shift at λ=300 nm. Generally, this represents a non-intercalative binding mode through the minor DNA groove, resulting in damage to DNA double-helical structure [420,422]. The binding constant was calculated according to equation 2.7 (**section 2.5.4 chapter 2***)*, from the plots of $[DNA]/(\varepsilon_a-\varepsilon_f)$ *vs*. [DNA], where the binding constant, K_b, was derived as the ratio of the slope to the intercept (**Figure 5.14A, inset**). The determined K_b was 0.18×10^2 M^{-1} ($Y = 2.457*X - 0.1964$, $R^2=0.9983$), which is in agreement with other DNA groove binding agents and much lower than standard DNA intercalating agents [421].

This indicates that $Cu(TPZ)_2$ has a moderate DNA binding capacity, possibly through DNA groove binding, but intercalation cannot be ruled out, supporting previous evidence on the enhanced DNA damaging capacity of this complex [148].

TPZ was used as a negative control and showed no relevant spectral differences (**Figure 5.14B**), indicating that TPZ did not interact with DNA in the absence of its radical counterpart [438,537]. Further studies on DNA viscosity, damage and ROS production can further elucidate the mechanisms of action of this cupric-TPZ complex. Nevertheless, the data reveals plausible DNA-targeted improved potency of the complex that may help overcome TPZ's non-selective mitochondrial/cytoplasmic metabolism responsible for its clinical side-effects [537].

5.2.1.5. *In vitro* cytotoxicity and hypoxia selectivity of $Cu(TPZ)_2$-loaded liposomes

Firstly, the concept of liposomal biocompatibility was considered (**Figure 5.15**). Although it is generally recognized that liposomes are not particularly toxic, it is important to establish the cytotoxicity window of the empty vehicle for the cell models used [538]. C4-2B cells were incubated with varying doses of empty liposomes equivalent to those used in the assays involving $Cu(TPZ)_2$-loaded vesicles. The cells were incubated under normoxia (**Figure 5.15, left)** and 1% hypoxia (**Figure 5.15, right**) with increasing doses of empty DOPC (**Figure 5.15, top panel**), DPPC (**Figure 5.15, middle panel**) and DSPC (**Figure 5.15, bottom panel**) liposomes for 48, 72 and 96h. The liposomes displayed excellent biocompatibility, exhibiting cell viability >80% for all conditions tested [538], thus confirming that any toxicity obtained is solely due to $Cu(TPZ)_2$ activity.

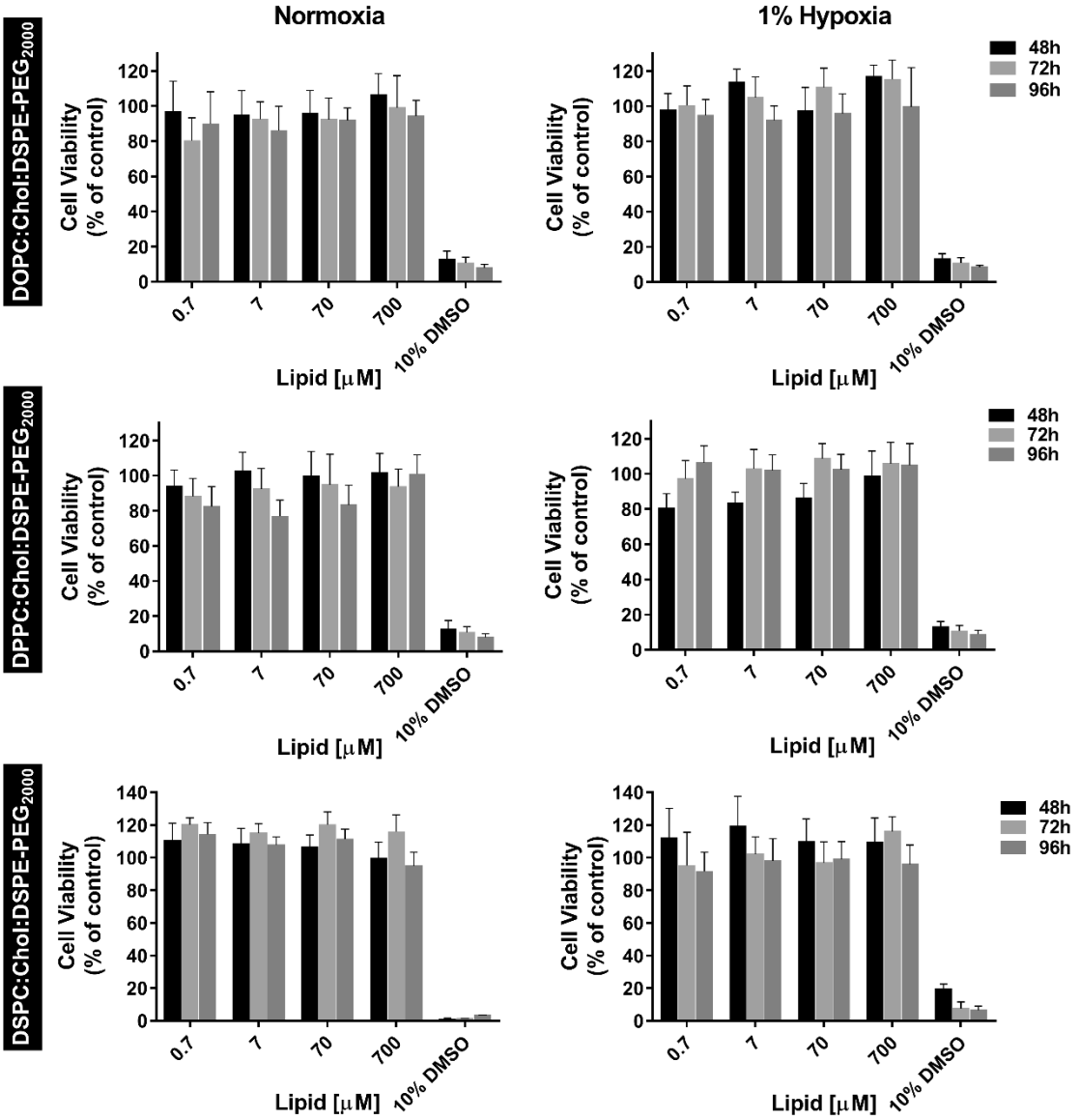

Figure 5.15. Analysis of cell viability in C4-2B prostate cancer cells, after continuous exposure to empty liposomes under different oxygen levels. C4-2B cells were incubated under normoxia (left panel) and hypoxia (right panel) with increasing concentration of empty DOPC:Chol:DSPE-PEG_{2000} (top panel), DPPC:Chol:DSPE-PEG_{2000} (middle panel), and DSPC:Chol:DSPE-PEG_{2000} liposomes (bottom panel) (95:50:5 molar ratio). 10% DMSO was used as a positive control. Cell viability was assessed by the resazurin assay, normalized to untreated and data was expressed as mean ± SD for six replicates of three independent experiments (n=3).

Next, drug loaded liposome toxicity was evaluated in both normoxia and hypoxia to establish the *in vitro* activity in PCa. As detailed in **chapter 4**, liposomal formulations encompassing a 60:1 lipid-to-drug molar ratio were chosen due to their biocompatible mean size, PDI, good EE, sustained release profile and long-term stability. C4-2B monolayers were incubated under normoxia (**Figure 5.16, left)** and 1% hypoxia (**Figure 5.16, right**) with increasing concentrations of sterile $Cu(TPZ)_2$-DOPC (**Figure 5.16, top panel**), $Cu(TPZ)_2$-DPPC (**Figure 5.16, middle panel**) and $Cu(TPZ)_2$-DSPC (**Figure 5.16, bottom panel**) for 48, 72 and 96h.

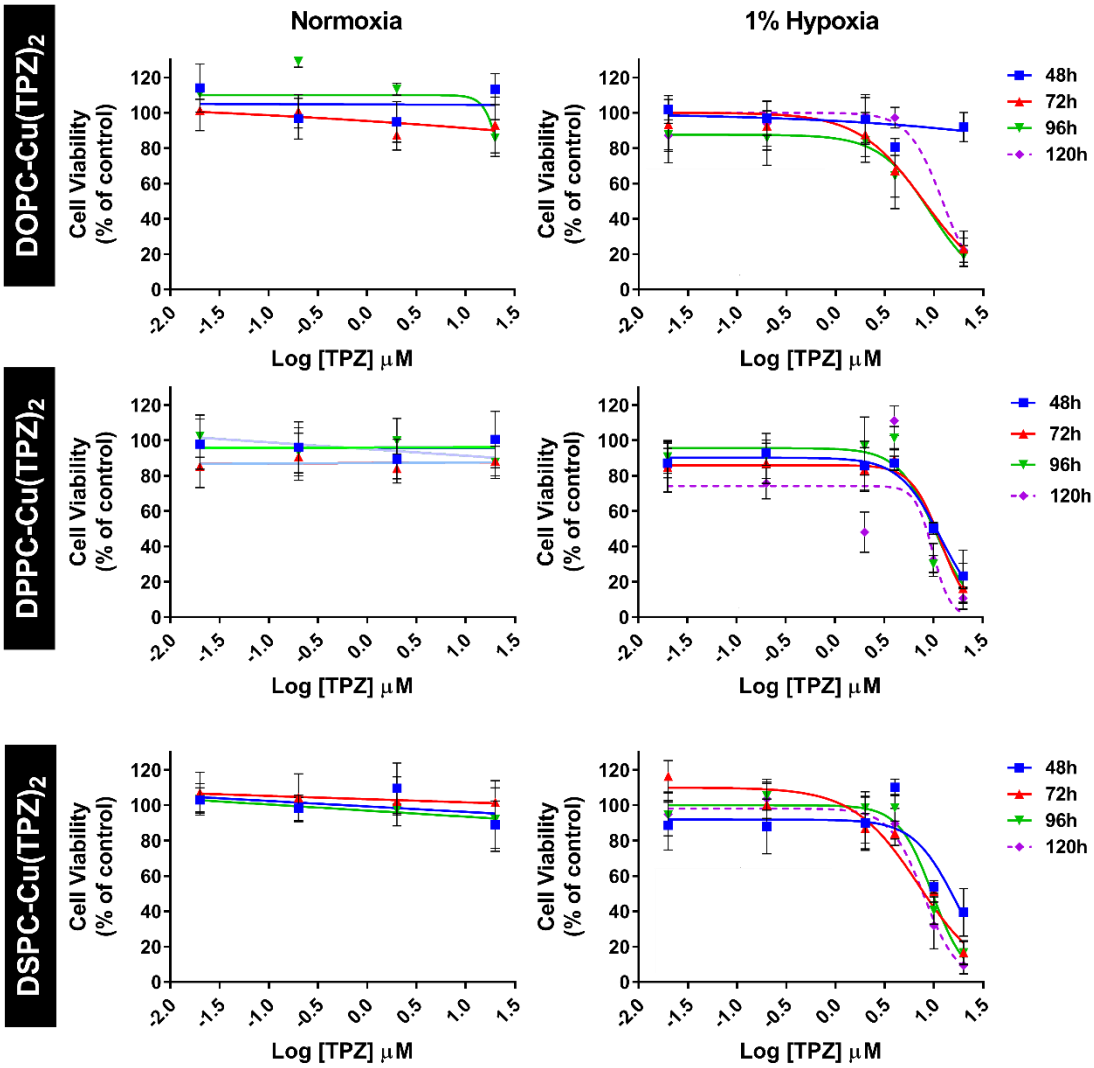

Figure 5.16. Analysis of cell viability in C4-2B prostate cancer cells, after continuous exposure to free Cu(TPZ)$_2$ and Cu(TPZ)$_2$-loaded liposomes (60:1) under different oxygen levels. C4-2B cells were incubated under normoxia (left panel) and hypoxia (right panel) with increasing concentration *of* Cu(TPZ)$_2$-loaded liposomes [DOPC-Cu(TPZ)$_2$, DPPC-Cu(TPZ)$_2$, and DSPC-Cu(TPZ)$_2$] (up to 120h). Cell viability was assessed by the resazurin assay, normalized to untreated and data was expressed as mean ± SD for six replicates of three independent experiments (n=3).

The results showed that cell viability was maintained >80% under normoxia for all three formulations tested (**Figure 5.16, left**), even at higher doses (> 20 µM), proving that selectivity of the Cu(TPZ)$_2$-loaded liposomes was maintained. A sigmoidal type response was obtained under 1% hypoxia conditions that was formulation-dependent (**Figure 5.16, right**). The results also showed a time-dependent effect for DOPC-Cu(TPZ)$_2$ liposomes, illustrated by the marked left-shift of the dose-response curve under hypoxia after 48 h. In contrast, DPPC and DSPC exhibited similar activity over-time with only mild differences in dose response starting from 48 h. Nonetheless, the data confirmed that hypoxia selectivity of the complex was maintained, even after liposomal encapsulation, establishing this nanocarrier as a promising alternative strategy for hypoxia cancer therapy.

The cell viability studies were further complemented by representative phase contrast images after treatment, where well spread adherent cells with tight cell contact withdraw and become round and eventually detached, suggesting cell death (**Figure 5.17**). Membrane blebs were also observed, indicating cleavage of the cortical cytoskeleton.

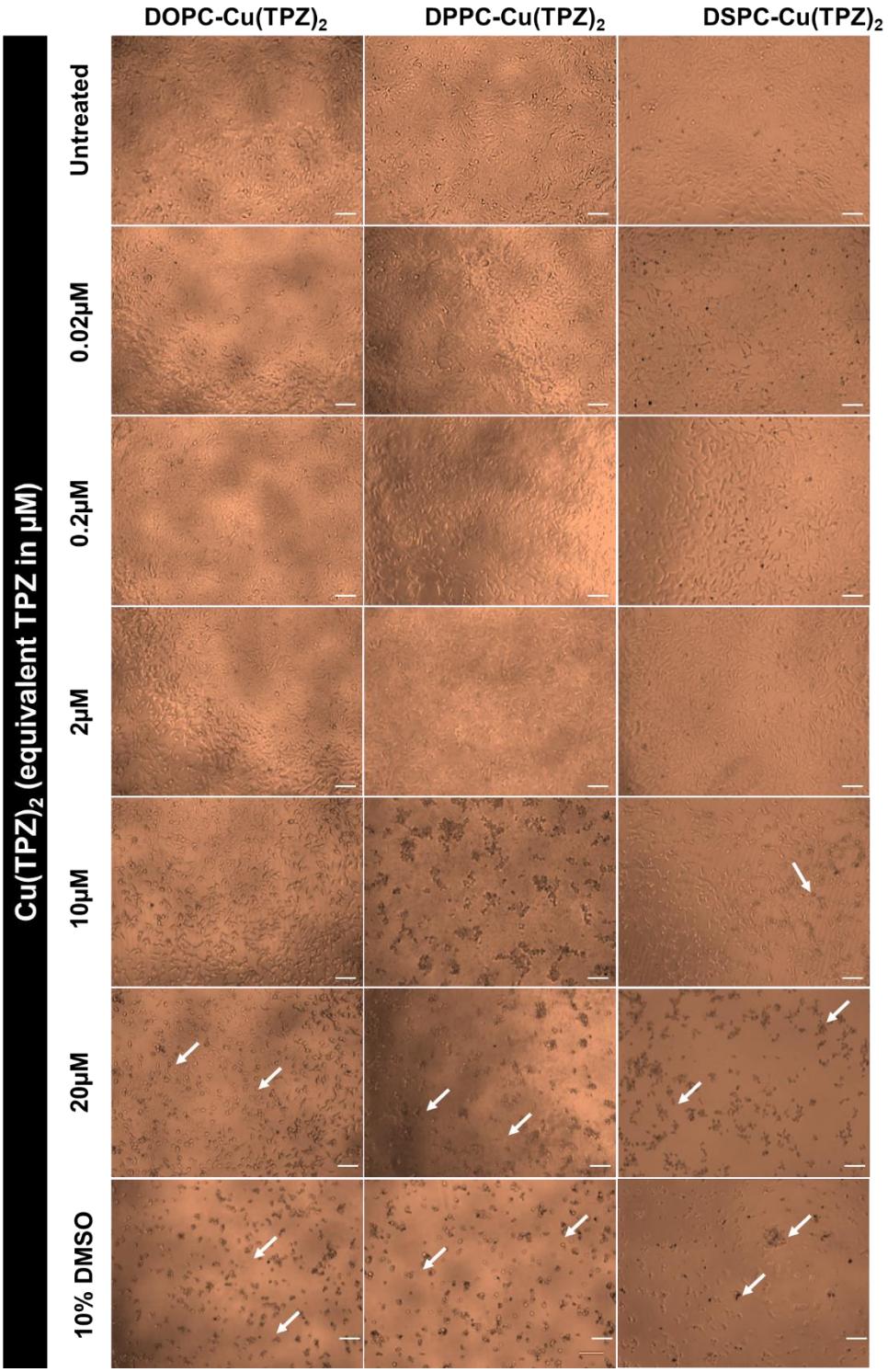

Figure 5.17. Phase contrast images representative of C4-2B prostate cancer cells, after continuous exposure to $Cu(TPZ)_2$-loaded liposomes (60:1). Cells were exposed to increasing concentrations of DOPC-$Cu(TPZ)_2$ (top panel), DPPC-$Cu(TPZ)_2$ (middle panel), and DSPC-$Cu(TPZ)_2$, (bottom panel), at 72h post-treatment. White arrows depict cell detachment and membrane blebbing, which resulted in cell death by apoptosis. Scale bar, 50 µm.

The mean data were then used to calculate the IC_{50} values for inhibition, after fitting to a nonlinear regression using a four-parameter equation (GraphPad Prism version 7.0) (summarised in **table 5.1)**. It is important to note that only EE concentrations up to 20 µM were used in these assays. Given the drug loading obtained in this work, higher concentrations of encapsulated $Cu(TPZ)_2$ could lead to unwanted cytotoxic effects from the carrier itself (**Figure 5.15**). Therefore, contrary to the experiments conducted with the free drugs, the HCR values were estimated using an IC_{50} under normoxia of 20 µM, where no significant toxicity was observed. The results showed *ca.* 2-3-fold increase in liposomal potency under hypoxia, emphasizing that encapsulated $Cu(TPZ)_2$ still maintains adequate selectivity under low oxygenated conditions, unlike other studies [539]. Future work could help develop liposomes with increased lipid content that could improve on drug loading. This strategy may aid in determining the actual IC_{50} value under normoxia, which in turn could highlight the pronounced liposomal hypoxia selectivity.

Table 5.2. IC_{50} values and hypoxia cytotoxicity ratio (HCR, normoxia IC_{50}/hypoxic IC_{50}) in C4-2B prostate cancer cell line, following continuous exposure to $Cu(TPZ)_2$-loaded liposomes (60:1, lipid-to-complex molar ratio), under normoxic and hypoxic conditions. IC_{50} values were determined by nonlinear regression analysis of the data fit to a four-parameter equation (GraphPad Prism version 7) and HCR for $Cu(TPZ)_2$-loaded liposomes was estimated assuming IC_{50} under normoxia as ≥20 µM. Results for free $Cu(TPZ)_2$ were included for direct comparison. Values represent mean ± SD of six replicates of three independent experiments (n = 3).

IC_{50} (µM) - 1% Hypoxia								
C4-2B	**$Cu(TPZ)_2$[a]**	**HCR**	**DOPC 60:1**	**HCR[a]**	**DPPC 60:1**	**HCR[a]**	**DSPC 60:1**	**HCR[a]**
8h	29.34 ± 1.057	3.81	49.48 ± 1.03	>0.4	11.92 ± 1.03	>1.68	14.15 ± 1.07	>1.41
72h	1.51 ± 1.036	69.66	9.169 ± 1.04	>2.18	11.9 ± 1.29	>1.68	6.92 ± 1.02	>2.90
96h	7.57 ± 1.032	7.68	6.83 ± 1.05	>2.93	10.8 ± 1.05	>1.85	8.231 ± 1.02	>2.43
120h	N.D.	N.D.	12.43 ± 1.04	>1.62	10.11 ± 1.04	>1.98	6.197 ± 1.03	>3.22

[a]values determined assuming normoxia IC_{50} of 20µM
N.D., not determined

A detailed statistical analysis was conducted to compare the efficacy of the liposomal formulations to the stand-alone $Cu(TPZ)_2$ cytotoxicity assays. Interestingly, the cytotoxicity results, revealed that, at 48h (**Figure 5.18A**), $Cu(TPZ)_2$ complex showed a 1.67-fold lower IC_{50} (29.92 ± 1.06 µM), compared to DOPC-$Cu(TPZ)_2$ (49.48 ± 1.03 µM, $p<0.0001$). In contrast, DPPC-$Cu(TPZ)_2$ (11.92 ± 1.034 µM, $p<0.0001$) and DSPC-$Cu(TPZ)_2$ (14.15 ± 1.075 µM, $p<0.0001$), displayed improved efficacy, compared to the free complex. These results are in good agreement with the liposome release profile discussed in **chapter 4** (**section 4.2.3.7.1**) where DOPC-$Cu(TPZ)_2$ liposomes possessed a slower early-onset release, whilst both DPPC-$Cu(TPZ)_2$ and DSPC-$Cu(TPZ)_2$ liposomes presented a rapid burst release, followed by a plateau phase.

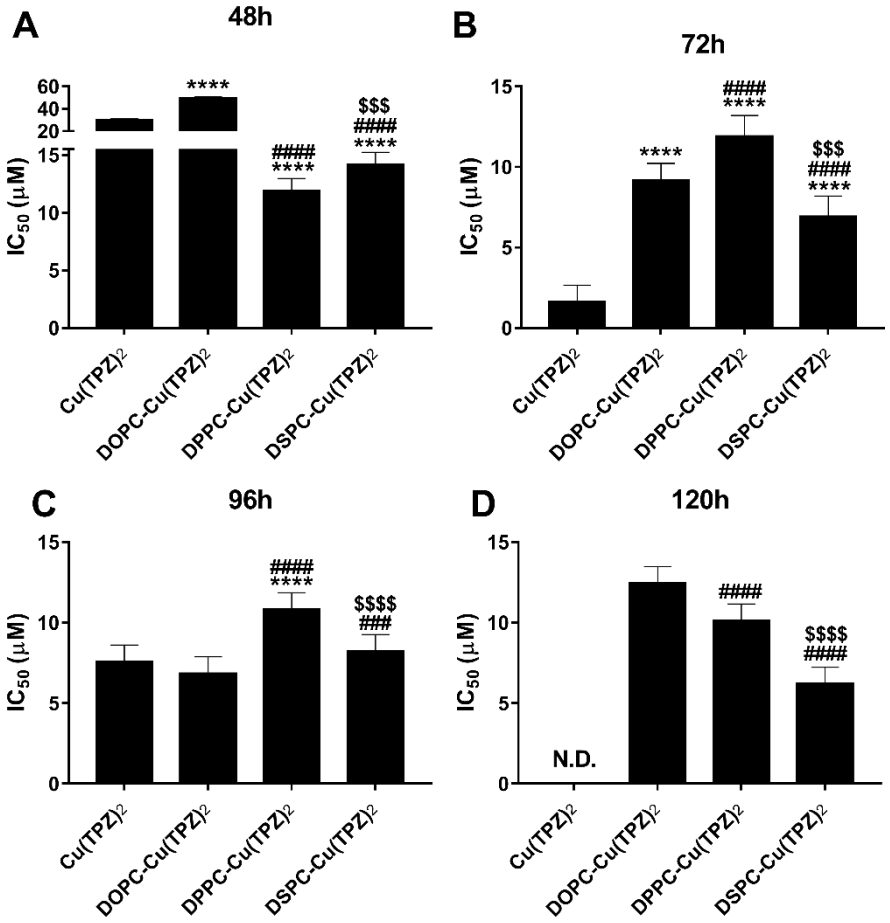

Figure 5.18. IC_{50} values in C4-2B prostate cancer cell line, following continuous exposure to $Cu(TPZ)_2$ and $Cu(TPZ)_2$-loaded liposomes (60:1, lipid-to-complex ratio), under hypoxic conditions. Values were determined at A) 48h, B) 72h, C) 96h and D) 120h. Data was expressed as mean ± SD of six replicates of three independent experiments (n = 3). Statistical analysis using Two-way ANOVA multiple comparison with Bonferroni Post-test (GraphPad Prism version 7.0) was performed to compare multiple groups: ($^{****}p<0.0001$, compared to free $Cu(TPZ)_2$; $^{###}p<0.001$ and $^{####}p<0.0001$, compared to $Cu(TPZ)_2$-DOPC and $^{\$\$\$}p<0.001$, $^{\$\$\$\$}p<0.0001$ compared to $Cu(TPZ)_2$-DPPC).

Promisingly, at longer incubation times (72h, **Figure 5.18B**) the toxicity was more pronounced with all formulations, but with superior activity of the $Cu(TPZ)_2$ complex (1.613 ± 1.04 µM) compared to DOPC-$Cu(TPZ)_2$ (9.169 ± 1.045 µM), DPPC-$Cu(TPZ)_2$ (11.9 ± 1.298 µM) and DSPC-$Cu(TPZ)_2$ (6.92 ± 1.027 µM). All $Cu(TPZ)_2$-loaded liposomes (DOPC, DPPC, DSPC) exhibited 5.7 ($p<0.0001$), 7.2 ($p<0.0001$) and 4.2-fold ($p<0.001$) higher IC_{50} compared to the free complex, respectively.

However, at 96h the complex IC_{50} increased from 1.51± 1.036 µM to 7.57± 1.032 µM, indicating some cell recovery over time (**Figure 5.18C**), resulting in IC_{50} comparable to the liposomal formulations. Which maintained a steady biological activity. Interestingly, DPPC-$Cu(TPZ)_2$ were slightly less potent than $Cu(TPZ)_2$ and DOPC-$Cu(TPZ)_2$ at 72h ($p<0.0001$) and 9 h ($p<0.0001$). At 120h (**Figure 5.18D**), DOPC-$Cu(TPZ)_2$ showed slight cytotoxic recovery, while DPPC-$Cu(TPZ)_2$ and DSPC-$Cu(TPZ)_2$ still maintained significant potent activity ($p<0.0001$).

It is also important to highlight that DSPC-$Cu(TPZ)_2$ resulted in the most effective biological response over time, even after 120h (IC_{50}: 6.197 ± 1.032 μM, $p<0.0001$). This data shows that the liposomes developed herein could be a promising DDS for TPZ, maintaining hypoxia selectivity, whilst improving on earlier onset cytotoxicity compared to the drug itself.

NPs developed for TPZ delivery mainly focused on the strong combinatorial effects of small doses of this HAP with radiation [377,378,380] and chemotherapy [376,383] but failed to show TPZ-NP activity alone. Only two studies showed the effect of encapsulated TPZ in the absence of synergistic treatment modalities, reporting an IC_{50} of 140 μM at 96 h (under 3% O_2) for mesoporous silica-NPs [379] and 98 μM at 24 h (under 2% O_2) for biomimetic metal-porphyrinic NPs [381]. The results obtained here showed enhanced potency compared to the aforementioned studies and also superior activity compared to cationic-TPZ liposomes, where PDT was essential to induce liposome efficacy [384].

Parameters such as size, aggregation, charge, EE, release and lipid composition could affect the therapeutic outcome of developed liposomes [277,278,280]. However, as concluded in **chapter 4** (**table 4.6**) none of the developed liposomes differed significantly in their core physicochemical properties displaying biocompatible size, PDI, charge and good EE for *in vitro* applications. It was plausible to assume that the improved potency $Cu(TPZ)_2$-liposomes could be attributed to their increased uptake and sustained release. Both Wu *et al.* [376] and Liu *et al.* [377] revealed enhanced uptake and anti-tumour efficacy of TPZ-Tf conjugates and TPZ-gold NPs, respectively. Furthermore, Broekgaarden *et al.* [384] engineered cationic-liposomes for TPZ encapsulation where a *ca.*10 fold-increase in cellular uptake and bioavailability was obtained after TPZ loading. Presumably, $Cu(TPZ)_2$-loaded liposomes may also possess increased cell uptake. Future studies involving labelled $Cu(TPZ)_2$-liposomes and FACs analysis, alongside confocal microscopy could determine the specific mechanistic of uptake.

Together, the data presented here highlighted the therapeutic potential of $Cu(TPZ)_2$-liposomes as a monotherapy, along with improved TPZ encapsulation *via* copper-complexation, which could translate into higher therapeutic efficacy *in vivo.* Supporting this claim, Shah *et al.* [539] reported significant tumour growth delay using liposomal vinblastine-*N*-oxide compared to the free HAP, with reduced systemic off-target effects.

5.2.2. Part II: Biological assays conducted in 3D PCa models

Monolayer cell cultures (2D) are a rapid way to gain invaluable information on molecular cell aspects, as well as drug response. However, 2D cultures have caused controversy in the drug screening field, due to limited data, whilst failing to adequately represent the whole of the tumour environment [425,540]. In addition, *in vivo* models have also led to attrition rates in translational drug efficacy and are associated to high costs of maintenance. There was an unmet need to develop an intermediary cell model that could provide essential data for positive and negative drug screening, maintaining essential cellular functions and well-mimicked tumour architecture [502,503]. Over the past years the concept of 3D models has emerged as a promising tool to bridge the gap between conventional monolayer cultures and *in vivo* models. These 3D models offer a better understanding of the tumour microenvironment and are now considered the best *in vitro* representation of small avascular tumours and even micro metastasis [427,500]. More and more, there has been a shift in the drug screening paradigm calling out for a higher use of 3D models in order to complement classical *in vitro* studies. Many improvements have sought to apply high throughput cell screening methods to this model. It is now possible to rapidly establish homogenously sized spheroids, which are easily adapted for use with typical viability/proliferation studies, as well as, imaging and FACs analysis, with greater translational predicative capacity [419,423,541].

Previously, $Cu(TPZ)_2$ displayed remarkable selectivity and potency in C4-2B cells, particularly at 72 h post-treatment. In line with the potential of 3D models it was interesting to complement these data and evaluate drug response in C4-2B spheroid models, to better understand the translational potential of this new metal-complex. Therefore, the next section offers a detailed analysis of drug cytotoxicity against C4-2B 3D models. These results confirmed the promising therapeutic efficiency of $Cu(TPZ)_2$ as a free drug, but also after liposomal-encapsulation in a more complex biological set-up.

5.2.2.1. Development of C4-2B spheroid model: growth evaluation and circularity analysis

Previous studies have reported the formation of PCa tumour spheroids *in vitro* [542] and their relevance in drug screening due to enhanced treatment resistance and consistency with *in vivo* results [543]. In the current research group different PCa cell lines were used to establish 3D cell cultures. The models were chosen accordingly, taking into consideration which parameters are essential for the specific drug screenings. In this thesis C4-2B cells were chosen due to the enhanced therapeutic sensitivity shown in 2D cultures. Moreover, given the hypoxia-dependent nature of the prodrugs it was essential to develop homogenous spheroids of spherical shape that had prominent development of hypoxia gradients to reproduce the *in vivo* environment. According to numerous literature reports [425,501,502] spheroids with diameters above 400 µm present significant physiological nutrient and oxygen gradients, concomitantly associated with a well-defined outer-shell of proliferating cells and

an inner core of quiescent hypoxia cells with developed necrosis. The development of these pathophysiological gradients modulates the 3D cell response to treatment, compared to 2D models, leading to alterations in cell-cell contacts, signalling pathways, and DNA damaging and repair mechanisms [424,541]. It is therefore expected that these models can provide essential translational information [500].

C4-2B spheroids were prepared using the liquid overlay technique [426], described in **chapter 2** (**section 2.5.5.1**), by agarose pre-coating to minimize cell attachment and promote cell self-assembly and aggregation. The agarose filled micro-wells that provided a well-confined space to generate spheroids of uniform size. The growth of C4-2B cells (5×10^3 cells/well) was then monitored over culture periods of 14 days where a half-volume culture medium was exchanged every second day. Images obtained by using phase contrast microscopy showed the spontaneous formation of uniform spheroids which started to fuse from day 2 and were well compacted on day 3 (**Figure 5.19A**). The images clearly indicated continuous spheroid growth over the 14-day period. From day 5, the darkest region of the image in bright-field suggested the presence of quiescent/dead cells (necrosis) [425]. Additionally, with the aid of a previously written ImageJ macro (Macro S1) [427] it was possible to rapidly process a great number of spheroid images, which facilitated the determination of their diameter and volume over time (**Figure 5.19B**). The macro was optimized for phase-contrast images and was easily adapted to the magnification calibration for reliable quantification of size. Spheroids displayed diameters of 421.4 ± 40.9 μm from day 2, achieving values of 706.4 ± 65.3 μm on day 14 (**Figure 5.19B, left Y axis**) and each group was highly uniform (SD≤10%). This was also accompanied by increased spheroid volume (**Figure 5.19B, right Y axis**). These data agreed well with the initial seeding density and with a previous report [544], establishing maintained growth kinetics for this PCa model, which only plateaued around day 12.

Moreover, the parameters circularity and solidity (**Figure 5.19C**) were also determined *via* ImageJ analysis to assess spheroid proximity to a circle and its relative roughness, respectively. These indicators can have values ranging from 0 to 1.0, where values closer to 1, imply high circularity or tightness of the projected spheroids [428,544]. The values of circularity were between 0.6 and 0.9 for the duration of the experiment. The initial value around 0.6 is partially due to lack of total compactness of the spheroid that greatly increased after day 3. The solidity values were in good agreement with the circularity and were overall maintained above 0.8 for the 14 days, confirming circular uniformity and dense morphology of the spheroids. These findings suggest that C4-2B spheroids at this seeding density and after 5-day culture (> 400μm diameter) may possess the necessary physiological features to assess TPZ and $Cu(TPZ)_2$ cytotoxicity.

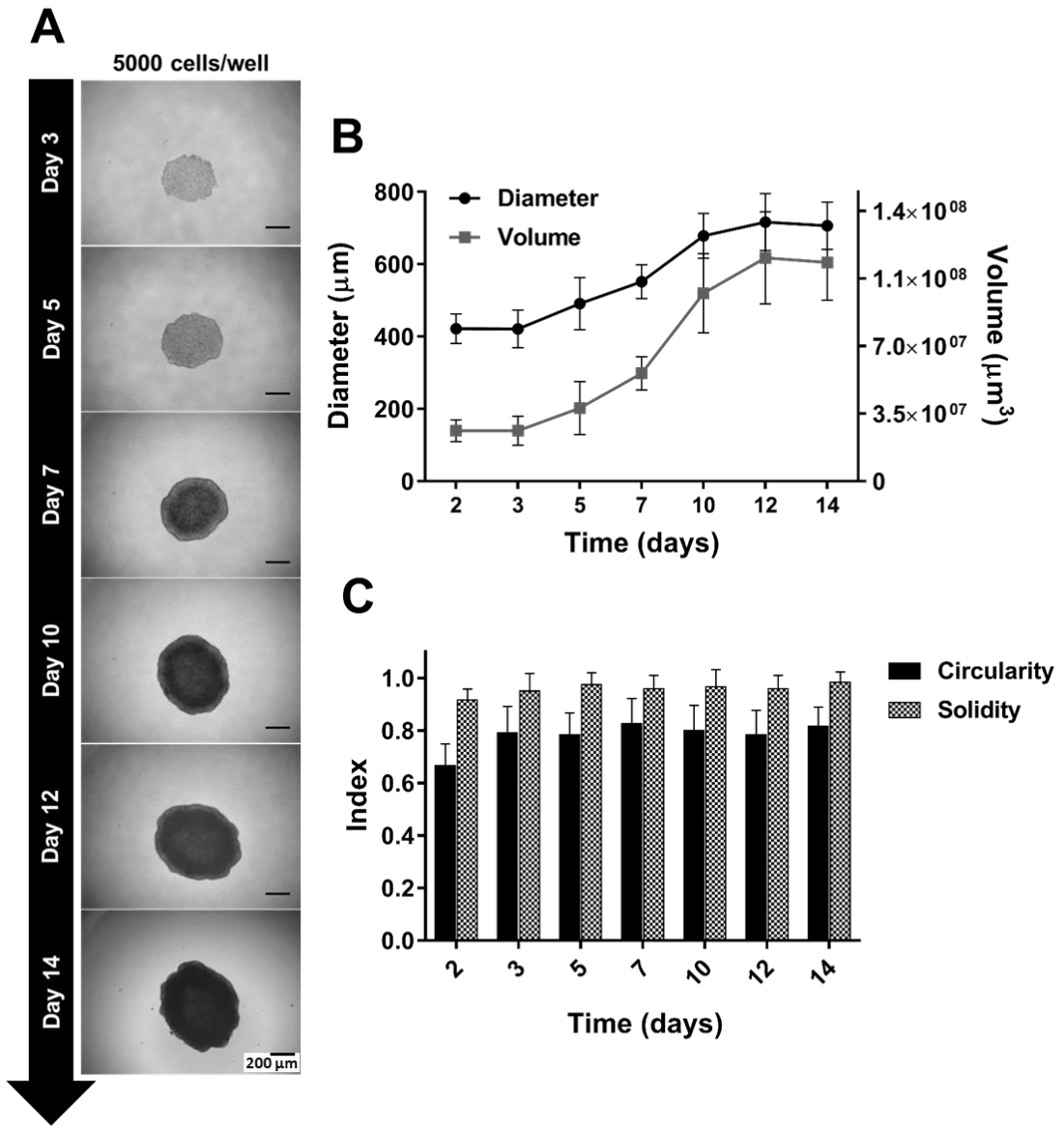

Figure 5.19. C4-2B prostate cancer spheroid characterisation. A) Spheroid growth assay with representative phase-contrast images of spheroids seeded at an initial density of 5000 cells/well and monitored over a period of 14 days. Scale bars, 200 µm; B) Spheroid diameter and volume determined using a automated macro implemented in ImageJ open source software (NIH, Bethesda, MD, USA: http://imagej.nih.gov/ij) and C) the change circularity and solidity, also assessed via ImageJ, to analyse spheroid uniformity and roughness. Data was expressed as mean ± SD of six replicates of at least two experiments ($n \geq 12$ spheroids), representative of specific growth assays. Further studies using this model guarantee a similar size and characteristics. Data were produced with the help of Moustafa Abdelhamid and Duuamene Nyimanu.

5.2.2.2. *In vitro* hypoxia validation

An advantage of *in vitro* tumour spheroids, is their capability of representing physiological gradients of nutrients and oxygen consumption [501]. *In vivo* tumours are readily recognized for their heterogeneity and differential regions of oxygen pressure, where hypoxia and necrosis become prominent features. The generation of heterogeneous oxygen pressure within the tumour mass associated with the simultaneous formation of both acute and chronic hypoxia zones, leads to altered

gene expression, which in turn affects cell survival mechanisms, leading to cancer drug resistance and aggressiveness [545]. Many studies have been dedicated to establishing and characterising hypoxia within spheroids and have agreed that, although cell line dependent, most spheroids sized > 200 µm [546] already present marked hypoxia features even at depths of 20-30 µm, which become more intense and heterogeneous at diameters above 400 µm and where necrosis is also developed.

This experimental set-up has allowed the assessment of many drug regimens including the activity of bioreductive prodrugs, such as TPZ [505].

Taking into account previous protocols [382,547] the hypoxia expression in C4-2B models was evaluated over time using the CYTO-ID® Hypoxia/Oxidative Stress Detection kit (Enzo Life Sciences. UK) and an epifluorescence microscope equipped with a Zeiss ApoTome to create robust optical Z-sections free of scattered light (**chapter 2, section 2.5.5.2**). The spheroids were incubated for 4 h with 500 nM of the hypoxia probe to ensure adequate penetration. The analysis was performed through sections up to 120 µm depth. However, after about 90 µm into the spheroid structure, the pixel densities in the core area became very low, due to the faltered imaging penetration [153], therefore only sections up to 70 µm were considered (**Figure 5.20, upper lanes)**.

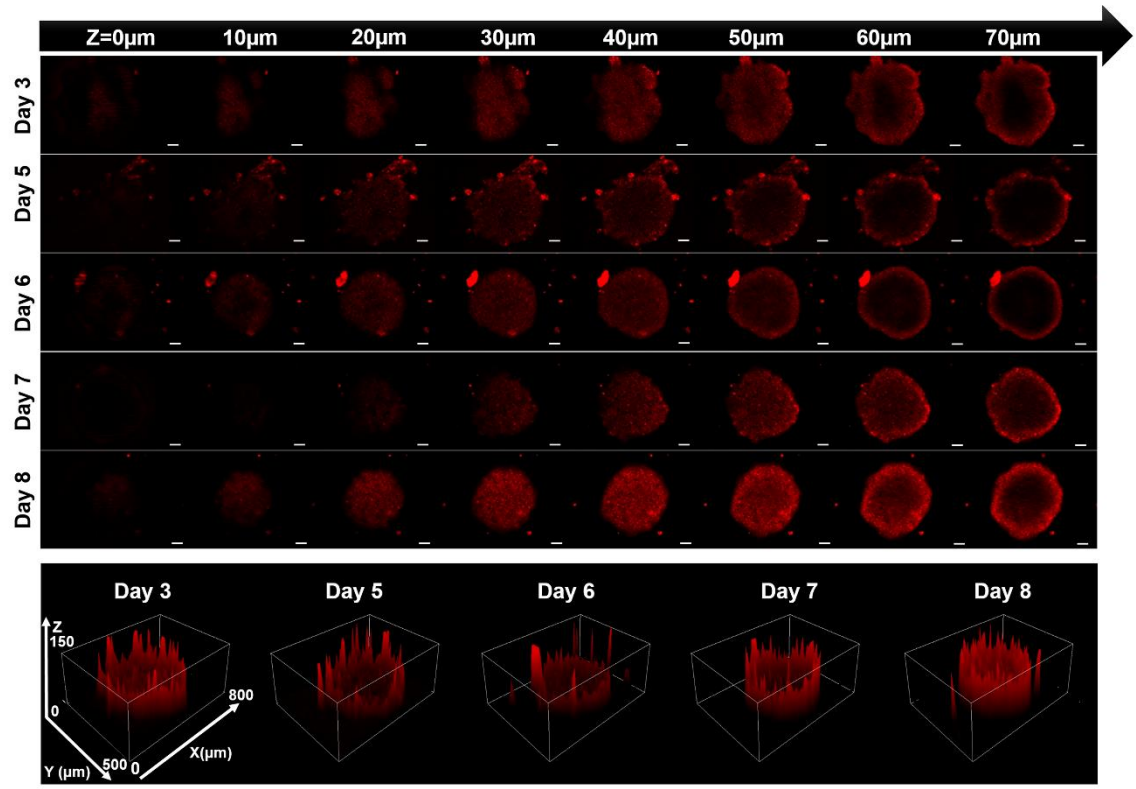

Figure 5.20. Analysis hypoxia in C4-2B prostate cancer spheroids. Fluorescent images of 3D C4-2B spheroids incubated with CYTO-ID® Hypoxia Detection probe (500 nM, (Enzo Life Sciences. UK) for 4h, taken using an inverted Zeiss Axiovert 200M with Texas Red (596/670 nm) filter and equipped with a Zeiss ApoTome (Carl Zeiss, UK) to create optical sections free of scattered light. For each spheroid a Z-stack with 10 µm intervals was generated. Scale bar: 100 µm. The bottom panel depicts surface plots of reconstructed 3D images of spheroids, produced in ImageJ (NIH, Bethesda, MD, USA: http://imagej.nih.gov/ij). Hypoxia is present from early time-points even at peripheral areas of the spheroid (Z<30 µm). From day 6, a clear increase in fluorescence intensity is visualized in deeper regions of the spheroid (Z>30 µm), with a more homogenous hypoxia core.

Hypoxia was visible from day 3 and was present even at more peripheral areas of the spheroid (<30 μm) [546] and became more intense and homogeneous at deeper thickness from day 5 (>40 μm) [503]. In larger/older spheroids (after day 6), remarkable fluorescence intensity (confirmed by the surface plots generated in ImageJ, **figure 5.20 bottom lane**) was observed in the centre of the spheroids with a distance of approximately 40 to 70 μm from the outer edge, suggesting a hypoxic region in what is considered the centre of the spheroid. These results confirmed that C4-2B spheroids possessed heterogeneous expression of hypoxia, which was time-dependent. These findings established this model as an adequate in vivo mimetic of hypoxic tumours to test the activity of TPZ and $Cu(TPZ)_2$.

5.2.2.3. *In vitro* cytotoxicity and hypoxia selectivity of TPZ and $Cu(TPZ)_2$ complexes

In order to determine the effectiveness of TPZ and $Cu(TPZ)_2$ against 3D C4-2B PCa models, spheroids on day 5 of culture were continuously exposed to the drugs for a period of 96h and their viability was assessed at pre-determined intervals. Given the physiological oxygen gradients formed in spheroids a previous report suggested higher activity of TPZ against these models compared to their 2D counterparts [505]. However, numerous reports with different drug screenings reported decreased drug activity in 3D models compared to 2D, highlighting their use as an important link between 2D cultures and animal models [501,503,540]. Moreover, standard biological assays (resazurin assay, MTT, FACs, *etc*.) have been continuously optimised to be applied to 3D culture for rapid and high throughput screening [427,501]. Initially, C4-2B spheroids were cultured for 5 days with media replenishment every two days and then treated with increasing doses of TPZ and $Cu(TPZ)_2$ up to 96h, as performed previously for their 2D counterparts. Phase-contrast images were taken over the course of treatment to observe spheroid morphology (**Figure 5.21A, representing 48h post-treatment**). The images illustrated spheroids that became more refractive and darker in light microscopy, where cells became looser and more recognizable, possibly due to loss of cell-cell contacts when exposed to high doses (100 μM) of TPZ and 10% DMSO. Spheroids exposed to $Cu(TPZ)_2$ (100 μM equivalent TPZ) appeared smaller in size compared to control, but seemed to maintain cell compactness. Moreover, when exposed to low concentrations of both drugs (0.02-2 μM equivalent TPZ), spheroids remained unchanged and were comparable to the untreated. Next, the resazurin assay was used to evaluate cell viability, after exposure to treatment, and non-linear regression of dose-response curves was used to determine the corresponding IC_{50} values. For TPZ, the results were dose and time-dependent (**Figure 5.21B**) and IC_{50} were in the submicromolar range suggesting high sensitivity of the spheroids to TPZ and increased potency compared to C4-2B in monolayer. At 96h, the IC_{50} was increased resulting in loss of TPZ activity [460,548]. For $Cu(TPZ)_2$ (**Figure 5.21C**), spheroids were also highly responsive (IC_{50} in the nanomolar range), showing a *ca*.10-fold and 1000-fold decrease in IC_{50} values at 72 and 96h, respectively, compared to TPZ.

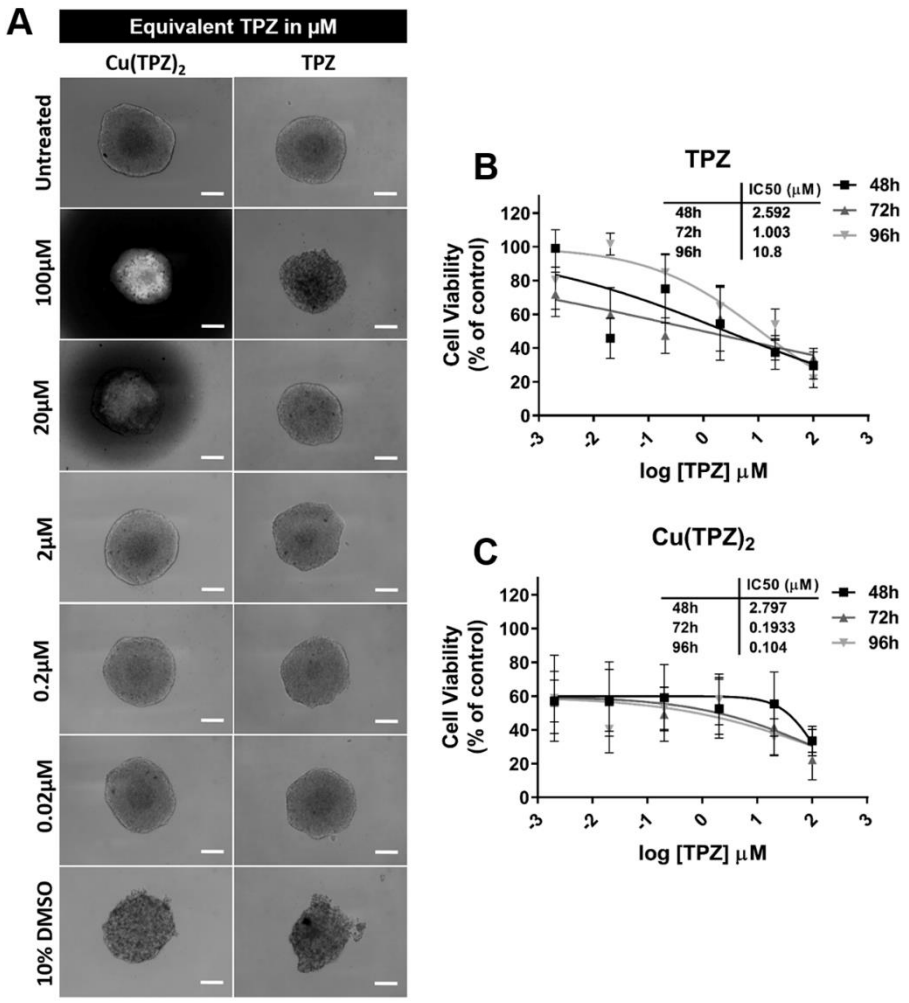

Figure 5.21. Analysis of cell viability in C4-2B prostate cancer spheroid models, after continuous drug exposure. A) Phase-contrast microscope images representative of C4-2B spheroids, exposed to increasing concentrations of $Cu(TPZ)_2$ and TPZ, after 48h treatment. Scale bar, 100µm. Dose and time-dependent effects of B) TPZ and C) $Cu(TPZ)_2$ for 48, 72 and 96h. Cells were incubated with equivalent doses of TPZ in free and complex forms for pre-determined intervals and different oxygen levels. Cell viability was assessed by the resazurin assay, normalized to untreated and data was expressed as mean ± SD for six replicates of three independent experiments (n=3). The IC_{50} values for inhibition were also presented (inset).

Moreover, these results suggested enhanced potency of the complex against 3D models compared to 2D (IC_{50}: 48h, 29.92 ± 1.06 µM; 72h, 1.61 ± 1.03 µM, 96h: 7.57 ± 1.03 µM). Although the data were promising and suggestive of high therapeutic efficacy for both drugs against spheroid models, they must be analysed with caution. The decreased cell viability observed for high doses of the drug were in good agreement with the phase contrast images (**Figure 5.21A**) and previous reports of TPZ activity against other 3D models [460,462,548,549]. Also, TPZ depicted a sigmoidal-like response, while $Cu(TPZ)_2$ showed a plateau from very low doses (0.002 µM) with cell viability already decreased to *ca*. 60%. These results do not agree with those obtained using microscopy. In line with this, it was questioned whether the resazurin assay was providing misleading results and overestimating cell death. An interesting study by Walzel *et al.* [419] demonstrated striking evidence that resazurin may depict low penetration in large compact spheroid models leading to erroneous data especially with cytostatic drugs that do not interfere with cell-cell contacts. Their results showed

reduced levels of resorfurin fluorescence (comparable to those obtained herein in **figures 5.21B** and **5.21C**) due to limited dye diffusion within the inner part of the spheroids, and cell viability measurements only representing the spheroid surface layer. Alternatively, the authors suggested trypsin dissociation prior to resazurin incubation, but this process is time-consuming in high throughput cell screening. In addition, Ca^{2+} chelating agents such as EDTA were found to be an effective strategy to disrupt cell-cell contacts, whilst maintaining spheroid integrity, and aid with resazurin diffusion. This protocol can be a useful and cheaper alternative to commercially available optimized kits for 3D models, such as Cell-titer Glo® (Promega), which also relies on cell-cell contact lysis to increase dye penetration. In line with this, the cell cytotoxicity assays conducted here were repeated, adding a 30 min EDTA (5 mM) pre-treatment followed by overnight incubation of spheroids with the resazurin dye to ensure penetration (**Figure 5.22**).

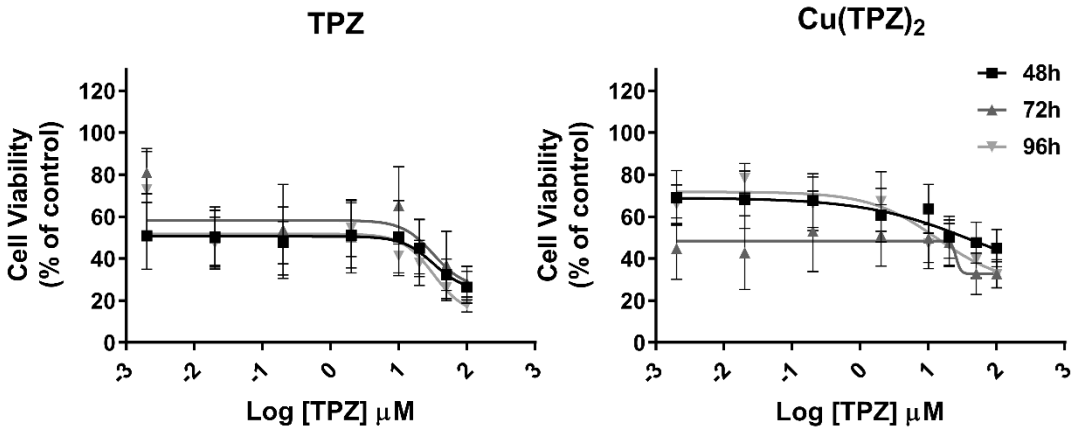

Figure 5.22. Analysis of cell viability in C4-2B prostate cancer spheroid models, after continuous drug exposure and EDTA pre-treatment. Dose and time-dependent effects of TPZ (left) and $Cu(TPZ)_2$ (right) for 48, 72 and 96h. Cells were incubated with equivalent doses of TPZ in free and complex forms for pre-determined intervals and different oxygen levels. Cell viability was assessed by the resazurin assay, with spheroids pre-treated for 30 min with EDTA (5 mM). Results were normalized to untreated and data was expressed as mean ± SD for six replicates of at least two independent experiments ($n \geq 2$).

The results showed loss of the sigmoidal-like shape dose response curve for TPZ (**Figure 5.22, left**), compared to the previous analysis in **figure 5.21B**. The IC_{50} values showed slight enhancement of drug potency at 72h, which was then lost at 96h, with no apparent dose or time-dependent changes in TPZ cytotoxicity (**Table. 5.3**). In accordance with the hypothesis on resazurin penetration the data indicated that TPZ's previous enhanced potency against C4-2B cells was somewhat restricted to the spheroid surface layer, which agrees well with numerous literature reports on the limited diffusion of this drug in tumour models [73,435,460,462,548,549].

Table 5.3. IC_{50} values of TPZ and $Cu(TPZ)_2$, after continuous drug exposure in C4-2B spheroids treated on day 5 of culture. The IC_{50} values for inhibition were assessed by the resazurin assay after pre-treatment with EDTA (5 mM) for 30 min. Data was expressed as mean ± SD for six replicates of at least two independent experiments (n≥2). Statistical analysis: Two-way ANOVA multiple comparison Bonferroni Post-hoc test ($^{****}p<0.0001$, comparing TPZ to $Cu(TPZ)_2$).

C4-2B Spheroids (day 5)		
C4-2B	**TPZ**	**$Cu(TPZ)_2$**
	IC_{50} (μM) ± SD	IC_{50} (μM) ± SD
48h	35.17 ± 1.17	41.78 ± 5.67
72h	26.21 ± 1.18	25.58 ± 3.78
96h	36.02 ± 1.89	$13.33 \pm 1.43^{****}$

High doses of TPZ have been shown to compromise spheroid integrity and induce pronounced toxicity in both the outer and inner rim of the spheroids, concordant with the phase-contrast images presented here and the previous cell viability results. However, lower drug doses are sensitive to oxygen fluctuations throughout the spheroid layers and are easily consumed as it penetrates, limiting its selective hypoxia activity. The data presented in **figure 5.22A** and **table 5.3** agree well with these findings, suggesting decreased response of the C4-2B 3D models to TPZ, compared to the 2D (invariable IC_{50} values).

To overcome these limitations, TPZ analogues have been thoroughly characterised for their structure-activity relationship [73,147,460]. The most promising analogue - SN30000 (**Figure 5.23**), showed increased lipophilicity (due to removal of H-bond donor of the $3NH_2$ group), which was a major determinant for augmented spheroid diffusion [73]. In addition, a cobalt-mustard based HAP [85] exhibited faster uptake and increased hypoxia selectivity, also attributed to its lipophilicity and more electronegative redox-potential. This metal-complex displayed excellent stability allowing for a sustained release of the hypoxia-sensitive ligand under low oxygenated conditions. After dissociation, deeper in the spheroid rim, the ligand induces back-diffusion and potential toxicity to both severe hypoxia cells and also to cells located in the periphery [85].

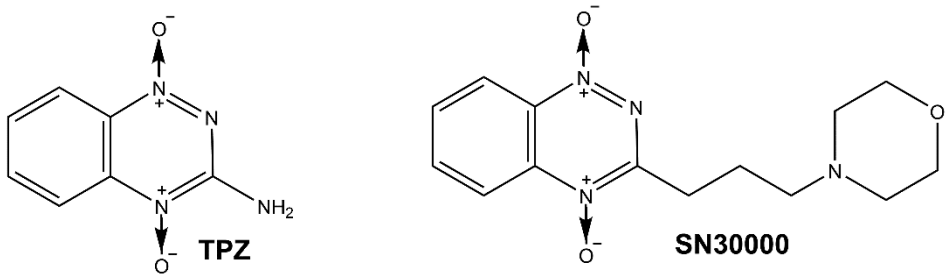

Figure 5.23. Chemical structure of TPZ and its most promising analogue SN30000.

As discussed in **chapter 3**, $Cu(TPZ)_2$ resulted from copper(II) coordination to the 3-NH_2 and 4-*N*-oxide group, which resulted in both increased lipophilicity (log P = 2.88) and more electronegative redox-potential [$E^0(1)$, -0.75 V] compared to TPZ. In line with the analogues discussed above this chemical coordination at the amine position of TPZ was essential in conferring alterations of physicochemical parameters such as log P and $E^0(1)$. Consequently, it can define $Cu(TPZ)_2$'s hypoxia selectivity and also tumour diffusion, which agreed well with the dose and time-dependent cytotoxic profile of this complex against C4-2B spheroids (**Figure 5.22, right**). Surprisingly, even after spheroid EDTA pre-treatment $Cu(TPZ)_2$ continued to exhibit improved therapeutic response over-time compared to TPZ with slightly less cytotoxicity at lower doses. These results suggested that even in the absence of EDTA, $Cu(TPZ)_2$ may provide improved spheroid diffusion and hypoxia cytotoxicity. Together, these data suggested different metabolic reduction rates of the complex compared to TPZ, where at 48h, the cells were less responsive to $Cu(TPZ)_2$ compared to TPZ. In addition to its more electronegative redox-potential, which makes it harder to reduce this complex intracellularly, the strong Cu-N bond in Cu(II)-TPZ stabilizes the complex conferring a mechanism of hypoxia selectivity [550]. Presumably, $Cu(TPZ)_2$ may be reduced into the putative Cu(I)-TPZ, which is more labile than the Cu(II) complex. Under normoxia this intermediary may be reoxidized (by molecular oxygen) to the stable $Cu(TPZ)_2$ complex, which can easily escape the cell through diffusion. In contrast, under hypoxia, the unstable Cu(I) complex is readily dissociated to copper (and TPZ), which is irreversibly sequestered by intracellular proteins. This selective reduction of the complex may originate a sustained dissociation while penetrating the spheroid, resulting in less toxicity to the outer layer of the spheroid; and improved hypoxia cytotoxicity. The decrease in IC_{50} value over time (**Table 5.3**), also suggested continuous penetration of the complex and a mechanism similar to that proposed for cobalt-prodrugs, where the free ligand possibly back-diffuses from the inner spheroid to induce high cell toxicity. This effect resulted in a pronounced therapeutic efficacy of $Cu(TPZ)_2$ at 96h (IC_{50}: 13.33 ± 1.43 μM), compared to TPZ alone (IC_{50}: 36.02 ± 1.89 μM, $p<0.0001$).

In conclusion, the data presented herein call for caution in the development and interpretation of cell viability assays adapted to 3D models. Despite the expectations that TPZ should be readily activated in hypoxic spheroids, the results suggested that oxygenation may not be the sole parameter defining the activity of these drugs. This underpins the invaluable complementary data taken from these models, in contrast to simple monolayers. Moreover, $Cu(TPZ)_2$ showed remarkable time and dose-dependent toxicity in the spheroid model, compared to the limited metabolic activity of TPZ alone. This enhanced activity of the complex may be a result of decreased reduction/consumption of $Cu(TPZ)_2$ in the spheroid environment, but the exact mechanism of toxicity has yet to be investigated.

5.2.2.3.1. Cell cycle analysis

Previous reports showed significant TPZ-induced cell cycle arrest (S-phase) in monolayer nasopharyngeal carcinoma cells due to the drugs' potent DNA damaging and Topo-II cleavable complexes, thus halting DNA replication [115]. As for spheroid models apoptosis assays have reported high resistance of these cells to TPZ treatment with only slight induction of detectable early-stage apoptosis compared to 2D [112]. In order to analyse the cellular responses after TPZ and $Cu(TPZ)_2$ drug exposure a cell cycle and apoptosis analysis was also conducted. C4-2B spheroids cultured for 5 days, were treated for 72h with 20 and 2 μM equivalent TPZ in both free and complex forms. Next the spheroids were isolated, pooled (>10 spheroids per condition), washed, dissociated (to avoid aggregates) and stained with PI for FACs analysis. The left upper panel of **figure 5.24A** shows the forward-scattered light (FSC) and side-scattered light (SSC) plot with gating of untreated spheroids to avoid the undesired noises from debris. In addition, a second singlet gating was also performed to minimize debris and cell aggregates, which are prone in 3D cell protocols. Finally, the FlowJo software was used to generate the cell cycle histograms, statistically indicating the percentage population of cells in G1 (2n DNA content), S and G2/M (4n DNA content). Apoptotic cells present DNA fragmentation with decreased PI fluorescence and were represented by a sub G0/G1 population seen to the left of the G1 peak that was also quantified (**Figure 5.24A, bottom panel**).

The results were then plotted as percentage cell population in each cell cycle phase and compared between treatment modalities (**Figure 5.24B**). The results showed significant increase in S-phase population followed by decrease in G1 for $Cu(TPZ)_2$ treated spheroids at both 10 ($p<0.05$) and 1 μM ($p<0.01$), compared to untreated. TPZ did not exert the same effect on cell cycle arrest, as reported before for monolayer cells [115], suggesting that TPZ cytotoxicity in C4-2B spheroids may be mediated by a non-selective mitochondrial and ROS induced cell death [110] which also agrees with the decreased potency shown by the resazurin assay (**Figure 5.22**). In contrast, $Cu(TPZ)_2$ showed a marked arrest in S-phase, likely derived from a DNA damage-induced cell death after inhibition of DNA synthesis [551] and agrees well with the enhanced DNA binding capacity of this complex discussed before (**section 5.2.1.4**). Furthermore, increased apoptosis after $Cu(TPZ)_2$ (10 μM) treatment was also observed compared to untreated ($p<0.05$) and TPZ groups (20 μM, $p<0.001$; 2 μM, $p<0.01$).

It is reasonable to conclude that $Cu(TPZ)_2$ may exert an increased DNA selective cytotoxic activity in spheroid models. This mechanism of action may have valuable translation applications, by enhancing selective hypoxic nuclear DNA damage. This mechanism agrees well with a previously proposed strategy to improve on TPZ's DNA targeting, minimizing mitochondrial and ROS induced side-effects of TPZ [537].

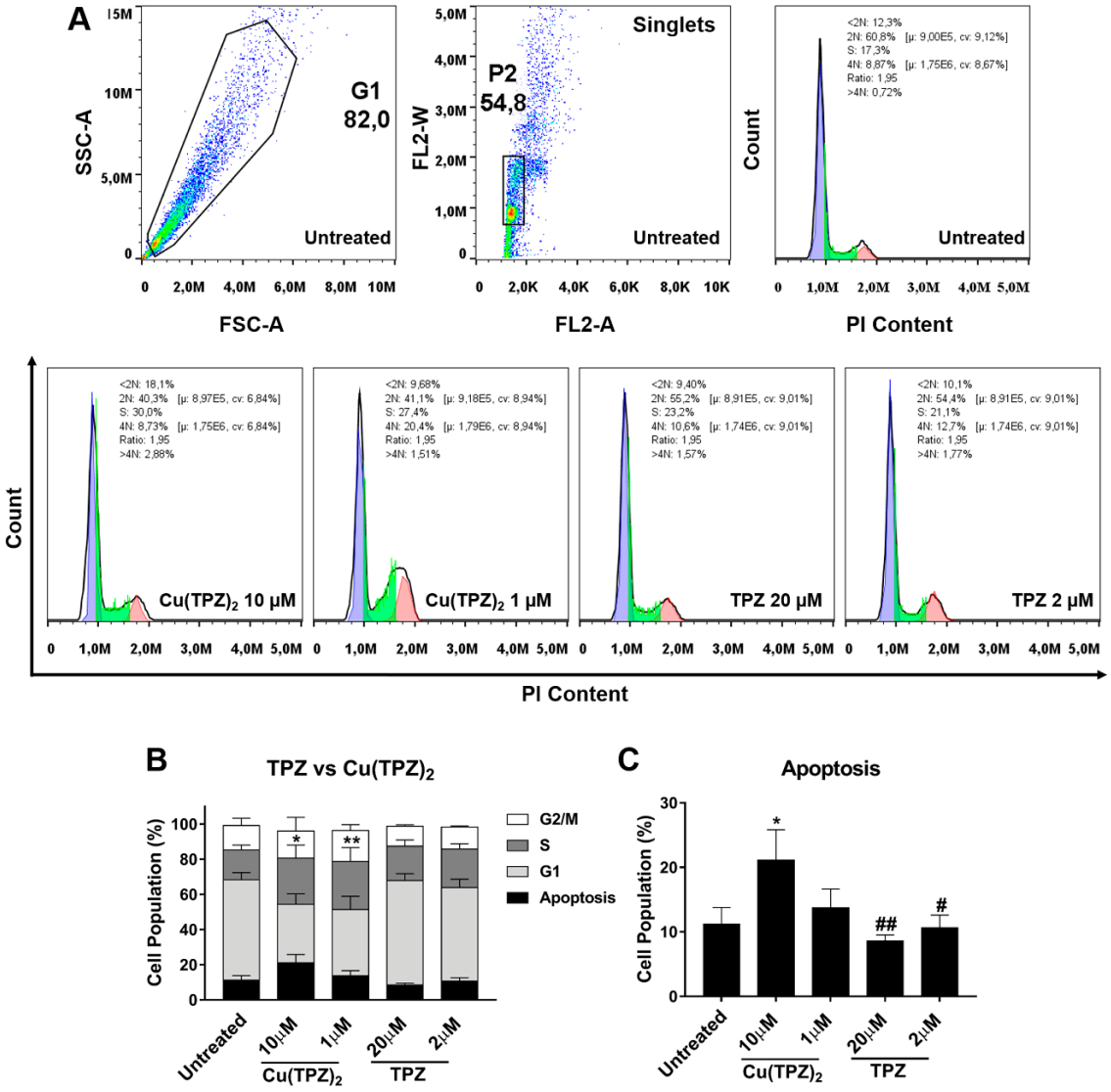

Figure 5.24. Cell cycle analysis of C4-2B spheroids (day 5), after 72h post-treatment with TPZ and Cu(TPZ)$_2$. A) Representative dot plots for cell population and singlet gating are shown, as well as, cell cycle histograms for untreated (upper panel) and treated spheroids (bottom panel); B) cell cycle distribution and C) percentage of cells in apoptosis. Each flow cytometry plot depicts the mean ± SD percentage of G1 (2n), S and G2/M (4n) fraction population. The data represents the mean of at least ten pooled spheroids of two independent experiments (n=2). Statistical analysis: Two-way ANOVA multiple comparison Bonferroni Post-test ($^{*}p<0.05$ $^{**}p<0.01$, compared to control and $^{\#}p<0.05$ $^{\#\#}p<0.01$, comparing TPZ *vs.* Cu(TPZ)$_2$, GraphPad Prism version 7.0).

5.2.2.4. *In vitro* cytotoxicity and hypoxia selectivity of Cu(TPZ)$_2$-loaded liposomes

Liposomes provide drug encapsulation and protection, which could be important for rapidly consumed drugs such as TPZ. In addition, Cu(TPZ)$_2$-loaded liposomes have shown to maintain remarkable *in vitro* hypoxia activity and can therefore provide substantial improvement on TPZ activity *in vivo*. In this section the effectiveness of Cu(TPZ)$_2$-loaded liposomes was evaluated in C4-2B spheroid models, and compared to the free drugs.

C4-2B spheroids were cultured for 5 days and treated with increasing doses of $Cu(TPZ)_2$-loaded liposomes up to 96h as performed for their 2D counterparts. Phase-contrast images were taken over the course of treatment, to assess spheroid morphology (**Figure 5.25, representing 48h post-treatment**). The images illustrated spheroids that became looser at the dose of 20 µM $Cu(TPZ)_2$-loaded liposomes, suggesting cytotoxicity. At lower doses, spheroid shedding was also macroscopically visible, especially for $Cu(TPZ)_2$-DPPC. When exposed to 10% DMSO spheroids became dark and refractive, suggestive of prominent late apoptosis and even necrosis.

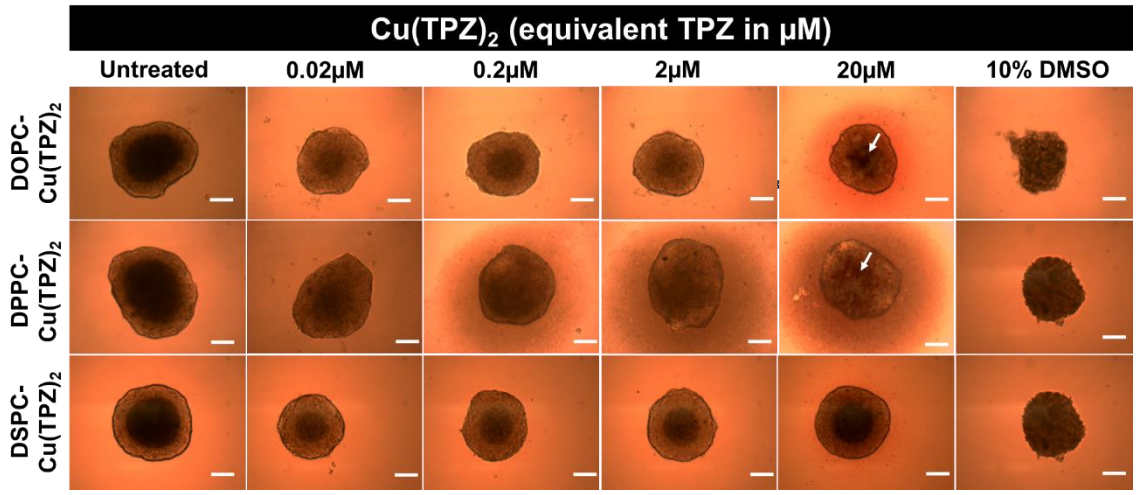

Figure 5.25. Phase-contrast microscope images representative of C4-2B spheroids (day 5 of culture), at 48h post-treatment. Spheroids were exposed to increasing concentrations of $Cu(TPZ)_2$-DOPC (top panel), $Cu(TPZ)_2$-DPPC (middle panel) and $Cu(TPZ)_2$-DSPC, (bottom panel). White arrows depict shedding of spheroids and decrease in volume. Scale bar, 100µm**.**

The resazurin assay with EDTA pre-treatment was then used to accurately quantify cell viability, and non-linear regression of dose-response curves was used to determine the corresponding IC_{50} values. Data were produced and plotted for $Cu(TPZ)_2$-DOPC (**Figure 5.26A**), $Cu(TPZ)_2$-DPPC (**Figure 5.26B**) and $Cu(TPZ)_2$-DSPC (**Figure 5.26C**). At 48h, DSPC did not converge at 50% cell viability, limiting IC_{50} calculation; and showed ambiguous fits at both 72 and 96h. Surprisingly, both DOPC and DPPC loaded formulations resulted in significant left shift of the dose response curves, especially at 72 and 96h, fitting to an adequate sigmoidal model that yielded the determination of the therapeutic effectiveness of these formulations in 3D. The IC_{50} data was compiled (**Figure 5.26D**) and statistical analysis was performed to compare free $Cu(TPZ)_2$ activity to its encapsulated $Cu(TPZ)_2$-DOPC and $Cu(TPZ)_2$-DPPC counterparts. At 48h, post-*hoc* statistical analysis was suggestive of an approximate 2-fold more potent activity from both $Cu(TPZ)_2$-DOPC and $Cu(TPZ)_2$-DPPC ($p<0.0001$) compared to free $Cu(TPZ)_2$. More promisingly, higher activity was obtained at 72h post-treatment where $Cu(TPZ)_2$-DOPC (IC_{50}: 8.52 ± 1.18 µM, $p<0.0001$) and $Cu(TPZ)_2$-DPPC (6.08 ± 1.22 µM, $p<0.0001$), exhibited *ca.* 3- and 4.17-fold increased potency, respectively, compared to free $Cu(TPZ)_2$.

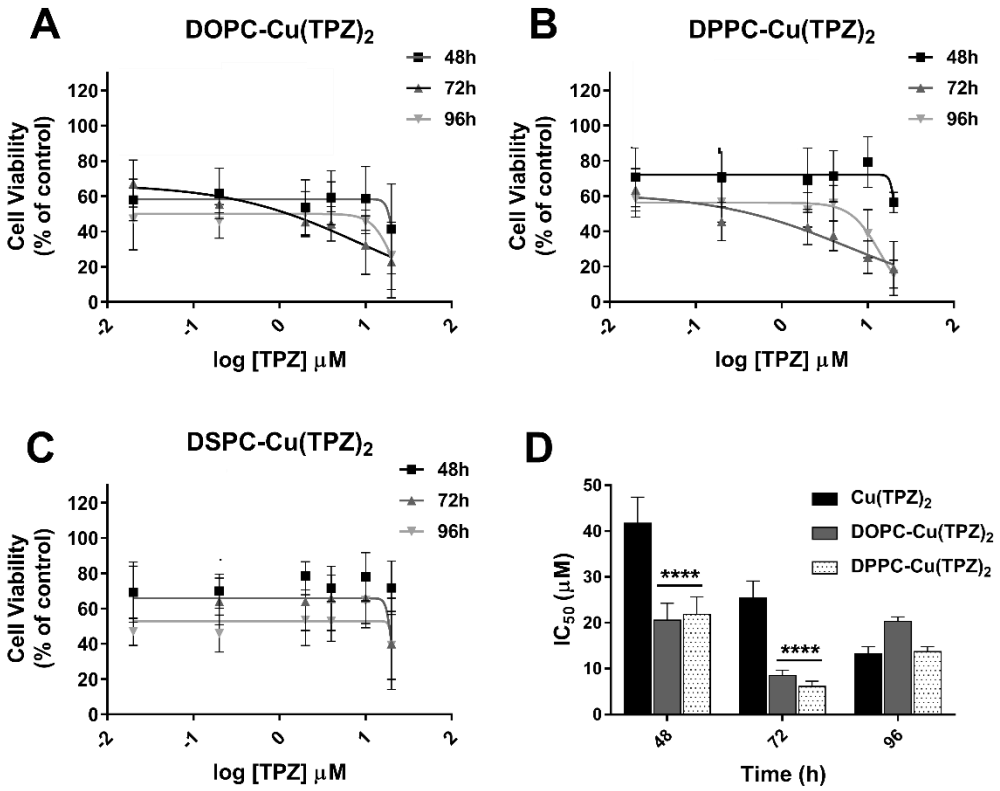

Figure 5.26. Analysis of cell viability and IC_{50} in C4-2B prostate cancer spheroid models after continuous exposure to $Cu(TPZ)_2$-loaded liposomes (60:1, lipid-to-complex molar ratio). Dose and time-dependent effects of A) DOPC-$Cu(TPZ)_2$ liposomes; B) DPPC-$Cu(TPZ)_2$ liposomes and C) DSPC-$Cu(TPZ)_2$ liposomes for 48, 72 and 96 h. D) Summary of IC_{50} values, following continuous exposure to free $Cu(TPZ)_2$ and $Cu(TPZ)_2$-loaded liposomes. Cell viability was assessed by the resazurin assay, with spheroids pre-treated for 30 min with EDTA (5 mM). Results were normalized to untreated and expressed as mean ± SD for six replicates of at least two independent experiments ($n \geq 2$). Statistical analysis using Two-way ANOVA multiple comparison with Bonferroni Post-test (GraphPad Prism version 7.0) was performed to compare multiple groups: ($^{****}p<0.0001$ compared to free $Cu(TPZ)_2$)

This can well be associated with improved drug protection, and enhanced liposomal interaction and penetration within the spheroid models, which potentiated drug activity [379,382,500]. Finally, at 96h, no significant differences in potency were found between the liposomal formulations and the free complex.

The therapeutic response in 3D was both drug, formulation and time-dependent. As concluded before, C4-2B spheroids were less responsive to $Cu(TPZ)_2$ treatment (compared to 2D models), but the data gathered here indicated that liposomal encapsulation may provide substantial improvement on drug activity in an *in vivo* environment. Previous studies on the interaction of liposomes with spheroid models have established a range of physicochemical properties that may determine the therapeutic activity of these formulations [552-555]. These investigations concluded that size, surface charge, morphology, steric stabilization and lipid fluidity play a detrimental role in binding, diffusion and cytotoxicity [552,554]. Overall, the researchers found that electrostatically neutral round SUVs (100-150 μm) displayed efficient interaction and penetration in tumour spheroids. All three formulations developed herein (at 60:1 lipid-to-complex molar ratios) met these criteria, exhibiting size range of 130-140 nm with ζ-potential *ca.* -12 mV (**chapter 4, table 4.6**). However,

their lipid fluidity and composition may have had a detrimental impact on spheroid diffusion and, consequently, cell viability. Likewise, DOPC liposomes (liquid crystalline formulation at 37ºC) showed remarkable improvement in drug delivery and cytotoxicity, compared to the free drug, which could be attributed to its fluid and deformable nature, yielding better interaction and spheroid penetration [552,554]. Surprisingly, a similar trend was obtained for DPPC (gel formulation at 37ºC), contrary to previous data that suggested less penetration from this more rigid formulation [554]. However, the PEG grafting led to marked electrostatic neutralization, conferring a relatively low negative charge to these liposomes, which could have enhanced their diffusion and, consequently, improved biological activity. Moreover, rigid lipid compositions such as DSPC had limited interaction and spheroid penetration [553,555] that may explain the conflicting results obtained for the DSPC-$Cu(TPZ)_2$ liposomes, compared to the other formulations. Intriguingly, most studies on NP penetration in 3D models concluded that PEGylation may inhibit effective drug delivery and intratumour distribution. The steric hindrance created by addition of PEG groups creates a strong barrier that inhibits cellular binding, uptake and diffusion through tumour masses. Given that all formulations were prepared with equivalent 10 mol % PEG_{2000} it is plausible to conclude that the density and grafting coverage of the different lipid compositions, may have also altered their binding and penetration in the spheroid rim [556]. Generally, this concentration of PEG_{2000} should prevent serum protein adsorption and a strong 'stealth' effect [556]. It is possible that DOPC and DPPC liposomes may have allowed better accommodation of PEG chains within the bilayer, creating only a partial surface coverage, due to diminished density and length of the polymer chains ('mushroom' regime) (**Figure 5.27**). In contrast, rigid DSPC bilayers may have limited PEG penetration, generating a higher coverage and increased thickness of the PEG grafting ('brush' regime), creating a stronger steric hindrance. This transition of mushroom-brush morphology could have implicated liposomal spheroid diffusion.

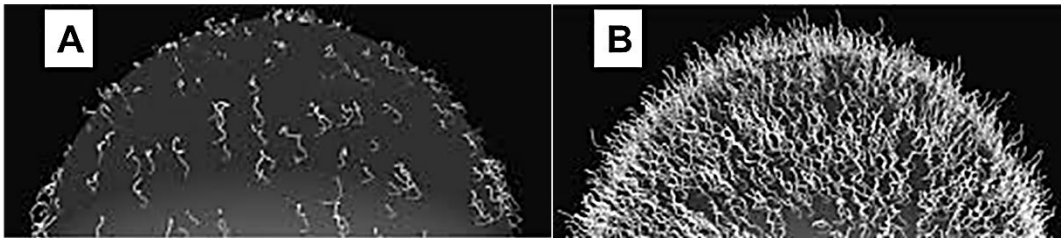

Figure 5.27. Schematic illustration of the PEG coverage and configurations. A) 'Mushroom' regime, where lower grafting is available and fewer coverage, leading to increased protein adsorption and surface interactions. B) "Brush" configuration, where most of the chains are extended, providing full coverage and steric repulsion. Adapted from [557].

Future studies utilising labelled $Cu(TPZ)_2$-liposomes along with confocal microscopy (including spheroid sectioning) and FACs analysis would provide detailed analysis on uptake and penetration [153,382]. These experiments would include non-PEGylated and PEGylated formulations to confirm the role of this polymer on liposomal spheroid penetration. These data along with the release studies conducted in this work, would determine the exact parameters defining the spheroid *in vitro* activity.

More importantly, the striking differences obtained between 2D and 3D models for both the free complex and the liposomal systems, reinforce the concept that spheroid models may have a better prediction of the translational outcome of these treatments.

This figure highlights the work performed in this thesis. The encapsulation of TPZ *via* $Cu(TPZ)_2$ led to the successful development of liposomal formulations that showed marked improvement of efficacy in 3D models. This is not only important in terms of maximizing TPZs hypoxia activity but also provides important translational information, confirming that this DDS may be a means of repurposing TPZ as a potent hypoxic pro-drug for clinical purposes.

5.3. Summary and conclusions

The development of HAPs has emerged as a promising strategy to selectively target and disseminate low oxygenated tumour cells with aggressive phenotypes. Many active cytotoxins from different classes of these prodrugs (nitro compounds, quinones, tertiary amine *N*-oxides) are metabolized by 2-, 4- and 6-electron reduction pathways that compromise their hypoxia selectivity [89,90]. In contrast, TPZ has been thoroughly investigated as an advanced bioreductive prodrug due to its remarkable hypoxia selectivity *via* a 1-electron reduction pathway that generates substantial DNA damage. This drug has shown encouraging results in pre-clinical studies, but failed to improve overall survival in recent clinical trials [91]. Most of the drawbacks associated to this prodrug are attributed to its fast metabolism, poor cellular uptake and most importantly compromised tissue diffusion, which limits its hypoxia toxicity. Therefore, considerable efforts to develop TPZ analogues have been made, to rationally improve on its current biological limitations and fully exploit the potential of this drug [147,460].

Copper(II) complexes have emerged as potential anti-cancer compounds and rendered the development of hypoxia selective prodrugs. Given that these complexes are generally well-tolerated *in vivo*, coordination of TPZ to copper may offer a means of reducing its systemic toxicity and enhancing cellular uptake and diffusion. In this chapter, the hypoxia potency and selectivity of a cupric-TPZ complex was evaluated against a panel of 4 different PCa cell lines, representing differential stages of disease progression. The results clearly showed that sensitivity was cell-line dependant and that potency was not overall improved compared to TPZ (aside from C4-2B cells), but selectivity was markedly affected. Moreover, the lipophilic nature and electronegative redox-potential evaluated in **chapter 3** may corroborate the increased and selective uptake in PCa cells, confirming the increased hypoxia toxicity observed. The cytotoxicity profile was further extended to spheroid models to gain a better prediction of the therapeutic outcome of these HAPs. Furthermore, $Cu(TPZ)_2$-loaded liposomes were also tested in 2D and 3D models of C4-2B cells, confirming the potential encapsulation and hypoxia activity of these nanocarriers.

Concurrently, the following conclusions were drawn from this chapter:

- Experimental set-up in both 2D and 3D resulted in optimum hypoxic conditions to test both TPZ and its cupric-complex
- Screening of 4 different PCa cell lines revealed that hypoxia treatment was cell-line dependent. LNCap and C4-2B exhibited remarkable sensitivity, with significant hypoxia selectivity conferred by $Cu(TPZ)_2$. In contrast DU145 and PC3 were refractory to therapy. The best results were obtained at 72h post-treatment where $Cu(TPZ)_2$ potency and selectivity improved in the following order: C4-2B>LNCap>DU145>PC3.
- In agreement with the increased hydrophobic nature and more electronegative redox-potential, $Cu(TPZ)_2$ had marked cellular uptake in C4-2B cells, compared to TPZ and displayed remarkable hypoxia selective uptake at 4h.
- The determined binding constant of $Cu(TPZ)_2$ for CT-DNA was $0.18 \times 10^2\ M^{-1}$ that implies moderate DNA binding capacity for this complex.
- $Cu(TPZ)_2$-loaded liposomes exhibited an *in vitro* cytotoxicity profile that correlate well with their release kinetics. DOPC-$Cu(TPZ)_2$ had a delayed effect, but resulted in potent cytotoxicity over time (IC_{50}<12 µM), as compared to both DPPC- and DSPC- $Cu(TPZ)_2$ liposomes. Encapsulated $Cu(TPZ)_2$ maintained its hypoxia selectivity.
- $Cu(TPZ)_2$ resulted in higher treatment resistance in 3D, compared to 2D, but had improved hypoxia selectivity in spheroids, compared to TPZ with an IC_{50} of 13.33 ± 1.43 µM at 96h. Cell cycle analysis revealed S-phase, with pronounced apoptosis after $Cu(TPZ)_2$ treatment
- $Cu(TPZ)_2$-DOPC and $Cu(TPZ)_2$-DPPC liposomes resulted in remarkable therapeutic activity in 3D cultures that was particularly effective at 48 and 72 h, compared to the free complex. 3D models are essential for therapeutic prediction; although $Cu(TPZ)_2$-DSPC was selected as the best formulation in C4-2B monolayers, it failed to translate its potency in 3D;
- Liposomes showed best activity at 72 h, where potency matched or was improved compared to their 2D counterparts.

Chapter 6

General discussion, future work and conclusions

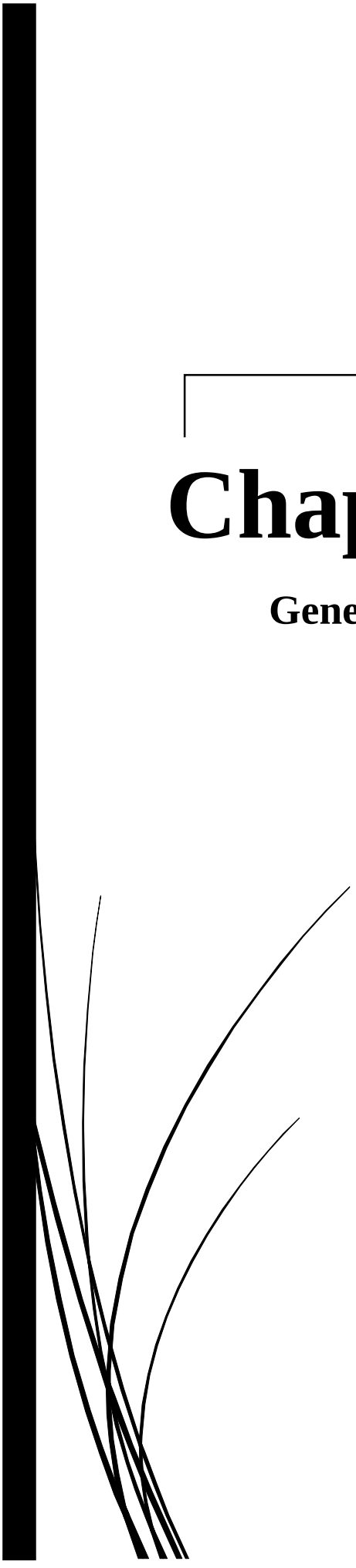

6.1. General discussion

Hypoxia is a common feature amongst solid tumours [558]. In the last years it has become a challenging yet exciting new target to develop novel anti-cancer therapies [558]. TPZ is the most established and characterised HAP and has shown excellent hypoxia selectivity *in vitro* [99,100]. Its advantage over other developed HAPs relies on its activation under moderate (pO_2<5%) to severe (pO_2<0.1%) hypoxia levels, affecting a larger proportion of low oxygenated cells in the tumour core [97]. However, its potent activity has failed to translate into a clinical setting [72,99] and recent data have suggested that the rapid reduction, and consequently limited tumour diffusion of TPZ significantly affects its biological activity [91,99]. The application of hypoxia selective therapies is now determined by two main parameters: 1) understanding SAR and rationally designing analogues with superior physicochemical properties that improve PK; and 2) simultaneously applying reliable hypoxia biomarkers, which can aid with patient standardization and the use of biologically relevant hypoxia models.

The challenges involved in the design of new small molecules are governed by the need for high specificity and desirable PK properties that can guarantee significant tumour uptake and drug bioavailability. Over the last two decades substantial evidence has provided insight on the chemical modifications that undermine the modulation of parameters such as lipophilicity, redox potential and diffusion, which seem to have a detrimental effect on hypoxia selectivity [147,181,194,455]. Many SAR studies with TPZ analogues have provided substantive correlation between specific substituents (and their position) with improved pharmacological outcome [68,147,194,441,442]. Moreover, the use of transition metal complexes has shown to be a particularly suitable strategy to modify existing pro-drugs, and develop a new biologically active molecule with improved hypoxia activity [167,455,559]. Copper(II) complexes have shown to coordinate well with 1,2,4-benzotriazine 1,4-di-*N*-oxides [168,169], similar to TPZ, generating prodrug complexes that are stable under physiological conditions, but become kinetically labile with changes in the redox status or pH of the environment. This metal-complex can thus provide a dual mechanism of action. Firstly, the biologically active ligand is deactivated upon coordination, minimizing off-target reduction and premature metabolism; or, the complex itself can provide alternative biological applications [560]. Alternatively, the development of nanocarriers for the delivery of TPZ has shown to significantly improve on drug uptake and bioavailability [376,378-384], providing substantive anti-tumour activity in combination with other chemotherapeutics or PDT. However, most of these studies have limited drug cargo and failed to exploit TPZ activity in the absence of combination therapies. The work developed in this thesis sets-off to develop a new liposomal formulation to encapsulate TPZ. It was found that copper(II) coordination, prior to TPZ encapsulation, substantially improved liposomal retention of this HAP. Moreover, the complex itself exhibited important modifications regarding the molecular weight, lipophilicity, redox-activation and hypoxia selectivity, compared to TPZ alone,

suggesting that this metal-complex may provide alternative biological targeting and effectiveness. Herein, the synthesis and basic characterisation of $Cu(TPZ)_2$ may warrant further SAR studies and the use of metal-complexation to boost TPZ *in vivo* activity. Moreover, a simple and inexpensive liposomal loading method *via* copper complexation provided marked TPZ loading, compared to a previous study, which can provide better *in vivo* toleration, reduced systemic effects and enhanced tumour accumulation.

6.1.1. SARs: TPZ analogues and the importance of copper(II) complexes

TPZ is a leading bioreductive drug known for its pronounced hypoxia selectivity [99]. Its MoA has been described in **chapter 1** and is marked by an oxygen-dependent rate limiting step where the lead compound is back-oxidized under normoxic conditions [116]. When oxygen levels decrease, TPZ is reduced to its radical counterpart that after fragmentation also produces hydroxyl radicals. Its extensive cytotoxicity has been correlated to the generation of DNA single- and double-strand damage. Recent clinical evaluation has caused controversy on whether this prodrug results in significant therapeutic outcome and pronounced survival rate [99]. Therefore, over the years, several researchers (Brown, Hicks, Hay, Wilson and Patterson) have developed a series of structurally diverse analogues of TPZ and analysed their effect on properties such as solubility, lipophilicity, redox-potential, tumour diffusion and hypoxia selectivity [73,147,441,442]. First, analogues with modifications of the A-ring with 5-, 6-, 7- and 8-subsituents were created [441], followed by another study where 3-subsituents [442] were also combined (**Figure 6.1**). The aim of these studies was to produce therapeutically optimized forms of TPZ to overcome its current clinical drawbacks. The compounds possessed a diverse range of physicochemical properties, with solubility ranging from 4.54 to over 250 mM, redox-potentials of –127 up to –670 mV and Log P values ranging from –1.61 to 1.18 [147,441,442]. Likewise, a differential pattern of biological activity was also observed (HCR values ranging from 1 to 180). Although it seemed difficult to find a pattern between specific substituents and the modified chemical properties, it was clear that it was possible to generate a diverse set of TPZ analogues with optimized properties [147].

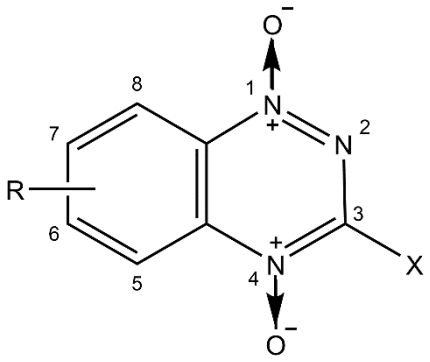

Figure 6.1. Chemical structure and atom numbering of TPZ, displaying primary positions of substituents used in SAR studies. A-ring substituents were done in R5, R6, R7 and R8 and other studies with 3-amino substituents (X).

The main conclusions drawn from these studies were as follows: 1) in general, 5- and 8-substituents were more soluble than TPZ, attributed to a distortion in the crystalline structure of the HAP; 2) substituents in all positions that resulted in increased lipophilicity had improved cellular uptake; 3) renal clearance of TPZ occurs after hydroxylation at the 7-position, new substituents may thus minimize rapid excretion; 4) a strong correlation was found between lower redox-potentials and hypoxia selectivity; 5) halo-substituted analogues in 5-, 6, 7- or 8-postions generated potent hypoxic activity and 6) heteroatoms at the 3-position had a more profound effect on the physicochemical properties and therapeutic outcome.

Overall, the results suggested that ring-A substituents could be used to modulate reduction potentials, and excellent HCR values (>50) were achieved by substituents that resulted in E(1) values between -0.45 to -0.51 V [147]. More importantly, a more recent analogue (SN30000), derived from the removal of the H-bond donor 3-NH_2 group of TPZ, yielded increased lipophilicity, 3-fold improved diffusion coefficient in multi-layered spheroid models and, consequently, higher hypoxia selectivity [73]. Coordination of Cu(II) to TPZ seems to comply with the observations discussed above. The addition of a transition metal *via* 3-subsituition (removal of H-bond donor), along with the addition of an extra TPZ moiety, may have well contributed to the increased lipophilicity (Log P = 2.88, predicted in this work) and its more electronegative redox-potential (-0.75 V). The modified physicochemical properties are also in good agreement with a previous study, where Cu(II) complexes of quinoxalines resulted in improved cellular uptake (higher log P, compared to free ligands) and good hypoxia selectivity [168,169]. Moreover, this $Cu(TPZ)_2$ complex exhibited properties, which are consistent with Lipinski's rules for small molecules: Mw <500, hydrogen bond donors and acceptors less than 5 and 10, respectively and log P <5, for optimum permeability and intestinal absorption.

Aside from the aforementioned properties that have a positive correlation with hypoxia selectivity, it is plausible to predict that this complex can act as an active organic metal or as a chaperone of TPZ, displaying slower metabolic reduction, with improved cellular uptake and diffusion coefficient. In addition, $Cu(TPZ)_2$ displayed increased pH stability, which can help bypass unwanted aerobic toxicity of TPZ [99,100]. In summary, although improved biological outcome was expected (discussed further on in this chapter), future SAR studies with this metal-complex, along with serum stability studies to predict association/dissociation kinetics, may provide more detail on the biological properties of $Cu(TPZ)_2$.

6.1.2. Liposomal encapsulation of TPZ: the advantage of copper-complexes

Previous reports have discussed the difficulty in encapsulating small drug molecules in DDS [270,384]. At the start of this project, only one study had reported the successful conjugation of TPZ to transferrin molecules and how this delivery system could provide improved cellular uptake and bioavailability of this HAP [376]. In a similar matter, this work also reported the difficulty in obtaining acceptable drug loading in the developed liposome formulations. Most of the developed protocols resulted in null encapsulation quantities or failed to show batch-to-batch reproducibility. Moreover, Broekgaarden and co-workers [384] only very recently reported the encapsulation of TPZ in cationic-liposomes, but obtained rather low drug loading and relied on high initial drug quantities to ensure encapsulation. Together, these findings indicated that TPZ might be a difficult drug to encapsulate in liposomes and that leakage may surpass any detectable drug loading. This is consistent with the fact that conjugation strategies resulted in the successful development of TPZ-NP carriers with maximum cargo obtained with transferrin mediated delivery (300 μM) [376].

With the notion that nanocarriers can minimize drug degradation from the external medium, along with improved cellular uptake and tumour bioavailability [348], it is possible that TPZ-NPs could result in better PK properties and maximize HAP biological activity [349]. In this work, a new protocol was developed, which resulted in significantly improved liposomal encapsulation of TPZ using coordination with copper(II). Previous reports have already discussed the advantages of forming metal-complexes and that precipitation of these compounds may induce drug retention and improve drug loading [402,448,477]. It appeared that the apparent lower aqueous solubility of $Cu(TPZ)_2$ compared to TPZ alone may be the key determinant for drug retention and the complex may function as a chaperone to increase TPZ loading. A detailed discussion on the optimization of this protocol was provided in **chapter 4**. The method developed herein offered a simple strategy to achieve good loading in different liposomal formulations at physiological pH. Liposomes with acceptable size and PDI were obtained, even at the maximum 20:1 lipid-to-complex molar ratios, but the 60:1 ratio was chosen for *in vitro* experiments, due to its long term stability. This strategy was similar to that reported by Kheirolomoom *et al.*[448] where copper-Dox complexes provided stability in both neutral pH and serum conditions. Dissociation of the complex was pH dependent (in agreement with this study), as well as albumin trans-chelation, confirming the extended circulation stability. In addition, the metal-complex resulted in 100% liposomal EE and *in vivo* data confirmed the reduced systemic toxicity and increased drug bioavailability. The presence of the encapsulated complexes were confirmed by EM, depicting the formation of diffused metal precipitates, in good agreement with the TEM imaging discussed in **chapter 4**. In conclusion, $Cu(TPZ)_2$ complexes may provide a dual mechanism by extending stability, due to their pH dependent mechanism and when encapsulated in liposomal formulations, improved drug accumulation.

Only very recently have other NPs been developed to deliver TPZ. These carriers have been summarised in **table 6.1**, depicting the EE and amount of encapsulated TPZ, which was calculated taken into consideration the information provided in each manuscript. Where values could not be determined the acronym - N.D. - appears. In summary, most NPs depicted rather low encapsulation efficiencies, which agrees well with previous discussions on the difficulty in encapsulating TPZ. In addition, strategies involving conjugation [376,377] or metal-cages [381,383] seem to provide higher amount of TPZ cargo. It becomes clear that methods relying on retention of the drug (either by covalent conjugation or metal-TPZ interactions) surely contributes to its superior NP encapsulation. In line with this, $Cu(TPZ)_2$-loaded liposomes developed in this work exhibit the highest EE values of the panel, for both ratios presented, accompanied by excellent amounts of TPZ content (ca.383.9 μM and ca.113.5 at 20:1 and 60:1 ratio, respectively). These values also confirmed a 5- and 16-fold increase in liposomal loading of TPZ, using copper(II) compared to previous formulations of cationic-TPZ liposomes.

Table 6.1. Summary of EE and TPZ cargo in different nanocarriers.

DDS	EE(%)	[TPZ](μM)	Ref.
TPZ-Tf	6:1(TPZ:Tf)	300	[376]
TPZ-Au	732:1 (TPZ:Au)	134.9	[377]
Upconversion silica NPs	6	168.4	[378]
Mesoporous silica NPs	3.9	218.4	[379]
Micelles (AVT-NPs/TPZ)	11.08 (Wt)	N.D.	[380]
Porphyrinic MOF	9.8	274.4	[381]
Polymeric/lipid NP	37	N.D.	[382]
Multifunctional tungsten oxide NPs	77.41	*ca.*168	[383]
Cationic liposomes	2.4	24	[384]
$Cu(TPZ)_2$-liposomes (60:1 lipid-to-complex)	***ca.*78.17**	***ca.*113.5**	
$Cu(TPZ)_2$-liposomes (20:1 lipid-to-complex)	***ca.*79.82**	***ca.*383.9**	

6.1.2.1. Proposed mechanism for liposomal encapsulation of $Cu(TPZ)_2$

To current knowledge, this is the first study to show pre-complexation of TPZ, followed by liposome encapsulation; other studies relied on complexation within the liposome core [402,448,477,479]. The protocol enabled the formation of a complex with lower solubility than TPZ that along with efficient bilayer permeation allowed drug retention *via* formation of complex precipitates (verified by TEM). Cheung *et al* [273] provided interesting evidence on how the reduced solubility of a manganese-Dox (Mn^{2+}-Dox) complex drove liposomal encapsulation. Even in the absence of pH gradients complex precipitation inside the liposome dissipated the apparent transmembrane gradient and *via* equilibrium processes increased complex loading. More complex molecules were encapsulated and, higher quantity of Mn^{2+}-Dox was further precipitated this process only stopped once the minimal amount of soluble drug in the core was equal to that of the external medium [270,273]. Gathering the results obtained for $Cu(TPZ)_2$ loading (**section 4.2.2.5**) along with TEM (**section 4.2.2.6**) the same principle may be applied to $Cu(TPZ)_2$. A schematic overview of the proposed mechanism of encapsulation is summarised in **figure 6.2**. With increasing $Cu(TPZ)_2$ content within the liposomes core complex precipitation may then be responsible for i) an apparent decrease in the concentration of soluble form of the complex; ii) a decrease in the ionic strength across the lipid bilayer; iii) higher drug loading with higher complex-to-lipid ratios, which iv) may be linked to further modulation of the rate of complex release *in vitro* and *in vivo*.

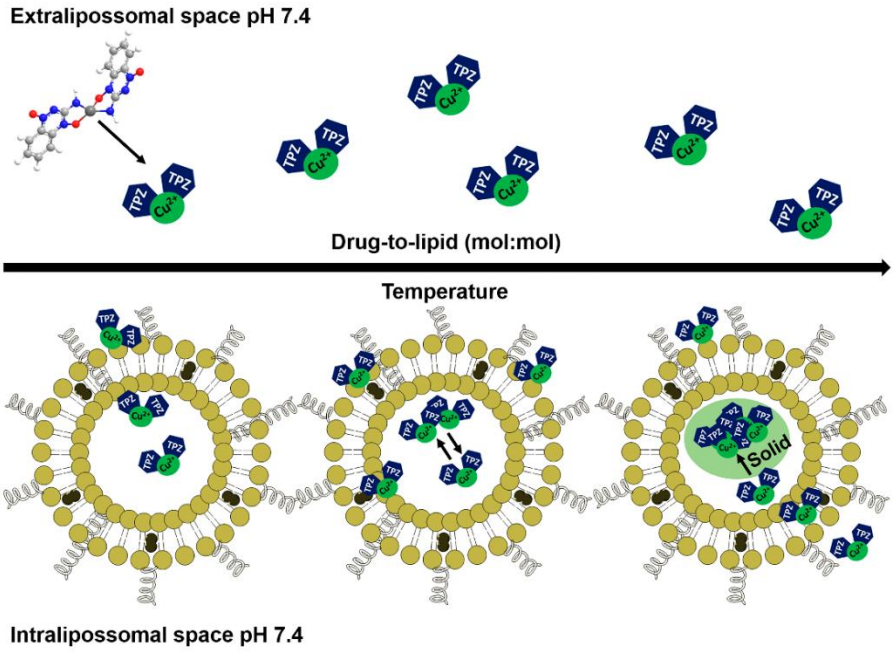

Figure 6.2. Proposed schematic representation of the process occurring during encapsulation of $Cu(TPZ)_2$ by a remote ion loading method in liposomes. Despite the lack of proton (pH) gradient, the drug is lipophilic and translocates throughout the bilayer. Here, it can form soluble forms at low drug-to-lipid ratios in the aqueous core of the liposome or, at high drug-to-lipid ratios, a low soluble coordinate complex precipitate. This solid precipitate causes an apparent decrease in concentration of the complex compared to the external medium, promoting further internalization of complex molecules in the liposome core, via an equilibrium process. With this, the apparent formed ionic gradient is reduced and the new complex molecules are further precipitated inside. Furthermore, the loading process stops when the concentration of some minimal solubilized complex forms inside the liposome equals that of the complex in the extralipossomal space.

6.1.2.2. Can $Cu(TPZ)_2$ be in the bilayer and aqueous core?

In light of the proposed mechanism of $Cu(TPZ)_2$ liposomal encapsulation along with the intriguing release kinetics obtained in **chapter 4** the question on whether the complex is located in the bilayer or aqueous core of the liposomes arose. Generally, fluid formulations composed of DOPC lipids should provide a faster drug release due to rapid destabilization in serum [495-497] compared to more gel-like formulations at 37ºC. However, according to the results obtained in this thesis, DOPC-$Cu(TPZ)_2$ liposomes generated a significantly slow early release compared to other formulations, and only at 10h showed a burst release, with over 80% of the complex in the medium. This unexpected release kinetics led to the assumption that $Cu(TPZ)_2$ may well accumulate in the aqueous core of DOPC liposomes, forming dense precipitates (validated by TEM), which could contribute to its sustained release. As shown previously, metal-complexes tend to form solid precipitates, due to low aqueous solubility, which confer stability and delayed release kinetics. The denser the precipitate, the slower the dissolution rate and drug leakage. In **figure 6.3**, a hypothetical scheme on the release mechanistic of all three formulations developed in this work is provided.

DOPC-$Cu(TPZ)_2$ liposomes may lead to the accumulation of complex precipitates in the aqueous core, with slower dissolution rate. In contrast, DPPC- and DSPC-$Cu(TPZ)_2$ liposomes, which showed similar release kinetics, may have a mixed bilayer and aqueous core encapsulation that result in faster dissolution and drug leakage. The change in the T_m of liposome bilayer depends on the presence of other chemical species and how they interact with the vesicles. The interactions of $Cu(TPZ)_2$ can be analysed using differential scanning calorimetry (DSC) [561] and electron paramagnetic resonance (EPR) [562] to provide information on the partitioning of these complexes in lipid moieties or aqueous environment. Additionally, cryo-EM [477] could reveal important structural information on the complex physical-state inside the various formulations.

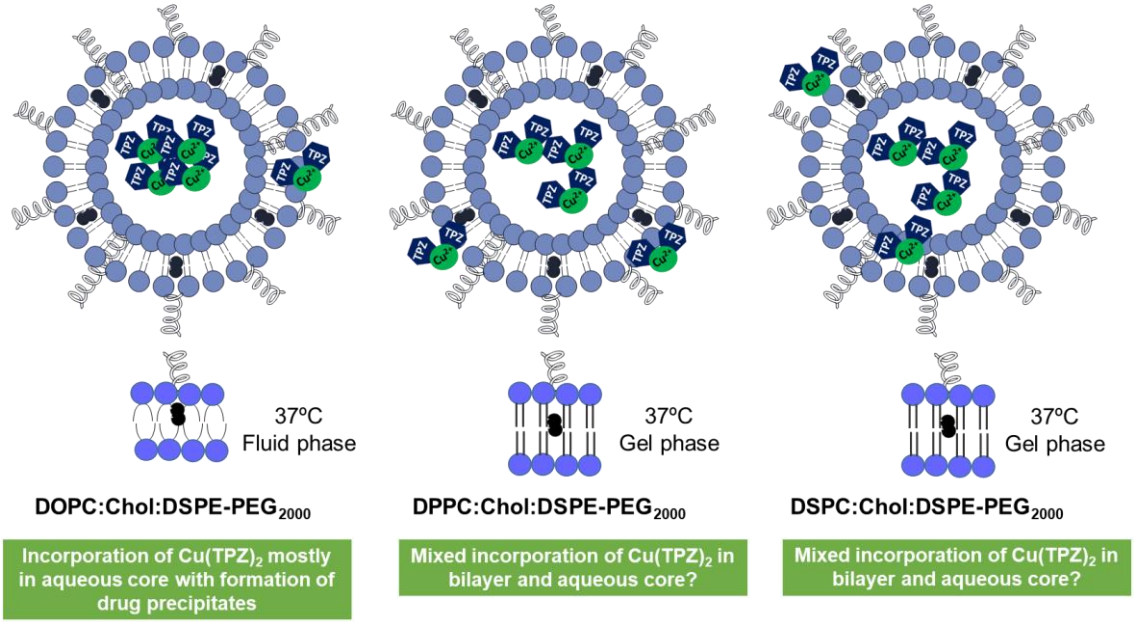

Figure 6.3. Schematic illustration on the proposed localization of $Cu(TPZ)_2$ in different liposome formulations.

6.1.3. Insight on cellular activity of Cu(TPZ)$_2$ complexes

Extensive work by J. Dearling, J. Holland and J. Dilworth has provided detailed analysis on the therapeutic and hypoxia imaging applications of copper-complexes [170,174,176,181,455,563]. Cu(ATSM) has a attracted special attention due to its significant 'trapping' in hypoxia cells and selectivity both *in vitro* and *in vivo* [176]. Moreover, the use of copper radionuclides during complexation has shown to generate stable and selective imaging probes for *in situ* evaluation of tumour hypoxia [563]. The low MW, lipophilicity and planar structure of these complexes allows rapid cellular internalization and targeting of hypoxia [455,459]. In line with the discussion in **section 6.1**, these complexes have also been subject of several SAR studies that have generated a significant amount of data that allows the prediction of important parameters that define hypoxia selectivity, such as lipophilicity and more importantly redox potential. A particular study by J. Dearling [455] showed that there was a positive correlation between enhanced hypoxia selectivity with increased log P and more electronegative values of Cu(II/I) reductive potential (**Figure. 6.4, highlighted in grey**).

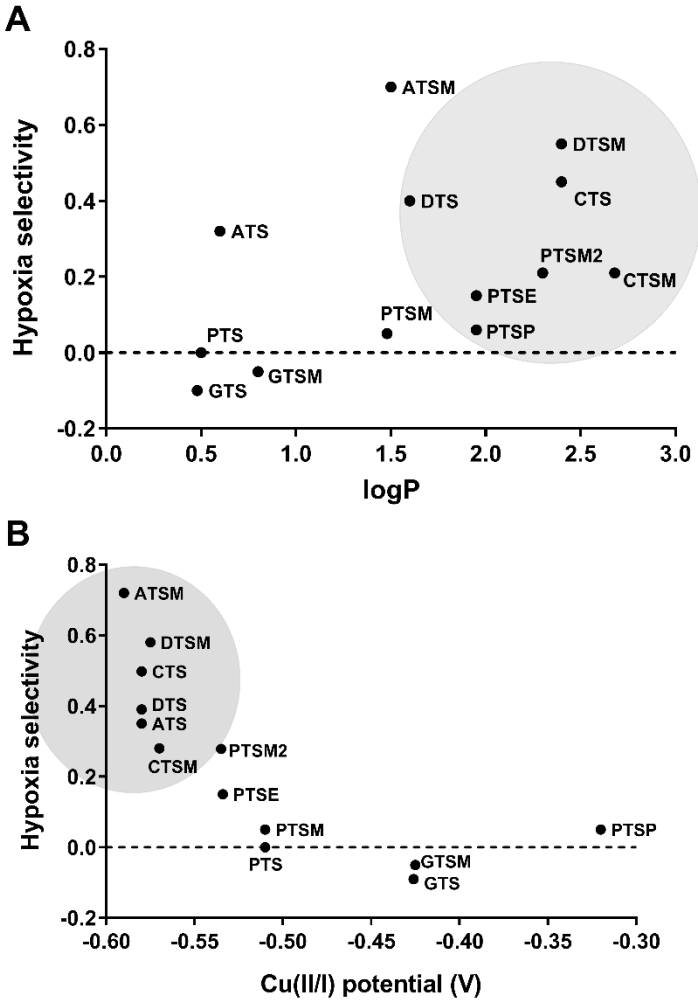

Figure 6.4. Plot depicting hypoxia selectivity for several analogues of Cu(II)-thiosemicarbazone complexes in relation to A) their lipophilicity values (log P octanol/water) and B) reductive potential (in DMSO *vs*. Ag/AgCl). The best hypoxia selective compounds are highlighted in grey. Adapted from [455].

Given the predicted data detailed in **chapter 3** for $Cu(TPZ)_2$ (log P of 2.88) and reductive potential of -0.75 V, it was expected that this complex exhibited potent and selective activity under hypoxic conditions.

6.1.3.1. Selectivity of $Cu(TPZ)_2$ complexes in PCa monolayers

TPZ's selectivity arises from its oxygen dependent one-electron reduction and enzymology reports concluded that this HAP is mainly bioactivated by cytochrome P450 and NADPH cytochrome P450 reductases, intracellularly [108,109,111,528]. Many studies have reported that selectivity can reach values of 30 up to 300-fold increased toxicity under low oxygenated conditions, but is cell-line dependent [100-102,115,124]. The same was observed in SAR studies, where analogues produced HCR values ranging from 0.18 to 37 against SCC and colorectal cell lines [147]. Most of these experiments reported toxicity using clonogenic assays, but a good correlation was obtained between this method and proliferation assays, validating the utility of these higher throughput assays [147]. Also, the developed analogues seemed to consistently maintain hypoxia potency, compared to TPZ, and mainly affect selectivity. In an effort to procure new prodrugs with improved therapeutic indices, copper(II)-complexes emerged as a new strategy for hypoxia applications [170,455]. The unique redox-chemistry of Cu^{II}/Cu^{I} enables a selective intracellular reduction that can lead to the accumulation of complexes inside low oxygenated cancer cells, compared to normal non-cancerous cells. Several reviews have portrayed the extensive anti-cancer properties of different copper complexes, highlighting the influence of different ligands and functional groups on the versatile application of these metal-complexes [167,171,559]. Despite the strong anti-cancer activity within the low submicromolar range (<10 µM), few studies have actually focused on discriminating the biological activity in normaxia *vs.* hypoxia. Reports on the effectiveness of copper(II) complexation to quinoxaline dioxide derivatives (similar to TPZ) showed that although potency was inferior to that of the free ligand, hypoxia selectivity was maintained [168,169].

In this thesis, PCa cell lines were used as models to evaluate the cytotoxicity of novel $Cu(TPZ)_2$ complexes compared to free TPZ taking into account the important role of hypoxia on PCa progression and resistance to treatment [218]. Adsule *et al.*[189] developed a potent quinoline-2-carboxaldehyde copper complex, which inhibited proteasome activity in PC-3 and LNCaP cells (IC_{50} of 4 and 3.2 µM, respectively). However, studies were only done under normoxia conditions, not specifying any hypoxia selectivity. In this work, $Cu(TPZ)_2$ resulted in poor cytotoxicity under normoxia with IC_{50} above *ca.* 50 µM for all cell lines, while under 1% hypoxia IC_{50} values ranged from moderate (>10 µM) to potent activity (<10 µM). These data confirmed the superior hypoxia therapy conferred by $Cu(TPZ)_2$ compared to the aforementioned study by Adsule and co-workers. Moreover, cupric-TPZ also resulted in superior potency under hypoxia compared to previous studies

[168,169]. Moreover, the overall potency of $Cu(TPZ)_2$ under hypoxia, was not improved compared to TPZ (aside from C4-2B cell line) but hypoxia selectivity was markedly affected, as shown previously for other copper complexes. The obtained HCR values were summarised using a heatmap to enable a simple comparison of the effectiveness against 4 different PCa cell lines (**Figure 6.5**). The results showed a moderate effect at 48h for both drugs against LNCap, C4-2B and DU145, in contrast to PC3, where selectivity was not observed. Over time, HCR values were consistently higher for $Cu(TPZ)_2$ (>10) in LNCap and C4-2B, compared to TPZ, confirming the potential of this complex as a new HAP. Outstanding selectivity was observed at 72h for C4-2B with HCR of 69.66. Opposed to this, DU145 cells were more resistant to both treatments maintaining moderate hypoxia selectivity (2-6), while PC3 exhibited the worst outcome. A previous report on the cytotoxicity of TPZ [73] showed an HCR value of *ca.* 60 with potency of less than 10 µM against PC3 cells which did not agree with the results obtained herein. A possible explanation for this may rely on the fact that these values were obtained using clonogenic assays under harsh anoxic conditions. In addition, both DU145 and PC3 cells exhibit increased basal levels of hypoxia markers [518,522], which may contribute to their higher resistance to treatment. It is therefore plausible to argue that oxygenation is only one parameter influencing the activity of these drugs and may well be a simplistic view of their MoA. All cell lines were cultured under the same conditions, yet they exhibit tremendous differences in toxicity and selectivity. Hypoxia adaptation and the reductive capacity of these cell lines will certainly influence the sensitivity to TPZ and $Cu(TPZ)_2$. Similar to that reported for TPZ [108], analysis of the expression of reductases from both cytosol and nucleus, could provide insight on the bioactivation of this cupric-complex and contribute to the understanding of its MoA.

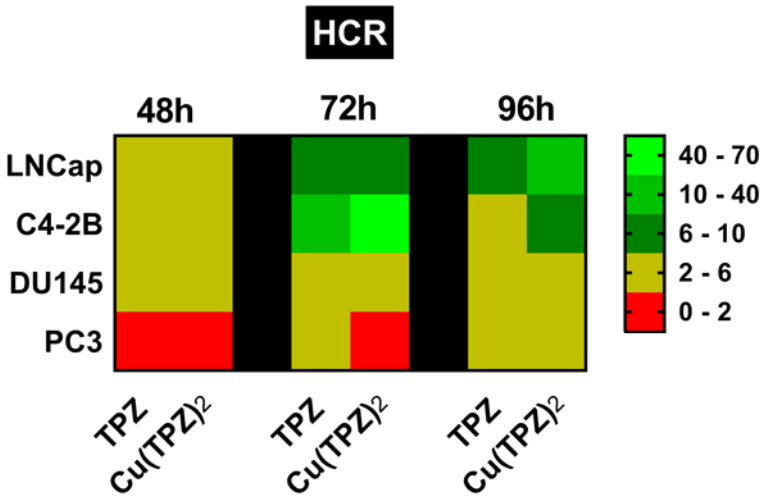

Figure 6.5. Heat map of the HCR values obtained for TPZ and $Cu(TPZ)_2$ in four different PCa cell lines.

6.1.3.2. Perspective on uptake, dissociation and intracellular MoA for $Cu(TPZ)_2$

Most research surrounding hypoxia selectivity is based on the unique cellular trapping mechanism proposed for Cu(ATSM) [175,176,563]. This copper(II) complex has been widely exploited *in vitro* and *in vivo* due to its enhanced accumulation in hypoxic tissues, which has played a fundamental role in the development of radiopharmaceuticals (using copper isotopes ^{60}Cu and ^{64}Cu) for hypoxia PET tracing [174,175,563]. SAR studies of this compound once again evidenced that hypoxia selectivity is greatly influenced by the redox-potential and reversibility of the copper(II) reduction [174,181]. Generally, complexes with reduction potential more electronegative than -0.57 V *vs.* Ag/AgCl in DMSO, should display optimum hypoxia selectivity. Upon reduction in low oxygenated cells, these copper(II) complexes will partially dissociate into an intermediary copper(I) compound, which is more labile and eventually undergoes complete dissociation, liberating the free ligand [564]. Copper(I) is then bound to specific binding proteins and chaperones such as Ctr1 and Atx1, respectively, which mediate the copper cellular pool [564]. In normoxia, the intermediary copper(I) compound should reversibly oxidize to its copper(II) counterpart and diffuse out of the cells. Although the redox-properties provide reliable gold-standard in hypoxia selectivity, other factors influencing reduction rate should not be ruled out. Indeed, the degree of expression of intracellular reductases has shown to influence dissociation, as well as other biological reductants such as ascorbate, thiols or $NADP(H^+)$ [170,176,564]. In **chapter 3**, it was established that $Cu(TPZ)_2$ was stable in several aqueous solutions and can undergo ligand dissociation under acidic conditions. Moreover, the coordinated and uncoordinated TPZ can be easily monitored using UV/Vis analysis, so future titration studies with different reductive molecules could help elucidate the lability and dissociation of the copper(II) and copper(I) forms. Furthermore, in **chapter 5**, fluorescent assays showed that $Cu(TPZ)_2$ diffused in the cytosol and accumulated in the perinuclear region of C4-2B cells. The uptake was significantly improved compared to TPZ alone and hypoxia selectivity was concentration-dependent and pronounced after 4h. These results agreed well with aforementioned mechanisms of uptake and were expected due to the lipophilic nature of this compound and its electronegative redox potential. It is therefore plausible that $Cu(TPZ)_2$ uptake and dissociation (**Figure 6.6)** following a similar pattern to that proposed for other copper(II) complexes.

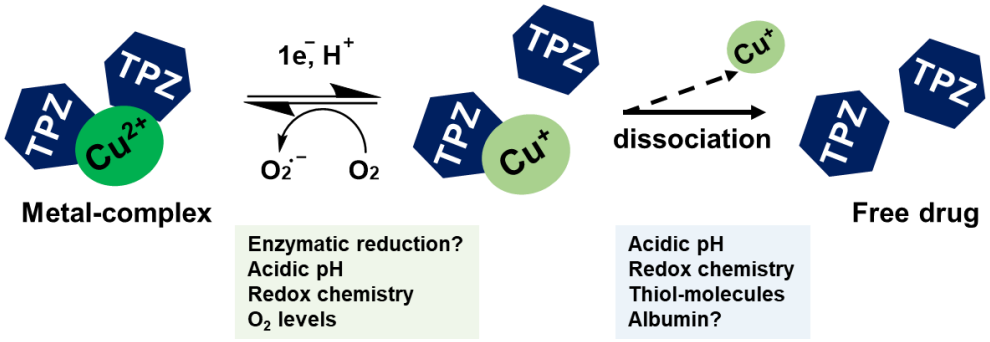

Figure 6.6. Proposed mechanism for the hypoxia selectivity of $Cu(TPZ)_2$. Under hypoxia, copper(II)-TPZ will partially dissociate into a labile copper(I) intermediary, which is then completely reduced liberating free TPZ. Aside from oxygen levels, other factors such as pH and presence of bioreductants could mediate the rate of dissociation of the copper(II) complex.

Copper complexes have been widely exploited for anti-cancer therapy and offer great potential [161,167,171,179]. Attention has been drawn to copper (II) complexes and their ability to induce DNA damage. Although this is the primary MoA of a large number of complexes, new cellular targets such as topoisomerases [171,184-186], proteasome complex [185,187-189], endoplasmic reticulum [190] and lysosome [191,192] have become rational pathways of cell death for cancer therapeutics. Taking into account previous reports [174,181,182,456,459] and the selectively enhanced hypoxia uptake obtained here for C4-2B cells, it is plausible that $Cu(TPZ)_2$ enters the cells through a combination of passive uptake, endocytosis, and copper-transporter 1 (Ctr1) (**Figure. 6.7**). Furthermore, in hypoxic conditions the complex is accumulated through a bioreductive cycle, where it can suffer partial, Cu(I)-TPZ, or complete dissociation, TPZ and Cu. This entrapment is further augmented by a reduced vesicle-mediated efflux of the complex, by lowered metabolism in low oxygenated cells [183]. The active compounds are then released from the lysosome where they can induce cell death through several mechanisms: 1) intact Cu(II)-TPZ that can bind/intercalate DNA, halting DNA replication; 2) Redox cycling can lead to complete dissociation where Cu can induce ROS mediated lysosome permeability, ER stress, mitochondrial membrane potential (MMP) impairment, DNA damage and eventually apoptosis; 3) dissociated TPZ can induce ROS-mediated DNA damage, MMP-induced caspase activation, topoisomerase(II) poisoning and DNA damage; 4) particularly under normoxia, $Cu(TPZ)_2$ can act as a superoxide dismutase (SOD) mimetic, generating non-selective ROS mediated cell death [169].

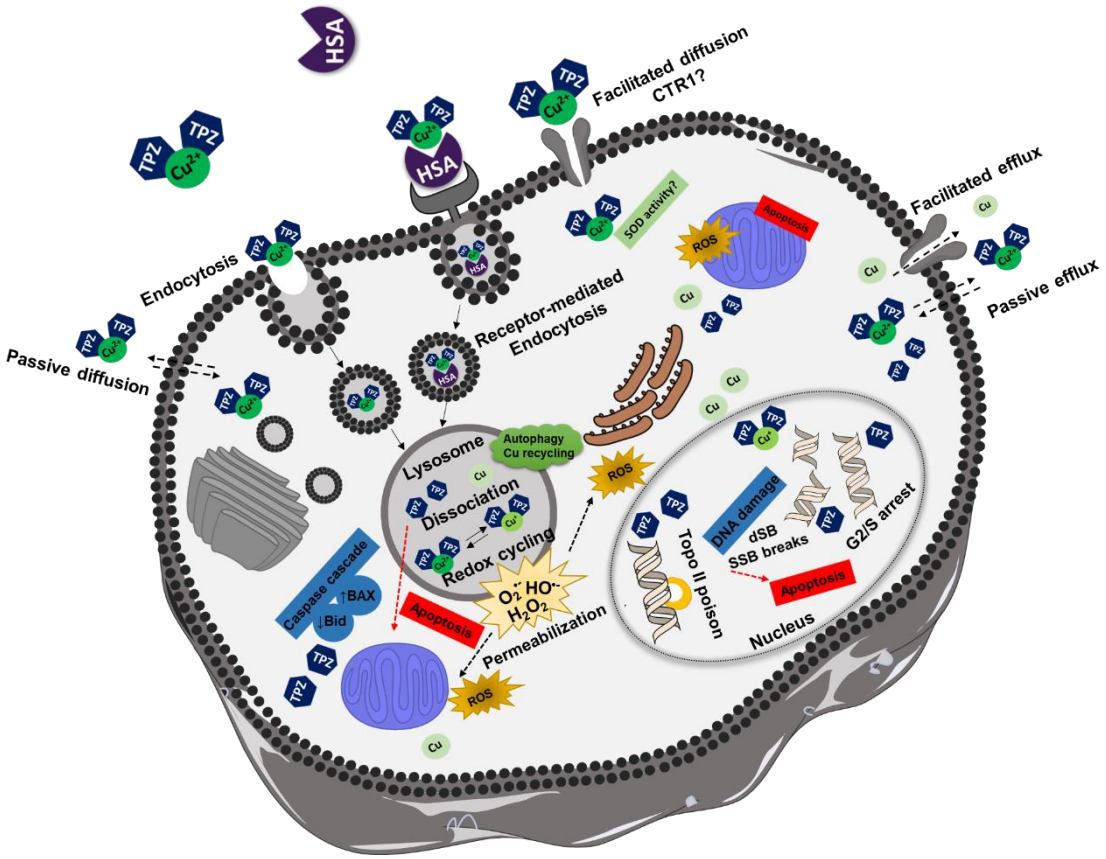

Figure 6.7. Proposed cellular uptake and death pathways in cancer cells. Perspective scheme depicting different cellular uptake and possible death pathways of $Cu(TPZ)_2$ in cancer cells. The hypothesis suggests that $Cu(TPZ)_2$ is taken up by both passive and facilitated diffusion. Once inside the cells, the complex can be either effluxed (normoxia) or accumulated by a bioreductive recycling mechanism in the lysosome (hypoxia). The complex can then dissociate (TPZ + Cu) or cycle between free and complexed form, initiating TPZ or complex induced ROS (lysosome, ER and/or mitochondria), DNA damaging and cell cycle arrest, which results in the activation of different apoptotic pathways.

6.1.3.3. Potency of free drugs and liposomes in 2D *vs.* 3D: relevance of spheroids

Hypoxia has become one of the most attractive targets in cancer [558]. Many small molecule inhibitors, HAPs and hypoxia-responsive nanocarriers have shown a great promise in cancer therapy. However, hypoxia-targeted therapy has shown limited activity in mouse models and humans. These high attrition rates of failure are attributed not only to the high complexity of the tumour microenvironment, but also due to lack of veracity and fidelity in existing preclinical models and patient subsets. Therefore, substantial efforts have been made to develop more reliable *in vitro* methods that can then be successfully translated to *in vivo* set-up [60]. Tumour spheroids have now been widely accepted as favourable models that can create a more realistic understanding of the tumour microenvironment and heterogeneity, including hypoxia [423,501].

A vast amount of literature has shown poor diffusion of TPZ in tumour spheroids [104,435,462], which in turn compromised its hypoxia selectivity and translational efficacy. Very high doses of TPZ (100 µM) have been employed showing that 80/90% of both outer and inner cells of 3D cultures are effected, abrogating hypoxia selectivity [460]. In line with this, focus is on the development of

analogues [73] with the concept that the ideal HAP should penetrate enough through several layers of metabolically active cells, reaching the relevant hypoxic rim. To great surprise most SAR studies included analogues that did not improve on overall potency, but achieved better diffusion and more selective mechanism of cell killing [73,147,460]. Given that spheroids cultured in air already generate surface cells that are more hypoxic than monolayers grown in hypoxic conditions, TPZ's activity may be compromised by a rapid reduction as it diffuses the spheroid mass [460,549]. This limitation has been overcome by a promising analogue – SN30000 – which has shown increased lipophilicity and improved extravascular penetration after removal of the H-bond donor of TPZ's 3-NH_2 group [73,77]. In **chapter 5**, TPZ activity against C4-2B spheroids was also evaluated and was in good agreement with the above findings. These 3D models already displayed marked hypoxia at the spheroid surface (**section 2.5.5.2**), which correlated well with the decreased activity obtained after TPZ treatment. The IC_{50} values obtained did not significantly change over time, indicating that drug diffusion was not effective and that cells in both the outer and inner rim of the spheroid were effected (**Figure 6.8, top panel**). This finding was corroborated by light microscopy that confirmed complete disintegration of the spheroid mass at high doses of 100 µM and greater resistance of 3D models to treatment, compared to 2D.

It is noteworthy that the EDTA pre-treatment when coupled to resazurin assay provided a more reliable method to quantify spheroid cytotoxicity. A detailed review on spheroids as a cytotoxic screening tools, highlights the importance of using high throughput methods that determine both surface and inner cell viability [419,423,427]. Moreover, relying solely on size or volume changes may lead to false results as some drugs may affect spheroid viability, without compromising its integrity.

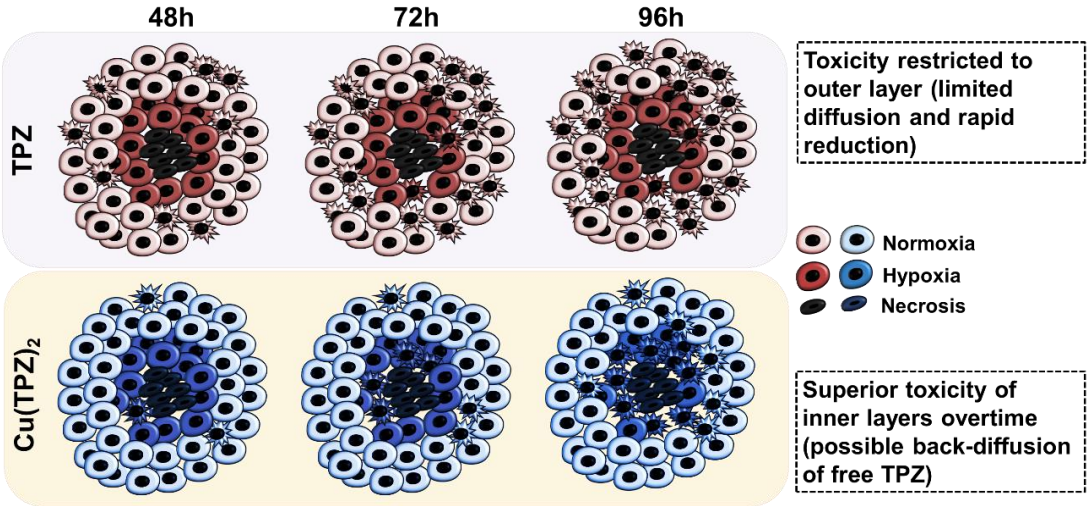

Figure 6.8. Schematic illustration on the possible mechanism of action for TPZ and $Cu(TPZ)_2$ in C4-2B spheroids. The image depicts the better penetration of cupric-TPZ that by metal-coordination diminishes drug reactivity in the spheroid surface. Therefore, only the more hypoxic cells in the rim are killed and selectivity is maintained. In contrast, TPZ's activity is compromised by its more facile reduction and poor diffusion.

As discussed previously for SN30000, the removal of two hydrogen donors at the 4-*N*-oxide and $3NH_2$ positons by copper coordination led to an overall increase in hydrophobicity. In addition, the redox-potential was also decreased significantly indicating that $Cu(TPZ)_2$ may possess favourable properties over TPZ for hypoxia selectivity even in tumour models. To current knowledge, no relevant literature on the effect of copper(II) complexes against tumour spheroids was found. However, other metal-complexes have been used to develop sophisticated luminescent and fluorescent probes that confirmed the penetration and hypoxia specificity of such compounds in 3D models [153,560]. In addition, a promising cobalt-mustard complex [85] also generated strong hypoxia activity with back-diffusion of the free ligand that resulted in significant anti-tumour effect. Likewise, $Cu(TPZ)_2$ did not show a more potent effect at earlier time-points compared to TPZ, but displayed marked spheroid cytotoxicity at 96h post-treatment. This finding suggested that copper functions as a chaperone of TPZ, reducing its bioreductive activity (harder to reduce), which confers advantageous penetration of the spheroid mass and selective toxicity of the more hypoxic cells in the rim (**Figure 6.8, bottom panel**). As reported for other analogues [168,169], despite the apparent loss of potency for $Cu(TPZ)_2$ this complex seems to provide selective activity over time and penetration should be confirmed using confocal microscopy and flow cytometry analysis. Nevertheless, as predicted $Cu(TPZ)_2$ and its improved selectivity should be translated to higher maximum tolerated doses *in vivo*, minimizing TPZ's unwanted side-effects. Together these data highlighted the importance of 3D models on gaining translational information for hypoxia therapeutics. Despite the potent activity displayed for both TPZ and its copper form in monolayers, the therapeutic outcome in more sophisticated models was clearly restricted and more complex.

The main drawback that could be pointed out is the limited aqueous solubility of $Cu(TPZ)_2$ at therapeutically relevant concentrations [565]. Thus, the use of DDS could offer a means of overcoming this and also provide a more favourable therapeutic outcome [565,566]. As already discussed, the low solubility of the complex led to optimum liposomal encapsulation, which markedly improved on TPZ loading. The question was whether these formulations maintained the promising *in vitro* activity exhibited by the complex itself. As summarised in **figure 6.9**, apart from DOPC-$Cu(TPZ)_2$ all formulations displayed a potent selective effect (>12 μM) under hypoxia, at 48h. After 72 and 96h post-treatment the activity was comparable between all formulations and suggested a more sustained release, compared to the complex alone.

The most promising finding was found when spheroids were treated with $Cu(TPZ)_2$-loaded liposomes. Surprisingly, DSPC-$Cu(TPZ)_2$ failed to translate its potent monolayer activity, while both DOPC- and DPPC-$Cu(TPZ)_2$ exhibited pronounced cytotoxicity even compared to TPZ and $Cu(TPZ)_2$ alone at both 48 and 72h. The findings indicated that the type of lipid used in the formulations played a detrimental role on spheroid penetration, where more fluid formulations resulted in improved therapeutic outcome.

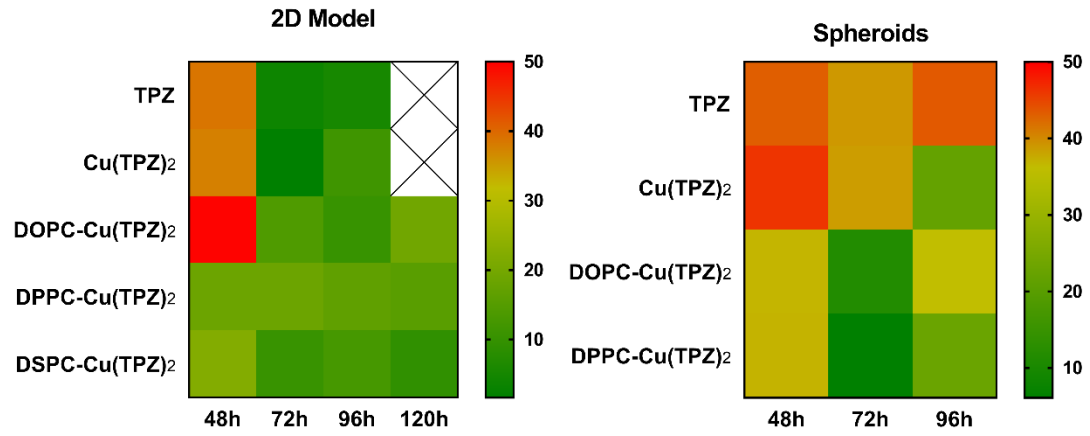

Figure 6.9. Heat map of the IC_{50} values obtained for TPZ, $Cu(TPZ)_2$ and $Cu(TPZ)_2$-loaded liposomes in C4-2B monolayers (left) and spheroids (right).

Moreover, liposomes seemed to accelerate activity compared to $Cu(TPZ)_2$ alone, possibly due to better penetration. At 96h, recovery was observed and can be correlated to previous studies, which argued that both reoxygenation and liberation of free TPZ could slightly compromise hypoxia activity. Therefore, the use of combinatorial regimens or even frequent dosing could help modulate a continuous and potent anti-cancer effect. Nonetheless, the combination of the already improved properties emerging from $Cu(TPZ)_2$ coupled with improved solubility and protection provided by liposomal encapsulation did improve significantly on TPZ activity *in vitro*, especially in 3D models. Shah *et al.* [567] provided an interesting perspective on TPZ activity evidencing that the maximum tolerated dose for TPZ in clinic is 390 mg/m^2, and therefore most trials (summarised in **table 1.3**) showed therapeutic doses ranging from 220-300 mg/m^2. The authors estimated that a dose of 300 mg/m^2 corresponds to *ca.* 65 µM *in vitro*, a concentration which is well above the IC_{50} values determined in this work for both free and encapsulated $Cu(TPZ)_2$. Together this data highlights the potential therapeutic translation of this complex and these novel cupric-TPZ liposomes as alternative hypoxia agents.

6.1.4. Hypoxia therapies: a note on clinical translation

Hypoxia targeted strategies are now an emerging topic in anti-cancer therapies. The work presented here offers a relevant perspective on how redefining classical HAPs combined with the use of nanomedicine could present potential on improving the main drawbacks of these prodrugs. It was important to ensure that $Cu(TPZ)_2$ provided selective therapeutic efficiency as a single agent and also after liposomal encapsulation. The data seem to suggest that this complex could not only improve on TPZs current biological limitations, but also aid with nano-encapsulation strategies. Furthermore, when developing such strategies one must consider the complexity of the tumour microenvironment [26,558]. The use of combinatorial strategies should not be disregarded for future studies and can ensure strong synergistic effects that can render tumours more susceptible to hypoxia therapeutics

[348]. Recent studies have proved this hypothesis right by developing 'smart' nanocarriers that combine HAPs with different chemotherapeutics, radiotherapy or PDT [26]. Moreover, the use of targeting moieties [8,558] or TAMs as 'Trojan horses' [26,369] have presented optimum ways to deliver drugs more effectively to hypoxic regions of tumours. Nonetheless, more than improving on HAP delivery and finding strong drug regimens, researchers need to focus on adequate pre-clinical evaluation alongside standardized patient selection for hypoxia relevant tumours. The selection of new biomarkers that could offer personalised medicine for cancer patients can lead to the development of new targeted systems, and also aid in identifying tumours that will respond better to certain hypoxia regimens. Efforts are in place to take nanomedicine closer to clinical translation by producing more reliable and positive treatment outcomes through selection of adequate hypoxic models.

6.2. Future work

The following ideas are proposed to build-on the current work presented in this thesis:

In **chapter 3**, a detailed validation and characterisation of the complexation of TPZ was provided. Nonetheless, although a putative structure was provided, the growth of singular crystals and their crystallographic analysis could provide substantive structural information on $Cu(TPZ)_2$. Moreover, the use of TLC could help validate the predicted Log P values, as could cyclic voltammetry to confirm the redox-potential retrieved from the literature. Also, UV/Vis analysis can be easily used to discriminate between free and complexed TPZ and titrations involving thiol-reductants such as glutathione and ascorbate could help assess the dissociation rate and stability of the complex in different reductive conditions, including serum.

In **chapter 4**, $Cu(TPZ)_2$ was successfully encapsulated in different liposomal formulations. The use of higher lipid content could aid with encapsulation and stability, as could lyophilisation of the vesicles. Moreover, labelling of these liposomes with specific probes coupled with the intrinsic fluorescence of $Cu(TPZ)_2$ could help elucidate uptake mechanism using both confocal microscopy and FACs. Cryo-EM along with X-ray diffraction could be used to determine the morphology and complex's structure within the different formulations and at varying lipid-to-complex ratios. Finally, DSC and EPR would provide information on the localization of the complex within the liposomal vesicles.

In **chapter 5**, the biological activity of TPZ, $Cu(TPZ)_2$ and $Cu(TPZ)_2$-loaded liposomes was evaluated in 2D and 3D PCa models. To complement the monolayer studies, clonogenic assays could be conducted to assess long-term cytotoxicity, which can be particularly interesting for more resistant cell lines such as PC3. In addition, cell death mechanisms can be exploited by evaluating ROS, DNA-damage (electrophoresis or comet assay) and caspase expression. These cytotoxic assays could also be coupled with fractionation of the cytosol and nucleus to determine which enzymes are responsible for complex reduction. Moreover, a full screening on the expression of hypoxia markers and reductases using qPCR and western blot could help elucidate the differential sensitivity to treatment.

Concerning uptake studies, these could be repeated under low temperature conditions (4ºC) or using endocytosis inhibitors to discriminate between the passive and facilitated cellular uptake of $Cu(TPZ)_2$. Likewise, fluorescent imaging provided preliminary evidence on the cellular localization of these complex, but should be complemented with the use of endocytic and lysosome markers to prove co-localization. The use of fluorescent lifetime imaging along with X-ray absorption spectroscopy could offer a complete overview on the localisation and, more importantly, the oxidation state and coordination environment of $Cu(TPZ)_2$. Finally, spheroid assays could be concluded by evaluating the uptake and diffusion of the free complex and $Cu(TPZ)_2$-loaded liposomes *via* confocal microscopy and FACs.

6.3. Overall conclusions

1. Coordination of copper through 4-*N*-oxide and $3NH_2$ groups generated a 2:1 TPZ:Cu complex with overall good stability in a wide range of solvents. The complex showed increased lipophilicity and more electronegative redox-potential, which were relevant factors determining hypoxia selectivity. It showed optimum stability under physiological pH and dissociation under harsh acidic conditions (pKa 2.7), with unique intrinsic fluorescent properties that were exploited for bioimaging purposes.

2. The altered physicochemical properties rendered the successful encapsulation of $Cu(TPZ)_2$ in different liposomal formulations. Drug loading was greatly improved, which was essential to potentiate TPZ encapsulation. The simple remote loading method (developed herein) was independent of pH gradients and generated liposomes with different lipid compositions, good stability and optimum drug retention over time. The low aqueous solubility of the complex rendered the formation of drug precipitates in the liposomes aqueous core, which improved drug loading, but did not compromise release kinetics. Liposomes displayed a sustained release in serum over time, which was particularly relevant for the *in vitro* behaviour.

3. The $Cu(TPZ)_2$ complexes resulted in improved hypoxia selectivity in a range of PCa cells, compared to TPZ. The complex showed particular effectiveness in a bone-derived metastatic cell line – C4-2B – displaying potent and remarkable selectivity at 72h post-treatment. This complete screening of different cell lines was important to gain knowledge on the sensitivity of different models to both TPZ and $Cu(TPZ)_2$. After encapsulation, $Cu(TPZ)_2$-loaded liposomes maintained hypoxia selectivity and cytotoxicity was formulation-dependent, which correlated well with their release profile. Both free $Cu(TPZ)_2$ and $Cu(TPZ)_2$-loaded liposomes showed promising use as alternative hypoxia therapies, over TPZ alone, in 2D models.

4. The use of spheroid models was essential to generate data that could provide a more realistic therapeutic outcome. Hypoxic C4-2B spheroids were more refractory to TPZ treatment, with no overall change in cytotoxicity over time. In contrast, although more resistant than monolayers, $Cu(TPZ)_2$ caused remarkable therapeutic effect at 96h, suggesting improved penetration and a slower reduction of the prodrug, which might be beneficial when diffusing large tumour masses. Moreover, more rigid liposomal formulations [DSPC- $Cu(TPZ)_2$], with potent activity in 2D, failed to show relevant activity in 3D models; while other formulations [DOPC- $Cu(TPZ)_2$ and DPPC-$Cu(TPZ)_2$] translated well to more complex models. These findings enabled important information on choosing the best treatment regimens and formulations, which can then be applied to *in vivo* set-up.

References

1. Siegel, R.L., *et al.*, Cancer Statistics, 2017. *CA Cancer J Clin*, **2017**. 67(1): p. 7-30.

2. World Health Organization. [Accessed: 31 January **2018**]; Available from: http://www.who.int/mediacentre/factsheets/fs297/en/.

3. Cancer Research UK. Cancerstats - terminology and calculations, Cancer Research UK. [Accessed: 31 January **2018**]; Available from: www.cruk.org/cancerstats.

4. Gatenby, R.A., A change of strategy in the war on cancer. *Nature*, **2009**. 459: p. 508.

5. Chabner, B.A., *et al.*, Chemotherapy and the war on cancer. *Nat Rev Cancer*, **2005**. 5: p. 65.

6. Haber, D.A., *et al.*, The Evolving War on Cancer. *Cell*, **2011**. 145(1): p. 19-24.

7. Hanahan, D., Rethinking the war on cancer. *The Lancet*, **2014**. 383(9916): p. 558-563.

8. Danhier, F., *et al.*, To exploit the tumor microenvironment: Passive and active tumor targeting of nanocarriers for anti-cancer drug delivery. *J Control Release*, **2010**. 148(2): p. 135-146.

9. Siegel, R., *et al.*, Cancer statistics. *CA Cancer J Clin*, **2013**. 63(1): p. 11-30.

10. Hanahan, D., *et al.*, Hallmarks of cancer: the next generation. *Cell*, **2011**. 144(5): p. 646-674.

11. Hanahan, D., *et al.*, Biological hallmarks of cancer. *Holland-Frei Cancer Medicine*, **2017**.

12. Qureshi, S., *et al.*, Application of nanotechnology in cancer treatment. *J of Pharm Res & Opin*, **2014**. 1(2): p. 34-36.

13. Gotwals, P., *et al.*, Prospects for combining targeted and conventional cancer therapy with immunotherapy. *Nat Rev Cancer*, **2017**. 17: p. 286.

14. Farrell, D., *et al.*, Nanotechnology-based cancer therapeutics--promise and challenge--lessons learned through the NCI Alliance for Nanotechnology in Cancer. *Pharm Res*, **2011**. 28(2): p. 273-278.

15. Peer, D., *et al.*, Nanocarriers as an emerging platform for cancer therapy. *Nat Nano*, **2007**. 2(12): p. 751-760.

16. Borst, P., *et al.*, A family of drug transporters: the multidrug resistance-associated proteins. *J Natl Cancer Inst*, **2000**. 92(16): p. 1295-1302.

17. Wang, F., *et al.*, Synergistic effect of folate-mediated targeting and verapamil-mediated P-gp inhibition with paclitaxel -polymer micelles to overcome multi-drug resistance. *Biomaterials*, **2011**. 32(35): p. 9444-9456.

18. Moeller, B.J., *et al.*, Hypoxia and radiotherapy: opportunities for improved outcomes in cancer treatment. *Cancer Metast Rev*, **2007**. 26(2): p. 241-248.

19. Feng, S.-S., *et al.*, Chemotherapeutic engineering: Application and further development of chemical engineering principles for chemotherapy of cancer and other diseases. *Chem Eng Sci*, **2003**. 58(18): p. 4087-4114.

20. Gu, F.X., *et al.*, Targeted nanoparticles for cancer therapy. *Nano Today*, **2007**. 2(3): p. 14-21.

21. Swartz, M.A., *et al.*, Tumor microenvironment complexity: emerging roles in cancer therapy. *Cancer Res*, **2012**. 72(10): p. 2473-2480.

22. Weis, S.M., *et al.*, Tumor angiogenesis: molecular pathways and therapeutic targets. *Nat Med*, **2011**. 17: p. 1359.

23. Feron, O., Pyruvate into lactate and back: from the Warburg effect to symbiotic energy fuel exchange in cancer cells. *Radiother Oncol*, **2009**. 92(3): p. 329-333.

24. Coffelt, S.B., *et al.*, Tumor-associated macrophages: effectors of angiogenesis and tumor progression. *Biochim Biophys Acta*, **2009**. 1796(1): p. 11-18.

25. Riabov, V., *et al.*, Role of tumor associated macrophages in tumor angiogenesis and lymphangiogenesis. *Front Physiol*, **2014**. 5: p. 75.

26. Silva, V.L., *et al.*, Exploiting the cancer niche: Tumor-associated macrophages and hypoxia as promising synergistic targets for nano-based therapy. *J Control Release*, **2017**. 253: p. 82-96.

27. Koppenol, W.H., *et al.*, Otto Warburg's contributions to current concepts of cancer metabolism. *Nat Rev Cancer*, **2011**. 11(5): p. 325-337.

28. Hockenbery, D., *et al.*, The Warburg Effect and Beyond: Metabolic Dependencies for Cancer Cells, in Cell Death Signalling in Cancer Biology and Treatment, D.E. Johnson, Editor. **2013**, Springer New York. p. 35-51.

29. Azzi, S., *et al.*, Vascular permeability and drug delivery in cancers. *Front Oncol*, **2013**. 3: p. 211.

30. Chen, J.J., *et al.*, Tumor-associated macrophages: the double-edged sword in cancer progression. *J Clin Oncol*, **2005**. 23(5): p. 953-964.

31. Ahsan, F., *et al.*, Targeting to macrophages: role of physicochemical properties of particulate carriers--liposomes and microspheres--on the phagocytosis by macrophages. *J Control Release*, **2002**. 79(1-3): p. 29-40.

32. Ruffell, B., *et al.*, Differential macrophage programming in the tumor microenvironment. *Trends Immunol*, **2012**. 33(3): p. 119-126.

33. Allavena, P., *et al.*, The Yin-Yang of tumor-associated macrophages in neoplastic progression and immune surveillance. *Immunol Rev*, **2008**. 222: p. 155-161.

34. Qian, B.Z., *et al.*, Macrophage diversity enhances tumor progression and metastasis. *Cell*, **2010**. 141(1): p. 39-51.

35. Solinas, G., *et al.*, Tumor-associated macrophages (TAM) as major players of the cancer-related inflammation. *J Leukoc Biol*, **2009**. 86(5): p. 1065-1073.

36. Hughes, R., *et al.*, Perivascular M2 Macrophages Stimulate Tumor Relapse after Chemotherapy. *Cancer Res*, **2015**. 75(17): p. 3479-3491.

37. Hagemann, T., *et al.*, "Re-educating" tumor-associated macrophages by targeting NF-kappaB. *J Exp Med*, **2008**. 205(6): p. 1261-1268.

38. Hao, N.B., *et al.*, Macrophages in tumor microenvironments and the progression of tumors. *Clin Dev Immunol*, **2012**. 2012: p. 1-11.

39. Petrova, V., *et al.*, The hypoxic tumour microenvironment. *Oncogenesis*, **2018**. 7(1): p. 10.

40. Chaffer, C.L., *et al.*, A perspective on cancer cell metastasis. *Science*, **2011**. 331(6024): p. 1559-1564.

41. Fidler, I.J., The pathogenesis of cancer metastasis: the 'seed and soil' hypothesis revisited. *Nat Rev Cancer*, **2003**. 3: p. 453.

42. Joan, M., *et al.*, Understanding the molecular mechanisms driving metastasis. *Mol Oncol*, **2017**. 11(1): p. 3-4.

43. Brown, J.M., *et al.*, Exploiting tumour hypoxia in cancer treatment. *Nat Rev Cancer*, **2004**. 4(6): p. 437-447.

44. Thomlinson, R.H., Hypoxia and tumours. *J Clin Pathol*, **1977**. s3-11(1): p. 105-113.

45. Brown, J.M., Exploiting the hypoxic cancer cell: mechanisms and therapeutic strategies. *Mol Med Today*, **2000**. 6(4): p. 157-162.

46. Dhani, N., *et al.*, The clinical significance of hypoxia in human cancers. *Semin Nucl Med*, **2015**. 45(2): p. 110-121.

47. Kizaka-Kondoh, S., *et al.*, Tumor hypoxia: a target for selective cancer therapy. *Cancer Sci*, **2003**. 94(12): p. 1021-1028.

48. Wilson, W.R., *et al.*, Targeting hypoxia in cancer therapy. *Nat Rev Cancer*, **2011**. 11(6): p. 393-410.

49. Semenza, G.L., Defining the role of hypoxia-inducible factor 1 in cancer biology and therapeutics. *Oncogene*, **2009**. 29: p. 625.

50. Zeng, W., *et al.*, Hypoxia and hypoxia inducible factors in tumor metabolism. *Cancer Lett*, **2015**. 356(2 Pt A): p. 263-267.

51. Wilhide, M.E., *et al.*, Potential Therapeutic Gene for the Treatment of Ischemic Disease: Ad2/Hypoxia-Inducible Factor-1α (HIF-1)/VP16 Enhances B-Type Natriuretic Peptide Gene Expression via a HIF-1-Responsive Element. *Mol Pharmacol*, **2006**. 69(6): p. 1773-1778.

52. Mabjeesh, N.J., *et al.*, Geldanamycin induces degradation of hypoxia-inducible factor 1alpha protein via the proteosome pathway in prostate cancer cells. *Cancer Res*, **2002**. 62(9): p. 2478-2582.

53. Sun, H.L., *et al.*, YC-1 inhibits HIF-1 expression in prostate cancer cells: contribution of Akt/NF-kappaB signalling to HIF-1alpha accumulation during hypoxia. *Oncogene*, **2007**. 26(27): p. 3941-3951.

54. Patnaik, A., *et al. EZN-2968, a novel hypoxia-inducible factor-1 {alpha}(HIF-1 {alpha}) messenger ribonucleic acid (mRNA) antagonist: Results of a phase I, pharmacokinetic (PK), dose-escalation study of daily administration in patients (pts) with advanced malignancies*. in *ASCO Annual Meeting Proceedings*. 2009.

55. Zhang, H., *et al.*, Digoxin and other cardiac glycosides inhibit HIF-1α synthesis and block tumor growth. *PNAS*, **2008**. 105(50): p. 19579-19586.

56. Patnaik, A., *et al.*, Phase I dose-escalation study of EZN-2208 (PEG-SN38), a novel conjugate of poly(ethylene) glycol and SN38, administered weekly in patients with advanced cancer. *Cancer Chemother Pharmacol*, **2013**. 71(6): p. 1499-1506.

57. Terzuoli, E., *et al.*, Aminoflavone, a ligand of the aryl hydrocarbon receptor, inhibits HIF-1alpha expression in an AhR-independent fashion. *Cancer Res*, **2010**. 70(17): p. 6837-6848.

58. Jacoby, J.J., *et al.*, Treatment with HIF-1alpha antagonist PX-478 inhibits progression and spread of orthotopic human small cell lung cancer and lung adenocarcinoma in mice. *J Thorac Oncol*, **2010**. 5(7): p. 940-949.

59. Wang, R., *et al.*, Cancer therapeutic agents targeting hypoxia-inducible factor-1. *Curr Med Chem*, **2011**. 18(21): p. 3168-3189.

60. Burroughs, S.K., *et al.*, Hypoxia inducible factor pathway inhibitors as anticancer therapeutics. *Future Med Chem*, **2013**. 5(5): p. 553-572.

61. Gu, J., *et al.*, Knockdown of HIF-1α by siRNA-expressing plasmid delivered by attenuated Salmonella enhances the antitumor effects of cisplatin on prostate cancer. *Sci Rep*, **2017**. 7(1): p. 7546.

62. Liu, X.Q., *et al.*, Therapeutic delivery of siRNA silencing HIF-1 alpha with micellar nanoparticles inhibits hypoxic tumor growth. *Mol Pharm*, **2012**. 9(10): p. 2863-2874.

63. Perche, F., *et al.*, Hypoxia-targeted siRNA delivery. *Angew Chem Int Ed Engl*, **2014**. 53(13): p. 3362-3366.

64. Shibata, T., *et al.*, Development of a hypoxia-responsive vector for tumor-specific gene therapy. *Gene Ther*, **2000**. 7(6): p. 493-498.

65. Hsiao, H.T., *et al.*, Hypoxia-targeted triple suicide gene therapy radiosensitizes human colorectal cancer cells. *Oncol Rep*, **2014**. 32(2): p. 723-729.

66. Melillo, G., Inhibiting hypoxia-inducible factor 1 for cancer therapy. *Mol Cancer Res*, **2006**. 4(9): p. 601-605.

67. Denny, W.A., *et al.*, Recent developments in the design of bioreductive drugs. *Br J Cancer Suppl*, **1996**. 27: p. S32-38.

68. Foehrenbacher, A., *et al.*, Design of Optimized Hypoxia-Activated Prodrugs Using Pharmacokinetic/Pharmacodynamic Modeling. *Frontiers in Oncology*, **2013**. 3(314).

69. Guise, C.P., *et al.*, Bioreductive prodrugs as cancer therapeutics: targeting tumor hypoxia. *Chin J Cancer*, **2014**. 33(2): p. 80-86.

70. Aghajanian, C., *et al.*, Phase I Study of Tirapazamine and Cisplatin in Patients with Recurrent Cervical Cancer. *Gynecol Oncol*, **1997**. 67(2): p. 127-130.

71. Bedikian, A.Y., *et al.*, Phase II trial of tirapazamine combined with cisplatin in chemotherapy of advanced malignant melanoma. *Ann Oncol*, **1997**. 8(4): p. 363-367.

72. DiSilvestro, P.A., *et al.*, Phase III randomized trial of weekly cisplatin and irradiation versus cisplatin and tirapazamine and irradiation in stages IB2, IIA, IIB, IIIB, and IVA cervical carcinoma limited to the pelvis: a Gynecologic Oncology Group study. *J Clin Oncol*, **2014**. 32(5): p. 458-464.

73. Hicks, K.O., *et al.*, Pharmacokinetic/pharmacodynamic modeling identifies SN30000 and SN29751 as tirapazamine analogues with improved tissue penetration and hypoxic cell killing in tumors. *Clin Cancer Res*, **2010**. 16(20): p. 4946-4957.

74. Anderson, R.F., *et al.*, Characterisation of radicals formed by the triazine 1,4-dioxide hypoxia-activated prodrug, SN30000. *Org Biomol Chem*, **2014**. 12(21): p. 3386-3392.

75. Gu, Y., *et al.*, Reductive Metabolism Influences the Toxicity and Pharmacokinetics of the Hypoxia-Targeted Benzotriazine Di-Oxide Anticancer Agent SN30000 in Mice. *Frontiers in Pharmacology*, **2017**. 8(531).

76. Gu, Y., *et al.*, Photodegradation of the Benzotriazine 1,4-Di-N-Oxide Hypoxia-Activated Prodrug SN30000 in Aqueous Solution. *J Pharm Sci* **2014**. 103(11): p. 3464-3472.

77. Hay, M.P., *et al.*, Discovery of the Hypoxia-Activated Prodrug SN30000 in Comprehensive Medicinal Chemistry III, D. Rotella and S.E. Ward, Editors. **2017**, Elsevier: Oxford. p. 58-94.

78. Choudry, G.A., *et al.*, A novel strategy for NQO1 (NAD(P)H:quinone oxidoreductase, EC 1.6.99.2) mediated therapy of bladder cancer based on the pharmacological properties of EO9. *Br J Cancer*, **2001**. 85(8): p. 1137-1146.

79. Ross, D., *et al.*, NAD (P) H: quinone oxidoreductase 1 (NQO1, DT-diaphorase), functions and pharmacogenetics. *Method Enzymol*, **2004**. 382: p. 115-144.

80. Schellens, J.H.M., *et al.*, Phase I and Pharmacologic Study of the Novel Indoloquinone Bioreductive Alkylating Cytotoxic Drug E09. *J Natl Cancer Inst*, **1994**. 86(12): p. 906-912.

81. Borad, M.J., *et al.*, Randomized Phase II Trial of Gemcitabine Plus TH-302 Versus Gemcitabine in Patients With Advanced Pancreatic Cancer. *J Clin Oncol*, **2014**: p. 1474-1481.

82. Sun, J.D., *et al.*, Selective tumor hypoxia targeting by hypoxia-activated prodrug TH-302 inhibits tumor growth in preclinical models of cancer. *Clin Cancer Res*, **2012**. 18(3): p. 758-770.

83. Weiss, G.J., *et al.*, Phase 1 study of the safety, tolerability, and pharmacokinetics of TH-302, a hypoxia-activated prodrug, in patients with advanced solid malignancies. *Clin Cancer Res*, **2011**. 17(9): p. 2997-3004.

84. Cutsem, E.V., *et al.*, Evofosfamide (TH-302) in combination with gemcitabine in previously untreated patients with metastatic or locally advanced unresectable pancreatic ductal adenocarcinoma: Primary analysis of the randomized, double-blind phase III MAESTRO study. *J Clin Oncol*, **2016**. 34(4_suppl): p. 193-193.

85. Wilson, W.R., *et al.*, Exploiting tumor hypoxia through bioreductive release of diffusible cytotoxins: The cobalt(III)-nitrogen mustard complex SN 24771. *Int J Radiat Oncol Biol Phys*, **1994**. 29(2): p. 323-327.

86. Guise, C.P., *et al.*, The bioreductive prodrug PR-104A is activated under aerobic conditions by human aldo-keto reductase 1C3. *Cancer Res*, **2010**. 70(4): p. 1573-1584.

87. Konopleva, M., *et al.*, Phase I/II study of the hypoxia-activated prodrug PR104 in refractory/relapsed acute myeloid leukemia and acute lymphoblastic leukemia. *Haematologica*, **2015**.

88. McKeage, M.J., *et al.*, A phase I trial of PR-104, a pre-prodrug of the bioreductive prodrug PR-104A, given weekly to solid tumour patients. *BMC Cancer*, **2011**. 11: p. 432.

89. Phillips, R.M., Targeting the hypoxic fraction of tumours using hypoxia-activated prodrugs. *Cancer Chemother Pharmacol*, **2016**. 77(3): p. 441-457.

90. Hunter, F.W., *et al.*, Hypoxia-activated prodrugs: paths forward in the era of personalised medicine. *Br J Cancer*, **2016**. 114(10): p. 1071-1077.

91. Mistry, I.N., *et al.*, Clinical Advances of Hypoxia-Activated Prodrugs in Combination With Radiation Therapy. *Int J Radiat Oncol Biol Phys*, **2017**. 98(5): p. 1183-1196.

92. Patterson, A.V., *et al.*, TH-4000, a hypoxia-activated EGFR/Her2 inhibitor to treat EGFR-TKI resistant T790M-negative NSCLC. *J Clin Oncol*, **2015**. 33(15_suppl): p. e13548-e13548.

93. Patterson, A.V., *et al.*, Abstract 5358: The hypoxia-activated EGFR-TKI TH-4000 overcomes erlotinib-resistance in preclinical NSCLC models at plasma levels achieved in a Phase 1 clinical trial. *Cancer Res*, **2015**. 75(15 Supplement): p. 5358-5358.

94. Trinkaus, M.E., *et al.*, Correlation of p16 status, hypoxic imaging using [18F]-misonidazole positron emission tomography and outcome in patients with loco-regionally advanced head and neck cancer. *J Med Imaging Radiat Oncol*, **2014**. 58(1): p. 89-97.

95. Toustrup, K., *et al.*, Gene expression classifier predicts for hypoxic modification of radiotherapy with nimorazole in squamous cell carcinomas of the head and neck. *Radiother Oncol*. 102(1): p. 122-129.

96. Onnis, B., *et al.*, Development of HIF-1 inhibitors for cancer therapy. *J Cell Mol Med*, **2009**. 13(9A): p. 2780-2786.

97. Brown, J.M., SR 4233 (tirapazamine): a new anticancer drug exploiting hypoxia in solid tumours. *Br J Cancer*, **1993**. 67(6): p. 1163-1170.

98. Zeman, E.M., *et al.*, SR-4233: a new bioreductive agent with high selective toxicity for hypoxic mammalian cells. *Int J Radiat Oncol Biol Phys*, **1986**. 12(7): p. 1239-1242.

99. Marcu, L., *et al.*, Tirapazamine: from bench to clinical trials. *Curr Clin Pharmacol*, **2006**. 1(1): p. 71-79.

100. Reddy, S.B., *et al.*, Tirapazamine: a novel agent targeting hypoxic tumor cells. *Expert Opin Investig Drugs*, **2009**. 18(1): p. 77-87.

101. Lartigau, E., *et al.*, Does tirapazamine (SR-4233) have any cytotoxic or sensitizing effect on three human tumour cell lines at clinically relevant partial oxygen pressure? *Int J Radiat Biol*, **1995**. 67(2): p. 211-216.

102. Chinje, E.C., *et al.*, Does reductive metabolism predict response to tirapazamine (SR 4233) in human non-small-cell lung cancer cell lines? *Br J Cancer*, **1999**. 81(7): p. 1127-1133.

103. Moriwaki, T., *et al.*, Cytotoxicity of Tirapazamine (3-Amino-1,2,4-benzotriazine-1,4-dioxide)-Induced DNA Damage in Chicken DT40 Cells. *Chem Res Toxicol*, **2017**. 30(2): p. 699-704.

104. Olive, P.L., *et al.*, Use of the comet assay to identify cells sensitive to tirapazamine in multicell spheroids and tumors in mice. *Cancer Res*, **1996**. 56(19): p. 4460-4463.

105. Graham, M.A., *et al.*, Pharmacokinetics of the hypoxic cell cytotoxic agent tirapazamine and its major bioreductive metabolites in mice and humans: retrospective analysis of a pharmacokinetically guided dose-escalation strategy in a phase I trial. *Cancer chemotherapy and pharmacology*, **1997**. 40(1): p. 1-10.

106. Olive, P., Detection of hypoxia by measurement of DNA damage in individual cells from spheroids and murine tumours exposed to bioreductive drugs. I. Tirapazamine. *Br J Cancer Suppl*, **1995**. 71(3): p. 529.

107. Walton, M.I., *et al.*, Pharmacokinetics and bioreductive metabolism of the novel benzotriazine di-N-oxide hypoxic cell cytotoxin tirapazamine (WIN 59075; SR 4233; NSC 130181) in mice. *J Pharmacol Exp Ther*, **1993**. 265(2): p. 938-947.

108. Patterson, A.V., *et al.*, Enzymology of tirapazamine metabolism: a review. *Anticancer Drug Des*, **1998**. 13(6): p. 541-573.

109. Patterson, A.V., *et al.*, Overexpression of human NADPH:cytochrome c (P450) reductase confers enhanced sensitivity to both tirapazamine (SR 4233) and RSU 1069. *Br J Cancer*, **1997**. 76(10): p. 1338-1347.

110. Wouters, B.G., *et al.*, Mitochondrial Dysfunction after Aerobic Exposure to the Hypoxic Cytotoxin Tirapazamine. *Cancer Res*, **2001**. 61(1): p. 145-152.

111. Delahoussaye, Y.M., *et al.*, Metabolism of tirapazamine by multiple reductases in the nucleus. *Biochem Pharmacol*, **2001**. 62(9): p. 1201-1209.

112. Jones, G.D.D., *et al.*, Dual Action of Tirapazamine in the Induction of DNA Strand Breaks. *Cancer Res*, **1996**. 56(7): p. 1584-1590.

113. Peters, K.B., *et al.*, Tirapazamine: a hypoxia-activated topoisomerase II poison. *Cancer Res*, **2002**. 62(18): p. 5248-5253.

114. Lin, P.-S., *et al.*, Tirapazamine (SR 4233) interrupts cell cycle progression and induces apoptosis. *Cancer Lett*, **1996**. 105(2): p. 249-255.

115. Hong, B., *et al.*, Hypoxia-targeting by tirapazamine (TPZ) induces preferential growth inhibition of nasopharyngeal carcinoma cells with Chk1/2 activation. *Invest New Drugs*, **2011**. 29(3): p. 401-410.

116. Siim, B.G., *et al.*, Selective potentiation of the hypoxic cytotoxicity of tirapazamine by its 1-N-oxide metabolite SR 4317. *Cancer Res*, **2004**. 64(2): p. 736-742.

117. Elwell, J.H., *et al.*, Adaptation of human tumor cells to tirapazamine under aerobic conditions: implications of increased antioxidant enzyme activity to mechanism of aerobic cytotoxicity. *Biochem Pharmacol*, **1997**. 54(2): p. 249-257.

118. Aboagye, E.O., *et al.*, Hypoxic cell cytotoxin tirapazamine induces acute changes in tumor energy metabolism and pH: a 31P magnetic resonance spectroscopy study. *Radiat Oncol Investig*, **1998**. 6(6): p. 249-254.

119. Hong, B.-J., *et al.*, Tumor hypoxia and reoxygenation: the yin and yang for radiotherapy. *Radiat Oncol J*, **2016**. 34(4): p. 239-249.

120. Lunt, S.J., *et al.*, Tirapazamine administered as a neoadjuvant to radiotherapy reduces metastatic dissemination. *Clin Cancer Res*, **2005**. 11(11): p. 4212-4216.

121. Gandara, D.R., *et al.*, Tirapazamine: prototype for a novel class of therapeutic agents targeting tumor hypoxia. *Semin Oncol*, **2002**. 29(1 Suppl 4): p. 102-109.

122. Zeman, E.M., *et al.*, Enhancement of radiation-induced tumor cell killing by the hypoxic cell toxin SR 4233. *Radiother Oncol*, **1988**. 12(3): p. 209-218.

123. Bhattacharya, A., *et al.*, Hypoxia-Specific Drug Tirapazamine Does Not Abrogate Hypoxic Tumor Cells in Combination Therapy with Irinotecan and Methylselenocysteine in Well-Differentiated Human Head and Neck Squamous Cell Carcinoma A253 Xenografts. *Neoplasia* **2008**. 10(8): p. 857-865.

124. Cai, T.-Y., *et al.*, Tirapazamine Sensitizes Hepatocellular Carcinoma Cells to Topoisomerase I Inhibitors via Cooperative Modulation of Hypoxia-Inducible Factor-1α. *Mol Cancer Ther*, **2014**. 13(3): p. 630-642.

125. Huxham, L.A., *et al.*, Tirapazamine causes vascular dysfunction in HCT-116 tumour xenografts. *Radiother Oncol*, **2006**. 78(2): p. 138-145.

126. Durand, R.E., *et al.*, Physiologic and cytotoxic effects of tirapazamine in tumor-bearing mice. *Radiat Oncol Investig*, **1997**. 5(5): p. 213-219.

127. Weitman, S., *et al.*, Evidence of enhanced in vivo activity using tirapazamine with paclitaxel and paraplatin regimens against the MV-522 human lung cancer xenograft. *Cancer Chemotherapy and Pharmacology*, **1999**. 43(5): p. 402-408.

128. Doherty, N., *et al.*, Muscle cramping in phase I clinical trials of tirapazamine (SR 4233) with and without radiation. *Int J Radiat Oncol Biol Phys*, **1994**. 29(2): p. 379-382.

129. Senan, S., *et al.*, Phase I and pharmacokinetic study of tirapazamine (SR 4233) administered every three weeks. *Clin Cancer Res*, **1997**. 3(1): p. 31-38.

130. Johnson, C.A., *et al.*, Phase I trial of tirapazamine in combination with cisplatin in a single dose every 3 weeks in patients with solid tumors. *J Clin Oncol*, **1997**. 15(2): p. 773-780.

131. Shulman, L.N., *et al.*, Phase I trial of the hypoxic cell cytotoxin tirapazamine with concurrent radiation therapy in the treatment of refractory solid tumors. *Int J Radiat Oncol Biol Phys*, **1999**. 44(2): p. 349-353.

132. Peters, L.J., *et al.*, Extraordinary tumor control in phase I trial of concurrent tirapazamine cisplatin and radiotherapy for far advanced head and neck cancer. *Int J Radiat Oncol Biol Phys*, **1999**. 45(3): p. 148-149.

133. Rischin, D., *et al.*, Tirapazamine, Cisplatin, and Radiation versus Fluorouracil, Cisplatin, and Radiation in patients with locally advanced head and neck cancer: a randomized phase II trial of the Trans-Tasman Radiation Oncology Group (TROG 98.02). *J Clin Oncol*, **2005**. 23(1): p. 79-87.

134. Rischin, D., *et al.*, Phase I trial of concurrent tirapazamine, cisplatin, and radiotherapy in patients with advanced head and neck cancer. *J Clin Oncol*, **2001**. 19(2): p. 535-542.

135. Lee, D.J., *et al.*, Concurrent tirapazamine and radiotherapy for advanced head and neck carcinomas: a Phase II study. *Int J Radiat Oncol Biol Phys*, **1998**. 42(4): p. 811-815.

136. Craighead, P.S., *et al.*, A phase I/II evaluation of tirapazamine administered intravenously concurrent with cisplatin and radiotherapy in women with locally advanced cervical cancer. *Int J Radiat Oncol Biol Phys*, **2000**. 48(3): p. 791-795.

137. Le, Q.T., *et al.*, Phase I study of tirapazamine plus cisplatin/etoposide and concurrent thoracic radiotherapy in limited-stage small cell lung cancer (S0004): a Southwest Oncology Group study. *Clin Cancer Res*, **2004**. 10(16): p. 5418-5424.

138. Le, Q.T., *et al.*, Phase II study of tirapazamine, cisplatin, and etoposide and concurrent thoracic radiotherapy for limited-stage small-cell lung cancer: SWOG 0222. *J Clin Oncol*, **2009**. 27(18): p. 3014-3019.

139. Reck, M., *et al.*, [Phase II-trial of tirapazamine in combination with cisplatin and gemcitabine in patients with advanced non-small-cell-lung-cancer (NSCLC)]. *Pneumologie*, **2004**. 58(12): p. 845-849.

140. Treat, J., *et al.*, Tirapazamine with cisplatin in patients with advanced non-small-cell lung cancer: a phase II study. *J Clin Oncol*, **1998**. 16(11): p. 3524-3527.

141. Miller, V.A., *et al.*, Phase II study of the combination of the novel bioreductive agent, tirapazamine, with cisplatin in patients with advanced non-small-cell lung cancer. *Ann Oncol*, **1997**. 8(12): p. 1269-1271.

142. von Pawel, J., *et al.*, Tirapazamine plus cisplatin versus cisplatin in advanced non-small-cell lung cancer: A report of the international CATAPULT I study group. Cisplatin and Tirapazamine in Subjects with Advanced Previously Untreated Non-Small-Cell Lung Tumors. *J Clin Oncol*, **2000**. 18(6): p. 1351-1359.

143. Shepherd, F., *et al.*, Comparison of Tirazone (Tirapazamine) and cisplatin vs. etoposide and cisplatin in advanced non-small cell lung cancer (NSCLC): Final results of the international Phase III CATAPULT II Trial. *Lung Cancer*, **2000**. 29(1): p. 28.

144. Ltd, T., *Dose-defining Study of Tirapazamine Combined With Embolization in Liver Cancer*. 2014, Bethesda (MD): National Library of Medicine (US): In: ClinicalTrials.gov [Internet].

145. Ltd, T., *TATE Versus TACE in Intermediate Stage HCC (TATE)*. 2017, Bethesda (MD): National Library of Medicine (US): In: ClinicalTrials.gov [Internet].

146. Ltd, T., *Combination of TATE and PD-1 Inhibitor in Liver Cancer (TATE-PD1)*. 2017, Bethesda (MD): National Library of Medicine (US): In: ClinicalTrials.gov [Internet].

147. Hay, M.P., *et al.*, Structure-activity relationships of 1,2,4-benzotriazine 1,4-dioxides as hypoxia-selective analogues of tirapazamine. *J Med Chem*, **2003**. 46(1): p. 169-182.

148. Lin, P.-S., *et al.*, New cytotoxic mechanism of the bioreductive agent Tirapazamine (SR 4233) mediated by forming complex with copper. *Radiat Oncol Investig*, **1996**. 4(5): p. 211-220.

149. Ndagi, U., *et al.*, Metal complexes in cancer therapy – an update from drug design perspective. *Drug Des Devel Ther*, **2017**. 11: p. 599-616.

150. Bruijnincx, P.C.A., *et al.*, 'New Trends for Metal Complexes with Anticancer Activity'. *Curr Opin Chem Biol*, **2008**. 12(2): p. 197-206.

151. Kalinowski, D.S., *et al.*, Redox cycling metals: Pedaling their roles in metabolism and their use in the development of novel therapeutics. *Biochim Biophys Acta*, **2016**. 1863(4): p. 727-748.

152. Bergamo, A., *et al.*, The mechanism of tumour cell death by metal-based anticancer drugs is not only a matter of DNA interactions. *Coord Chem Rev*, **2018**. 360: p. 17-33.

153. Sun, L., *et al.*, Azo-Based Iridium(III) Complexes as Multicolor Phosphorescent Probes to Detect Hypoxia in 3D Multicellular Tumor Spheroids. *Sci Rep*, **2015**. 5: p. 14837.

154. Her, S., *et al.*, Gold nanoparticles for applications in cancer radiotherapy: Mechanisms and recent advancements. *Adv Drug Deliv Rev*, **2017**. 109: p. 84-101.

155. Denny, W.A., The role of hypoxia-activated prodrugs in cancer therapy. *Lancet Oncol*, **2000**. 1(1): p. 25-29.

156. Graf, N., *et al.*, Redox activation of metal-based prodrugs as a strategy for drug delivery. *Adv Drug Deliv Rev*, **2012**. 64(11): p. 993-1004.

157. Daniel, K.G., *et al.*, Copper storage diseases: Menkes, Wilsons, and cancer. *Front Biosci*, **2004**. 9: p. 2652-2662.

158. Finney, L., *et al.*, Copper and angiogenesis: unravelling a relationship key to cancer progression. *Clin Exp Pharmacol Physiol*, **2009**. 36(1): p. 88-94.

159. Lowndes, S.A., *et al.*, The Role of Copper in Tumour Angiogenesis. *J Mammary Gland Biol Neoplasia*, **2005**. 10(4): p. 299-310.

160. Gupte, A., *et al.*, Elevated copper and oxidative stress in cancer cells as a target for cancer treatment. *Cancer Treat Rev*, **2009**. 35(1): p. 32-46.

161. Denoyer, D., *et al.*, Targeting copper in cancer therapy: 'Copper That Cancer'. *Metallomics*, **2015**. 7(11): p. 1459-1476.

162. Majumder, S., *et al.*, The role of copper in drug-resistant murine and human tumors. *BioMetals*, **2008**. 22(2): p. 377.

163. Rizk, S.L., *et al.*, Comparison between concentrations of trace elements in normal and neoplastic human breast tissue. *Cancer Res*, **1984**. 44(11): p. 5390-5394.

164. Qayyum, M.A., *et al.*, Comparative Study of Trace Elements in Blood, Scalp Hair and Nails of Prostate Cancer Patients in Relation to Healthy Donors. *Biol Trace Elem Res*, **2014**. 162(1): p. 46-57.

165. Denoyer, D., *et al.*, Copper as a target for prostate cancer therapeutics: copper-ionophore pharmacology and altering systemic copper distribution. *Oncotarget*, **2016**. 7(24): p. 37064-37080.

166. Denoyer, D., *et al.*, Heterogeneous copper concentrations in cancerous human prostate tissues. *Prostate*, **2015**. 75(14): p. 1510-1517.

167. Marzano, C., *et al.*, Copper complexes as anticancer agents. *Anticancer Agents Med Chem*, **2009**. 9(2): p. 185-211.

168. Torre, M.H., *et al.*, Novel Cu(II) quinoxaline N1,N4-dioxide complexes as selective hypoxic cytotoxins. *Eur J Med Chem*, **2005**. 40(5): p. 473-480.

169. Urquiola, C., *et al.*, New copper-based complexes with quinoxaline N1,N4-dioxide derivatives, potential antitumoral agents. *J Inorg Biochem*, **2008**. 102(1): p. 119-126.

170. Blower, P.J., *et al.*, Towards new transition metal-based hypoxic selective agents for therapy and imaging. *J Inorg Biochem*, **2001**. 85(1): p. 15-22.

171. Santini, C., *et al.*, Advances in copper complexes as anticancer agents. *Chem Rev*, **2014**. 114(1): p. 815-862.

172. Clarke, M.J., *et al.*, Non-Platinum Chemotherapeutic Metallopharmaceuticals. *Chem Rev*, **1999**. 99(9): p. 2511-2534.

173. Anderson, C.J., *et al.*, Copper-64 Radiopharmaceuticals for PET Imaging of Cancer: Advances in Preclinical and Clinical Research. *Cancer Biother Radiopharm*, **2009**. 24(4): p. 379-393.

174. Dearling, J.L., *et al.*, Design of hypoxia-targeting radiopharmaceuticals: selective uptake of copper-64 complexes in hypoxic cells in vitro. *Eur J Nucl Med*, **1998**. 25(7): p. 788-792.

175. Vavere, A.L., *et al.*, Cu-ATSM: a radiopharmaceutical for the PET imaging of hypoxia. *Dalton Trans*, **2007**(43): p. 4893-4902.

176. Lewis, J.S., *et al.*, Evaluation of 64Cu-ATSM in vitro and in vivo in a hypoxic tumor model. *J Nucl Med* **1999**. 40(1): p. 177.

177. Lewis, J.S., *et al.*, Tumor Uptake of Copper-Diacetyl-Bis(N4-Methylthiosemicarbazone): Effect of Changes in Tissue Oxygenation. *J Nucl Med* **2001**. 42(4): p. 655-661.

178. Chao, K.S.C., *et al.*, A novel approach to overcome hypoxic tumor resistance: Cu-ATSM-guided intensity-modulated radiation therapy. *Int J Radiat Oncol Biol Phys*, **2001**. 49(4): p. 1171-1182.

179. Frezza, M., *et al.*, Novel metals and metal complexes as platforms for cancer therapy. *Curr Pharm Des*, **2010**. 16(16): p. 1813-1825.

180. Knight, J.C., *et al.*, Synthesis, characterisation and evaluation of a novel copper-64 complex with selective uptake in EMT-6 cells under hypoxic conditions. *Dalton Trans*, **2013**. 42(33): p. 12005-12014.

181. Dearling, J.L., *et al.*, Copper bis(thiosemicarbazone) complexes as hypoxia imaging agents: structure-activity relationships. *J Biol Inorg Chem*, **2002**. 7(3): p. 249-259.

182. Palanimuthu, D., *et al.*, In Vitro and in Vivo Anticancer Activity of Copper Bis(thiosemicarbazone) Complexes. *J Med Chem*, **2013**. 56(3): p. 722-734.

183. Price, K.A., *et al.*, Mechanisms controlling the cellular accumulation of copper bis(thiosemicarbazonato) complexes. *Inorg Chem*, **2011**. 50(19): p. 9594-9605.

184. Tabassum, S., *et al.*, Molecular drug design, synthesis and structure elucidation of a new specific target peptide based metallo drug for cancer chemotherapy as topoisomerase I inhibitor. *Dalton Trans*, **2012**. 41(16): p. 4955-4964.

185. Zeglis, B.M., *et al.*, Role of metalation in the topoisomerase IIalpha inhibition and antiproliferation activity of a series of alpha-heterocyclic-N4-substituted thiosemicarbazones and their Cu(II) complexes. *J Med Chem*, **2011**. 54(7): p. 2391-2398.

186. Sandhaus, S., *et al.*, A novel copper(II) complex identified as a potent drug against colorectal and breast cancer cells and as a poison inhibitor for human topoisomerase IIα. *Inorg Chem Comm*, **2016**. 64: p. 45-49.

187. Liu, N., *et al.*, Inhibition of 19S proteasome-associated deubiquitinases by metal-containing compounds. *Oncoscience*, **2015**. 2(5): p. 457-466.

188. Zhang, Z., *et al.*, 1,10-Phenanthroline promotes copper complexes into tumor cells and induces apoptosis by inhibiting the proteasome activity. *J Biol Inorg Chem*, **2012**. 17(8): p. 1257-1267.

189. Adsule, S., *et al.*, Novel Schiff Base Copper Complexes of Quinoline-2 Carboxaldehyde as Proteasome Inhibitors in Human Prostate Cancer Cells. *J Med Chem*, **2006**. 49(24): p. 7242-7246.

190. Tardito, S., *et al.*, The thioxotriazole copper(II) complex A0 induces endoplasmic reticulum stress and paraptotic death in human cancer cells. *J Biol Chem*, **2009**. 284(36): p. 24306-24319.

191. Stefani, C., *et al.*, Identification of differential anti-neoplastic activity of copper bis(thiosemicarbazones) that is mediated by intracellular reactive oxygen species generation and lysosomal membrane permeabilization. *J Inorg Biochem*, **2015**. 152(Supplement C): p. 20-37.

192. Kovacevic, Z., *et al.*, Copper that cancer with lysosomal love! *Aging* **2016**. 8(2): p. 210-211.

193. Lin, P.S., *et al.*, CuTira brachytherapy: a new combination of radioactive copper isotopes and the hypoxic cytotoxin, tirapazamine, for targeted tumor therapy. *J Nucl Med*, **1998**. 39(4): p. 677-678.

194. Gali-Muhtasib, H.U., *et al.*, Quinoxaline 1,4-dioxides as anticancer and hypoxia-selective drugs. *Oncol Rep*, **2001**. 8(3): p. 679-684.

195. Wong, M.C.S., *et al.*, Global Incidence and Mortality for Prostate Cancer: Analysis of Temporal Patterns and Trends in 36 Countries. *Eur Urol*. 70(5): p. 862-874.

196. Ramalingam, S., *et al.*, Dissecting major signalling pathways in prostate cancer development and progression: Mechanisms and novel therapeutic targets. *J Steroid Biochem Mol Biol*, **2017**. 166: p. 16-27.

197. Hayes, J.H., *et al.*, Screening for prostate cancer with the prostate-specific antigen test: a review of current evidence. *JAMA*, **2014**. 311(11): p. 1143-1149.

198. Stenman, U.-H., *et al.*, Prostate-specific antigen. *Semin Cancer Biol*, **1999**. 9(2): p. 83-93.

199. Ali, A., *et al.*, Identification and evaluation of clinically significant prostate cancer: a step towards personalized diagnosis. *Curr Opin Urol*, **2017**. 27(3): p. 217-224.

200. Culig, Z., *et al.*, Androgen receptor signalling in prostate cancer. *Cancer Metast Rev*, **2014**. 33(2-3): p. 413-427.

201. Lonergan, P.E., *et al.*, Androgen receptor signalling in prostate cancer development and progression. *J Carcinog*, **2011**. 10: p. 20.

202. Pienta, K.J., *et al.*, Mechanisms Underlying the Development of Androgen-Independent Prostate Cancer. *Clin Cancer Res*, **2006**. 12(6): p. 1665-1671.

203. Davies, A.H., *et al.*, Castration-Resistant Prostate Cancer, in Precision Molecular Pathology of Prostate Cancer, B.D. Robinson, et al., Editors. **2018**, Springer International Publishing: Cham. p. 297-322.

204. Feldman, B.J., *et al.*, The development of androgen-independent prostate cancer. *Nat Rev Cancer*, **2001**. 1(1): p. 34-45.

205. Al Olama, A.A., *et al.*, A meta-analysis of 87,040 individuals identifies 23 new susceptibility loci for prostate cancer. *Nat Genet*, **2014**. 46: p. 1103.

206. Cancer Genome Atlas Research, N., The Molecular Taxonomy of Primary Prostate Cancer. *Cell*, **2015**. 163(4): p. 1011-1025.

207. Taplin, M.E., Drug insight: role of the androgen receptor in the development and progression of prostate cancer. *Nat Clin Pract Oncol*, **2007**. 4(4): p. 236-244.

208. Mottet, N., *et al.*, EAU-ESTRO-SIOG Guidelines on Prostate Cancer. Part 1: Screening, Diagnosis, and Local Treatment with Curative Intent. *Eur Urol*, **2017**. 71(4): p. 618-629.

209. Huggins, C., *et al.*, Studies on Prostatic Cancer. I. The Effect of Castration, of Estrogen and of Androgen Injection on Serum Phosphatases in Metastatic Carcinoma of the Prostate. *Cancer Res*, **1941**. 1(4): p. 293-297.

210. Cornford, P., *et al.*, EAU-ESTRO-SIOG Guidelines on Prostate Cancer. Part II: Treatment of Relapsing, Metastatic, and Castration-Resistant Prostate Cancer. *Eur Urol*, **2017**. 71(4): p. 630-642.

211. Wheeler, T.M., *et al.*, Clinical and pathological significance of the level and extent of capsular invasion in clinical stage T1-2 prostate cancer. *Hum Pathol*, **1998**. 29(8): p. 856-862.

212. Ghafar, M.A., *et al.*, Acute hypoxia increases the aggressive characteristics and survival properties of prostate cancer cells. *Prostate*, **2003**. 54(1): p. 58-67.

213. Danielska, J., *et al.*, Hypoxia in prostate cancer. *J Oncol*, **2017**. 67(2): p. 132-136.

214. Shabsigh, A., *et al.*, Biomarker analysis demonstrates a hypoxic environment in the castrated rat ventral prostate gland. *J Cell Biochem*, **2001**. 81(3): p. 437-444.

215. Shabsigh, A., *et al.*, Rapid reduction in blood flow to the rat ventral prostate gland after castration: preliminary evidence that androgens influence prostate size by regulating blood flow to the prostate gland and prostatic endothelial cell survival. *Prostate*, **1998**. 36(3): p. 201-206.

216. Rasey, J.S., *et al.*, Quantifying regional hypoxia in human tumors with positron emission tomography of [18F]fluoromisonidazole: a pretherapy study of 37 patients. *Int J Radiat Oncol Biol Phys*, **1996**. 36(2): p. 417-428.

217. O'Donoghue, J.A., *et al.*, Assessment of regional tumor hypoxia using 18F-fluoromisonidazole and 64Cu(II)-diacetyl-bis(N4-methylthiosemicarbazone) positron emission tomography: Comparative study featuring microPET imaging, Po2 probe measurement, autoradiography, and fluorescent microscopy in the R3327-AT and FaDu rat tumor models. *Int J Radiat Oncol Biol Phys*, **2005**. 61(5): p. 1493-1502.

218. Marignol, L., *et al.*, Hypoxia in prostate cancer: a powerful shield against tumour destruction? *Cancer Treat Rev*, **2008**. 34(4): p. 313-327.

219. Lawrence, Y.R., *et al.*, Hypoxia in prostate cancer: observation to intervention. *Lancet Oncol*, **2008**. 9(4): p. 308-309.

220. Zhong, H., *et al.*, Up-regulation of hypoxia-inducible factor 1alpha is an early event in prostate carcinogenesis. *Cancer Detect Prev*, **2004**. 28(2): p. 88-93.

221. Wang, L., *et al.*, Expression of hypoxia-inducible factor 1 alpha and vascular endothelial growth factor in prostate cancer and its significance. *Zhonghua Nan Ke Xue*, **2006**. 12(1): p. 57-59.

222. Carnell, D.M., *et al.*, An immunohistochemical assessment of hypoxia in prostate carcinoma using pimonidazole: implications for radioresistance. *Int J Radiat Oncol Biol Phys*, **2006**. 65(1): p. 91-99.

223. Movsas, B., *et al.*, Hypoxia in human prostate carcinoma: an Eppendorf PO2 study. *Am J Clin Oncol*, **2001**. 24(5): p. 458-461.

224. Parker, C., *et al.*, Polarographic electrode study of tumor oxygenation in clinically localized prostate cancer. *Int J Radiat Oncol Biol Phys*, **2004**. 58(3): p. 750-757.

225. Fraga, A., *et al.*, Hypoxia and Prostate Cancer Aggressiveness: A Tale With Many Endings. *Clin Genitourin Cancer*, **2015**. 13(4): p. 295-301.

226. Ranasinghe, W.K.B., *et al.*, The Role of Hypoxia-Inducible Factor 1α in Determining the Properties of Castrate-Resistant Prostate Cancers. *PLOS ONE*, **2013**. 8(1): p. e54251.

227. Chan, N., *et al.*, Tumor hypoxia, DNA repair and prostate cancer progression: new targets and new therapies. *Future Oncology*, **2007**. 3(3): p. 329-341.

228. Johansson, A., *et al.*, Targeting castration-induced tumour hypoxia enhances the acute effects of castration therapy in a rat prostate cancer model. *BJU International*, **2011**. 107(11): p. 1818-1824.

229. Naguib, Y.W., *et al.*, Nanomedicine: The Promise and Challenges in Cancer Chemotherapy, in Nanomaterial: Impacts on Cell Biology and Medicine, D.G. Capco and Y. Chen, Editors. **2014**, Springer Netherlands: Dordrecht. p. 207-233.

230. Xu, X., *et al.*, Cancer nanomedicine: from targeted delivery to combination therapy. *Trends Mol Med*, **2015**. 21(4): p. 223-232.

231. Etheridge, M.L., *et al.*, The big picture on nanomedicine: the state of investigational and approved nanomedicine products. *Nanomedicine*, **2013**. 9(1): p. 1-14.

232. Singh, M., *et al.*, Nanoparticles: A new technology with wide applications. *Res J Nanosci Nanotechnol*, **2011**. 1(1): p. 1-11.

233. Kreuter, J., Nanoparticles—a historical perspective. *Int J Pharm*, **2007**. 331(1): p. 1-10.

234. Ochekpe, N.A., *et al.*, Nanotechnology and drug delivery part 1: background and applications. *Trop J Pharm Res*, **2009**. 8(3): p. 265-274.

235. Sun, T., *et al.*, Engineered Nanoparticles for Drug Delivery in Cancer Therapy. *Angew Chem Int Ed Engl*, **2014**. 53(46): p. 12320-12364.

236. Wicki, A., *et al.*, Nanomedicine in cancer therapy: Challenges, opportunities, and clinical applications. *J Control Release*, **2015**. 200(0): p. 138-157.

237. Mura, S., *et al.*, Stimuli-responsive nanocarriers for drug delivery. *Nat Mater*, **2013**. 12(11): p. 991-1003.

238. Chen, H., *et al.*, Rethinking cancer nanotheranostics. *Nat Rev Mater*, **2017**. 2: p. 17024.

239. Boisseau, P., *et al.*, Nanomedicine, nanotechnology in medicine. *C R Phys*, **2011**. 12(7): p. 620-636.

240. Svenson, S., What nanomedicine in the clinic right now really forms nanoparticles? *Wiley Interdiscipl Rev: Nanomed Nanobiotechnol*, **2014**. 6(2): p. 125-135.

241. Allen, T.M., *et al.*, Liposomal drug delivery systems: from concept to clinical applications. *Adv Drug Deliv Rev*, **2013**. 65(1): p. 36-48.

242. Bangham, A.D., *et al.*, Diffusion of univalent ions across the lamellae of swollen phospholipids. *J Mol Biol*, **1965**. 13(1): p. 238-IN227.

243. Gregoriadis, G., The carrier potential of liposomes in biology and medicine (first of two parts). *N Engl J Med*, **1976**. 295(13): p. 704-710.

244. Akbarzadeh, A., *et al.*, Liposome: classification, preparation, and applications. *Nanoscale Res Lett*, **2013**. 8(1): p. 102.

245. Fenske, D.B., *et al.*, Liposomal nanomedicines: an emerging field. *Toxicol Pathol*, **2008**. 36(1): p. 21-29.

246. Mayer, L.D., *et al.*, Influence of Vesicle Size, Lipid Composition, and Drug-to-Lipid Ratio on the Biological Activity of Liposomal Doxorubicin in Mice. *Cancer Res*, **1989**. 49(21): p. 5922-5930.

247. Çağdaş, M., *et al.*, Liposomes as Potential Drug Carrier Systems for Drug Delivery. **2014**.

248. Bozzuto, G., *et al.*, Liposomes as nanomedical devices. *Int J Nanomedicine*, **2015**. 10: p. 975-999.

249. Monteiro, N., *et al.*, Liposomes in tissue engineering and regenerative medicine. *J R Soc Interface*, **2014**. 11(101).

250. Pattni, B.S., *et al.*, New Developments in Liposomal Drug Delivery. *Chem Rev*, **2015**. 115(19): p. 10938-10966.

251. Li, J., *et al.*, A review on phospholipids and their main applications in drug delivery systems. *Asian J Pharm Sci*, **2015**. 10(2): p. 81-98.

252. Eze, M.O., Phase transitions in phospholipid bilayers: Lateral phase separations play vital roles in biomembranes. *Biochem Educ*, **1991**. 19(4): p. 204-208.

253. Chen, J., *et al.*, Influence of lipid composition on the phase transition temperature of liposomes composed of both DPPC and HSPC. *Drug Dev Ind Pharm*, **2013**. 39(2): p. 197-204.

254. Laouini, A., *et al.*, Preparation, Characterization and Applications of Liposomes: State of the Art. *J Colloid Sci Biotechnol*, **2012**. 1(2): p. 147-168.

255. De Gier, J., *et al.*, Lipid composition and permeability of liposomes. *Biochim Biophys Acta-Biomembranes*, **1968**. 150(4): p. 666-675.

256. Taylor, K.M.G., *et al.*, Drug entrapment and release from multilamellar and reverse-phase evaporation liposomes. *Int J Pharm*, **1990**. 58(1): p. 49-55.

257. Manojlovic, V., *et al.*, Membrane interactions of ternary phospholipid/cholesterol bilayers and encapsulation efficiencies of a RIP II protein. *Colloids Surf B Biointerfaces*, **2008**. 64(2): p. 284-296.

258. Senior, J., *et al.*, Stability of small unilamellar liposomes in serum and clearance from the circulation: The effect of the phospholipid and cholesterol components. *Life Sciences*, **1982**. 30(24): p. 2123-2136.

259. Rissanen, S., *et al.*, Effect of PEGylation on Drug Entry into Lipid Bilayer. *J Phys Chem B*, **2014**. 118(1): p. 144-151.

260. Garbuzenko, O., *et al.*, Effect of grafted PEG on liposome size and on compressibility and packing of lipid bilayer. *Chem Phys Lipids*, **2005**. 135(2): p. 117-129.

261. Maruyama, K., *et al.*, Prolonged circulation time in vivo of large unilamellar liposomes composed of distearoyl phosphatidylcholine and cholesterol containing amphipathic poly(ethylene glycol). *Biochim Biophys Acta*, **1992**. 1128(1): p. 44-49.

262. Barenholz, Y., Doxil(R)--the first FDA-approved nano-drug: lessons learned. *J Control Release*, **2012**. 160(2): p. 117-134.

263. Lichtenberg, D., *et al.*, Liposomes: Preparation, Characterization, and Preservation, in Methods of Biochemical Analysis. **2006**, John Wiley & Sons, Inc. p. 337-462.

264. Pons, M., *et al.*, Liposomes obtained by the ethanol injection method. *Int J Pharm*, **1993**. 95(1–3): p. 51-56.

265. Mayer, L.D., *et al.*, Solute distributions and trapping efficiencies observed in freeze-thawed multilamellar vesicles. *Biochim Biophys Acta*, **1985**. 817(1): p. 193-196.

266. Costa, A.P., *et al.*, Freeze-anneal-thaw cycling of unilamellar liposomes: effect on encapsulation efficiency. *Pharm Res*, **2014**. 31(1): p. 97-103.

267. Riaz, M., Liposomes preparation methods. *Pak J Pharm Sci*, **1996**. 9(1): p. 65-77.

268. Szoka, F., Jr., *et al.*, Procedure for preparation of liposomes with large internal aqueous space and high capture by reverse-phase evaporation. *Proc Natl Acad Sci* **1978**. 75(9): p. 4194-4198.

269. Xu, H., *et al.*, Development of high-content gemcitabine PEGylated liposomes and their cytotoxicity on drug-resistant pancreatic tumour cells. *Pharm Res*, **2014**. 31(10): p. 2583-2592.

270. Gubernator, J., Active methods of drug loading into liposomes: recent strategies for stable drug entrapment and increased in vivo activity. *Expert Opin Drug Deliv*, **2011**. 8(5): p. 565-580.

271. Abraham, S.A., *et al.*, Formation of transition metal–doxorubicin complexes inside liposomes. *Biochim Biophys Acta-Biomembranes*, **2002**. 1565(1): p. 41-54.

272. Fenske, D.B., *et al.*, Ionophore-mediated uptake of ciprofloxacin and vincristine into large unilamellar vesicles exhibiting transmembrane ion gradients. *Biochim Biophys Acta-Biomembranes*, **1998**. 1414(1): p. 188-204.

273. Cheung, B.C.L., *et al.*, Loading of doxorubicin into liposomes by forming Mn2+-drug complexes. *Biochim Biophys Acta-Biomembranes*, **1998**. 1414(1–2): p. 205-216.

274. Patil, Y.P., *et al.*, Novel methods for liposome preparation. *Chem Phys Lipids*, **2014**. 177: p. 8-18.

275. Basu, S.C., *et al.*, Liposome methods and protocols. **2002**: Springer Science & Business Media.

276. Vemuri, S., *et al.*, Preparation and characterization of liposomes as therapeutic delivery systems: a review. *Pharm Acta Helv*, **1995**. 70(2): p. 95-111.

277. Deshpande, P.P., *et al.*, Current trends in the use of liposomes for tumor targeting. *Nanomedicine* **2013**. 8(9): p. 1509-1528.

278. Litzinger, D.C., *et al.*, Effect of liposome size on the circulation time and intraorgan distribution of amphipathic poly(ethylene glycol)-containing liposomes. *Biochim Biophys Acta*, **1994**. 1190(1): p. 99-107.

279. Nagayasu, A., *et al.*, The size of liposomes: a factor which affects their targeting efficiency to tumors and therapeutic activity of liposomal antitumor drugs. *Adv Drug Deliv Rev*, **1999**. 40(1): p. 75-87.

280. Smith, M.C., *et al.*, Zeta potential: a case study of cationic, anionic, and neutral liposomes. *Anal Bioanal Chem*, **2017**. 409(24): p. 5779-5787.

281. Kraft, J.C., *et al.*, Emerging Research and Clinical Development Trends of Liposome and Lipid Nanoparticle Drug Delivery Systems. *J Pharm Sci*, **2014**. 103(1): p. 29-52.

282. Owens Iii, D.E., *et al.*, Opsonization, biodistribution, and pharmacokinetics of polymeric nanoparticles. *Int J Pharm*, **2006**. 307(1): p. 93-102.

283. Senat, K., *et al.*, Effect of the surface charge of liposomes on their uptake by angiogenic tumor vessels. *Int J Cancer*, **2003**. 105(4): p. 561-567.

284. Sawant, R.R., *et al.*, Challenges in Development of Targeted Liposomal Therapeutics. *The AAPS Journal*, **2012**. 14(2): p. 303-315.

285. Noble, G.T., *et al.*, Ligand-targeted liposome design: challenges and fundamental considerations. *Trends Biotechnol*, **2014**. 32(1): p. 32-45.

286. Sinha, R., *et al.*, Nanotechnology in cancer therapeutics: bioconjugated nanoparticles for drug delivery. *Mol Cancer Ther*, **2006**. 5(8): p. 1909-1917.

287. Torchilin, V., Antibody-modified liposomes for cancer chemotherapy. *Expert Opin Drug Deliv*, **2008**. 5(9): p. 1003-1025.

288. Gupta, B., *et al.*, Intracellular delivery of large molecules and small particles by cell-penetrating proteins and peptides. *Adv Drug Deliv Rev*, **2005**. 57(4): p. 637-651.

289. Xiong, X.B., *et al.*, Intracellular delivery of doxorubicin with RGD-modified sterically stabilized liposomes for an improved antitumor efficacy: in vitro and in vivo. *J Pharm Sci*, **2005**. 94(8): p. 1782-1793.

290. Konigsberg, P.J., *et al.*, The development of IL-2 conjugated liposomes for therapeutic purposes. *Biochim Biophys Acta*, **1998**. 1370(2): p. 243-251.

291. Junbo, H., *et al.*, Receptor-mediated interleukin-2 gene transfer into human hepatoma cells. *Int J Mol Med*, **1999**. 3(6): p. 601-608.

292. Li, X., *et al.*, Targeted delivery of doxorubicin using stealth liposomes modified with transferrin. *Int J Pharm*, **2009**. 373(1-2): p. 116-123.

293. Gabizon, A., *et al.*, In vivo fate of folate-targeted polyethylene-glycol liposomes in tumor-bearing mice. *Clin Cancer Res*, **2003**. 9(17): p. 6551-6559.

294. Wu, J., *et al.*, Increased liver uptake of liposomes and improved targeting efficacy by labeling with asialofetuin in rodents. *Hepatology*, **1998**. 27(3): p. 772-778.

295. Sliedregt, L.A., *et al.*, Design and synthesis of novel amphiphilic dendritic galactosides for selective targeting of liposomes to the hepatic asialoglycoprotein receptor. *J Med Chem*, **1999**. 42(4): p. 609-618.

296. Wu, X., *et al.*, Aptamers: active targeting ligands for cancer diagnosis and therapy. *Theranostics*, **2015**. 5(4): p. 322-344.

297. Plourde, K., *et al.*, Aptamer-based liposomes improve specific drug loading and release. *J Control Release*, **2017**. 251: p. 82-91.

298. Lian, T., *et al.*, Trends and developments in liposome drug delivery systems. *J Pharm Sci*, **2001**. 90(6): p. 667-680.

299. Torchilin, V.P., Recent advances with liposomes as pharmaceutical carriers. *Nat Rev Drug Discov*, **2005**. 4(2): p. 145-160.

300. Parveen, S., *et al.*, Nanoparticles: a boon to drug delivery, therapeutics, diagnostics and imaging. *Nanomed Nanotechnol*, **2012**. 8(2): p. 147-166.

301. Anselmo, A.C., *et al.*, An overview of clinical and commercial impact of drug delivery systems. *J Control Release*, **2014**. 190(0): p. 15-28.

302. Thompson , I.M.J., *et al.*, Long-Term Survival of Participants in the Prostate Cancer Prevention Trial. *N Engl J Med*, **2013**. 369(7): p. 603-610.

303. Ouvinha de Oliveira, R., *et al.*, Nanomedicine and its applications to the treatment of prostate cancer. *Anna Pharma Fr*, **2014**. 72(5): p. 303-316.

304. Sanna, V., *et al.*, Nanoparticle therapeutics for prostate cancer treatment. *Nanomedicine*, **2012**. 8 Suppl 1: p. S31-36.

305. Siddiqui, I.A., *et al.*, Nanochemoprevention by bioactive food components: a perspective. *Pharm Res*, **2010**. 27(6): p. 1054-1060.

306. Sanna, V., *et al.*, Targeted nanoparticles encapsulating (−)-epigallocatechin-3-gallate for prostate cancer prevention and therapy. *Sci Rep*, **2017**. 7: p. 41573.

307. Rocha, S., *et al.*, Epigallocatechin gallate-loaded polysaccharide nanoparticles for prostate cancer chemoprevention. *Nanomedicine* **2011**. 6(1): p. 79-87.

308. Arnida, *et al.*, Cellular uptake and toxicity of gold nanoparticles in prostate cancer cells: a comparative study of rods and spheres. *J Appl Toxicol*, **2010**. 30(3): p. 212-217.

309. Wolfe, T., *et al.*, Targeted gold nanoparticles enhance sensitization of prostate tumors to megavoltage radiation therapy in vivo. *Nanomedicine*, **2015**. 11(5): p. 1277-1283.

310. Yang, Q., *et al.*, Polymeric nanomedicine for tumor-targeted combination therapy to elicit synergistic genotoxicity against prostate cancer. *ACS Appl Mater Interfaces*, **2015**. 7(12): p. 6661-6673.

311. Lee, J.Y., *et al.*, Poly(styrene)-b-poly(DL-lactide) copolymer-based nanoparticles for anticancer drug delivery. *Int J Nanomedicine*, **2014**. 9: p. 2803-2813.

312. Brazhnik, K., *et al.*, Quantum dot-based lab-on-a-bead system for multiplexed detection of free and total prostate-specific antigens in clinical human serum samples. *Nanomedicine*, **2015**. 11(5): p. 1065-1075.

313. Taurin, S., *et al.*, A novel role for raloxifene nanomicelles in management of castrate resistant prostate cancer. *Biomed Res Int*, **2014**. 2014: p. 323594.

314. Pritchard, T., *et al.*, Raloxifene nanomicelles reduce the growth of castrate-resistant prostate cancer. *J Drug Target*, **2016**. 24(5): p. 441-449.

315. Yan, J., *et al.*, Targeted nanomedicine for prostate cancer therapy: docetaxel and curcumin co-encapsulated lipid–polymer hybrid nanoparticles for the enhanced anti-tumor activity in vitro and in vivo. *Drug Deliv*, **2016**. 23(5): p. 1757-1762.

316. Chen, B., *et al.*, Effective small interfering RNA delivery in vitro via a new stearylated cationic peptide. *Int J Nanomedicine*, **2015**. 10: p. 3303-3314.

317. Mohandas, A., *et al.*, Chitosan Based AGR2 siRNA Nanoparticle Delivery System for Prostate Cancer Cells. *Journal of Chitin and Chitosan Science*, **2013**. 1(2): p. 161-165.

318. Shen, S., *et al.*, Magnetic nanoparticle clusters for photothermal therapy with near-infrared irradiation. *Biomaterials*, **2015**. 39: p. 67-74.

319. Kawai, N., *et al.*, Anticancer effect of hyperthermia on prostate cancer mediated by magnetite cationic liposomes and immune-response induction in transplanted syngeneic rats. *Prostate*, **2005**. 64(4): p. 373-381.

320. Sanna, V., *et al.*, Novel docetaxel-loaded nanoparticles based on poly(lactide-co-caprolactone) and poly(lactide-co-glycolide-co-caprolactone) for prostate cancer treatment: formulation, characterization, and cytotoxicity studies. *Nanoscale Res Lett*, **2011**. 6(1): p. 260.

321. Davis, M.I., *et al.*, Crystal structure of prostate-specific membrane antigen, a tumor marker and peptidase. *Proc Natl Acad Sci* **2005**. 102(17): p. 5981-5986.

322. Farokhzad, O.C., *et al.*, Targeted nanoparticle-aptamer bioconjugates for cancer chemotherapy in vivo. *Proc Natl Acad Sci* **2006**. 103(16): p. 6315-6320.

323. Thangapazham, R.L., *et al.*, Evaluation of a nanotechnology-based carrier for delivery of curcumin in prostate cancer cells. *Int J Oncol*, **2008**. 32(5): p. 1119-1123.

324. Chen, Z., *et al.*, PSMA-Targeted Theranostic Nanoplex for Prostate Cancer Therapy. *ACS Nano*, **2012**. 6(9): p. 7752-7762.

325. Wu, X., *et al.*, Second-generation aptamer-conjugated PSMA-targeted delivery system for prostate cancer therapy. *Int J Nanomedicine*, **2011**. 6: p. 1747-1756.

326. Tse, B.W.-C., *et al.*, PSMA-targeting iron oxide magnetic nanoparticles enhance MRI of preclinical prostate cancer. *Nanomedicine*, **2014**. 10(3): p. 375-386.

327. Sahoo, S.K., *et al.*, Efficacy of transferrin-conjugated paclitaxel-loaded nanoparticles in a murine model of prostate cancer. *Int J Cancer*, **2004**. 112(2): p. 335-340.

328. Goodarzi, N., *et al.*, CD44-targeted docetaxel conjugate for cancer cells and cancer stem-like cells: a novel hyaluronic acid-based drug delivery system. *Chem Biol Drug Des*, **2014**. 83(6): p. 741-752.

329. Vaillant, O., *et al.*, Mannose-6-phosphate receptor: a target for theranostics of prostate cancer. *Angew Chem Int Ed Engl*, **2015**. 54(20): p. 5952-5956.

330. Kulhari, H., *et al.*, Cyclic-RGDfK peptide conjugated succinoyl-TPGS nanomicelles for targeted delivery of docetaxel to integrin receptor over-expressing angiogenic tumours. *Nanomedicine*, **2015**. 11(6): p. 1511-1520.

331. Goldstein, D., *et al.*, Anti-HER2 cationic immunoemulsion as a potential targeted drug delivery system for the treatment of prostate cancer. *Cancer Res*, **2007**. 67(1): p. 269-275.

332. Kroon, J., *et al.*, Liposomal nanomedicines in the treatment of prostate cancer. *Cancer Treat Rev*, **2014**. 40(4): p. 578-584.

333. Jantscheff, P., *et al.*, Liposomal gemcitabine (GemLip)-efficient drug against hormone-refractory Du145 and PC-3 prostate cancer xenografts. *Prostate*, **2009**. 69(11): p. 1151-1163.

334. Kroon, J., *et al.*, Liposomal delivery of dexamethasone attenuates prostate cancer bone metastatic tumor growth in vivo. *Prostate*, **2015**. 75(8): p. 815-824.

335. Aleku, M., *et al.*, Atu027, a Liposomal Small Interfering RNA Formulation Targeting Protein Kinase N3, Inhibits Cancer Progression. *Cancer Res*, **2008**. 68(23): p. 9788-9798.

336. Pal, A., *et al.*, Systemic delivery of RafsiRNA using cationic cardiolipin liposomes silences Raf-1 expression and inhibits tumor growth in xenograft model of human prostate cancer. *Int J Oncol*, **2005**. 26(4): p. 1087-1091.

337. Hagtvet, E., *et al.*, Liposomal doxorubicin improves radiotherapy response in hypoxic prostate cancer xenografts. *Radiat Oncol* **2011**. 6(1): p. 135.

338. Hagtvet, E., *et al.*, Ultrasound enhanced antitumor activity of liposomal doxorubicin in mice. *J Drug Target*, **2011**. 19(8): p. 701-708.

339. Eggen, S., *et al.*, Ultrasound Improves the Uptake and Distribution of Liposomal Doxorubicin in Prostate Cancer Xenografts. *Ultrasound Med Biol*. 39(7): p. 1255-1266.

340. Chen, X., *et al.*, Improved tumor-targeting drug delivery and therapeutic efficacy by cationic liposome modified with truncated bFGF peptide. *J Control Release*, **2010**. 145(1): p. 17-25.

341. Garde, S.V., *et al.*, Binding and internalization of NGR-peptide-targeted liposomal doxorubicin (TVT-DOX) in CD13-expressing cells and its antitumor effects. *Anticancer Drugs*, **2007**. 18(10): p. 1189-1200.

342. Xiang, B., *et al.*, PSA-responsive and PSMA-mediated multifunctional liposomes for targeted therapy of prostate cancer. *Biomaterials*, **2013**. 34(28): p. 6976-6991.

343. Marra, M., *et al.*, New self-assembly nanoparticles and stealth liposomes for the delivery of zoledronic acid: a comparative study. *Biotechnol Adv*, **2012**. 30(1): p. 302-309.

344. Miselis, N.R., *et al.*, Targeting tumor-associated macrophages in an orthotopic murine model of diffuse malignant mesothelioma. *Mol Cancer Ther*, **2008**. 7(4): p. 788-799.

345. Montanari, M., *et al.*, Phase II trial of non-pegylated liposomal doxorubicin and low-dose prednisone in second-line chemotherapy for hormone-refractory prostate cancer. *Tumori*, **2012**. 98(6): p. 696-701.

346. Shi, J., *et al.*, Cancer nanomedicine: progress, challenges and opportunities. *Nat Rev Cancer*, **2017**. 17(1): p. 20-37.

347. Du, J., *et al.*, Stimuli-responsive nanoparticles for targeting the tumor microenvironment. *J Control Release*, **2015**. 219: p. 205-214.

348. Overchuk, M., *et al.*, Overcoming obstacles in the tumor microenvironment: Recent advancements in nanoparticle delivery for cancer theranostics. *Biomaterials*, **2018**. 156: p. 217-237.

349. Jahanban-Esfahlan, R., *et al.*, Modulating tumor hypoxia by nanomedicine for effective cancer therapy. *J Cell Physiol*, **2018**. 233(3): p. 2019-2031.

350. Huang, W.C., *et al.*, Tumortropic monocyte-mediated delivery of echogenic polymer bubbles and therapeutic vesicles for chemotherapy of tumor hypoxia. *Biomaterials*, **2015**. 71: p. 71-83.

351. Huang, W.-C., *et al.*, Monocytic delivery of therapeutic oxygen bubbles for dual-modality treatment of tumor hypoxia. *J Control Release*, **2015**. 220, Part B: p. 738-750.

352. Luo, Z., *et al.*, Self-Monitoring Artificial Red Cells with Sufficient Oxygen Supply for Enhanced Photodynamic Therapy. *Sci Rep*, **2016**. 6: p. 23393.

353. Song, G., *et al.*, Perfluorocarbon-Loaded Hollow Bi2Se3 Nanoparticles for Timely Supply of Oxygen under Near-Infrared Light to Enhance the Radiotherapy of Cancer. *Adv Mater*, **2016**. 28(14): p. 2716-2723.

354. Xu, L., *et al.*, Liposome encapsulated perfluorohexane enhances radiotherapy in mice without additional oxygen supply. *J Transl Med*, **2016**. 14: p. 268.

355. Song, M., *et al.*, Bioconjugated Manganese Dioxide Nanoparticles Enhance Chemotherapy Response by Priming Tumor-Associated Macrophages toward M1-like Phenotype and Attenuating Tumor Hypoxia. *ACS Nano*, **2016**. 10(1): p. 633-647.

356. Chen, H., *et al.*, H2O2-Activatable and O2-Evolving Nanoparticles for Highly Efficient and Selective Photodynamic Therapy against Hypoxic Tumor Cells. *J Am Chem Soc*, **2015**. 137(4): p. 1539-1547.

357. Chen, Q., *et al.*, Intelligent Albumin-MnO2 Nanoparticles as pH-/H2 O2 -Responsive Dissociable Nanocarriers to Modulate Tumor Hypoxia for Effective Combination Therapy. *Adv Mater*, **2016**. 28(33): p. 7129-7136.

358. Poon, Z., *et al.*, Layer-by-layer nanoparticles with a pH-sheddable layer for in vivo targeting of tumor hypoxia. *ACS Nano*, **2011**. 5(6): p. 4284-4292.

359. Meng, H., *et al.*, Autonomous in Vitro Anticancer Drug Release from Mesoporous Silica Nanoparticles by pH-Sensitive Nanovalves. *J Am Chem Soc*, **2010**. 132(36): p. 12690-12697.

360. Liu, P., *et al.*, Tf-PEG-PLL-PLGA nanoparticles enhanced chemosensitivity for hypoxia-responsive tumor cells. *Onco Targets Ther*, **2016**. 9: p. 5049-5059.

361. Kulkarni, P., *et al.*, Hypoxia Responsive, Tumor Penetrating Lipid Nanoparticles for Delivery of Chemotherapeutics to Pancreatic Cancer Cell Spheroids. *Bioconjug Chem*, **2016**. 27(8): p. 1830-1838.

362. Liu, H.M., *et al.*, Hypoxia-responsive ionizable liposome delivery siRNA for glioma therapy. *Int J Nanomedicine*, **2017**. 12: p. 1065-1083.

363. Molina, A.M., *et al.*, Redox-sensitive cross-linking enhances albumin nanoparticle function as delivery system for photodynamic cancer therapy. *J Nanomed Nanotechnol*, **2016**. 6(3).

364. Qian, C., *et al.*, Light-Activated Hypoxia-Responsive Nanocarriers for Enhanced Anticancer Therapy. *Adv Mater*, **2016**. 28(17): p. 3313-3320.

365. Wang, Y., *et al.*, A novel cancer therapy: combined liposomal hypoxia inducible factor 1 alpha antisense oligonucleotides and an anticancer drug. *Biochem Pharmacol*, **2004**. 68(10): p. 2031-2042.

366. Luo, C.-H., *et al.*, Bacteria-Mediated Hypoxia-Specific Delivery of Nanoparticles for Tumors Imaging and Therapy. *Nano Lett*, **2016**. 16(6): p. 3493-3499.

367. Felfoul, O., *et al.*, Magneto-aerotactic bacteria deliver drug-containing nanoliposomes to tumour hypoxic regions. *Nature Nanotech*, **2016**. 11: p. 941.

368. Vinogradov, S., *et al.*, Macrophages associated with tumors as potential targets and therapeutic intermediates. *Nanomedicine* **2014**. 9(5): p. 695-707.

369. Choi, M.R., *et al.*, A cellular Trojan Horse for delivery of therapeutic nanoparticles into tumors. *Nano Lett*, **2007**. 7(12): p. 3759-3765.

370. Muthana, M., *et al.*, Use of macrophages to target therapeutic adenovirus to human prostate tumors. *Cancer Res*, **2011**. 71(5): p. 1805-1815.

371. Muthana, M., *et al.*, Macrophage delivery of an oncolytic virus abolishes tumor regrowth and metastasis after chemotherapy or irradiation. *Cancer Res*, **2013**. 73(2): p. 490-495.

372. Feng, L., *et al.*, Theranostic Liposomes with Hypoxia-Activated Prodrug to Effectively Destruct Hypoxic Tumors Post-Photodynamic Therapy. *ACS Nano*, **2017**. 11(1): p. 927-937.

373. Shen, S., *et al.*, Versatile hyaluronic acid modified AQ4N-Cu(II)-gossypol infinite coordination polymer nanoparticles: Multiple tumor targeting, highly efficient synergistic chemotherapy, and real-time self-monitoring. *Biomaterials*, **2018**. 154: p. 197-212.

374. Zhang, D., *et al.*, Smart Cu(II)-aptamer complexes based gold nanoplatform for tumor micro-environment triggered programmable intracellular prodrug release, photodynamic treatment and aggregation induced photothermal therapy of hepatocellular carcinoma. *Theranostics*, **2017**. 7(1): p. 164-179.

375. Zhang, R., *et al.*, Glucose & oxygen exhausting liposomes for combined cancer starvation and hypoxia-activated therapy. *Biomaterials*, **2018**. 162: p. 123-131.

376. Wu, L., *et al.*, Enhanced antitumor efficacy of cisplatin by tirapazamine-transferrin conjugate. *Int J Pharm*, **2012**. 431(1-2): p. 190-196.

377. Liu, X., *et al.*, The synergistic radiosensitizing effect of tirapazamine-conjugated gold nanoparticles on human hepatoma HepG2 cells under X-ray irradiation. *Int J Nanomedicine*, **2016**. 11: p. 3517-3531.

378. Yanyan, L., *et al.*, Hypoxia Induced by Upconversion-Based Photodynamic Therapy: Towards Highly Effective Synergistic Bioreductive Therapy in Tumors. *Angew Chem Int Ed Engl*, **2015**. 54(28): p. 8105-8109.

379. Chen, W.H., *et al.*, Mesoporous silica-based versatile theranostic nanoplatform constructed by layer-by-layer assembly for excellent photodynamic/chemo therapy. *Biomaterials*, **2017**. 117: p. 54-65.

380. Guo, D., *et al.*, Prodrug-embedded angiogenic vessel-targeting nanoparticle: A positive feedback amplifier in hypoxia-induced chemo-photo therapy. *Biomaterials*, **2017**. 144: p. 188-198.

381. Li, S.-Y., *et al.*, Cancer cell membrane-coated biomimetic platform for tumor targeted photodynamic therapy and hypoxia-amplified bioreductive therapy. *Biomaterials*, **2017**. 142: p. 149-161.

382. Wang, Y., *et al.*, Tumor-Penetrating Nanoparticles for Enhanced Anticancer Activity of Combined Photodynamic and Hypoxia-Activated Therapy. *ACS Nano*, **2017**. 11(2): p. 2227-2238.

383. Zhao, P., *et al.*, PL–W18O49–TPZ Nanoparticles for Simultaneous Hypoxia-Activated Chemotherapy and Photothermal Therapy. *ACS Appl Mater Interfaces*, **2018**. 10(4): p. 3405-3413.

384. Broekgaarden, M., *et al.*, Photodynamic Therapy with Liposomal Zinc Phthalocyanine and Tirapazamine Increases Tumor Cell Death via DNA Damage. *J Biomed Nanotechnol*, **2017**. 13(2): p. 204-220.

385. Dux, E.L., *The Development Of Transition Metal Complexes To Target Hypoxic Cells*, in *Department of Chemistry*. 2011, University of York. p. 538.

386. Fadeeva, V.P., *et al.*, Elemental analysis of organic compounds with the use of automated CHNS analyzers. *J Analyt Chem*, **2008**. 63(11): p. 1094-1106.

387. Mucciarone, D.A., and R. B. Dunba, Collection of CO2 for $^{13}C/^{13}C$ measurements and simultaneous C, H, N, and S analysis using an elemental analyze. *J Sediment Petrol*, **1992**. 62: p. 731-733.

388. Griffiths, P.R., *et al.*, Fourier Transform Infrared Spectrometry. **2007**: Wiley.

389. Kazarian, S.G., *et al.*, Applications of ATR-FTIR spectroscopic imaging to biomedical samples. *Biochim Biophys Acta-Biomembranes*, **2006**. 1758(7): p. 858-867.

390. Jocelyn Paré, J.R., *et al.*, Chapter 7 Mass spectrometry: Principles and applications, in Techniques and Instrumentation in Analytical Chemistry, J.R.J. Paré and J.M.R. Bélanger, Editors. **1997**, Elsevier. p. 239-266.

391. Singhal, N., *et al.*, MALDI-TOF mass spectrometry: an emerging technology for microbial identification and diagnosis. *Front Microbiol*, **2015**. 6: p. 791.

392. Valeur, B., *et al.*, Absorption of Ultraviolet, Visible, and Near-Infrared Radiation, in Molecular Fluorescence. **2012**, Wiley-VCH Verlag GmbH & Co. KGaA. p. 31-51.

393. Albani, J.R., Principles and Applications of Fluorescence Spectroscopy. **2008**: Wiley.

394. Lakowicz, J.R., Principles of fluorescence spectroscopy. **2007**: Springer Science & Business Media.

395. Lakowicz, J.R., Instrumentation for Fluorescence Spectroscopy, in Principles of Fluorescence Spectroscopy. **1983**, Springer US: Boston, MA. p. 19-49.

396. Egerton, R.F., *Physical Principles of Electron Microscopy*, in *An Introduction to TEM, SEM, and AEM*. 2005, Springer US.

397. Bélanger, J.M.R., *et al.*, Chapter 2 High performance liquid chromatography (HPLC): Principles and applications, in Techniques and Instrumentation in Analytical Chemistry, J.R.J. Paré and J.M.R. Bélanger, Editors. **1997**, Elsevier. p. 37-59.

398. Walton, M.I., *et al.*, High-performance liquid chromatographic assay for the benzotriazine di-N-oxide (SR 4233) and its reduced metabolites in biological materials. *J Chromatogr*, **1988**. 430(2): p. 429-437.

399. Leo, A., *et al.*, Calculation of hydrophobic constant (log P) from .pi. and f constants. *J Med Chem*, **1975**. 18(9): p. 865-868.

400. Mui, B., *et al.*, Extrusion technique to generate liposomes of defined size. *Methods Enzymol*, **2003**. 367: p. 3-14.

401. Fritze, A., *et al.*, Remote loading of doxorubicin into liposomes driven by a transmembrane phosphate gradient. *Biochim Biophys Acta-Biomembranes*, **2006**. 1758(10): p. 1633-1640.

402. Li, C., *et al.*, Copper ion-mediated liposomal encapsulation of mitoxantrone: the role of anions in drug loading, retention and release. *Eur J Pharm Sci*, **2008**. 34(4-5): p. 333-344.

403. Abraham, S.A., *et al.*, An evaluation of transmembrane ion gradient-mediated encapsulation of topotecan within liposomes. *J Control Release*, **2004**. 96(3): p. 449-461.

404. Pecora, R., Dynamic light scattering: applications of photon correlation spectroscopy. **1985**: Springer Science & Business Media.

405. Uskokovic, V., Dynamic Light Scattering Based Microelectrophoresis: Main Prospects and Limitations. *J Dispers Sci Technol*, **2012**. 33(12): p. 1762-1786.

406. Danaei, M., *et al.*, Impact of Particle Size and Polydispersity Index on the Clinical Applications of Lipidic Nanocarrier Systems. *Pharmaceutics*, **2018**. 10(2).

407. Gittings, M.R., *et al.*, The determination of hydrodynamic size and zeta potential from electrophoretic mobility and light scattering measurements. *Colloids Surf A Physicochem Eng Asp*, **1998**. 141(1): p. 111-117.

408. Stewart, J.C.M., Colorimetric determination of phospholipids with ammonium ferrothiocyanate. *Anal Biochem*, **1980**. 104(1): p. 10-14.

409. Liu, G.X., *et al.*, Dual targeting biomimetic liposomes for paclitaxel/DNA combination cancer treatment. *Int J Mol Sci*, **2014**. 15(9): p. 15287-15303.

410. Gibco, *Cell Culture Basics Handbook*. 2015, Thermo Fisher Scientific.

411. Cunningham, D., *et al.*, In vitro and in vivo model systems used in prostate cancer research. *J Biol Methods*, **2015**. 2(1).

412. Russell P.J., K.E.A., *Prostate Cancer Methods and Protocols. Methods in Molecular Medicine*, in *Prostate cancer methods and protocols*, P.J. Pamela J. Russell, Elizabeth A. Kingsley, Editor. 2003, Springer New York: Springer, Totowa, NJ.

413. Wu, X., *et al.*, Current mouse and cell models in prostate cancer research. *Endocr Relat Cancer*, **2013**. 20(4): p. R155-170.

414. Wu, D., *et al.*, Induction and testing of hypoxia in cell culture. *J Vis Exp*, **2011**(54).

415. Apte, S., *et al.*, Molecular Imaging of Hypoxia: Strategies for Probe Design and Application. *Curr Org Synth*, **2011**. 8(4): p. 593-603.

416. Sciences, E.L., *ROS-ID® Hypoxia/Oxidative Stress Detection Kit*, in *Product Manual*.

417. Vega-Avila, E., *et al.*, An overview of colorimetric assay methods used to assess survival or proliferation of mammalian cells. *Proc West Pharmacol Soc*, **2011**. 54: p. 10-14.

418. O'Brien, J., *et al.*, Investigation of the Alamar Blue (resazurin) fluorescent dye for the assessment of mammalian cell cytotoxicity. *Eur J Biochem*, **2000**. 267(17): p. 5421-5426.

419. Walzl, A., *et al.*, The Resazurin Reduction Assay Can Distinguish Cytotoxic from Cytostatic Compounds in Spheroid Screening Assays. *J Biomol Screen*, **2014**. 19(7): p. 1047-1059.

420. Meenongwa, A., *et al.*, DNA-interacting and biological properties of copper(ii) complexes from amidino-O-methylurea. *New J Chem*, **2015**. 39(1): p. 664-675.

421. Kathiresan, S., *et al.*, Mixed-ligand copper(ii)-phenolate complexes: structure and studies on DNA/protein binding profiles, DNA cleavage, molecular docking and cytotoxicity. *RSC Advances*, **2016**. 6(3): p. 1810-1825.

422. Shahabadi, N., *et al.*, DNA binding affinity of a macrocyclic copper(II) complex: Spectroscopic and molecular docking studies. *Nucleosides Nucleotides Nucleic Acids*, **2017**. 36(8): p. 497-510.

423. Hirschhaeuser, F., *et al.*, Multicellular tumor spheroids: an underestimated tool is catching up again. *J Biotechnol*, **2010**. 148(1): p. 3-15.

424. Mikhail, A.S., *et al.*, Multicellular Tumor Spheroids for Evaluation of Cytotoxicity and Tumor Growth Inhibitory Effects of Nanomedicines In Vitro: A Comparison of Docetaxel-Loaded Block Copolymer Micelles and Taxotere®. *PLOS ONE*, **2013**. 8(4): p. e62630.

425. Zanoni, M., *et al.*, 3D tumor spheroid models for in vitro therapeutic screening: a systematic approach to enhance the biological relevance of data obtained. *Sci Rep*, **2016**. 6: p. 19103.

426. Achilli, T.M., *et al.*, Advances in the formation, use and understanding of multi-cellular spheroids. *Expert Opin Biol Ther*, **2012**. 12(10): p. 1347-1360.

427. Ivanov, D.P., *et al.*, Multiplexing Spheroid Volume, Resazurin and Acid Phosphatase Viability Assays for High-Throughput Screening of Tumour Spheroids and Stem Cell Neurospheres. *PLOS ONE*, **2014**. 9(8): p. e103817.

428. Amaral, R.L.F., *et al.*, Comparative Analysis of 3D Bladder Tumor Spheroids Obtained by Forced Floating and Hanging Drop Methods for Drug Screening. *Front Physiol*, **2017**. 8: p. 605.

429. Brown, M., *et al.*, Flow cytometry: principles and clinical applications in hematology. *Clin Chem*, **2000**. 46(8 Pt 2): p. 1221-1229.

430. Flow Cytometry Facility, U.o.I.

431. Darzynkiewicz, Z., *et al.*, Flow cytometry in analysis of cell cycle and apoptosis. *Semin Hematol*, **2001**. 38(2): p. 179-193.

432. Ormerod, M.G., Consensus on DNA analysis by flow cytometry **2008**, De Novo Software

433. Pozarowski, P., *et al.*, Analysis of cell cycle by flow cytometry. *Methods Mol Biol*, **2004**. 281: p. 301-311.

434. Priyadarsini, K.I., *et al.*, The one-electron reduction potential of 3-amino-1,2,4-benzotriazine 1,4-dioxide (tirapazamine): a hypoxia-selective bioreductive drug. *Free Radic Res*, **1996**. 25(5): p. 393-399.

435. Hicks, K.O., *et al.*, Extravascular diffusion of tirapazamine: effect of metabolic consumption assessed using the multicellular layer model. *Int J Radiat Oncol Biol Phys*, **1998**. 42(3): p. 641-649.

436. Poole, J.S., *et al.*, Photochemical electron transfer reactions of tirapazamine. *Photochem Photobiol*, **2002**. 75(4): p. 339-345.

437. Shi, X., *et al.*, Time-resolved spectroscopy of the excited singlet states of tirapazamine and desoxytirapazamine. *J Phys Chem A*, **2005**. 109(8): p. 1491-1496.

438. Inbaraj, J.J., *et al.*, Photochemical and Photobiological Studies of Tirapazamine (SR 4233) and Related Quinoxaline 1,4-Di-N-oxide Analogues. *Chem Res Toxicol*, **2003**. 16(2): p. 164-170.

439. Zagorevskii, D., *et al.*, A mass spectrometry study of tirapazamine and its metabolites. insights into the mechanism of metabolic transformations and the characterization of reaction intermediates. *J Am Soc Mass Spectrom*, **2003**. 14(8): p. 881-892.

440. McLaughlin, K.J., *et al.*, Microdialysis sampling with on-line microbore HPLC for the determination of tirapazamine and its reduced metabolites in rats. *Analyst*, **2000**. 125(1): p. 105-110.

441. Zeman, E.M., *et al.*, Structure-activity relationships for benzotriazine di-N-oxides. *Int J Radiat Oncol Biol Phys*, **1989**. 16(4): p. 977-981.

442. Kelson, A.B., *et al.*, 1,2,4-Benzotriazine 1,4-dioxides. An important class of hypoxic cytotoxins with antitumor activity. *Anticancer Drug Des*, **1998**. 13(6): p. 575-592.

443. Denny, W.A., Prodrug strategies in cancer therapy. *Eur J Med Chem*, **2001**. 36(7-8): p. 577-595.

444. Chen, Y., *et al.*, Design of anticancer prodrugs for reductive activation. *Medicinal Research Reviews*, **2009**. 29(1): p. 29-64.

445. Olalekan, T.E., *et al.*, Copper(II) Complexes of 2-(Methylthiomethyl)anilines: Spectral and Structural Properties and In Vitro Antimicrobial Activity. *J Inorg Biochem*, **2014**. 2014: p. 10.

446. Bist, H.D., *et al.*, The 341 nm band system of pyridine-N-oxide. Analysis of the in-plane vibrational structure. *J Mol Spectrosc*, **1976**. 59(3): p. 435-441.

447. Valderrama-Negrón, A.C., *et al.*, Synthesis, spectroscopic characterization and radiosensitizing properties of acetato-bridged copper(II) complexes with 5-nitroimidazole drugs. *Inorganica Chim Acta*, **2011**. 367(1): p. 85-92.

448. Kheirolomoom, A., *et al.*, Copper-doxorubicin as a nanoparticle cargo retains efficacy with minimal toxicity. *Mol pharm*, **2010**. 7(6): p. 1948-1958.

449. Kim, E.Y., *et al.*, Preliminary studies with a new hypoxia-selective cytotoxin, KS119W, in vitro and in vivo. *Radiat Res*, **2012**. 178(3): p. 126-137.

450. Skarsgard, L.D., *et al.*, The effect of pH on the aerobic and hypoxic cytotoxicity of SR4233 in HT-29 cells. *Br J Cancer*, **1993**. 68(4): p. 681-683.

451. Domaille, D.W., *et al.*, Visualizing Ascorbate-Triggered Release of Labile Copper within Living Cells using a Ratiometric Fluorescent Sensor. *J Am Chem Soc*, **2010**. 132(4): p. 1194-1195.

452. Que, E.L., *et al.*, Metals in Neurobiology: Probing Their Chemistry and Biology with Molecular Imaging. *Chem Rev*, **2008**. 108(5): p. 1517-1549.

453. Dean, K.M., *et al.*, Visualizing metal ions in cells: An overview of analytical techniques, approaches, and probes. *Biochim Biophys Acta-General Subjects-Mol Cell Res*, **2012**. 1823(9): p. 1406-1415.

454. Xu, Z., *et al.*, Ratiometric and Selective Fluorescent Sensor for CuII Based on Internal Charge Transfer (ICT). *Org Lett*, **2005**. 7(5): p. 889-892.

455. L. J. Dearling, J., *et al.*, Redox-active metal complexes for imaging hypoxic tissues: structure-activity relationships in copper(II) bis(thiosemicarbazone) complexes. *Chem Comm*, **1998**(22): p. 2531-2532.

456. Hickey, J.L., *et al.*, Intracellular Distribution of Fluorescent Copper and Zinc Bis(thiosemicarbazonato) Complexes Measured with Fluorescence Lifetime Spectroscopy. *Inorg Chem*, **2015**. 54(19): p. 9556-9567.

457. Eros, D., *et al.*, Reliability of Log P Predictions Based on Calculated Molecular Descriptors: A Critical Review. *Curr Med Chem*, **2002**. 9(20): p. 1819-1829.

458. Machatha, S.G., *et al.*, Comparison of the octanol/water partition coefficients calculated by CLog P®, ACDLog P and KowWin® to experimentally determined values. *Int J Pharm*, **2005**. 294(1): p. 185-192.

459. Kate, A.N., *et al.*, Monitoring Cellular Uptake and Cytotoxicity of Copper(II) Complex Using a Fluorescent Anthracene Thiosemicarbazone Ligand. *Bioconjug Chem*, **2014**. 25(1): p. 102-114.

460. Monge, A., *et al.*, Hypoxia-Selective Agents Derived from Quinoxaline 1,4-Di-N-oxides. *J Med Chem*, **1995**. 38(10): p. 1786-1792.

461. Husanu, E., *et al.*, Chiral ionic liquid assisted synthesis of some metal oxides. *RSC Advances*, **2017**. 7(2): p. 1154-1160.

462. Hicks, K.O., *et al.*, Multicellular resistance to tirapazamine is due to restricted extravascular transport: a pharmacokinetic/pharmacodynamic study in HT29 multicellular layer cultures. *Cancer Res*, **2003**. 63(18): p. 5970-5977.

463. Liu, H., *et al.*, Development of hypoxia-triggered prodrug micelles as doxorubicin carriers for tumor therapy. *RSC Advances*, **2015**. 5(27): p. 20848-20857.

464. Liu, Y., *et al.*, Hypoxia Induced by Upconversion-Based Photodynamic Therapy: Towards Highly Effective Synergistic Bioreductive Therapy in Tumors. *Angew Chem Int Ed Engl*, **2015**. 54(28): p. 8105-8109.

465. Albertella, M.R., *et al.*, Hypoxia-selective targeting by the bioreductive prodrug AQ4N in patients with solid tumors: results of a phase I study. *Clin Cancer Res*, **2008**. 14(4): p. 1096-1104.

466. Drummond, D.C., *et al.*, Optimizing liposomes for delivery of chemotherapeutic agents to solid tumors. *Pharmacol Rev*, **1999**. 51(4): p. 691-743.

467. Gregoriadis, G., Liposomes in Drug Delivery: How It All Happened. *Pharmaceutics*, **2016**. 8(2): p. 19.

468. Subongkot, T., *et al.*, Effect of liposomal fluidity on skin permeation of sodium fluorescein entrapped in liposomes. *Int J Nanomedicine*, **2015**. 10: p. 4581-4592.

469. Soema, P.C., *et al.*, Predicting the influence of liposomal lipid composition on liposome size, zeta potential and liposome-induced dendritic cell maturation using a design of experiments approach. *Eur J Pharm Biopharm*, **2015**. 94: p. 427-435.

470. Modi, S., *et al.*, Determination of drug release kinetics from nanoparticles: overcoming pitfalls of the dynamic dialysis method. *Mol Pharm*, **2013**. 10(8): p. 3076-3089.

471. Eloy, J.O., *et al.*, Liposomes as carriers of hydrophilic small molecule drugs: strategies to enhance encapsulation and delivery. *Colloids Surf B Biointerfaces*, **2014**. 123: p. 345-363.

472. Wehbe, M., *et al.*, A simple passive equilibration method for loading carboplatin into pre-formed liposomes incubated with ethanol as a temperature dependent permeability enhancer. *J Control Release*, **2017**. 252: p. 50-61.

473. Batzri, S., *et al.*, Single bilayer liposomes prepared without sonication. *Biochim Biophys Acta-Biomembranes*, **1973**. 298(4): p. 1015-1019.

474. Haran, G., *et al.*, Transmembrane ammonium sulfate gradients in liposomes produce efficient and stable entrapment of amphipathic weak bases. *Biochim Biophys Acta-Biomembranes*, **1993**. 1151(2): p. 201-215.

475. Zucker, D., *et al.*, Liposome drugs' loading efficiency: a working model based on loading conditions and drug's physicochemical properties. *J Control Release*, **2009**. 139(1): p. 73-80.

476. Modi, S., *et al.*, Enhanced active liposomal loading of a poorly soluble ionizable drug using supersaturated drug solutions. *J Control Release*, **2012**. 162(2): p. 330-339.

477. Taggar, A.S., *et al.*, Copper-topotecan complexation mediates drug accumulation into liposomes. *J Control Release*, **2006**. 114(1): p. 78-88.

478. Ramsay, E., *et al.*, Transition Metal-Mediated Liposomal Encapsulation of Irinotecan (CPT-11) Stabilizes the Drug in the Therapeutically Active Lactone Conformation. *Pharm Res*, **2006**. 23(12): p. 2799-2808.

479. Ramsay, E., *et al.*, A novel liposomal irinotecan formulation with significant anti-tumour activity: use of the divalent cation ionophore A23187 and copper-containing liposomes to improve drug retention. *Eur J Pharm Biopharm*, **2008**. 68(3): p. 607-617.

480. Petersen, A.L., *et al.*, 64Cu loaded liposomes as positron emission tomography imaging agents. *Biomaterials*, **2011**. 32(9): p. 2334-2341.

481. Henriksen, J.R., *et al.*, Remote Loading of 64Cu2+ into Liposomes without the Use of Ion Transport Enhancers. *ACS Appl Mater Interfaces*, **2015**. 7(41): p. 22796-22806.

482. Wolfram, J., *et al.*, Evaluation of anticancer activity of celastrol liposomes in prostate cancer cells. *J Microencapsul*, **2014**. 31(5): p. 501-507.

483. Moghaddam, B., *et al.*, The application of monolayer studies in the understanding of liposomal formulations. *Int J Pharm*, **2011**. 417(1): p. 235-244.

484. Mohanraj, V., *et al.*, Nanoparticles-a review. *Trop J Pharm Res*, **2007**. 5(1): p. 561-573.

485. Bunker, A., Poly(Ethylene Glycol) in Drug Delivery, Why Does it Work, and Can We do Better? All Atom Molecular Dynamics Simulation Provides Some Answers. *Physics Procedia*, **2012**. 34: p. 24-33.

486. Dzieciuch, M., *et al.*, PEGylated Liposomes as Carriers of Hydrophobic Porphyrins. *J Phys Chem B*, **2015**. 119(22): p. 6646-6657.

487. Zhen Pan, S., *et al.*, Noncovalent interaction of polyethylene glycol with copper complex of ethylenediaminetetraacetic acid and its application in constructing inorganic nanomaterials. *Dalton Trans*, **2011**. 40(39): p. 10117-10124.

488. Han, H.-K., *et al.*, Improved oral bioavailability of alendronate via the mucoadhesive liposomal delivery system. *Eur J Pharm Sci*, **2012**. 46(5): p. 500-507.

489. Johnston, M.J., *et al.*, Therapeutically optimized rates of drug release can be achieved by varying the drug-to-lipid ratio in liposomal vincristine formulations. *Biochim Biophys Acta*, **2006**. 1758(1): p. 55-64.

490. Zhigaltsev, I.V., *et al.*, Liposome-encapsulated vincristine, vinblastine and vinorelbine: A comparative study of drug loading and retention. *J Control Release*, **2005**. 104(1): p. 103-111.

491. Cullis, P.R., *et al.*, Influence of pH gradients on the transbilayer transport of drugs, lipids, peptides and metal ions into large unilamellar vesicles. *Biochim Biophys Acta-General Subjects-Rev Biomembranes*, **1997**. 1331(2): p. 187-211.

492. Zambito, Y., *et al.*, Is dialysis a reliable method for studying drug release from nanoparticulate systems?—A case study. *Int J Pharm*, **2012**. 434(1): p. 28-34.

493. Abouelmagd, S.A., *et al.*, Release kinetics study of poorly water-soluble drugs from nanoparticles: are we doing it right? *Mol Pharm*, **2015**. 12(3): p. 997-1003.

494. Gou, Y., *et al.*, Developing Anticancer Copper(II) Pro-drugs Based on the Nature of Cancer Cells and the Human Serum Albumin Carrier IIA Subdomain. *Mol Pharm*, **2015**. 12(10): p. 3597-3609.

495. Bonté, F., *et al.*, Interactions of liposomes with serum proteins. *Chem Phys Lipids*, **1986**. 40(2): p. 359-372.

496. Allen, T.M., *et al.*, Serum-induced leakage of liposome contents. *Biochim Biophys Acta-Biomembranes*, **1980**. 597(2): p. 418-426.

497. Wolfram, J., *et al.*, Shrinkage of pegylated and non-pegylated liposomes in serum. *Colloids Surf B Biointerfaces*, **2014**. 114: p. 294-300.

498. Glavas-Dodov, M., *et al.*, The effects of lyophilization on the stability of liposomes containing 5-FU. *Int J Pharm*, **2005**. 291(1): p. 79-86.

499. Hosta-Rigau, L., *et al.*, Recent progress of liposomes in nanomedicine. *J Mater Chem B*, **2014**. 2(39): p. 6686-6691.

500. Leong, D.T., *et al.*, Probing the relevance of 3D cancer models in nanomedicine research. *Adv Drug Deliv Rev*, **2014**. 79-80: p. 95-106.

501. Mehta, G., *et al.*, Opportunities and challenges for use of tumor spheroids as models to test drug delivery and efficacy. *J Control Release*, **2012**. 164(2): p. 192-204.

502. Hamilton, G., Multicellular spheroids as an in vitro tumor model. *Cancer Lett*, **1998**. 131(1): p. 29-34.

503. Kimlin, L.C., *et al.*, In vitro three-dimensional (3D) models in cancer research: an update. *Mol Carcinog*, **2013**. 52(3): p. 167-182.

504. Kunz-Schughart, L.A., *et al.*, The use of 3-D cultures for high-throughput screening: the multicellular spheroid model. *J Biomol Screen*, **2004**. 9(4): p. 273-285.

505. Tung, Y.-C., *et al.*, High-throughput 3D spheroid culture and drug testing using a 384 hanging drop array. *Analyst*, **2011**. 136(3): p. 473-478.

506. Millard, M., *et al.*, Drug delivery to solid tumors: the predictive value of the multicellular tumor spheroid model for nanomedicine screening. *Int J Nanomedicine*, **2017**. 12: p. 7993-8007.

507. Wang, J., *et al.*, All-in-One Theranostic Nanoplatform Based on Hollow MoSx for Photothermally-maneuvered Oxygen Self-enriched Photodynamic Therapy. *Theranostics*, **2018**. 8(4): p. 955-971.

508. Liu, C.P., *et al.*, Self-Supplying O2 through the Catalase-Like Activity of Gold Nanoclusters for Photodynamic Therapy against Hypoxic Cancer Cells. *Small*, **2017**. 13(26): p. 1700278.

509. Sobel, R., *et al.*, Cell lines used in prostate cancer research: a compendium of old and new lines—part 1. *J Urol*, **2005**. 173(2): p. 342-359.

510. Sobel, R., *et al.*, Cell lines used in prostate cancer research: a compendium of old and new lines—part 2. *J Urol*, **2005**. 173(2): p. 360-372.

511. Russell, P.J., *et al.*, Human prostate cancer cell lines. *Methods Mol Med*, **2003**. 81: p. 21-39.

512. Horoszewicz, J.S., *et al.*, The LNCaP cell line--a new model for studies on human prostatic carcinoma. *Prog Clin Biol Res*, **1980**. 37: p. 115-132.

513. Thalmann, G.N., *et al.*, Androgen-independent cancer progression and bone metastasis in the LNCaP model of human prostate cancer. *Cancer Res*, **1994**. 54(10): p. 2577-2581.

514. Wu, H.C., *et al.*, Derivation of androgen-independent human LNCaP prostatic cancer cell sublines: role of bone stromal cells. *Int J Cancer*, **1994**. 57(3): p. 406-412.

515. Kaighn, M.E., *et al.*, Establishment and characterization of a human prostatic carcinoma cell line (PC-3). *Invest Urol*, **1979**. 17(1): p. 16-23.

516. Stone, K.R., *et al.*, Isolation of a human prostate carcinoma cell line (DU 145). *Int J Cancer*, **1978**. 21(3): p. 274-281.

517. Carroll, A.G., *et al.*, p53 oncogene mutations in three human prostate cancer cell lines. *Prostate*, **1993**. 23(2): p. 123-134.

518. Higgins, L.H., *et al.*, Hypoxia and the metabolic phenotype of prostate cancer cells. *Biochim Biophys Acta-Bioenergetics*, **2009**. 1787(12): p. 1433-1443.

519. Ta, H.Q., *et al.*, The convergence of DNA damage checkpoint pathways and androgen receptor signalling in prostate cancer. *Endocr Relat Cancer*, **2014**. 21(5): p. R395-407.

520. Lin, D.L., *et al.*, Bone metastatic LNCaP-derivative C4-2B prostate cancer cell line mineralizes in vitro. *The Prostate*, **2001**. 47(3): p. 212-221.

521. Espinoza, I., *et al.*, Hypoxia on the Expression of Hepatoma Upregulated Protein in Prostate Cancer Cells. *Front Oncol*, **2016**. 6: p. 144.

522. Jayakumar, S., *et al.*, Differential response of DU145 and PC3 prostate cancer cells to ionizing radiation: role of reactive oxygen species, GSH and Nrf2 in radiosensitivity. *Biochim Biophys Acta*, **2014**. 1840(1): p. 485-494.

523. Patterson, A.V., *et al.*, Mechanism of action and preclinical antitumor activity of the novel hypoxia-activated DNA cross-linking agent PR-104. *Clin Cancer Res*, **2007**. 13(13): p. 3922-3932.

524. Ravenna, L., *et al.*, Distinct Phenotypes of Human Prostate Cancer Cells Associate with Different Adaptation to Hypoxia and Pro-Inflammatory Gene Expression. *PLOS ONE*, **2014**. 9(5): p. e96250.

525. Yang, B., *et al.*, Tirapazamine cytotoxicity for neuroblastoma is p53 dependent. *Clin Cancer Res*, **2005**. 11(7): p. 2774-2780.

526. Wouters, B.G., *et al.*, Tirapazamine: a new drug producing tumor specific enhancement of platinum-based chemotherapy in non-small-cell lung cancer. *Ann Oncol*, **1999**. 10 Suppl 5: p. S29-33.

527. Nagasawa, H., *et al.*, Design, synthesis and biological activities of antiangiogenic hypoxic cytotoxin, triazine-N-oxide derivatives. *Comp Biochem Physiol A Mol Integr Physiol*, **2002**. 132(1): p. 33-40.

528. Saunders, M.P., *et al.*, NADPH:cytochrome c (P450) reductase activates tirapazamine (SR4233) to restore hypoxic and oxic cytotoxicity in an aerobic resistant derivative of the A549 lung cancer cell line. *Br J Cancer*, **2000**. 82(3): p. 651-656.

529. Skarsgard, L.D., *et al.*, The effect of low pH and hypoxia on the cytotoxic effects of SR4233 and mitomycin C in vitro. *Int J Radiat Oncol Biol Phys*, **1994**. 29(2): p. 363-367.

530. Evans, J.W., *et al.*, Homologous recombination is the principal pathway for the repair of DNA damage induced by tirapazamine in mammalian cells. *Cancer Res*, **2008**. 68(1): p. 257-265.

531. Meng, A.X., *et al.*, Hypoxia down-regulates DNA double strand break repair gene expression in prostate cancer cells. *Radiother Oncol*, **2005**. 76(2): p. 168-176.

532. Cater, M.A., *et al.*, Increasing Intracellular Bioavailable Copper Selectively Targets Prostate Cancer Cells. *ACS Chem Biol*, **2013**. 8(7): p. 1621-1631.

533. Lim, S., *et al.*, Copper and zinc bis(thiosemicarbazonato) complexes with a fluorescent tag: synthesis, radiolabelling with copper-64, cell uptake and fluorescence studies. *J Biol Inorg Chem*, **2010**. 15(2): p. 225-235.

534. Pascu, S.I., *et al.*, Fluorescent Copper(II) Bis(thiosemicarbazonates): Synthesis, Structures, Electron Paramagnetic Resonance, Radiolabeling, In Vitro Cytotoxicity and Confocal Fluorescence Microscopy Studies. *Chem – An Asian J*, **2010**. 5(3): p. 506-519.

535. Illien, F., *et al.*, Quantitative fluorescence spectroscopy and flow cytometry analyses of cell-penetrating peptides internalization pathways: optimization, pitfalls, comparison with mass spectrometry quantification. *Sci Rep*, **2016**. 6: p. 36938.

536. Marjanovic, I., *et al.*, Comparison of flow cytometry, fluorescence microscopy and spectrofluorometry for analysis of gene electrotransfer efficiency. *J Membr Biol*, **2014**. 247(12): p. 1259-1267.

537. Delahoussaye, Y.M., *et al.*, Improved potency of the hypoxic cytotoxin tirapazamine by DNA-targeting. *Biochem Pharmacol*, **2003**. 65(11): p. 1807-1815.

538. Puapermpoonsiri, U., *et al.*, Synergistic Effect of Phospholipid-Based Liposomes and Propylthiouracil on U-937 Cell Growth. *J Liposome Res*, **2005**. 15(3-4): p. 215-227.

539. Shah, V.M., *et al.*, Characterization of pegylated and non-pegylated liposomal formulation for the delivery of hypoxia activated vinblastine-N-oxide for the treatment of solid tumors. *J Control Release*, **2017**. 253: p. 37-45.

540. Xu, X., *et al.*, Three-dimensional in vitro tumor models for cancer research and drug evaluation. *Biotechnol Adv*, **2014**. 32(7): p. 1256-1268.

541. Page, H., *et al.*, Three-dimensional tissue cultures: current trends and beyond. *Cell Tissue Res*, **2013**. 352(1): p. 123-131.

542. Hedlund, T.E., *et al.*, Three-dimensional spheroid cultures of human prostate cancer cell lines. *Prostate*, **1999**. 41(3): p. 154-165.

543. Chambers, K.F., *et al.*, 3D Cultures of Prostate Cancer Cells Cultured in a Novel High-Throughput Culture Platform Are More Resistant to Chemotherapeutics Compared to Cells Cultured in Monolayer. *PLOS ONE*, **2014**. 9(11): p. e111029.

544. Mosaad, E.O., *et al.*, The Microwell-mesh: A high-throughput 3D prostate cancer spheroid and drug-testing platform. *Sci Rep*, **2018**. 8(1): p. 253.

545. Barisam, M., *et al.*, Prediction of Necrotic Core and Hypoxic Zone of Multicellular Spheroids in a Microbioreactor with a U-Shaped Barrier. *Micromachines*, **2018**. 9(3): p. 94.

546. Grimes, D.R., *et al.*, A method for estimating the oxygen consumption rate in multicellular tumour spheroids. *J R Soc Interface*, **2014**. 11(92).

547. Larson, B., *et al.*, *Inhibition of Hypoxic Tumor Cells using a Three-Dimensional Spheroid Model*, in *Application Note: Enzo Life Sciences*. 2014.

548. Kyle, A.H., *et al.*, Measurement of delivery and metabolism of tirapazamine to tumour tissue using the multilayered cell culture model. *Cancer Chemother Pharmacol*, **1999**. 43(3): p. 213-220.

549. Durand, R.E., *et al.*, Evaluation of bioreductive drugs in multicell spheroids. *Int J Radiat Oncol Biol Phys*, **1992**. 22(4): p. 689-692.

550. Maurer, R.I., *et al.*, Studies on the Mechanism of Hypoxic Selectivity in Copper Bis(Thiosemicarbazone) Radiopharmaceuticals. *J Med Chem*, **2002**. 45(7): p. 1420-1431.

551. Mahendiran, D., *et al.*, Copper complexes as prospective anticancer agents: in vitro and in vivo evaluation, selective targeting of cancer cells by DNA damage and S phase arrest. *RSC Advances*, **2018**. 8(30): p. 16973-16990.

552. Kostas, K., *et al.*, Binding and interstitial penetration of liposomes within avascular tumor spheroids. *Int J Cancer*, **2004**. 112(4): p. 713-721.

553. Takechi-Haraya, Y., *et al.*, Control of Liposomal Penetration into Three-Dimensional Multicellular Tumor Spheroids by Modulating Liposomal Membrane Rigidity. *Mol Pharm*, **2017**. 14(6): p. 2158-2165.

554. Kostarelos, K., *et al.*, Engineering Lipid Vesicles of Enhanced Intratumoral Transport Capabilities: Correlating Liposome Characteristics with Penetration into Human Prostate Tumor Spheroids. *J Liposome Res*, **2005**. 15(1-2): p. 15-27.

555. Gao, Y., *et al.*, Predictive Models of Diffusive Nanoparticle Transport in 3-Dimensional Tumor Cell Spheroids. *The AAPS Journal*, **2013**. 15(3): p. 816-831.

556. Lee, H., *et al.*, Adsorption of Plasma Proteins onto PEGylated Lipid Bilayers: The Effect of PEG Size and Grafting Density. *Biomacromolecules*, **2016**. 17(5): p. 1757-1765.

557. Yu, M.K., *et al.*, Targeting Strategies for Multifunctional Nanoparticles in Cancer Imaging and Therapy. *Theranostics*, **2012**. 2(1): p. 3-44.

558. Patel, A., *et al.*, Hypoxic tumor microenvironment: Opportunities to develop targeted therapies. *Biotechnol Adv*, **2016**. 34(5): p. 803-812.

559. Denoyer, D., *et al.*, Copper Complexes in Cancer Therapy. *Met Ions Life Sci*, **2018**. 18.

560. Renfrew, A.K., Transition metal complexes with bioactive ligands: mechanisms for selective ligand release and applications for drug delivery. *Metallomics*, **2014**. 6(8): p. 1324-1335.

561. Demetzos, C., Differential Scanning Calorimetry (DSC): a tool to study the thermal behavior of lipid bilayers and liposomal stability. *J Liposome Res*, **2008**. 18(3): p. 159-173.

562. Rangel, M., *et al.*, Distinctive EPR signals provide an understanding of the affinity of bis-(3-hydroxy-4-pyridinonato) copper(II) complexes for hydrophobic environments. *Dalton Trans*, **2014**. 43(25): p. 9722-9731.

563. Holland, J.P., *et al.*, Assessing tumor hypoxia by positron emission tomography with Cu-ATSM. *Q J Nucl Med Mol Imaging*, **2009**. 53(2): p. 193-200.

564. Xiao, Z., *et al.*, Transfer of copper between bis(thiosemicarbazone) ligands and intracellular copper-binding proteins. insights into mechanisms of copper uptake and hypoxia selectivity. *Inorg Chem*, **2008**. 47(10): p. 4338-4347.

565. Wehbe, M., *et al.*, A Perspective – can copper complexes be developed as a novel class of therapeutics? *Dalton Trans*, **2017**. 46(33): p. 10758-10773.

566. Wehbe, M., *et al.*, Nanoscale Reaction Vessels Designed for Synthesis of Copper-Drug Complexes Suitable for Preclinical Development. *PLOS ONE*, **2016**. 11(4): p. e0153416.

567. Shah, Z., *et al.*, The anticancer drug tirapazamine has antimicrobial activity against Escherichia coli, Staphylococcus aureus and Clostridium difficile. *FEMS Microbiol Lett*, **2013**. 347(1): p. 61-69.

Appendix

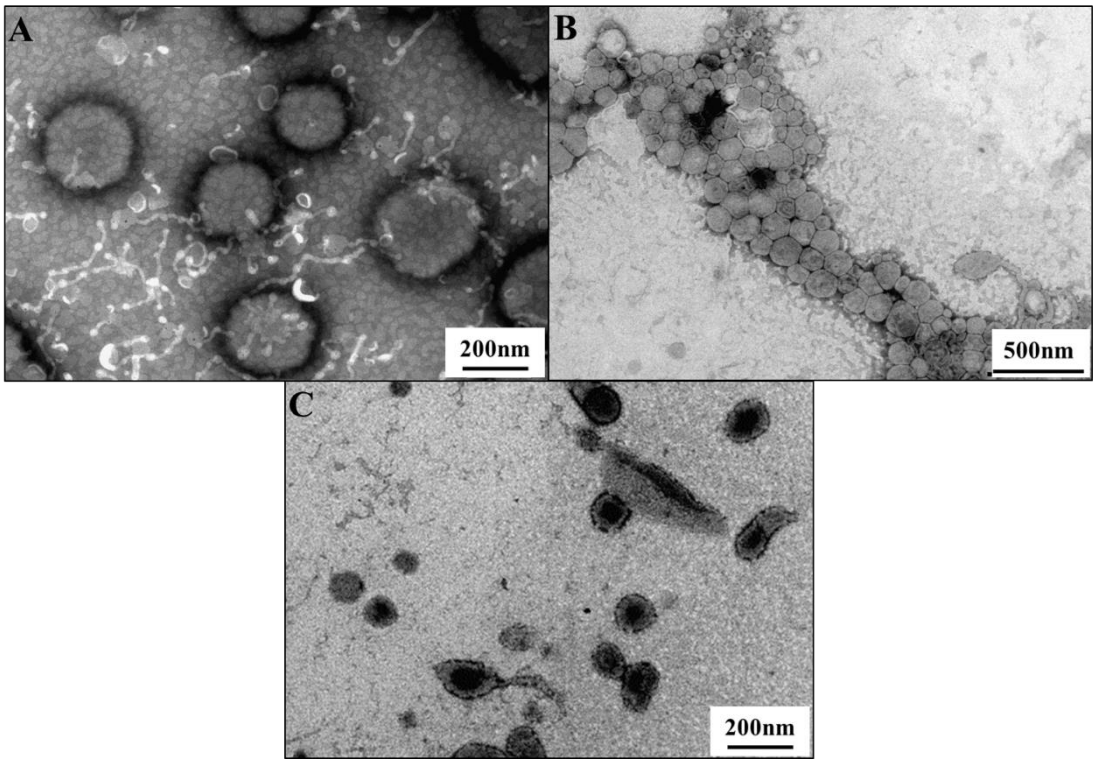

Figure A1. Structural elucidation of $Cu(TPZ)_2$-loaded liposomes. TEM images of DOPC:Chol:DSPE-PEG_{2000} (5 mM, 95:50:5 molar ratio) liposomes incubated for 30 min at 55 ºC with $Cu(TPZ)_2$ at varying lipid-to-complex molar ratios of A) 1:0, (empty); B) 140:1 and C) 60:1, followed by purification. Micrographs were taken after staining with 2% uranyl acetate. Each panel is representative of at least 5 images per condition.

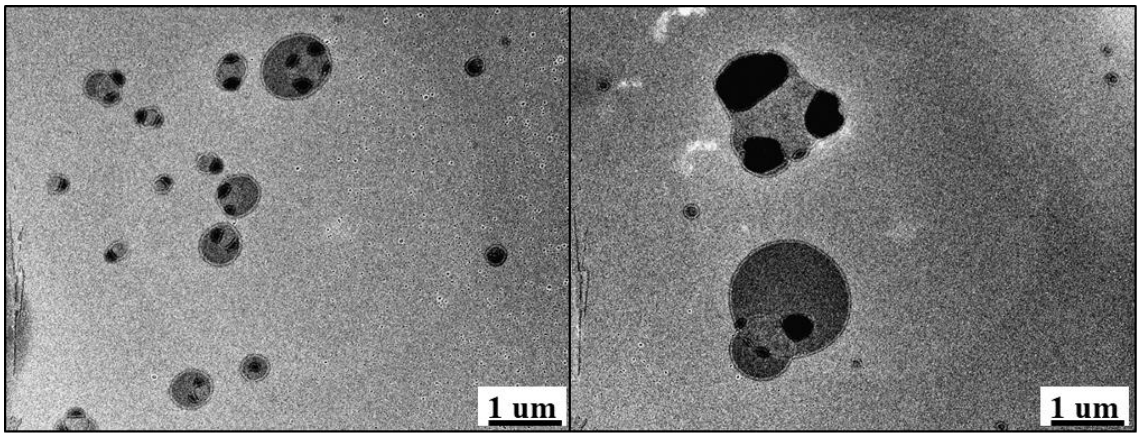

Figure A2. Structural elucidation of $Cu(TPZ)_2$-loaded liposomes. TEM images of DOPC:Chol:DSPE-PEG_{2000} (5 mM, 95:50:5 molar ratio) liposomes incubated for 30 min at 55 ºC with $Cu(TPZ)_2$ at 20:1 lipid-to-complex molar ratios, followed by purification. Micrographs were taken after staining with 2% uranyl acetate.